

Rangefinding in Fire Smoke Environments

Joseph Wesley Starr

Dissertation submitted to the faculty of the Virginia Polytechnic Institute and State University in partial fulfillment of the requirements for the degree of

Doctor of Philosophy
In
Mechanical Engineering

Brian Y. Lattimer, Co-Chair
Alexander Leonessa, Co-Chair
Alfred L. Wicks
Daniel Stilwell
Daniel D. Lee

November 30, 2015
Blacksburg, VA

Keywords: Long-wavelength infrared, thermal infrared, stereo vision, fire, smoke, sensor fusion, LIDAR

Rangefinding in Fire Smoke Environments

Joseph Wesley Starr

ABSTRACT

The field of robotics has advanced to the point where robots are being developed for use in fire environments to perform firefighting tasks. These environments contain varying levels of fire and smoke, both of which obstruct robotic perception sensors. In order to effectively use robots in fire environments, the issue of perception in the presence of smoke and fire needs to be addressed. The goal of this research was to address the problem of perception, specifically rangefinding, in fire smoke environments.

A series of tests were performed in fire smoke filled environments to evaluate the performance of different commercial rangefinders and cameras as well as a long-wavelength infrared (LWIR) stereo vision system developed in this research. The smoke was varied from dense, low temperature smoke to light, high temperature smoke for evaluation in a range of conditions. Through small-scale experiments on eleven different sensors, radar and LWIR cameras outperformed other perception sensors within both smoke environments. A LWIR stereo vision system was developed for rangefinding and compared to radar, LIDAR, and visual stereo vision in large-scale testing, demonstrating the ability of LWIR stereo vision to rangefind in dense smoke when LIDAR and visual stereo vision fail.

LWIR stereo vision was further developed for improved rangefinding in fire environments. Intensity misalignment between cameras and stereo image filtering were addressed quantitatively. Tests were performed with approximately isothermal scenes and thermally diverse scenes to select subsystem methods. In addition, the effects of image filtering on feature distortion were assessed. Rangefinding improvements were quantified with comparisons to ground truth data.

Improved perception in varying levels of clear and smoke conditions was developed through sensor fusion of LWIR stereo vision and a spinning LIDAR. The data were fused in a multi-resolution 3D voxel domain using evidential theory to model occupied

and free space states. A heuristic method was presented to separate significantly attenuated LIDAR returns from low-attenuation returns. Sensor models were developed for both return types and LWIR stereo vision. The fusion system was tested in a range of conditions to demonstrate its ability for improved performance over individual sensor use in fire environments.

Dedication

I dedicate this work to my friends and family for their help and encouragement – and most importantly to God, for everything.

Acknowledgements

I want to thank and acknowledge

- Professor Brian Lattimer for the opportunity to join and research in the EXTREME Lab to work with robots and fire and for guidance and assistance on the dissertation research and other research
- Professors Alexander Leonessa, Alfred Wicks, Daniel Stilwell, and Daniel Lee on my committee for direction and high-quality support along the way
- All of the non-committee professors who have provided great help during undergraduate and graduate studies, especially Professor Robert West for all of the assistance and advice beginning before the start of the undergraduate research project and continuing since
- The Mechanical Engineering office ladies, especially Jackie Woodyard for countless times assisting with purchases and travel arrangements
- The other Mechanical Engineering faculty and staff who have provided assistance, especially Ben Poe and Jamie Archual with computer-related assistance and encouraging support
- My old teachers and sport coaches, especially those who have had a large influence on my life
- The EXTREME Lab members, for all of the assistance and encouragement, both in and out of the academic environment along the way, especially
 - Josh McNeil, for all of the hard work in the tasks we've completed together for the SAFFiR project and other projects over the last 5 years
 - Jong-Hwan Kim and Brian Keller, for the hard work put into the SAFFiR project and the continuing support after
 - Christian, Nahid, and Patrick, for the assistance throughout the years
- The Combustion System Dynamics Lab (CSDL), Reacting Flows Lab (RFL), and the Terrestrial Robotics Engineering and Controls (TREC) lab members for assistance in undergraduate and graduate studies
- My family for a high-level of support and encouragement, especially, Mom and Dad; Ben and Michael and their wives; Kent, Jen, and Jake; and Grandma
- My other friends, for great encouragement and assistance, especially those from Christ's Church at Virginia Tech (CCVT), Mountain View Christian Academy, and the Alleghany Church of Christ
- And most importantly God for everything, especially salvation in the Lord Jesus Christ
 - "who gave Himself for us to redeem us from every lawless deed, and to purify for Himself a people for His own possession, zealous for good deeds." (Titus 2:14, NASB)

Table of Contents

ABSTRACT	ii
Dedication	iv
Acknowledgements	v
Table of Contents	vi
List of Figures	xi
List of Tables	xvii
Nomenclature	xviii
1 Introduction	1
1.1 Previous Work on Rangefinders in Environments with Obscurants	1
1.2 Research Contributions	3
1.2.1 Quantification of rangefinder and camera performance in fire smoke conditions	4
1.2.2 Development of LWIR stereo vision system architecture for rangefinding in fire environments	4
1.2.3 Development of a sensor fusion method to combine LWIR stereo vision and a spinning LIDAR for improved rangefinding in fire environments	4
1.3 Overview	5
1.4 References	7
2 Evaluation of Navigation Sensors in Fire Smoke Environments*	9
2.1 Introduction	9
2.2.1 Small-Scale Smoke Layer Apparatus	13
2.2.2 Small-Scale Experiment Sensors	15
2.2.3 Large-Scale Test Facility	15
2.2.4 Large-Scale Experiment Sensors	16
2.2.5 Experimental Procedure	17
2.3 Results	17
2.3.1 Small-Scale Results	17
2.3.1.1 LIDAR	18
2.3.1.2 Sonar	20
2.3.1.3 Visible Region Cameras	21
2.3.1.4 Kinect™ Distance Sensor	22
2.3.1.5 Thermal IR Cameras	22
2.3.1.6 Night Vision	23
2.3.1.7 Radar Rangefinder	24

2.3.2	Large-Scale Results.....	25
2.4	Discussion of Results.....	28
2.5	Conclusion.....	31
2.6	References.....	33
3	Stereoscopic Vision System using Long-Wave IR Thermal Imagers.....	38
3.1	Introduction.....	38
3.1.1	Challenges with LWIR Stereo Vision.....	38
3.1.2	Previous Work with LWIR Stereo Vision.....	38
3.1.3	Focus of Research.....	40
3.2	LWIR Stereo Vision System Description.....	40
3.2.1	Intensity Alignment.....	41
3.2.2	Stereo Image Filtering.....	43
3.2.3	Calibration/Rectification.....	43
3.2.4	Noise Handling with Matching Algorithm Selection.....	44
3.2.5	Disparity Post-Processing.....	44
3.3	Test Scenario Description.....	45
3.4	Intensity Alignment.....	46
3.4.1	Evaluation Details.....	46
3.4.2	Results and Discussion.....	47
3.5	Noise Filtering.....	59
3.5.1	Stereo Matching Performance.....	59
3.5.1.1	Evaluation Details.....	59
3.5.1.1.1	Object Location.....	63
3.5.1.1.2	Boundary Location.....	66
3.5.1.2	Results and Discussion.....	67
3.5.1.2.1	Object Location.....	67
3.5.1.2.2	Boundary Location.....	71
3.5.1.2.3	Overall.....	76
3.5.2	Effects on Feature Distortion.....	76
3.5.2.1	Evaluation Details.....	76
3.5.2.2	Results and Discussion.....	77
3.6	Conclusions and Proposed Approach.....	81
3.7	References.....	83
4	Evidential Sensor Fusion of LWIR Stereo Vision and 3D-LIDAR for Ranging in Fire Environments.....	87

4.1	Introduction to Fusion System	87
4.1.1	Challenges with Rangefinding in Fire Environments	87
4.1.2	Background of Relevant Research	88
4.1.3	Chapter Focus.....	88
4.2	Fusion Process	90
4.2.1	Fusion Space	90
4.2.2	Evidential Fusion Method	91
4.2.2.1	Basic Probability Assignments from Sensor models	92
4.2.2.1.1	LIDAR Basic Probability Assignments	94
4.2.2.1.2	LWIR Basic Probability Assignments	95
4.2.2.2	Evidential Fusion of Basic Probability Assignments.....	95
4.2.3	Application of Fusion Method	96
4.2.4	Fusion Process Components	97
4.2.4.1	LIDAR Pre-Processing.....	97
4.2.4.2	LWIR Stereo Vision Pre-Processing.....	99
4.2.4.3	Sensor Models	100
4.2.4.3.1	3D LIDAR (Low-Attenuation and High-Attenuation).....	100
4.2.4.3.2	LWIR Stereo Vision.....	102
4.3	Experimental Method for Fusion Evaluation.....	105
4.3.1	Sensors	105
4.3.1.1	Spinning LIDAR	105
4.3.1.2	LWIR Stereo Vision System.....	106
4.3.2	Hallway Fire Environment Test Setup.....	106
4.3.3	SAFFiR Demonstration Test Setup.....	107
4.4	Results and Discussion	107
4.4.1	Hallway Fire Environment	107
4.4.1.1	Smoke Separation.....	107
4.4.1.2	Evidential Fusion during Latex Foam Test	110
4.4.1.2.1	Visual and LWIR Imagery	110
4.4.1.2.2	Evidential Fusion Results.....	112
4.4.2	SAFFiR Demonstration.....	126
4.5	Conclusion	129
4.6	References.....	132
5	Conclusion and Recommendations.....	134

5.1	Conclusion	134
5.2	Recommendations.....	136
Appendix A: Smoke Characterization		138
A.1	Introduction.....	138
A.2	Optical Properties of Smoke	138
A.2.1	General Energy Transfer through a Volume	138
A.2.2	General Energy Transfer through a Volume	139
A.2.3	Energy Transfer through Smoke	140
A.2.3.1	Gases	141
A.2.3.2	Liquids and Solids.....	141
A.2.3.3	Summary of Important Smoke Quantities.....	144
A.3	Experimental Approach	144
A.3.1	Test Setup.....	145
A.3.2	Fuel Types.....	145
A.3.3	Instrumentation.....	146
A.3.3.1	Laser Extinction System.....	146
A.3.3.2	Gravimetric Filtering.....	147
A.3.3.3	Electron Microscopy	148
A.3.3.4	Particle Analyzers (DRX, OPS).....	149
A.4	Results.....	150
A.4.1	Temperature	150
A.4.2	Laser Extinction Measurements	151
A.4.3	Gravimetric Filtering.....	153
A.4.3.1	Latex Foam Smoke.....	153
A.4.3.2	Propane Smoke.....	153
A.4.3.3	Wood Smoke	154
A.4.4	Particulate Physical Characteristics	155
A.4.4.1	Particulate Composition	155
A.4.4.2	Particulate Size and Shape	156
A.4.5	Particle Size Distribution	160
A.4.5.1	Latex Foam Smoke.....	160
A.4.5.2	Propane Smoke.....	162
A.4.5.3	Wood Smoke	164
A.5	Discussion.....	166

A.5.1	Gravimetric Filtering and Particle Analyzer Concentration Comparisons	166
A.5.2	Laser Extinction and Concentration Data Consistency with Literature	168
A.5.3	Expected Smoke Effects on Electromagnetic Sensors	170
A.6	Conclusion	170
A.7	References.....	171
Appendix B:	Bi-Directional SAD Stereo Correspondence Matching	174
Appendix C:	Filter Algorithm Descriptions	177
Appendix D:	LIDAR and LWIR Stereo Vision Alignment.....	189
Appendix E:	Tabulated Results for LWIR Stereo Vision System Filter Tests.....	191
Appendix F:	Analysis of Performance of Top LWIR Stereo Vision Image Filters.....	196
Appendix G:	Discussion of LIDAR Intensity Variations	210
Appendix H:	Algorithms for Sensor Model Application.....	212
Appendix I:	Permissions	215

List of Figures

Figure 1: Fire scenario in hallway test facility.....	1
Figure 2: Rangefinding sensors plotted with the electromagnetic and acoustic spectrums.	10
Figure 3: Experimental setup.....	13
Figure 4: Large-scale test facility.	16
Figure 5: Visibility and temperature data for the (a) high temperature tests and (b) dense smoke tests.....	18
Figure 6: Hokuyo UTM-30LX single-echo LIDAR results with smoke at different visibility levels.....	19
Figure 7: IBEO Lux multi-echo LIDAR results for smoke at different visibility levels. The outside of the test rig is outlined in gray.....	20
Figure 8: Sonar results for (a) light, high temperature smoke and (b) dense, low temperature smoke.....	21
Figure 9: Visual camera results using an edge detection algorithm for a dense, low temperature smoke test.	22
Figure 10: KinectTM depth sensor results for (a) no-smoke, (b) light, high temperature smoke with a bright and interfering smoke source, and (c) dense, low temperature smoke.....	22
Figure 11: Thermal IR camera results for (a) no smoke, (b) light, high temperature smoke, and (c) dense, low temperature smoke.	23
Figure 12: Night Vision Results for (a) no smoke, (b) light, high temperature smoke, and (c) dense, low temperature smoke.	24
Figure 13: 26 GHz radar results for (a) light, high temperature smoke and (b) dense, low temperature smoke.....	24
Figure 14: (a) Hallway ceiling gas temperature data and (b) middle of the hallway vertical gas temperature data for the large-scale experiment.....	25
Figure 15: Visibility data for the large-scale experiment.	26
Figure 16: LIDAR large-scale test results.	27
Figure 17: Radar large-scale test results not varying in clear or smoke conditions.	28
Figure 18: The effect of visibility on LIDAR, sonar, and radar rangefinders (left axis) and a visual camera (right axis).....	29
Figure 19: LWIR stereo vision system.	41
Figure 20: Example of the intensity offset changing with time between (a) a stereo pair of an initial room-temperature hallway and (b) a stereo pair taken later in time with fire smoke heating the upper portion of the hallway.....	42
Figure 21: Image of a cold metal grid in front of a heated LCD monitor (a) before application of calibration and (b) after application of calibration.	44
Figure 22: Approximately isothermal scene image pairs (a) before intensity alignment, (b) after application of the offset method for intensity alignment, and (c) after application of the linear scaling method for intensity alignment.....	49
Figure 23: Thermally diverse scene image pairs (a) before intensity alignment, (b) after application of the offset method for intensity alignment, and (c) after application of the linear scaling method for intensity alignment.....	50

Figure 24: Pair of images for the scene with fire present (a) before intensity alignment, (b) after application of the offset method for intensity alignment, and (c) after application of the linear scaling method for intensity alignment..... 51

Figure 25: Histograms for the left and right images for the approximately isothermal scene for (a) the original data, (b) intensity alignment with the offset method, and (c) intensity alignment with the linear fitting method. 53

Figure 26: Histograms for the left and right images for the thermally diverse scene for (a) the original data, (b) intensity alignment with the offset method, and (c) intensity alignment with the linear fitting method..... 54

Figure 27: Histograms for the left and right images for the scene with fire present for (a) the original data, (b) intensity alignment with the offset method, and (c) intensity alignment with the linear fitting method..... 55

Figure 28: Epipolar line plots for the approximately isothermal scene for (a) the original data, (b) intensity alignment with the offset method, and (c) intensity alignment with the linear fitting method..... 56

Figure 29: Epipolar line plots for the thermally diverse scene for (a) the original data, (b) intensity alignment with the offset method, and (c) intensity alignment with the linear fitting method..... 57

Figure 30: Epipolar line plots for the scene with fire present for (a) the original data, (b) intensity alignment with the offset method, and (c) intensity alignment with the linear fitting method..... 57

Figure 31: Top view of setup for object detection stereo matching evaluation of filters. 64

Figure 32: Top view of hallway setup for boundary location evaluation of filters. 66

Figure 33: Unfiltered LWIR view of the object detection scene for (a) the approximately isothermal case and (b) the thermally diverse case..... 68

Figure 34: Accurate, inaccurate, and accurate minus inaccurate matches for the top filter parameter and stereo parameter settings for each filter for the approximately isothermal scene..... 68

Figure 35: Accurate, inaccurate, and accurate minus inaccurate matches for the top filter parameter and stereo parameter settings for each filter for the thermally diverse scene. 69

Figure 36: Accurate, inaccurate, and accurate minus inaccurate matches for the top filter parameter and stereo parameter settings for each filter for the combined scenes. 70

Figure 37: Left image for boundary location for (a) the approximately isothermal scene, (b) the thermally diverse scene; (c) ground truth from the LIDAR..... 72

Figure 38: Accurate, inaccurate, and accurate minus inaccurate matches for the top filter parameter and stereo parameter settings for each filter for the approximately isothermal scene..... 73

Figure 39: Accurate, inaccurate, and accurate minus inaccurate matches for the top filter parameter and stereo parameter settings for each filter for the thermally diverse scene. 74

Figure 40: Accurate, inaccurate, and accurate minus inaccurate matches for the top filter parameter and stereo parameter settings for each filter for the combined scenes. 75

Figure 41: Process for evaluation of filter effects on feature detection using the Hough Transform for circles..... 77

Figure 42: Feature detection results for top filters from the object detection tests for (a) the approximately isothermal scene, (b) the thermally diverse scene, and (c) the combined scenes.	79
Figure 43: Feature detection results for top filters from the boundary location tests for (a) the approximately isothermal scene, (b) the thermally diverse scene, and (c) the combined scenes.	80
Figure 44: Recommended LWIR Stereo Vision System Architecture.	82
Figure 45: Hallway scene (a) with partially blocked LIDAR system due to smoke compared to (b) scene before smoke presence. Lighter values indicate closer distance out from the sensor.	87
Figure 46: Horizontal 2D slice multi-resolution view of a hallway scene for (a) the occupied voxel array and (b) the free space voxel array, along with (c) the layout of the boundaries of the hallway.	91
Figure 47: Sample sensor model giving basic probability assignment (evidence) versus distance to and beyond the nominal return distance.	93
Figure 48: (a) Application of the sensor model in Figure 47 to produce 2D maps of occupied and free space evidence and (b) thresholded evidence data for indication of free and occupied space.	94
Figure 49: Sensor fusion application.	97
Figure 50: Intensity-distance plots for a hallway environment (a) for clear conditions, (b) in smoke conditions, and (c) in smoke conditions with outliers removed.	98
Figure 51: Low-attenuation and high-attenuation point cloud separator.	99
Figure 52: LWIR stereo vision pre-processing method.	100
Figure 53: Sensor model for a return at 2.002 m showing (a) occupied evidence for low-attenuation returns and (b) free space evidence for low-attenuation and high-attenuation returns.	101
Figure 54: Plots of sample points for the LWIR stereo vision occupied state sensor model: (a) evidence distributed over more grid spaces at further distances, (b) evidence higher for higher costs, and (c) evidence higher for more points affecting the location.	103
Figure 55: Example application of the free space sensor model for the LWIR stereo vision system.	104
Figure 56: Robot head setup of LIDAR and LWIR cameras.	105
Figure 57: Hallway setup for the latex foam fire smoke test.	106
Figure 58: SAFFiR test scenario.	107
Figure 59: Smoke removal at several frames for a horizontal slice along the top and bottom of the hallway (a) as smoke is entering, (b) once smoke is dense, and (c) as smoke is thinning. Open red boxes indicate correct boundary returns from the LIDAR when comparing the data to the baseline data of the hallway boundaries. Blue dots denote returns removed due to the smoke separation algorithm. Black “x” marks are used to indicate smoke returns that were not removed from the low-attenuation LIDAR point cloud.	109
Figure 60: Percentage of smoke points not removed from low-attenuation point cloud by the smoke separation algorithm.	110
Figure 61: Visual images during the latex foam test (a) before the fire, (b) as smoke is entering, (c) as the smoke is becoming dense, and (d) once the smoke is dense.	111

Figure 62: Raw LWIR images before processing and with linear scaling to 8-bit data type for viewing during the latex foam test (a) before the fire, (b) as smoke is entering, (c) when smoke is dense, and (d) as smoke is thinning.	112
Figure 63: 3D view of baseline occupied state data in multi-resolution voxel domain..	113
Figure 64: Occupied state results for the LIDAR, LWIR stereo vision system, and evidential fusion for several frames at the beginning of testing.	114
Figure 65: Occupied state results for the LIDAR, LWIR stereo vision system, and evidential fusion for several frames at the beginning of testing.	115
Figure 66: 2D horizontal slice views of upper and lower elevations for frame 10, before the smoke is in view.....	117
Figure 67: 2D horizontal slice views of upper and lower elevations for frame 15, as the smoke enters the scene.....	118
Figure 68: 2D horizontal slice views of upper and lower elevations for frame 20, when the smoke is almost at its maximum thickness.	119
Figure 69: 2D horizontal slice views of upper and lower elevations for frame 25, when the smoke is thickest.	120
Figure 70: 2D horizontal slice views of upper and lower elevations for frame 75, as the smoke is thinning.	121
Figure 71: Accuracy for (a) occupied and (b) free space voxel data, overall.	122
Figure 72: Inaccuracy for (a) occupied and (b) free space voxel data, overall.....	123
Figure 73: Accuracy for (a) occupied and (b) free space voxel data, upper 2D slice.....	124
Figure 74: Inaccuracy for (a) occupied and (b) free space voxel data, upper 2D slice. .	124
Figure 75: Accuracy for (a) occupied and (b) free space voxel data, lower 2D slice.....	125
Figure 76: Inaccuracy for (a) occupied and (b) free space voxel data, lower 2D slice. .	125
Figure 77: LWIR image from the SAFFiR demonstration, (a) filtered, and (b) filtered and zoomed-in for comparison to point cloud data.	127
Figure 78: Occupied state results for the SAFFiR demonstration for (a) LIDAR with high-attenuation returns separation, (b) LIDAR without high-attenuation returns separation, (c) LWIR stereo vision, and (d) evidential sensor fusion.....	128
Figure 79: 2D horizontal slice views of upper and lower elevations for the SAFFiR demonstration data.	129
Figure 80: Radiation through a control volume around a medium.	139
Figure 81: Blackbody spectral emissive power from Planck’s Law for a blackbody emitting in air for four temperatures.	140
Figure 82: Venn diagram showing some methods of determining scattering effects of particles on radiation. Sources in the diagram are (a) [1], (b) [9, 10], and (c) [11].	142
Figure 83: Hallway setup for smoke characterization tests.	145
Figure 84: Filter-based system for obtaining smoke particulate concentration, particulate composition, particulate shape, and particulate size.	147
Figure 85: Latex fire smoke temperature measurements along the ceiling for (a) the room and (b) the hallway.....	150
Figure 86: Propane fire smoke temperature measurements along the ceiling for (a) the room and (b) the hallway.	151
Figure 87: Wood fire smoke temperature measurements along the ceiling for (a) the room and (b) the hallway.....	151

Figure 88: Intensity ratio data for (a) latex foam smoke, (b) propane smoke, and (c) wood smoke.	152
Figure 89: EDS analysis results: (a) image showing carbon from smoke (red) and silicon from filter strands (green) and (b) corresponding spectrum output plot for the image with carbon and silicon labeled.....	155
Figure 90: FESEM imaging results of filter for (a) latex foam smoke, (b) propane smoke, and (c) wood smoke at two magnification settings.....	157
Figure 91: ESEM imaging results for agglomerate collection for (a) latex foam smoke, (b) propane smoke, and (c) wood smoke at a two magnification settings.....	159
Figure 92: TSI DustTrak DRX results for the latex foam test showing concentrations for all bins.....	160
Figure 93: TSI DustTrak DRX results for the latex foam test showing the first bin and concentrations between bins.	161
Figure 94: TSI Model 3330 OPS results for the latex foam test.....	162
Figure 95: TSI DustTrak DRX results for the propane test showing concentrations for all bins.....	163
Figure 96: TSI DustTrak DRX results for the propane test showing the first bin and concentrations between bins.	163
Figure 97: TSI Model 3330 OPS results for the propane test.....	164
Figure 98: TSI DustTrak DRX results for the wood test showing concentrations for all bins.....	165
Figure 99: TSI DustTrak DRX results for the wood test showing the first bin and concentrations between bins.	165
Figure 100: TSI Model 3330 OPS results for the wood test.....	166
Figure 101: Images of LWIR stereo vision and LIDAR alignment for a hallway scene: (a) aligned LIDAR output of expected disparity map for the left LWIR camera frame; (b) left LWIR image of the scene after calibration and rectification processing; (c), (d) merged image of LIDAR disparity data and LWIR left image.	190
Figure 102: Effects from Non-Local Means filter on a row across both targets in the approximately isothermal scene for the object location tests. The top performing setting is shown (“Search area box size” = 5) and the results with a smaller search box is shown (“Search area box size” = 2).	197
Figure 103: Effects from the StereoAvgST filter on a row across both targets in the approximately isothermal scene for the object location tests. The “Number of frames” is shown for the top case for the approximately isothermal scene (7), for the thermally diverse scene (11), and for the combined scene (9).	199
Figure 104: Effects from the StereoAvgST filter on a row across both targets in the thermally diverse scene for the object location tests. The “Number of frames” is shown for the top case for the approximately isothermal scene (7), for the thermally diverse scene (11), and for the combined scene (9): (a) view of the entire row and (b) zoomed-in view at the left side of the left target.	199
Figure 105: Effects from the StereoWienFC (consecutive Wiener) filter on a row across both targets in the approximately isothermal scene for the object location tests for the top case number of passes (9) and two other values for “Number of consecutive applications”.	201

Figure 106: Effects from the StereoWienFC (consecutive Wiener) filter on a row across the hallway in the approximately isothermal scene for the boundary location tests for two settings: (a) lower portion of the hallway and (b) upper portion of the hallway.	202
Figure 107: Effects from the StereoWienFC (consecutive Wiener) filter on a row across the hallway in the thermally diverse scene for the boundary location tests for two settings: (a) lower portion of the hallway and (b) upper portion of the hallway.	202
Figure 108: Zoomed-in view showing effects from the StereoWienFC (consecutive Wiener) filter on a row across the upper portion of the hallway in the thermally diverse scene for the boundary location tests for two settings.....	203
Figure 109: Effects from the StereoAniDif function on a lower and upper row across the hallway in the approximately isothermal scene for the boundary location tests: (a) lower row and (b) upper row.	204
Figure 110: Effects from the StereoAniDif function on a lower and upper row across the hallway in the thermally diverse scene for the boundary location tests: (a) lower row and (b) upper row.....	205
Figure 111: Zoomed-in view of the area around the peak intensity shown in the upper row plot of the last figure for the thermally diverse scene for the boundary location tests.	205
Figure 112: Filter results from top performing filters for the approximately isothermal scene for the object location tests.	206
Figure 113: Filter results from top performing filters for the thermally diverse scene for the object location tests.	207
Figure 114: Zoomed-in view of (a) the left target and (b) the right target for the thermally diverse scene for the object location tests for top performing filter settings.	207
Figure 115: Effects from top performing filters for the approximately isothermal scene for the boundary location tests: (a) lower row and (b) upper row.	208
Figure 116: Effects from top performing filters for the thermally diverse scene for the boundary location tests: (a) lower row and (b) upper row.....	208
Figure 117: Intensity information for a hallway scene. (a) Intensity values scaled from 0 to max intensity with 0 indicating no return; (b) Intensity values with an added constant to differentiate low intensity values from locations with no LIDAR return information; (c) corresponding disparity information from the LIDAR; (d) IR image of the hallway after a test.....	211

List of Tables

Table 1: Sensors evaluated in study.....	15
Table 2: Distance to targets measured using vision systems.	26
Table 3: Summary of sensor performance in the small-scale smoke layer experiment....	29
Table 4: Change in feature intensities for both methods for the scenes.	58
Table 5: Filters under consideration for LWIR stereo vision noise removal.....	60
Table 6: Filter parameters.	62
Table 7: Target closest and second-closest disparity values.....	65
Table 8: Stereo matching settings: “Box size” determines the window size for the matching algorithm, and “Match quality cutoff between best and second-best match” limits the disparity map to only contain top-matching disparity values if they have a high enough cost compared to the next-best matched disparity value.....	65
Table 9: Parameters used for filters for feature detection tests. The parameters are in the same order as the previous tables.....	78
Table 10: Flow times for gravimetric sampling.....	148
Table 11: Propane and wood intensity ratios for different times during the tests.	152
Table 12: Concentration measurement data from the gravimetric sampling for latex foam.	153
Table 13: Concentration measurement data from the gravimetric sampling for propane.	154
Table 14: Concentration measurement data from the gravimetric sampling for wood. .	155
Table 15: Intensity ratio results for propane.....	169
Table 16: Intensity ratio results for wood.	169
Table 17: Parameter values for each filter for top performance for the object detection tests.	192
Table 18: Stereo settings for top filter settings for the object detection tests.	193
Table 19: Parameter values for each filter for top performance for the boundary location tests.	194
Table 20: Stereo settings for top filter settings for the boundary location tests.	195

Nomenclature

Symbol	Description	Units	Chapters/ Appendix
β	Extinction coefficient	$1/m$	2, A
L_P	Path length through obscurant	m	2, A
I_0	Intensity entering a control volume	W/m^2	2, A
I, I_λ	Intensity leaving a control volume	W/m^2	2, A
V	Visibility	m	2, A
C	Empirical constant for visibility equation	–	2, A
c	Speed of sound	m/s	2
γ	Specific heat ratio of a medium	–	2
R	Gas constant of a medium	$J/(kg * K)$	2
T	Temperature	K	2, A
R	Original right IR image (matrix of intensities)	(arbitrary)	3, B
R'	Updated right IR image (matrix of intensities)	(arbitrary)	3
\bar{R}	Mean of right IR image	(arbitrary)	3
L	Original left IR image (matrix of intensities)	(arbitrary)	3, B, C
L'	Updated left IR image (matrix of intensities)	(arbitrary)	3
\bar{L}	Mean of left IR image	(arbitrary)	3
u	Row location of pixel in IR image	pixels	3, B, C
v	Column location of pixel in IR image	pixels	3, B, C
L'_{upper}	Mask of IR image intensities greater than IR image mean, left image	–	3
L'_{lower}	Mask of IR image intensities less than IR image mean, left image	–	3
R'_{upper}	Mask of IR image intensities greater than IR image mean, right image	–	3
R'_{lower}	Mask of IR image intensities less than IR image mean, right image	–	3
$L'_{mean,up}$	Mean of IR image intensities greater than IR image mean, left image	(arbitrary)	3
$L'_{mean,low}$	Mean of IR image intensities less than IR image mean, left image	(arbitrary)	3
$R'_{mean,up}$	Mean of IR image intensities greater than IR image mean, right image	(arbitrary)	3
$R'_{mean,low}$	Mean of IR image intensities less than IR image mean, right image	(arbitrary)	3
Θ	Set of possible states	–	4
Occ	Occupied space state	–	4, H
F	Free space state	–	4, H
A	Set of all subsets of possible states	–	4, H
\emptyset	Null case	–	4, H
$\{Occ, F\}$	Ignorance of cases	–	4, H
i, j, k	Index for voxel location for x, y, and z directions	–	4, H

$Case$	Subset of A	—	4, H
S_{Occ}	Basic probability assignment for the occupied space state	—	4
S_F	Basic probability assignment for the free space state	—	4
$S_{\{Occ,F\}}$	Basic probability assignment for ignorance of occupied or free space states	—	4
$voxels_{i,j,k}$	Voxel located at location i, j, k	—	4, H
$m_{i,j,k}$	Set of basic probability assignments for voxel at location i, j, k	—	4
$S_{Occ,L}$	Basic probability assignment for the occupied space state from the LIDAR sensor model	—	4, H
$S_{F,L}$	Basic probability assignment for the free space state from the LIDAR sensor model	—	4, H
$S_{\{Occ,F\},L}$	Basic probability assignment for ignorance of occupied or free space states from the LIDAR sensor model	—	4, H
$m_{i,j,k,L}$	Set of basic probability assignments for voxel at location i, j, k from the LIDAR sensor model	—	4, H
$S_{Occ,IR}$	Basic probability assignment for the occupied space state from the LWIR stereo vision sensor model	—	4, H
$S_{F,IR}$	Basic probability assignment for the free space state from the LWIR stereo vision sensor model	—	4, H
$S_{\{Occ,F\},IR}$	Basic probability assignment for ignorance of occupied or free space states from the LWIR stereo vision sensor model	—	4, H
$m_{i,j,k,IR}$	Set of basic probability assignments for voxel at location i, j, k from the LWIR stereo vision sensor model	—	4, H
m_L	Shortened term for $m_{i,j,k,L}$	—	4
m_{IR}	Shortened term for $m_{i,j,k,IR}$	—	4
m_{Fused}	Set of basic probability assignments for a voxel from sensor fusion	—	4
E	Electromagnetic emission	$\frac{W}{m^2 * \mu m * sr}$	A
κ_λ	Absorption coefficient	—	A
$I_{\lambda,b}$	Blackbody radiation	$\frac{W}{m^2 * \mu m * sr}$	A
C_1	First constant for blackbody radiation equation	$\frac{W * \mu m^4}{m^2 * sr}$	A
C_2	Second constant for blackbody radiation equation	$\frac{\mu m * K}{m^2 * sr}$	A
n	Index of refraction	—	A
λ	Wavelength	μm	A
σ_λ	Scattering coefficient	—	A
$Q_{\lambda,a}$	Absorption efficiency factor	—	A
$Q_{\lambda,s}$	Scattering efficiency factor	—	A

D_p	Particle diameter	μm	A
N	Number concentration of particles (particles per volume)	$\#/m^3$	A
σ_s	Mass specific extinction coefficient	m^2/g	A
M_s	Mass concentration of smoke	g/m^3	A
τ_λ	Optical thickness	–	A
Z	Distance from stereo cameras	m	B
<i>Baseline</i>	Baseline distance between cameras	m	B, H
<i>Focal</i>	Focal length	<i>pixels</i>	B, H
d	Disparity value	<i>pixels</i>	B
C_L	SAD cost value for the left image	(<i>arbitrary</i>)	B
W	Spatial window of intensities centered at pixel of interest	–	B, C
d_{min}	Minimum disparity value allowed in calculations	<i>pixels</i>	B
d_{max}	Maximum disparity value allowed in calculations	<i>pixels</i>	B
$d_{selected,L}$	Selected disparity value for the left image at one pixel location	<i>pixels</i>	B
C_R	SAD cost value for the right image	(<i>arbitrary</i>)	B
$d_{selected,R}$	Selected disparity value for the right image at one pixel location	<i>pixels</i>	B
$d'_{selected,R}$	Selected disparity value for the right image at one pixel location translated to the left camera's frame of reference	<i>pixels</i>	B
L_{Out}	Filtered left IR image (intensity matrix)	(<i>arbitrary</i>)	C
a	Window size parameter based on "Box size"	<i>pixels</i>	C
u_2	Row location of pixel in IR image within spatial window	<i>pixels</i>	C
v_2	Column location of pixel in IR image within spatial window	<i>pixels</i>	C
h	Color closeness strength parameter	(<i>arbitrary</i>)	C
G_w	Spatial closeness strength window	–	C
f	Current frame number for temporal filtering	–	C
f_N	Frame number within set of frames used for temporal filtering	–	C
N_S	Box (kernel) size for spatial filtering	<i>pixels</i>	C
N_T	Total number of frames for temporal filtering	–	C
<i>Top</i>	Value of numerator in calculation of StereoWMeanST filter results	(<i>arbitrary</i>)	C
<i>Bottom</i>	Value of denominator in calculation of StereoWMeanST filter results	–	C
p_S	Power value for spatial closeness weight	–	C
p_T	Power value for temporal closeness weight	–	C
\bar{W}	Mean of spatial window of intensities centered at pixel of interest	(<i>arbitrary</i>)	C
v_f	Local variance of spatial window of intensities centered at pixel of interest	–	C

o_n	Assumed noise variance in image	–	C
g	“Gamma” parameter for StereoAniDif anisotropic diffusion filter	–	C
k	“K” parameter for StereoAniDif anisotropic diffusion filter	–	C
d_N	Measure of the intensity difference between the pixel of interest and the pixel above it	(arbitrary)	C
d_E	Measure of the intensity difference between the pixel of interest and the pixel to the right of it	(arbitrary)	C
d_W	Measure of the intensity difference between the pixel of interest and the pixel to the left of it	(arbitrary)	C
d_S	Measure of the intensity difference between the pixel of interest and the pixel below it	(arbitrary)	C
c_N	Function cost results for StereoAniDif filter based off of the intensity difference between the pixel of interest and the pixel above it	–	C
c_E	Function cost results for StereoAniDif filter based off of the intensity difference between the pixel of interest and the pixel to the right of it	–	C
c_W	Function cost results for StereoAniDif filter based off of the intensity difference between the pixel of interest and the pixel to the left of it	–	C
c_S	Function cost results for StereoAniDif filter based off of the intensity difference between the pixel of interest and the pixel below it	–	C
$Pres_O$	Binary indicator of presence of evidence for the occupied state for all voxels	–	H
$Cost_N$	Array for storing highest stereo matching cost affecting each voxel for the occupied state	–	H
$Disp_N$	Array for storing highest disparity affecting each voxel for occupied state	–	H
C_O	Array for counting number of points affecting each voxel for occupied state	–	H
C_F	Array for counting number of points affecting each voxel for free space state	–	H
$CostThresh$	Threshold for stereo matching cost effects	–	H
$Incr$	Amount to increment evidence based on number of points affecting each voxel for occupied or free space state	–	H
$HighProb$	Maximum value for evidence allowed	–	H
$Evid_O$	Array corresponding to voxel evidence for occupied state	–	H
$Evid_F$	Array corresponding to voxel evidence for free space state	–	H
N_d	Number of voxels affected by the maximum disparity	–	H

V_{x1}, V_{x2}, V_{x3} Arrays used in intermediate steps for determination of final LWIR stereo vision sensor model output for one point cloud — H

1 Introduction

The field of robotics has recently advanced to the point where robots are being developed for use in fire environments to assist with and perform firefighting tasks. These fire environments, such as the one shown in Figure 1, can contain varying levels of fire and smoke. Fire and smoke can each have adverse effects on sensor perception, as demonstrated in the figure where visual perception of the upper portion of the hallway is blocked by the smoke layer. Hindering of perception sensors can result in poor rangefinding to obstacles and boundaries in the environment, which leads to problems in navigation. In order to effectively use robots in fire environments, this issue of perception in the presence of smoke and fire needs to be addressed.



Figure 1: Fire scenario in hallway test facility.

1.1 Previous Work on Rangefinders in Environments with Obscurants

LIDAR is the most common rangefinder for robotic navigation, typically operating in the Near Infrared wavelength range (~ 0.7 to $1.5 \mu\text{m}$). Test data in the literature shows that LIDAR in this wavelength range can fail to provide accurate distances in the presence of fire smoke [1, 2]. This shows a need for alternative rangefinding technologies able to operate in smoke. Perception in environments with obscurants is part of an ongoing research focus in the literature addressing the problem of perception in harsh environments such as those containing smoke, fog, and dust.

Some of the solutions in the literature for better perception in smoke environments include the application of radar [3-6] and sonar [7].

Radar has been presented as capable of rangefinding harsh environments [3, 4]. Tests have shown the ability of a 76 GHz mm-wave Frequency-Modulated Continuous-Wave (FMCW) radar to range through smoke [3, 4], and Ultra Wide Band (UWB) radar has been shown to range in harsh environments such as fog, rain, and snow [5, 6]. A drawback to both systems is low resolution compared to LIDAR systems. A second drawback to both systems is that both technologies are still in development, not commercially available for direct robot integration. The UWB system has also been shown to perceive through vegetation [6], indicating the potential for the system to range through obstacles that should be detected for navigation purposes.

Sonar has also been presented as a rangefinder applicable to use in smoke environments [7]. A downside to this technology is that the speed of sound changes with temperature, which can cause distance accuracy errors if ranging through smoke with unknown thermal gradients present. Another drawback is that the beam angles are large, resulting in lower quality mapping results in clear environments compared to LIDAR mapping results.

Sensor fusion has been used to overcome sensor perception issues in some harsh environments. One example of using sensor fusion to overcome perception issues in smoke is a system designed to utilize LIDAR and sonar depending on the measured presence of smoke [8]. Although this system should have higher accuracy due to use of LIDAR in parts of the scene where smoke is not present, in regions where smoke is detected and the sonar is used without LIDAR returns, there will be the same accuracy issues inherent to individual use of sonar previously noted. Another system was devised to fuse LIDAR, visual stereo vision, and UWB radar into an occupancy grid for a mobile robot for use in harsh environments such as those with fog [9]. While the fusion of the sensors will improve perception in some scenarios with obscurant, it will still have the issues inherent to UWB radar in locations where the LIDAR and visual stereo vision are blocked by obscurant, such as the issue of UWB radar perceiving through vegetation.

An alternative rangefinding technology for smoke environments presented in this document is LWIR (long-wavelength infrared, ~ 7 to $14 \mu\text{m}$) stereo vision. Previous research on LWIR stereo vision includes the use of systems for human locating and tracking [14], medical equipment [15], and Unmanned Ground Vehicles [16]. LWIR visual odometry and stereo vision has been used on Unmanned Aerial Vehicles [17]. Work has also been performed for LWIR stereo vision use in indoor environments [18, 19]. From research on light attenuation in smoke at different wavelengths, the data indicate that smoke attenuation decreases with an increase in radiation wavelength [10, 11]. Currently, single LWIR thermal infrared cameras are being used by humans for perception in firefighting environments [12, 13]. While single LWIR imagers only provide intensity and/or temperature information, designing a vision system with two LWIR imagers allows for the application of stereo correspondence algorithms to provide depth information.

As with radar and sonar, there are difficulties in implementing LWIR stereo vision for rangefinding. Problems with LWIR stereo vision have been noted in the literature, such as low resolution [18], image noise [18], low texture regions [16], and difficulties in obtaining an accurate camera calibration [16]. Issues with camera intensity values have also been noted for some scenes when automatically reducing bit-depth of individual images of a stereo pair [16].

1.2 Research Contributions

This research addressed the issues with rangefinding in fire smoke environments. An assessment of sensor performance in smoke was made based on available literature and quantitative testing of available rangefinders and sensors. Based on test results, an initial LWIR stereo vision system was developed and tested against other rangefinders. The LWIR stereo vision system was further developed for improved rangefinding, by quantitatively addressing intensity misalignment between cameras and the issue of IR image noise. A final sensor fusion system was developed to combine LWIR stereo vision and a spinning LIDAR for improved rangefinding in a variety of conditions ranging from clear scenes to scenes partially or completely filled with smoke.

1.2.1 Quantification of rangefinder and camera performance in fire smoke conditions

The first comprehensive evaluation of robotic rangefinders and cameras in real fire smoke was conducted to identify the best performing sensor for future development in this study. Based on small-scale test results, large-scale testing on select sensor modalities was performed, quantitatively showing the abilities of LWIR stereo vision and radar to perceive through dense, low temperature smoke while other instruments such as LIDAR and visual stereo vision fail. The results of the small-scale and large-scale testing have been published in a journal article in *Fire Technology*, “Evaluation of Navigation Sensors in Fire Smoke Environments”. Results from the large-scale tests comparing LWIR stereo vision and LIDAR have been presented at the IEEE Sensors 2012 Conference and published, “A Comparison of IR Stereo Vision and LIDAR for Use in Fire Environments”; results from the tests comparing LWIR stereo vision and visual stereo vision have been presented at the AIM (Advanced Intelligent Mechatronics) 2013 Conference and published, “Application of Thermal Infrared Stereo Vision in Fire Environments”.

1.2.2 Development of LWIR stereo vision system architecture for rangefinding in fire environments

A LWIR stereo vision system architecture was developed based off of visual stereo vision system architectures but was improved for rangefinding in fire environments with the application of image processing steps prior to correspondence matching. Specifically, steps for addressing intensity misalignment between cameras and for stereo image filtering have been quantitatively selected for LWIR stereo vision, something not currently in the literature. Methods for the steps were quantitatively selected based off of their effects on approximately isothermal scenes and thermally diverse scenes. Filter selection in these two scene types was determined based on filter effects on object location and boundary location compared to ground truth information.

1.2.3 Development of a sensor fusion method to combine LWIR stereo vision and a spinning LIDAR for improved rangefinding in fire environments

A sensor fusion method has been developed to combine LWIR stereo vision and spinning LIDAR range data using evidential (Dempster-Shafer) theory in a 3D multi-resolution voxel space modeling occupied and free space. Significantly attenuated LIDAR returns have been

separated from low-attenuation LIDAR returns using a heuristic method developed here based off of return distance and intensity information. A new sensor model has been applied to these high-attenuation returns, only providing belief information about free space since the highly attenuated returns may correspond to range data in the smoke instead of to a solid boundary, while a basic sensor model was used for the remaining LIDAR returns. A new sensor model was developed for the LWIR stereo vision system based off of disparity values, stereo correspondence matching cost, and the number of points affecting each voxel. The fusion results have been compared to single sensor results, quantitatively indicating that the fusion system outperforms individual sensors in areas of the scene filled with smoke and when considering the entire range of smoke conditions together.

1.3 Overview

An overview of the research presented in this dissertation to accomplish the research contributions is provided below:

- Chapter 2 contains small-scale tests designed to evaluate the perception ability of eleven different sensors in fire smoke environments. Dense, low temperature smoke and light, high temperature smoke effects were evaluated. Radar and LWIR cameras were top performers in both smoke types. A LWIR stereo vision system was developed for rangefinding and was compared to radar, LIDAR, and visual stereo vision in large-scale testing.
- In Chapter 3, LWIR stereo vision was further developed for rangefinding in fire environments. Intensity misalignment between the cameras and stereo image filtering were addressed quantitatively. Tests were performed with approximately isothermal scenes and with thermally diverse scenes to select subsystem methods. In addition, the effects of image filtering on feature distortion were assessed.
- Chapter 4 contains the sensor fusion part of the research where LWIR stereo vision was fused with a spinning LIDAR for improved perception in ambient to smoke filled environments. The data was fused in a multi-resolution 3D voxel domain using evidential theory to model occupied and free space states. A heuristic method is presented that was developed to separate the LIDAR returns significantly attenuated by the smoke from the low-attenuation returns. Sensor models were developed for both

LIDAR return types, taking advantage of the free space state information provided by the high-attenuation returns. A sensor model was also presented for LWIR stereo vision, based off of disparity, stereo correspondence matching cost, and number of correspondence matches affecting each voxel. The fusion system was tested in a range of conditions to show its ability for improved rangefinding performance over individual sensor use in fire environments.

1.4 References

- [1] Uthe, E. E. (1981). Lidar evaluation of smoke and dust clouds. *Applied optics*, 20(9), 1503-1510.
- [2] Randhawa, J. S., & Van der Laan, J. E. (1980). Lidar observations during dusty infrared Test-1. *Applied optics*, 19(14), 2291-2297.
- [3] Sakai, M., Aoki, Y., & Takagi, M. (2005, December). The support system of the firefighter's activity by detecting objects in smoke space. In *Optomechatronic Technologies 2005* (pp. 60510L-60510L). International Society for Optics and Photonics.
- [4] Sakai, M., & Aoki, Y. (2006, August). Human and object detection in smoke-filled space using millimeter-wave radar based measurement system. In *Pattern Recognition, 2006. ICPR 2006. 18th International Conference on* (Vol. 3, pp. 750-750). IEEE.
- [5] Yamauchi, B. (2010, May). All-weather perception for man-portable robots using ultra-wideband radar. In *Robotics and Automation (ICRA), 2010 IEEE International Conference on* (pp. 3610-3615). IEEE.
- [6] Yamauchi, B. (2008, April). All-weather perception for small autonomous UGVs. In *SPIE Defense and Security Symposium* (pp. 696203-696203). International Society for Optics and Photonics.
- [7] Sales, J., Marín, R., Cervera, E., Rodríguez, S., & Pérez, J. (2010). Multi-sensor person following in low-visibility scenarios. *Sensors*, 10(12), 10953-10966.
- [8] Santos, J. M., Couceiro, M. S., Portugal, D., & Rocha, R. P. (2015). A sensor fusion layer to cope with reduced visibility in SLAM. *Journal of Intelligent & Robotic Systems*, 1-22.
- [9] Yamauchi, B. (2010, April). Fusing ultra-wideband radar and lidar for small UGV navigation in all-weather conditions. In *SPIE Defense, Security, and Sensing* (pp. 769200-769200). International Society for Optics and Photonics.
- [10] Köylü, U. O., & Faeth, G. M. (1996). Spectral extinction coefficients of soot aggregates from turbulent diffusion flames. *Journal of Heat Transfer*, 118(2), 415-421.
- [11] Kleindienst, S., Dimmeler, A., & Clement, D. (1995, June). Obscuration effects of smoke clouds. In *SPIE's 1995 Symposium on OE/Aerospace Sensing and Dual Use Photonics* (pp. 440-451). International Society for Optics and Photonics.

- [12] Amon, F., Bryner, N., & Hamins, A. (2004, August). Evaluation of thermal imaging cameras used in fire fighting applications. In *Defense and Security* (pp. 44-53). International Society for Optics and Photonics.
- [13] Amon, F., Hamins, A., Bryner, N., & Rowe, J. (2008). Meaningful performance evaluation conditions for fire service thermal imaging cameras. *Fire Safety Journal*, 43(8), 541-550.
- [14] Bertozzi, M., Broggi, A., Caraffi, C., Del Rose, M., Felisa, M., & Vezioni, G. (2007). Pedestrian detection by means of far-infrared stereo vision. *Computer vision and image understanding*, 106(2), 194-204.
- [15] Cheng, V. S., Zhang, S., Chen, Y., & Hao, L. (2005). A Stereo Thermographic System for Intra-operative Surgery. In *Engineering in Medicine and Biology Society, 2005. IEEE-EMBS 2005. 27th Annual International Conference of the* (pp. 1984-1987). IEEE.
- [16] Rankin, A., Huertas, A., Matthies, L., Bajracharya, M., Assad, C., Brennan, S., ... & Sherwin, G. W. (2011, May). Unmanned ground vehicle perception using thermal infrared cameras. In *SPIE Defense, Security, and Sensing* (pp. 804503-804503). International Society for Optics and Photonics.
- [17] Mouats, T., Aouf, N., Chermak, L., & Richardson, M. (2015). Thermal Stereo Odometry for UAVs.
- [18] Hajebi, K., & Zelek, J. S. (2006, June). Sparse disparity map from uncalibrated infrared stereo images. In *Computer and Robot Vision, 2006. The 3rd Canadian Conference on* (pp. 17-17). IEEE.
- [19] Hajebi, K., & Zelek, J. S. (2007, February). Dense surface from infrared stereo. In *Applications of Computer Vision, 2007. WACV'07. IEEE Workshop on* (pp. 21-21). IEEE.

2 Evaluation of Navigation Sensors in Fire Smoke Environments*

*Based off of the accepted form of a paper that appears as Starr, Joseph W. and Lattimer, B. Y. (2013) "Evaluation of Navigation Sensors in Fire Smoke Environments" in Fire Technology Journal. The final publication is available at link.springer.com. Location: <http://link.springer.com/article/10.1007/s10694-013-0356-3> and DOI: [10.1007/s10694-013-0356-3](https://doi.org/10.1007/s10694-013-0356-3)

2.1 Introduction

There are a variety of rangefinder technologies available that can be used by firefighters or on firefighting robots for locating walls and obstacles to support navigation inside structures. These rangefinder technologies measure the distance to surfaces in the field of view. Depending on the device, it may return a single distance, a plane of distances, or a distance map. Rangefinder devices can then be accompanied with algorithms to map out the environment and provide a path for movement. There are several rangefinders and cameras that work well for clear, ambient temperature conditions. However, there is little in the literature evaluating the effectiveness of rangefinders for use in thick smoke or high temperature environments that may be produced by fires. In order to improve human navigation and to enable robot navigation in fire environments, rangefinder technologies need to be assessed for performance in fire smoke environments.

Rangefinder technologies operate using sources or collected energy in electromagnetic or acoustic spectrums. Figure 2 provides some of the common rangefinding sensors plotted with the operating wavelength. The most common type of rangefinder is a time-of-flight sensor such as LIDAR, radar, and sonar. These rangefinders send out a signal and time how long it takes for that signal to return to the sensor. The flight time of the signal is related to the distance to the object. Due to the speed of light, LIDAR sensors can generate many detection points generating impressive planar and three-dimensional maps of spaces [1]. Visible cameras, night vision, and thermal imaging cameras contain sensors that collect light. For rangefinding, these types of sensors are typically put in a stereoscopic configuration (two or three cameras) and shifts in images are used to quantify distances to objects in the field of view. These also have the advantage of generating three-dimensional maps of spaces [2]; however, the speed and accuracy of generating these maps is not as high as that of LIDAR. A third type of sensor (such as the KinectTM commonly used in gaming) emits a light pattern onto the surroundings and a separate sensor collects the light pattern. The displayed and collected light patterns are compared to determine the location of objects in the field of view. However, this technology has been known

to have problems reading in the light pattern in the presence of sunlight [3], so interference from radiation emitted by fires may have an adverse affect on its usability in firefighting scenarios.

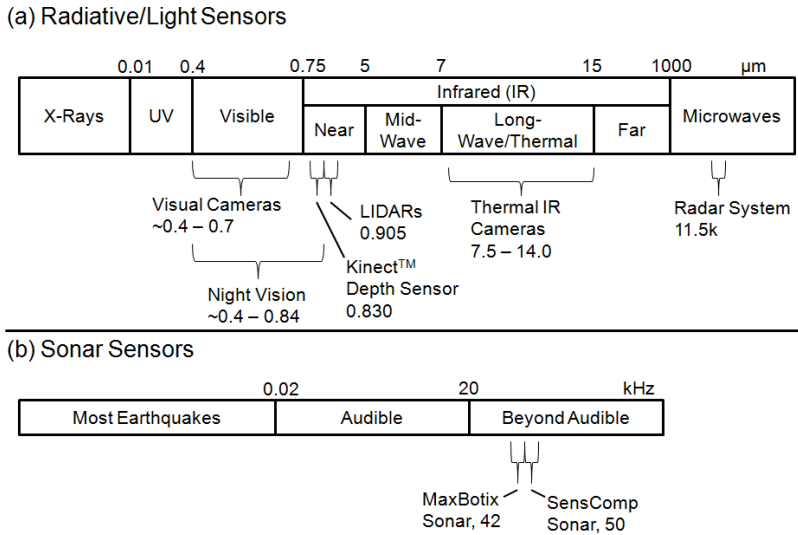


Figure 2: Rangefinding sensors plotted with the electromagnetic and acoustic spectrums.

Some research has been reported on evaluating the ability of different wavelengths of electromagnetic radiation to penetrate smoke [4-6]. All three of these papers show that for hydrocarbon smoke, the extinction coefficient decreases with increasing wavelength from the visible range to the thermal infrared range. These results imply that sensors operating at higher wavelengths such as radar (waves on the order of millimeters) will outperform ones operating at lower wavelengths (waves on the order of a micrometer). Limited work has been conducted to demonstrate these trends for rangefinding devices.

The most common rangefinder used for navigation is a LIDAR, which uses the time-of-flight of a laser to determine the distance to objects. Some research has been performed on the effects of fog [7-9] on LIDAR systems and on being able to use a LIDAR system as a transmissometer [10] or to detect or locate forest fires [11, 12]. Some of the effects of smoke on LIDAR have also been documented [13-19]. A recent study tested the ability of a single-echo LIDAR to quantify the distance to objects in a hallway filled with fire smoke [19]. Multi-echo LIDAR systems are designed specifically for use in harsh environments such as dust, fog, and precipitation where visibility conditions become low [20-22], although testing of the

commercially available multi-echo LIDAR systems has not made it into the literature. In these systems, the LIDAR looks for multiple light returns and uses these multiple returns to quantify the distance to objects in the field of view. Though the performance is claimed to be good in other low visibility environments, no studies have been reported in the literature on multi-echo LIDAR in fire smoke.

Several studies have investigated the use of Ultra Wide Band (UWB) radar systems for robot navigation in poor visibility conditions such as those produced by rain, snow, fog, and vegetation [23-25]. Some work has also been performed on the ability of radar to be used in some smoke environments [26-28]. These studies focused on the development and testing of a 76 ghz radar system for use on firefighters and used the Rayleigh Scattering Approximation to claim that their system would work in smoke [26-28]. A scanning radar was used to successfully scan the location of obstructions and people inside of a room filled with fire smoke. However, the visibility through the smoke was not quantified using obscuration measurements.

Sonar systems have also been evaluated as a rangefinder technology for person following in smoke situations [29], and some fires have been studied acoustically [30]. The evaluation of sonar for use in smoke in the literature used glycol-based liquid droplet fog to produce artificial smoke [29]. The visibility of the artificial smoke was recorded as a smoke density based on a visual smoke detection algorithm presented in the paper. The temperature of the artificial smoke was not recorded. Artificial smoke made from liquid fog is typically at or near room temperature and enters the air as droplets, unlike fire smoke which is generally at higher temperatures and made up of non-spherical particulates. As indicated from Ref. [31], smoke particulate are different at blocking light compared with artificial smoke droplets. As a result, the performance of these range finders needs to be evaluated using actual fire smoke [31]. In addition, sonar operates by sound waves travelling through the media that depend on the temperature. An assessment of sonar in real fire smoke at elevated temperatures would better quantify performance expectations for use in fire environments.

Another possible rangefinder technology is stereovision using visible cameras [32], which consists of two or more cameras used to locate the distance to objects present in the images.

Some research has been performed on locating smoke [33-35] and fire [34-37] using cameras and on using cameras to determine atmospheric weather visibility [38, 39]. Tests have been performed to quantify the ability of humans to read various types of signs in varying levels of smoke [40, 41]. These tests on human perception have been used as a basis to relate human perception visibility to the extinction coefficient of an obscurant [40]. In general, the maximum distance from which a human can read a sign has been found to be inversely proportional to the extinction coefficient of the obscurant the sign is viewed through [40]. Since visible cameras cover nearly the same electromagnetic region as humans, this implies that as smoke becomes thicker, the ability of the cameras to detect objects and surfaces through the smoke is expected to decrease.

IR imaging cameras could also be used in a stereoscopic configuration for rangefinding. In Ref. [19], a thermal IR stereovision system was used to effectively quantify the distance of objects in a hallway filled with smoke. The system was measured to quantify distances to within 10% when the smoke visibility was less than 1 m. The majority of use of thermal imaging cameras (tics) in firefighting has been on hand held systems [42-45]. Tics include a single thermal imager, so they do not provide distances to objects in the field of view. In these studies, the focus was on developing performance evaluations to determine how the different units performed relative to one another. Ref. [42] describes a test facility to analyze TIC firefighting performance. The contrasting ability of three tics imaging cold pipes in front of a warmer background was presented in Ref. [43] along with a performance criterion that can be used to compare tics. A set of performance criteria was developed in Refs. [44, 45] to be used to evaluate TIC use in different scenarios, including firefighting scenarios, focusing on spatial resolution, contrast, and thermal sensitivity. It was also shown that smoke has the potential to increase the optical thickness (that is, reduce the visibility) when it is at higher temperatures [44, 45]. While this research provides some insight on the effects of smoke on TIC performance and provides metrics for comparing tics to each other, they do not provide results directly relating TIC performance to smoke visibility or temperature.

An experimental study was performed to quantify the rangefinding and imaging capabilities of various sensors through different fire smoke conditions. A uniform smoke layer experiment was

used to evaluate the performance of eleven different rangefinders and cameras. Due to the uniformity of the smoke layer, the performance could be related to the visibility through and gas temperature of the smoke. Select rangefinders were evaluated in a large-scale room hallway fire experiment, which is more representative of a real firefighting scenario. The rangefinders were used to determine how far different objects were along the hallway with more temperature gradients and with flowing smoke present.

2.2 Experimental

2.2.1 Small-Scale Smoke Layer Apparatus

The small-scale apparatus shown in Figure 3 was used in this study to produce uniform smoke layer conditions that could be used to assess sensor performance. This apparatus is similar to the hood experiments previously used to generate smoke layers representative of compartment fire environments [49]. This was later determined to represent conditions that develop inside of compartment fires [50]. The advantage of this experiment is the uniformity of the smoke layer that is developed, which allows testing of the performance of the sensors in known environments. Since the goal of this testing was a side-by-side comparison of sensors at ranging through both dense, low temperature smoke and light, high temperature smoke, a vertical test path was chosen for the sensors that would provide approximately the same smoke level for both types of smoke. The sensors were kept below the smoke layer to prevent them from being damaged by elevated temperature or being coated by smoke particulates.

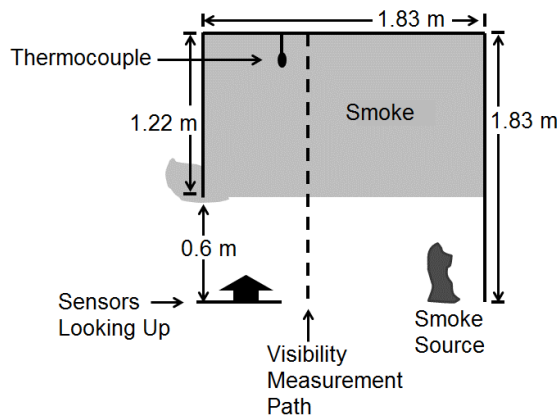


Figure 3: Experimental setup.

The test apparatus is shown in Figure 3 to be 1.22 m wide, 1.83 m high and 1.22 m deep. The boundaries were constructed using a steel frame with Type X drywall as the wall material. A fire is located on the right side of the setup while sensors are on the left side. During an experiment, the smoke collects in the upper portion of the test apparatus, filling the apparatus until smoke spills out the end above the sensors. This produces a uniform smoke layer approximately 1.3 m deep above the sensors. Targets were mounted on the ceiling to evaluate the sensors based on target color as well as temperature. Gas layer temperature was measured using a bare bead, Type K thermocouple inserted through the roof of the test rig and located 0.15 m below the ceiling.

The experiment includes a laser extinction system to quantify the visibility through the smoke during a test. The laser extinction system design is consistent with the systems provided in fire test standards [46]. The system includes a red HeNe ($\lambda = 632.8$ nm) laser passing through the smoke layer with the intensity of the laser passing through the smoke being measured using a silicon photodiode. The intensity with no smoke relative to the intensity with smoke present is used to calculate the extinction coefficient [47]

$$\beta = \frac{1}{L_P} \ln \left(\frac{I_0}{I} \right) \quad (1)$$

where β is the extinction coefficient (1/m), L_P is the smoke layer depth (m), I_0 is the intensity of the laser through no smoke (V), and I is the intensity of the laser through smoke (V).

The visibility through the smoke layer was quantified through the equation that relates the smoke extinction coefficient to the visibility. The visibility (by a human) through the smoke is related to the extinction coefficient using Jin's equation for the readability of a place-card sign [40],

$$V = \frac{C}{\beta} \quad (2)$$

where V is the visibility (m), β is the extinction coefficient (1/m), and C is an empirical constant from Jin's experiments. For a light reflecting object (i.e., not lighted), the constant was determined to be between 2 and 4 [40]. A value of $C = 2.3$ was used for the visibility calculations in this paper.

Two different type fires were included in the experiments to produce a range of smoke and temperature conditions. Dense smoke, low gas temperature conditions were produced by latex

foam fires. Propane gas fires were used to produce high temperature, light smoke conditions. Latex foam fire tests included an approximate 150 mm x 150 mm x 75 mm slab of foam that was ignited with a torch. Propane fire tests were produced using a standard sand burner with a 70 SLPM gas flow rate, generating a 100 kW fire. Appendix A contains more detail on the smoke types selected.

2.2.2 Small-Scale Experiment Sensors

A variety of common robotic navigation sensors were evaluated in this study. These included both rangefinders and cameras. Table 1 contains a list of these sensors, while Figure 2 shows a visual representation as to where the wavelengths of the devices are with respect to each other. Instruments that could interfere with each other (such as both LIDARs) were tested separately.

Table 1: Sensors evaluated in study.

Sensor	Type	Operating Wavelength/Frequency Range
Hokuyo UTM-30LX	Single-Echo LIDAR	0.905 μm
IBEO Lux	Multi-Echo LIDAR	0.905 μm
Senscomp 6500	Sonar	50 kHz, acoustic
Maxbotix 7092	Sonar	42 kHz, acoustic
HP Webcam	Camera	~ 0.4 to $0.7 \mu\text{m}$, Visual
Xbox Kinect™ Camera	Camera	~ 0.4 to $0.7 \mu\text{m}$, Visual
Xbox Kinect™ Depth Sensor	Depth Sensor (IR Laser Projector and CMOS Camera)	0.830 μm
FLIR SC655	Thermal IR Camera	7.5 to 13.5 μm
FLIR Tau320	Thermal IR Camera	8 to 14 μm
ATN Night Vision Gen 1 Monocular	Night Vision	~ 0.4 to $0.8 \mu\text{m}$
Endress Hauser Micropilot M Level Meter	Radar	26 GHz

2.2.3 Large-Scale Test Facility

The large-scale test facility shown in Figure 4 was used for evaluating sensor technologies deemed most promising from the small-scale testing. This test facility contains a hallway with a room at the end and a closet on the side. Smoke from the fire inside the room flowed down the hallway and out of the open end to an exhaust system. The upper 0.7 m of the wall was blocked to form a 1.0 m deep smoke layer in the hallway during the experiments. The hallway contains two laser extinction systems designed to measure the visibility of the smoke as described in the last section. These are located 1.1 m and 3.7 m from the hallway entrance measuring

horizontally across the hallway. The laser extinction systems were used at two elevations during the testing with similar results. Nine thermocouples were placed 12 mm below the ceiling to measure gas temperature at 0.9 m intervals in the room, hallway, and closet. The hallway and closet also contained thermocouples to measure the vertical temperature distribution at three separate locations using five thermocouples mounted in a vertical pattern. These vertical distributions are located 1.4 and 3.7 m from the hall entrance and in the middle of the back wall of the closet.

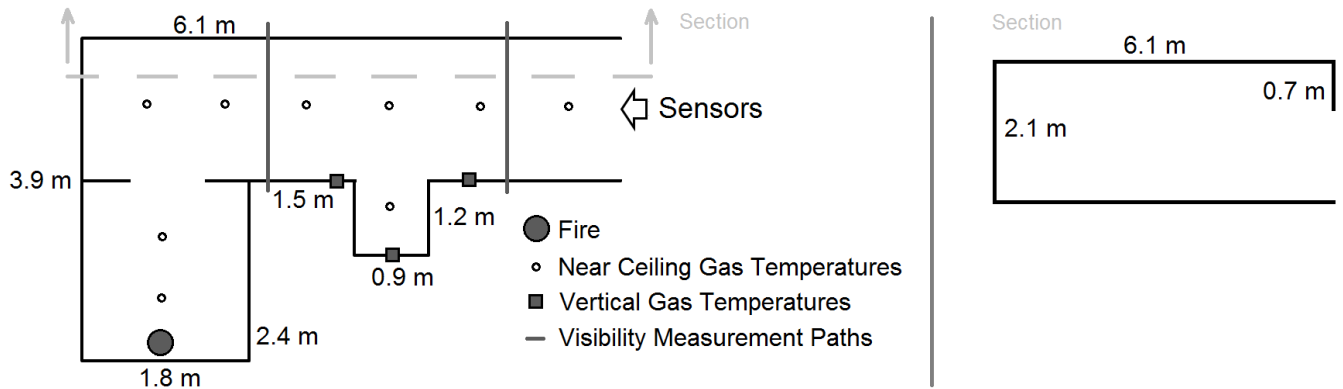


Figure 4: Large-scale test facility.

The sensors were placed at the entrance of the hallway and setup to range down the hallway. A series of targets were placed within the smoke layer at different locations along the length of the hallway. These different targets allowed the evaluation of the sensors to locate objects through smoke at a range of distances.

All fire experiments were performed using latex foam as the fuel. In these experiments, a foam block of approximately 200 mm x 200 mm x 150 mm was used. This produced a dense, low temperature smoke to evaluate the rangefinders.

2.2.4 Large-Scale Experiment Sensors

A series of experiments were performed to evaluate thermal IR stereo vision, visual stereo vision, LIDAR, and radar within the large-scale test facility shown in Figure 4. The thermal IR stereo vision system consisted of two FLIR Tau 324 far infrared cameras with 9 mm lenses. Each camera has a 320x256 pixel focal plane array with 25 μ m pixel spacing. A baseline separation distance of 150 mm was used for the thermal IR system. The thermal IR system

images were put through the row-based mean shift filter and processed using a bidirectional Sum of Absolute Differences (SAD) algorithm. Details of the bi-directional SAD correspondence matching algorithm are provided in Appendix B.

The visual stereo vision system was a Bumblebee2 fabricated by Point Grey. The visual system images were processed using the included software. Distance information from the visual system was gathered once in clear conditions and once when the visibility was below 1 m.

The LIDAR used in the full-scale tests was the Hokuyo UTM-30LX, the same model used in the small-scale tests. The radar system for the large-scale tests was chosen to be a 24 GHz FMCW (Frequency Modulated Continuous Wave) radar system with a horn antenna. This radar system is similar to the small-scale tested radar (the Endress Hauser Micropilot M Level Meter) but is more compact and designed for configurability.

2.2.5 Experimental Procedure

Each experiment followed the same test procedure to ensure repeatable test conditions. First, the sensors were setup and powered on for at least five minutes to ensure that any transient sensor responses due to initial power-on were not present. The smoke source was then setup (but not lit) and the data acquisition system was turned on to obtain 60-120 seconds of baseline data with no smoke. After this baseline, the fire was lit. In dense smoke tests with the latex foam, the fuel was allowed to burn until it was completely consumed. In the light smoke and high temperature tests, the propane flame was turned off after the gas temperature reached approximately 250°C. Following the fire, the data acquisition system was allowed to collect data for an additional 120 seconds.

2.3 Results

2.3.1 Small-Scale Results

Each sensor was evaluated for its ability to see through two different extremes of smoke: dense, low temperature smoke and light, high temperature smoke. The temperature and visibility for both of these cases are shown in Figure 5. During the dense smoke tests, the visibility dropped below 1 m within the first minute of the test while the smoke temperature stayed below 100°C.

During the high temperature smoke tests, the smoke visibility remained above 10 m except a 30 s period where it decreased to as low as 5 m. The smoke temperature reached 250°C prior to the fire being turned off at approximately 60 s. The performance of the sensors is discussed below for both of these test conditions.

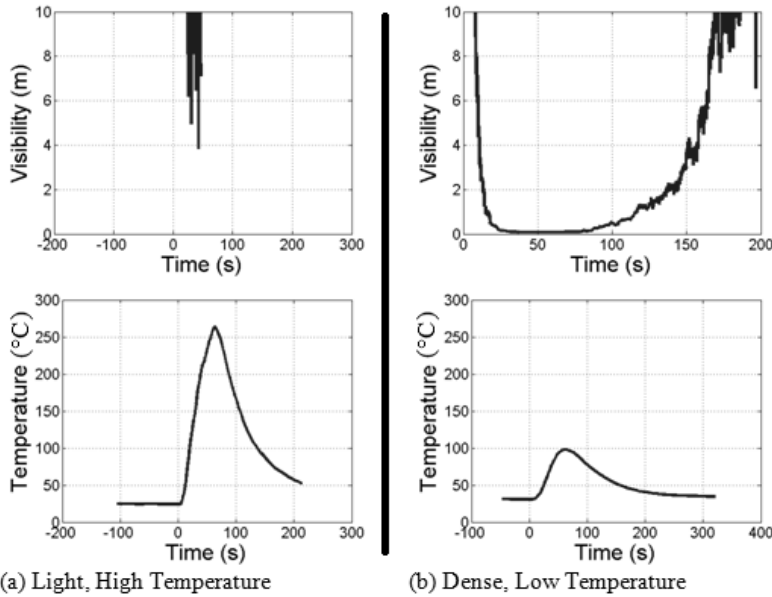


Figure 5: Visibility and temperature data for the (a) high temperature tests and (b) dense smoke tests.

2.3.1.1 LIDAR

Two LIDAR systems operating at 905 nm were tested, a single-echo Hokuyo UTM-30LX and a multi-echo IBEO Lux. Figure 6 shows the Hokuyo results as the smoke thickness increases. When the smoke reaches a visibility of 4 m, the LIDAR distance measurement is affected. After the smoke reaches a visibility of approximately 1 m, the LIDAR returns the distance to the bottom of the smoke and is not able to detect the upper boundaries of the test apparatus. With a high temperature, light smoke layer produced by the propane fire, the LIDAR returns a result consistent with the baseline no-smoke environment.

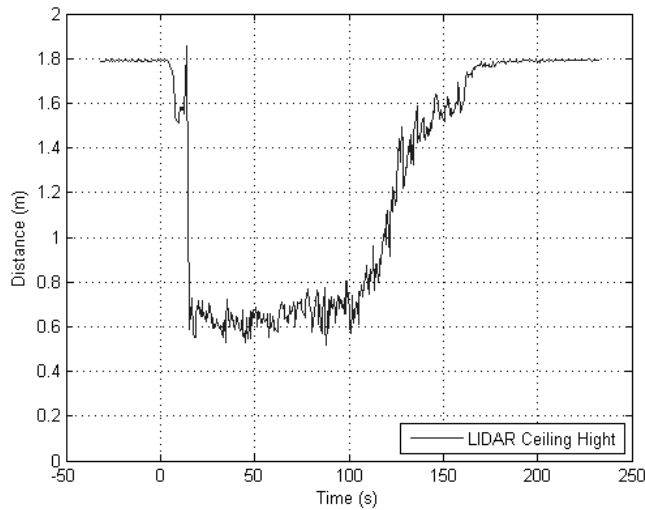


Figure 6: Hokuyo UTM-30LX single-echo LIDAR results with smoke at different visibility levels.

Figure 7 shows the results of the multi-echo IBEO Lux LIDAR for both tests. This multi-echo LIDAR provides the same results as the single-echo LIDAR for the thick smoke tests, showing only the distance to the bottom of the layer once the visibility drops to about 1 m. During the high temperature tests, however, the multi-echo LIDAR shows the distance to the upper boundaries as well as the distance to the middle of the smoke layer. The results indicate that both LIDAR systems would not be capable of providing accurate rangefinding information in dense smoke environments.

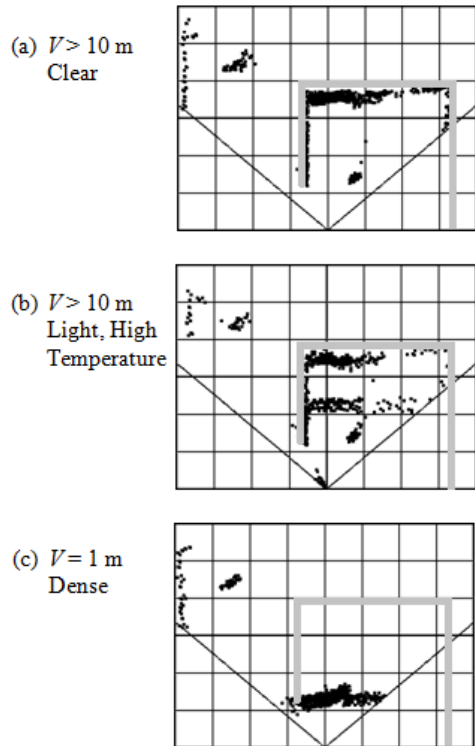


Figure 7: IBEO Lux multi-echo LIDAR results for smoke at different visibility levels. The outside of the test rig is outlined in gray.

2.3.1.2 Sonar

The results from the Maxbotix sonar operating at 42 kHz are shown in Figure 8 for both the dense smoke and the high temperature tests with the median value for every 1000 points also plotted. The results from the Senscomp sonar operating at 50 kHz are similar. During the tests, the measured distance to the ceiling reduces and then returns to its initial value. This results in a 10-20% error in boundary location for the conditions tested.

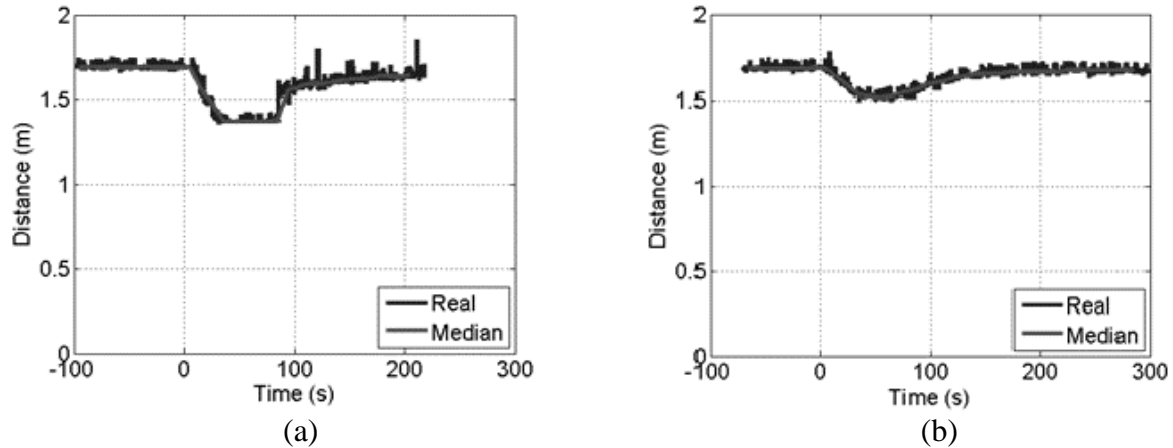


Figure 8: Sonar results for (a) light, high temperature smoke and (b) dense, low temperature smoke.

2.3.1.3 Visible Region Cameras

The performance of cameras operating in the visible region was evaluated using an edge detection code. The code looks at the change in value between each pixel and its adjacent pixels, moving left to right and top to bottom. It then compares each of these changes to a standard value to decide if it is an edge or not. The sum of the edge pixels identified in the picture is then quantified. The number of total edge pixels was used to quantify how well the camera could see through the smoke. The results of this test for the HP Webcam during a thick-smoke test are shown in Figure 9 along with an image from the tests with the edges highlighted. The results indicate that the recorded image is significantly attenuated due to the smoke when the visibility drops to about 4 m, while the code is completely unable to locate any features below a visibility of about 1 m. The results for the KinectTM visible camera were similar. The high temperature, light smoke tests had no effect on the edges identified with either camera, so the results are not shown.

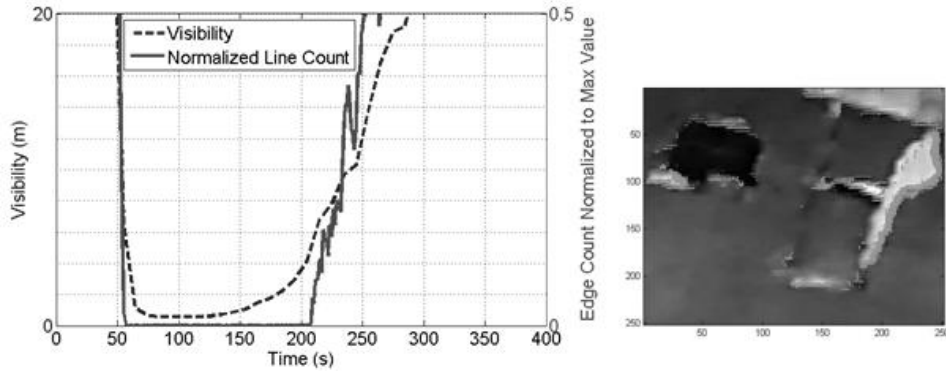


Figure 9: Visual camera results using an edge detection algorithm for a dense, low temperature smoke test.

2.3.1.4 Kinect™ Distance Sensor

The Kinect™ distance sensor results are shown in Figure 10. During the dense smoke, low temperature tests, the sensor detects the smoke layer, along with some signal interference from the fire source, and fails to provide useful depth information about the apparatus when the visibility decreases below about 8 m. In the light smoke, high temperature tests, the sensor also fails to provide depth information but this time due to the depth sensor being flooded with near infrared light from the flame.

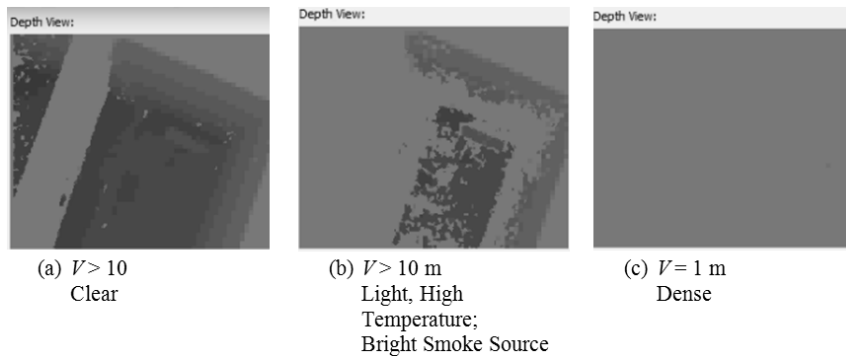


Figure 10: Kinect™ depth sensor results for (a) no-smoke, (b) light, high temperature smoke with a bright and interfering smoke source, and (c) dense, low temperature smoke.

2.3.1.5 Thermal IR Cameras

The results for the FLIR SC655 IR camera are shown in Figure 11. The ceiling surface and heated target are apparent in clear conditions as well as dense smoke conditions. The entire image remains clear with both thick smoke and high temperature smoke. The FLIR Tau320

provided similar results except with a lower resolution and with some pixels reaching maximum values when temperatures exceeded the camera range.

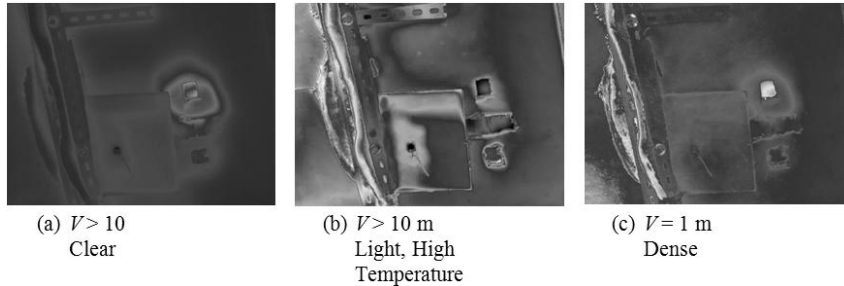


Figure 11: Thermal IR camera results for (a) no smoke, (b) light, high temperature smoke, and (c) dense, low temperature smoke.

2.3.1.6 Night Vision

The ATN night vision system was tested both with a protective cap on as well as with it taken off during the tests to alter the amount of light input to the sensor. Initially, tests were performed with the protective cap on to prevent damage from too much light entering the system. A second dense smoke, low temperature test was performed with the protective cap taken off since these tests conditions were much darker than the high temperature tests. The results for the tests are shown in Figure 12. For both dense smoke tests, the night vision system sees only the bottom of the smoke layer. For the high temperature test, even with the protective cap on, the system receives too much light to distinguish objects at the top of the test rig.

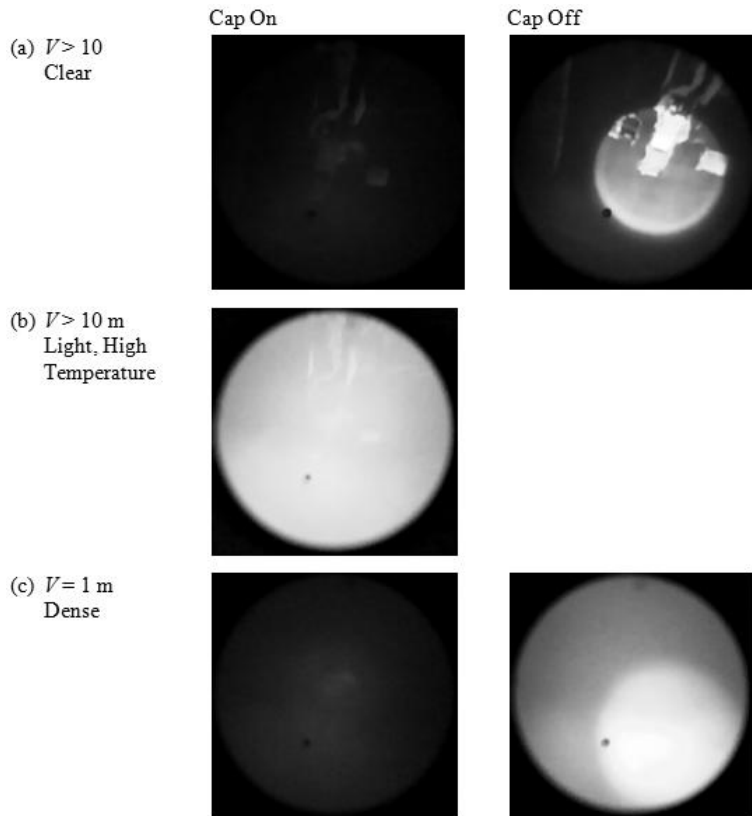


Figure 12: Night Vision Results for (a) no smoke, (b) light, high temperature smoke, and (c) dense, low temperature smoke.

2.3.1.7 Radar Rangefinder

The results for the Endress Hauser Micropilot M are shown in Figure 13. This 26 GHz radar system provides less than a 6% change in distance (including outliers) in the dense smoke test as well as the high temperature, light smoke test.

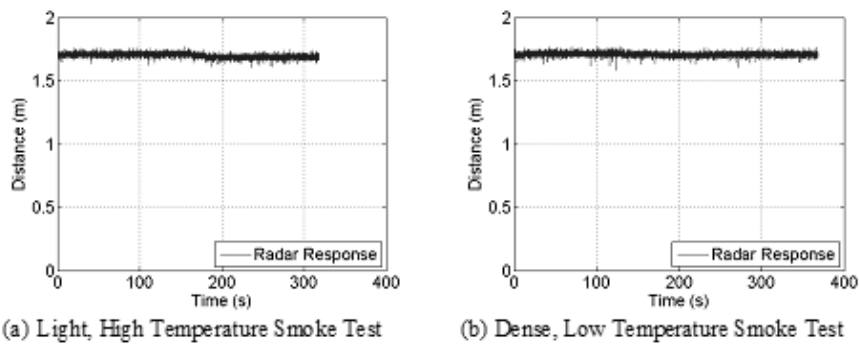
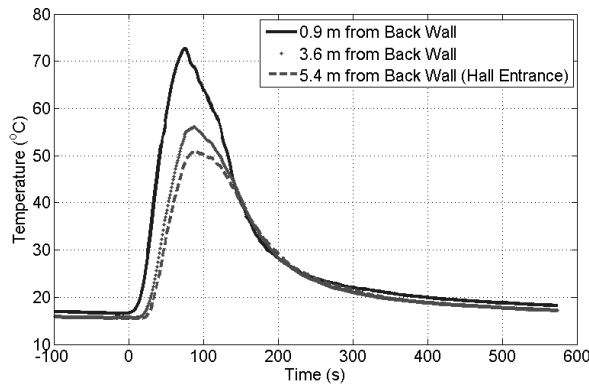


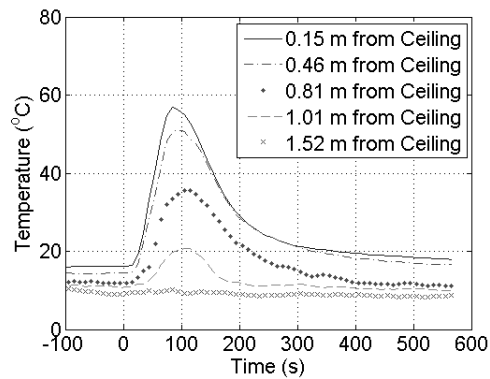
Figure 13: 26 GHz radar results for (a) light, high temperature smoke and (b) dense, low temperature smoke.

2.3.2 Large-Scale Results

Select sensors were evaluated for their ability to see through dense, low temperature smoke in the large-scale experiment. As shown in Figure 14, gas temperatures vary along the length of the hallway as well as the height of the smoke layer. Gas temperatures were 50-75°C during the experiment near the ceiling along the length of the hallway with the highest temperatures close to the room containing the fire, as expected. With height along the smoke layer 3.6 m into the hallway, the gas temperatures were 60°C near the ceiling to near ambient at the bottom of the smoke layer (1.0 m). This shows the nonuniformity of the gas temperatures within the hallway where the rangefinders were operated. The visibility through the smoke during the experiment is shown in Figure 15. The smoke was measured to decrease to less than 1 m and was similar at the two locations along the hallway until the fire began to decay. Smoke visibility remained lower at the end of the hallway closest to the rangefinders.



(a) Hallway Ceiling Gas Temperatures



(b) Hallway Vertical Gas Temperature Measurements 3.6 m into the hallway

Figure 14: (a) Hallway ceiling gas temperature data and (b) middle of the hallway vertical gas temperature data for the large-scale experiment.

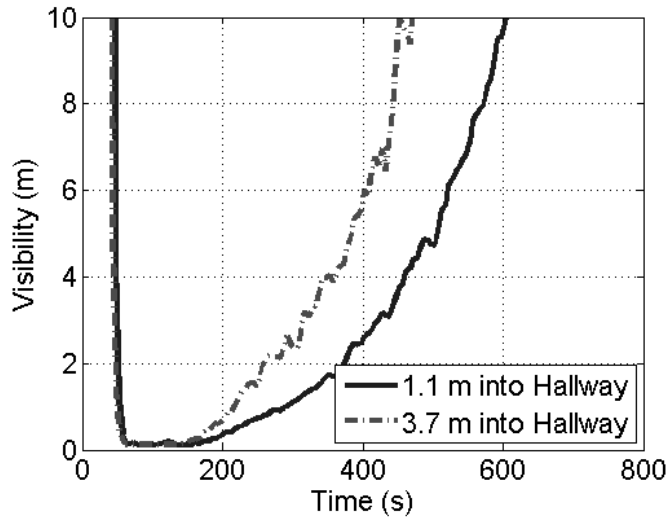


Figure 15: Visibility data for the large-scale experiment.

Two stereo vision systems (visual and thermal IR based) were tested in the large-scale test facility. Results of the tests are provided in Table 2. Prior to testing in smoke, the sensors were evaluated in clear conditions where both systems were able to determine distances to targets to within 3%. As the temperature of the target increased, the thermal IR stereo vision system provided better disparity mapping while the visible system remained the same. This implies the thermal IR stereo vision system will be enhanced as the temperature gradients in the scene increase as with a true fire scenario. As expected, the visible system was unable to identify either target, in dense, low temperature smoke. However, the thermal IR system provides approximately the same results for both targets as measured in clear conditions.

Table 2: Distance to targets measured using vision systems.

Rangefinder	Distance to Target 1 (3.0 m actual)		Distance to Target 2 (4.90 m actual)	
	Clear (m)	Dense Smoke (m)	Clear (m)	Dense Smoke (m)
Visible Stereo Vision	3.07	No value	4.96	No value
Thermal IR Stereo Vision	3.00	3.00	4.91	4.91

Results for using LIDAR to measure the distances to targets in the hallway are provided in Figure 16. In this case, the targets were located 1.25 m and 3.0 m away. As seen from the graph, the LIDAR was able to measure the distance in clear conditions before the fire. However, as the smoke density in the hallway increased, the distance measured using LIDAR decreased

and the error was significant. Based on the smoke measurements, the LIDAR response began decreasing when the smoke visibility decreased to 5 m. This is similar to the small scale test results where LIDAR performance began to degrade at a visibility of 4 m.

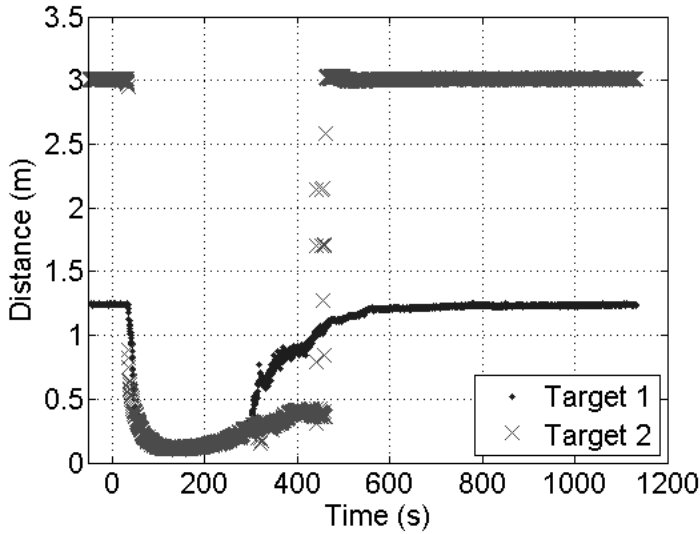


Figure 16: LIDAR large-scale test results.

The results from testing the radar system in the dense smoke, low visibility conditions are shown in Figure 17. In these experiments, the targets were 3.2 m and 4.2 m away from the sensor. The radar system varied by less than 5 mm during the entire test for both targets as the environment went from clear conditions to a visibility of less than 1 m.

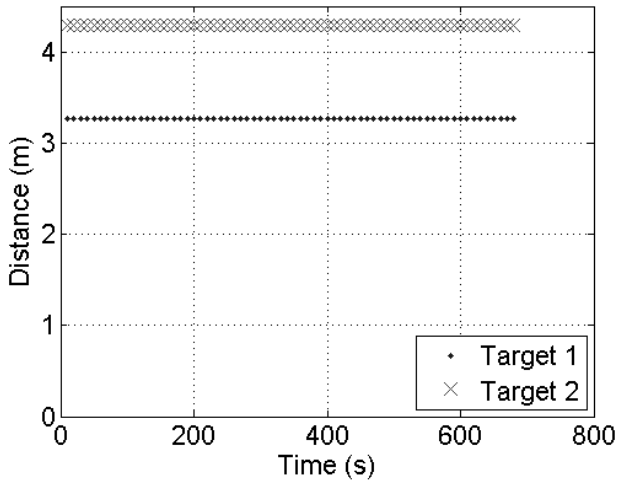


Figure 17: Radar large-scale test results not varying in clear or smoke conditions.

2.4 Discussion of Results

A summary of the small-scale results is shown in Table 3. This table includes the minimum visibility level each sensor can be used at with less than 10% signal attenuation due to the smoke density. In addition, this table provides the visibility at which the sensor completely fails, the effect of smoke temperature on performance, and flame light effects on the sensors. Figure 18 contains the response of LIDAR, sonar, radar, and visual camera with respect to the smoke visibility. The sonar in this plot has had a gas temperature correction applied for the change in the speed of sound. From this plot, the radar and corrected sonar maintain accurate range finding ability at all visibility levels while LIDAR and visible cameras lose accuracy at visibility less than 4 m and 8 m, respectively.

Table 3: Summary of sensor performance in the small-scale smoke layer experiment.

Sensor	Dense Smoke, Low Temperature	Light Smoke, High Temperature
Electromagnetic Sensors		
LIDAR Sensors	Attenuation at 4 m visibility; failure at 1m visibility	No effect
Visual Cameras	Attenuation at 8 m visibility; failure at 1m visibility	No effect
Kinect™ Depth Sensor	Poor results even with >8m Visibility (Combination of particle blocking and sensor being flooded by light from fire)	Sensor flooded by light from fire during whole test
Night Vision	Failure at about 4m visibility	Sensor flooded by light from fire during whole test
Thermal Cameras	No effect	No effect
Radar	No effect	No effect
Other		
Sonar	Some attenuation with temperature change	Attenuation with temperature change

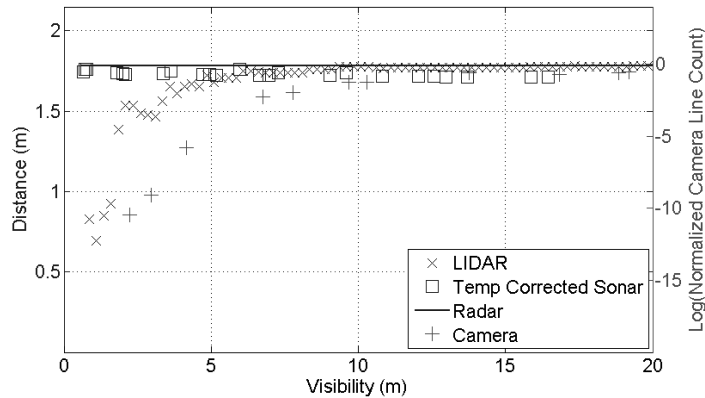


Figure 18: The effect of visibility on LIDAR, sonar, and radar rangefinders (left axis) and a visual camera (right axis).

From Table 3 and Figure 18, it can be seen that the lower electromagnetic wavelength sensors (LIDAR, visual cameras, the Kinect™ depth sensor, night vision) fail when there is dense smoke present, while the higher electromagnetic wavelength sensors (thermal cameras, radar) continue to provide useful results. This is attributed to emission and absorption of energy from soot particles decreasing with an increase in wavelength [4-6]. As the wavelength increases, the extinction coefficient decreases [4-6]. Since visibility varies by the reciprocal of the extinction coefficient [40], the visibility increases with increasing wavelength.

A visibility of 1.0 m in the visible range will have a visibility greater than 20 m in the far infrared range and much greater than this in the radar millimeter range if these trends are extrapolated. As a result, the thermal infrared cameras that operate in the range of 7 to 15 μm and the radar that operates at a wavelength of about 11.5 mm perform well at looking through dense smoke. Visual cameras (about 0.4 to 0.7 μm) as well as near infrared sensors such as LIDARs at 0.905 μm (even multi-echo types), the KinectTM depth sensor (0.83 μm), and night vision (about 0.4 to 0.84 μm), do not perform well in the dense smoke, low temperature tests when the visibility is too low. None of these sensors were measured to be reliable when the visibility decreased below about 4 m. The KinectTM Depth sensor failed much sooner (visibility at 8 m) due to interference at the sensor from light given off by the fire.

The results show that the all of the electromagnetic wavelength sensors performed well with high temperature, light smoke, with the exception of the KinectTM depth sensor and the Night Vision. The KinectTM depth sensor fails due to incoming radiation on the sensor from the fire interfering with the return from the speckle pattern being emitted by the sensor for calculating depths. The night vision system fails due to an overloading of light on the system. It is also important to note that the cameras can fail with too much or too little light present in the scene.

The sonar sensors provided results in both tests where the sensed distance to the target decreased during the tests. This is attributed to the speed of sound increasing but not being accounted for in the time of flight calculations. By approximating the speed of sound in smoke with the speed of sound for an ideal gas, the speed of sound follows the equation

$$c = \sqrt{\gamma RT} \quad (3)$$

where c is the speed of sound, γ is the specific heat ratio for the medium, R is the gas constant of the medium, and T is the temperature of the medium. During the high temperature tests, the temperature of the smoke increases enough to cause 20% error while the specific heat ratio and the gas constant only slightly change, assuming the smoke concentration is small (on the order of the diffusion flames studied in [48]). A temperature correction could be applied to the results if the average gas temperature to the target is known. Errors resulting from an error in the speed of sound will scale with the distance to the object being tested (i.e. Closer objects will have less

error). As a result, the correction may not be needed to produce sufficiently accurate results for path finding.

The results from the large-scale experiment are comparable to the small-scale tests. The experiment on the visual and thermal IR stereo vision systems confirms the small scale implications that thermal IR stereo vision systems will maintain distance accuracy in both clear and dense smoke environments while the visible stereo vision system fails in dense smoke. In large-scale experiments with LIDAR, the LIDAR shows strong attenuation when the visibility drops below 5 m. This is similar to the small-scale test results indicating LIDAR distance inaccuracy below 4 m. The experiment also confirms that dense smoke does not have significant effect on radar, with distances varying by less than 5 mm regardless of the presence of smoke.

2.5 Conclusion

A series of small and large-scale experiments were performed on various robotic rangefinders and cameras to evaluate their capability to see and locate surfaces through smoke. These experiments demonstrated the performance and failure points for different sensors for dense (<1 m visibility), low temperature as well as light (>5 m visibility), high temperature smoke. In both scales of tests, the sensors operating at higher wavelengths in the electromagnetic spectrum maintained the ability to locate objects through dense smoke and were unaffected by gas temperatures.

Lower wavelength sensors failed to operate for various reasons. The results of the tests show that the Kinect™ depth sensor and night vision did not perform well in any experiments. Both sensors are flooded with light from the smoke source during the light, high temperature tests. The night vision system failed when the visibility dropped to 4 m, and the Kinect™ depth sensor failed when the visibility dropped to 8 m, due in part to interference from the smoke source. The LIDARs and visual cameras work well with high temperature, light smoke but poorly with dense smoke below a visibility of 4 m and 8 m respectively. These results were confirmed in large scale experiments where the accuracy of the LIDAR decreased when the visibility fell below 5 m.

Sonar sensors were able to measure distances to surfaces through dense smoke; however, the distance measurement was sensitive to the gas temperature due to the change in the speed of sound of gas medium. A correction for the gas temperature can reduced the error in the sonar distance. Due to the presence of unknown temperature gradients in real fire environments, sonar sensors are not recommended.

Thermal IR cameras and radar maintained accuracy in both light and dense smoke conditions tested in a small-scale smoke layer test. In general, sensors operating above 7.5 μm gave the best results due to the wavelengths of these sensors not being attenuated by the smoke. Large-scale tests demonstrated thermal IR stereo vision was able to locate objects to within 2% of the actual distance in both clear and dense smoke (<1 m visibility) conditions. The radar rangefinder was also confirmed to provide accurate distance measurements in large-scale experiments with an accuracy of 5 mm. These results demonstrate that the longer wavelength sensors currently on the market are the most reliable sensors for measuring distances through dense smoke environments.

2.6 References

- [1] Haala, N., Peter, M., Kremer, J., & Hunter, G. (2008). Mobile LiDAR mapping for 3D point cloud collection in urban areas—A performance test. *Int. Arch. Photogramm. Remote Sens. Spat. Inf. Sci*, 37, 1119-1127.
- [2] Garcia, M. A., & Solanas, A. (2004, April). 3D simultaneous localization and modeling from stereo vision. In *Robotics and Automation, 2004. Proceedings. ICRA'04. 2004 IEEE International Conference on* (Vol. 1, pp. 847-853). IEEE.
- [3] Suarez, J., & Murphy, R. R. (2012, November). Using the kinect for search and rescue robotics. In *Safety, Security, and Rescue Robotics (SSRR), 2012 IEEE International Symposium on* (pp. 1-2). IEEE.
- [4] Dalzell, W. H., & Sarofim, A. F. (1969). Optical constants of soot and their application to heat-flux calculations. *Journal of Heat Transfer*, 91(1), 100-104.
- [5] Köylü, U. O., & Faeth, G. M. (1996). Spectral extinction coefficients of soot aggregates from turbulent diffusion flames. *Journal of Heat Transfer*, 118(2), 415-421.
- [6] Kleindienst, S., Dimmeler, A., & Clement, D. (1995, June). Obscuration effects of smoke clouds. In *SPIE's 1995 Symposium on OE/Aerospace Sensing and Dual Use Photonics* (pp. 440-451). International Society for Optics and Photonics.
- [7] Giles, J. W., Bankman, I. N., Sova, R. M., Green, W. J., King, T. R., Marcotte, F. J., ... & Millard, J. A. (2002, January). General-purpose lidar system model with experimental validation in fog, oil, and smoke conditions. In *International Symposium on Optical Science and Technology* (pp. 178-185). International Society for Optics and Photonics.
- [8] Sugimoto, N. (2003, November). Lidar methods for measuring distributions and characteristics of aerosols and clouds. In *12th International School on Quantum Electronics Laser Physics and Applications* (pp. 223-233). International Society for Optics and Photonics.
- [9] Bissonnette, L. R., & Hutt, D. L. (1995, September). Lidar remote sensing of cloud and fog properties. In *European Symposium on Optics for Environmental and Public Safety* (pp. 512-523). International Society for Optics and Photonics.
- [10] Streicher, J. (1995, September). Verification of lidar visibility. In *European Symposium on Optics for Environmental and Public Safety* (pp. 545-551). International Society for Optics and Photonics.

- [11] Utkin, A. B., Lavrov, A., & Vilar, R. (2008, October). Automatic recognition of smoke-plume signatures in lidar signal. In *XVII International Symposium on Gas Flow and Chemical Lasers and High Power Lasers* (pp. 71312K-71312K). International Society for Optics and Photonics.
- [12] Kovalev, V., Hao, W. M., Wold, C., Newton, J., Latham, D. J., & Petkov, A. (2008, August). Investigation of optical characteristics and smoke plume dynamics in the wildfire vicinity with lidar. In *Optical Engineering+ Applications* (pp. 708906-708906). International Society for Optics and Photonics.
- [13] Streicher, J., & Werner, C. (1999, May). Smoke detection using a compact and eye-safe lidar. In *AeroSense'99* (pp. 590-598). International Society for Optics and Photonics.
- [14] Uthe, E. E. (1981). Lidar evaluation of smoke and dust clouds. *Applied optics*, 20(9), 1503-1510.
- [15] Kovalev, V. A., Hao, W. M., & Wold, C. (2007). Determination of the particulate extinction-coefficient profile and the column-integrated lidar ratios using the backscatter-coefficient and optical-depth profiles. *Applied optics*, 46(36), 8627-8634.
- [16] Kovalev, V. A., Susott, R. A., & Hao, W. M. (2004, January). Inversion of lidar signals from dense smoke contaminated with multiple scattering. In *Remote Sensing* (pp. 214-222). International Society for Optics and Photonics.
- [17] Randhawa, J. S., & Van der Laan, J. E. (1980). Lidar observations during dusty infrared Test-1. *Applied optics*, 19(14), 2291-2297.
- [18] Uthe, E. E., Morley, B. M., & Nielsen, N. B. (1982). Airborne lidar measurements of smoke plume distribution, vertical transmission, and particle size. *Applied optics*, 21(3), 460-463.
- [19] Starr, J. W., & Lattimer, B. Y. (2012, October). A comparison of IR stereo vision and LIDAR for use in fire environments. In *Sensors, 2012 IEEE* (pp. 1-4). IEEE.
- [20] SICK LMS 511 Outdoor, data sheet. http://www.sick.com/group/EN/home/products/product_portfolio/laser_measurement_systems/Pages/outdoor_laser_measurement_technology.aspx. Accessed June 2013.
- [21] Hokuyo UTM 30-LX-EW, data sheet. <http://www.robotshop.com/content/PDF/scanning-laser-range-finder-utm-30lx-ew.pdf>. Accessed June 2013.

- [22] IBEO Lux HD, data sheet. <http://www.ibeo-as.com/images/stories/pdf/neu/salesblatt%20lux%20hd.pdf>. Accessed June 2013.
- [23] Yamauchi, B. (2010, May). All-weather perception for man-portable robots using ultra-wideband radar. In *Robotics and Automation (ICRA), 2010 IEEE International Conference on* (pp. 3610-3615). IEEE.
- [24] Deißler, T., & Thielecke, J. (2010, September). Uwb slam with rao-blackwellized monte carlo data association. In *Indoor Positioning and Indoor Navigation (IPIN), 2010 International Conference on* (pp. 1-5). IEEE.
- [25] Yamauchi, B. (2008, April). All-weather perception for small autonomous UGVs. In *SPIE Defense and Security Symposium* (pp. 696203-696203). International Society for Optics and Photonics.
- [26] Omine, Y., Sakai, M., Aoki, Y., & Takagi, M. (2004, October). Basic examination of a technique to visualize space filled with dense smoke using millimeter-wave radar. In *Optics east* (pp. 272-281). International Society for Optics and Photonics.
- [27] Sakai, M., & Aoki, Y. (2006, August). Human and object detection in smoke-filled space using millimeter-wave radar based measurement system. In *Pattern Recognition, 2006. ICPR 2006. 18th International Conference on* (Vol. 3, pp. 750-750). IEEE.
- [28] Sakai, M., Aoki, Y., & Takagi, M. (2005, December). The support system of the firefighter's activity by detecting objects in smoke space. In *Optomechatronic Technologies 2005* (pp. 60510L-60510L). International Society for Optics and Photonics.
- [29] Sales, J., Marín, R., Cervera, E., Rodríguez, S., & Pérez, J. (2010). Multi-sensor person following in low-visibility scenarios. *Sensors*, 10(12), 10953-10966.
- [30] Viegas, D. X., Pita, L. P., Nielsen, F., Haddad, K., Tassini, C. C., D'Altrui, G., ... & Dimino, I. (2008, August). Acoustic and thermal characterization of a forest fire event. In *Optical Engineering+ Applications* (pp. 708904-708904). International Society for Optics and Photonics.
- [31] Maxwell, F. D. (1971). A portable IR system for observing fire thru smoke. *Fire Technology*, 7(4), 321-331.
- [32] Dissanayake, G., Huang, S., Wang, Z., & Ranasinghe, R. (2011, August). A review of recent developments in Simultaneous Localization and Mapping. In *Industrial and*

- Information Systems (ICIIS), 2011 6th IEEE International Conference on* (pp. 477-482). IEEE.
- [33] Cui, Y., Dong, H., & Zhou, E. (2008, May). An early fire detection method based on smoke texture analysis and discrimination. In *Image and Signal Processing, 2008. CISP'08. Congress on* (Vol. 3, pp. 95-99). IEEE.
- [34] Liu, Z. G., Kashef, A. H., Loughheed, G. D., & Crampton, G. P. (2011). Investigation on the Performance of Fire Detection Systems for Tunnel Applications—Part 2: Full-Scale Experiments Under Longitudinal Airflow Conditions. *Fire Technology*, 47(1), 191-220.
- [35] Beji, T., Verstockt, S., Van de Walle, R., & Merci, B. (2014). On the use of real-time video to forecast fire growth in enclosures. *Fire Technology*, 50(4), 1021-1040.
- [36] Gottuk, D. T., Lynch, J. A., Rose-Pehrsson, S. L., Owrutsky, J. C., & Williams, F. W. (2006). Video image fire detection for shipboard use. *Fire safety journal*, 41(4), 321-326.
- [37] Verstockt, S., De Potter, P., Van Hoecke, S., Lambert, P., & Van de Walle, R. (2011, July). Multi-sensor fire detection using visual and time-of-flight imaging. In *Multimedia and Expo (ICME), 2011 IEEE International Conference on* (pp. 1-6). IEEE.
- [38] Zhang, B. (2010, June). Visibility measurement using digital cameras in Qingdao. In *Photonics and Optoelectronic (SOPO), 2010 Symposium on* (pp. 1-4). IEEE.
- [39] Ming-wei, A., Zong-liang, G., Jibin, L., & Tao, Z. (2010, June). Visibility detection based on traffic camera imagery. In *Information Sciences and Interaction Sciences (ICIS), 2010 3rd International Conference on* (pp. 411-414). IEEE.
- [40] DiNunno, P. J. (2008). *SFPE handbook of fire protection engineering* (4th ed.). SFPE.
- [41] Collins, B. L., Dahir, M. S., & Madrzykowski, D. (1993). Visibility of exit signs in clear and smoky conditions. *Fire Technology*, 29(2), 154-182.
- [42] Amon, F., Benetis, V., Kim, J., & Hamins, A. (2004, August). Development of a performance evaluation facility for fire fighting thermal imagers. In *Defense and Security* (pp. 244-252). International Society for Optics and Photonics.
- [43] Amon, F., Bryner, N., & Hamins, A. (2004, August). Evaluation of thermal imaging cameras used in fire fighting applications. In *Defense and Security* (pp. 44-53). International Society for Optics and Photonics.

- [44] Amon, F., Hamins, A., & Rowe, J. (2006, April). First responder thermal imaging cameras: establishment of representative performance testing conditions. In *Defense and Security Symposium* (pp. 62050Y-62050Y). International Society for Optics and Photonics.
- [45] Amon, F., Hamins, A., Bryner, N., & Rowe, J. (2008). Meaningful performance evaluation conditions for fire service thermal imaging cameras. *Fire Safety Journal*, 43(8), 541-550.
- [46] Fire Research Information Services (1990), ISO 9705, International Organization for Standardization.
- [47] Ostman, B. (1992). Smoke and soot. Heat Release in Fires. Elsevier Science.
- [48] Bard, S., & Pagni, P. J. (1986). Spatial variation of soot volume fractions in pool fire diffusion flames. *Fire Safety Science*, 1, 361-369.
- [49] Beyler, C. L. (1986). Major species production by diffusion flames in a two-layer compartment fire environment. *Fire Safety Journal*, 10(1), 47-56.
- [50] Gottuk, D. T., Roby, R. J., & Beyler, C. L. (1992, December). A study of carbon monoxide and smoke yields from compartment fires with external burning. In *Symposium (International) on Combustion* (Vol. 24, No. 1, pp. 1729-1735). Elsevier.

3 Stereoscopic Vision System using Long-Wave IR Thermal Imagers

3.1 Introduction

3.1.1 Challenges with LWIR Stereo Vision

Preliminary testing of a basic stereoscopic Long-Wave IR (LWIR) system showed promise for range finding in fire smoke environments [1-5]. However, it also showed that a LWIR stereo vision system cannot simply be treated as a low-resolution visual stereo vision system [3].

LWIR thermal cameras are typically non-radiometric uncooled microbolometer thermal cameras, and the LWIR stereo vision can suffer from intensity misalignment between the two cameras.

This misalignment can occur when the viewing scene changes, camera temperatures change, and non-uniform correction (NUC) is applied. In addition, determining intrinsic and extrinsic parameters for camera calibration and rectification is different than for visual systems since thermal camera intensities depend on the emissivity and temperature of the object being viewed (as opposed to color as with visual systems) [2,6,7,8]. Thermal cameras can also contain a higher level of noise than a typical visual stereo vision system [3], though some image filtering work has been performed for a single thermal camera [9]. The issue of noise is magnified by the low resolution of thermal cameras and becomes an even larger issue in approximately isothermal scenes since the correspondence matching is dealing with features that all have similar intensity. Handling intensity misalignment, calibration, and noise are all aspects in LWIR stereo vision that require special treatment.

3.1.2 Previous Work with LWIR Stereo Vision

In addition to fire-fighting scenarios, LWIR stereo vision has been used for human locating and tracking [10], medical equipment [11], and Unmanned Ground Vehicles [12]. LWIR visual odometry and stereo vision has been used on Unmanned Aerial Vehicles [13]. Work has also been performed for LWIR stereo vision use in indoor environments [14, 15]. Problems with LWIR stereo vision in these applications have been noted, such as low resolution [14], image noise [14], low texture regions [12], and difficulties in obtaining an accurate camera calibration [12]. Issues with camera intensity values have also been noted for some scenes when automatically reducing bit-depth of individual images of a stereo pair based on scene intensities using Automatic Gain Control (AGC) prior to correspondence matching [12].

One method to avoid issues from noise and low resolution is to perform stereo matching on only detected features in both images [14, 15]. However, this method provides a sparse disparity map [14, 15]. To make this map denser, interpolation with surfaces has been used, which requires some assumptions to be made about the scene [15]. Noise and low texture regions may be less of an issue with more thermally diverse scenes, and it may be possible to perform correspondence matching without directly addressing either issue [13], although it remains an issue for other cases. Image filtering for noise handling is common for visual cameras, and using image filters to handle noise in a single LWIR camera has been addressed for IR thermography purposes [9]. Filtering for LWIR stereo processing has briefly been mentioned in the literature where a row-based mean shift filter was used and compared to the unfiltered case for a scene [3].

Issues with LWIR stereo vision system calibration have been addressed in the literature [12, 2, 6, 7, 8]. These methods typically apply the same camera model used with visual systems [19] or a model simplified based on the low resolution of the system [2, 3]. The pattern used for determining the calibration varies from using a pattern of heated resistors on a plate [6] to using boards with varying emissivity [7, 8] to placing a cold grid in front of a heat source [2, 3].

Intensity alignment between cameras has been addressed by applying AGC to cameras individually [12]. AGC automatically reduces bit-depth of an image depending on the intensities present in the scene as viewed by the camera [12]. If the views from both cameras in a stereo pair are similar, then the reduced bit-depth images should have similar intensity values for features in the scene. This AGC can be applied based on only part of the scene in some scenarios to improve results [12]. Alternatively and dependent on hardware, correspondence matching could be performed on the higher bit-depth images with no reduction in bit-depth (i.e. no information loss before correspondence matching). If the higher bit-depth images are used for correspondence matching, the scene intensities may need to be aligned so that features in one camera will have the same intensity in the other camera.

3.1.3 Focus of Research

This chapter focuses on the development of LWIR stereo vision for robotic perception in environments that may be encountered in a fire scenario. These fire environments considered include approximately isothermal scenes such as a room temperature scene and thermally diverse scenes that may include a fire or hot smoke. For the LWIR stereo system developed in this work, individual subsystems for LWIR stereo vision are presented with a focus on intensity alignment and noise handling. Two methods of intensity alignment were tested and quantitatively evaluated for each of these environments. Noise was handled using a combination of stereo image filtering and selection of a robust matching algorithm.

For the filter selection, sixteen filters are presented and discussed. Each filter was quantitatively evaluated at a variety of filter parameter settings for effects on obstacle location and for processing time in an approximately isothermal scene and also with thermally diverse targets. Select filters were then quantitatively evaluated at a variety of filter parameter settings for effects on locating room boundaries in a hallway environment for both the approximately isothermal case and the thermally diverse case. The top filters as measured by effects on obstacle location and locating room boundaries were then evaluated for their effects on feature distortion by comparing feature detection results before and after application of the filters. The recommended LWIR stereo vision system architecture is presented based on the results of the tests performed.

3.2 LWIR Stereo Vision System Description

Figure 19 shows the outline for the LWIR stereo vision system discussed here. The LWIR stereo vision system discussed here follows the same basic algorithm as a visual stereo vision system with a few differences. First, if the cameras are non-radiometric, an intensity alignment step is needed to account for differences between the cameras. This is performed after any NUC is applied internally in each camera. Second, the prevalence of noise, especially in near-isothermal scenes, needs to be addressed. Both of these are addressed with pre-processing, and noise is also addressed in the selection of the matching algorithm. Obtaining the camera calibration and stereo rectification parameters is different than for visual systems. However, once the parameters are obtained, application of camera calibration and stereo rectification is the same as for visual systems. Post-processing of disparity maps into distance information formats is the

same as for visual systems. The remainder of this section discusses the steps from intensity alignment through disparity map fill-in. Intensity alignment and stereo image filtering for noise removal are further discussed in individual sections, including information about testing performed for method selection.

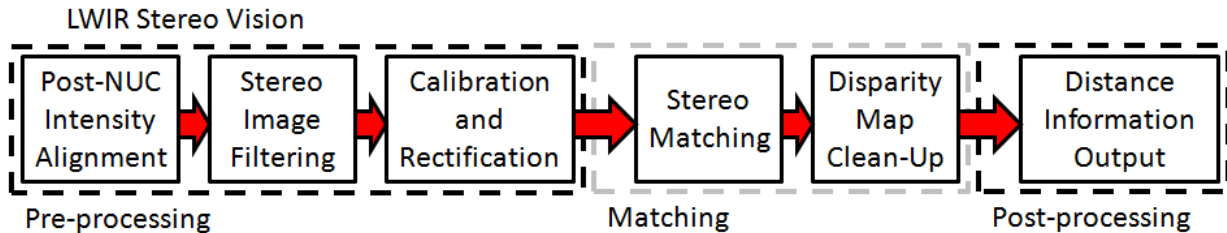


Figure 19: LWIR stereo vision system.

3.2.1 Intensity Alignment

Intensity misalignment arises from two thermal cameras not providing the same intensity values for features in a given scene. Figure 20 shows a visual example of this for a LWIR stereo vision system and how it can change with time. All images have been scaled in the same manner for this 8-bit grayscale view. The top two images are a left and right stereo view of a hallway in room temperature conditions. The bottom two images are of the same view later in time, once the upper portion of the hallway is heated with fire smoke. Initially, the cameras are offset in intensity values enough to visually see the difference in brightness between the left and right features. Later in time, the second pair appears to have less of an offset between left and right images. Quantitatively comparing the images shows that the intensities of features in the latter images are closer in value to each other than the intensities of the features in the first images are to each other but that there is still an offset in intensities present between the left and right images.

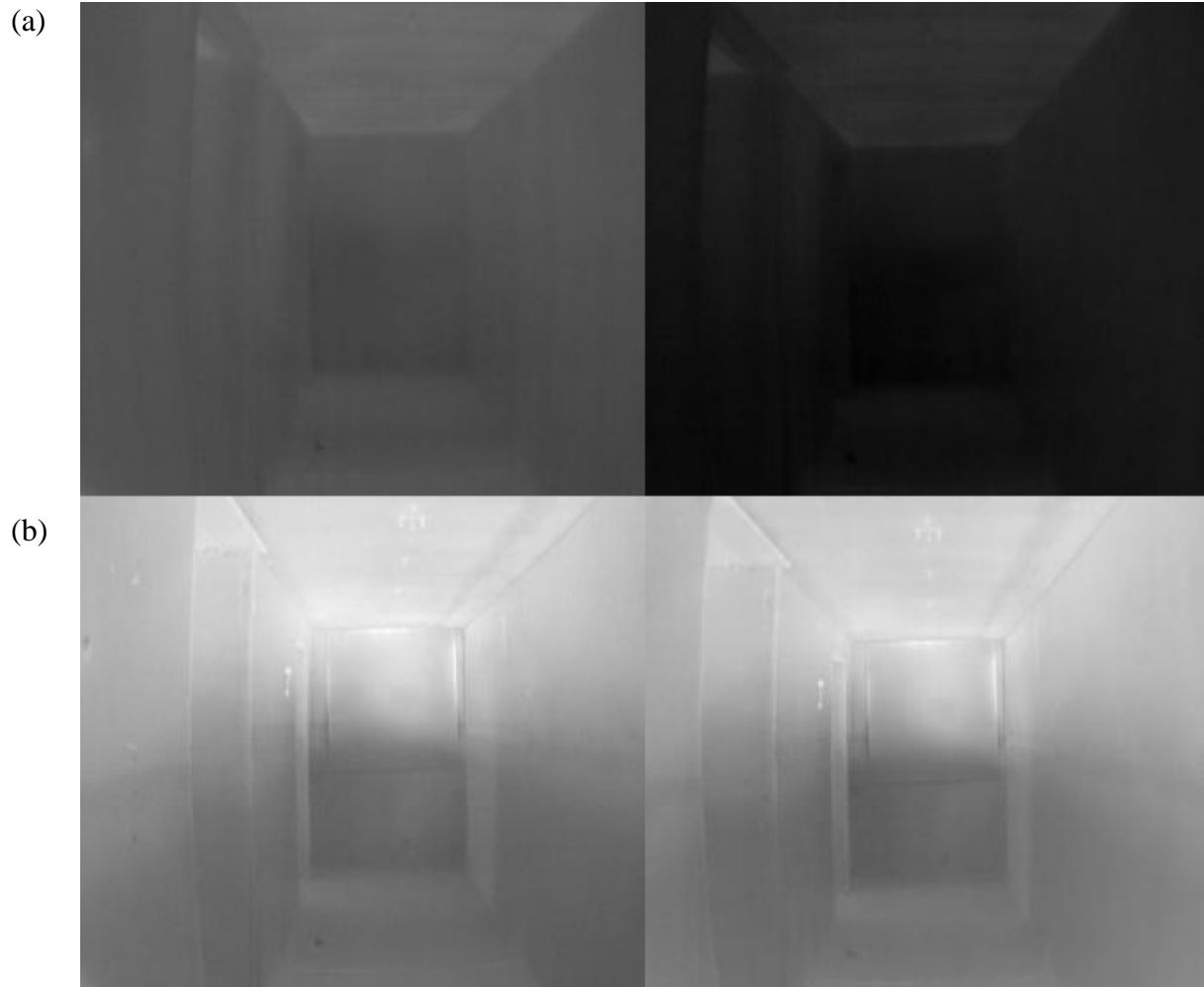


Figure 20: Example of the intensity offset changing with time between (a) a stereo pair of an initial room-temperature hallway and (b) a stereo pair taken later in time with fire smoke heating the upper portion of the hallway.

Stereo correspondence matching of near-isothermal scenes can result in errors if the intensity mismatch is not addressed. Several ways to address illumination issues in visual systems include stereo matching on transforms of the filtered or raw intensities [17, 18], histogram equalization techniques for stereo pairs [20], and advanced techniques that work to adjust brightness between stereo pairs for regions of an image (i.e. local) [21]. For the IR stereo pair here, NUC internal to the thermal cameras will account for sensor illumination issues in each camera due to thermal drift [22] but working individually on each camera and not on the stereo system as a whole. In other words, even without significant differences in the view of a scene per camera, the post-NUC left and right LWIR camera images will likely have global illumination (intensity)

differences. To correct this, an intensity alignment step is required. Tests were carried out on two intensity alignment methods under consideration in three scenarios, discussed in subsequent sections.

3.2.2 Stereo Image Filtering

Thermal cameras can contain a high level of noise [3, 9]. The effects of this noise on stereo matching are amplified by the low resolution of thermal imagers, especially with near-isothermal scenes, since features important to matching lose their distinguishability. Removal of noise via image filtering is desirable to improve stereo matching results. Tests were performed in order to quantitatively select a filter for improving stereo matching results, discussed in subsequent sections.

3.2.3 Calibration/Rectification

Typically, visual system calibration and rectification parameters are obtained using images collected by the system of a 2-dimensional black-and-white pattern placed at several locations and orientations within the field of view [6]. These image pairs are used to calculate the internal camera parameters necessary to remove image distortion (camera calibration) [19]. These images are also used to align the cameras for the matching algorithm (stereo rectification) [19]. A proper calibration and rectification are important to correspondence matching accuracy.

Design of scenes for LWIR stereo vision calibration and rectification should take into account that thermal infrared cameras image based on the emissivity and temperature of objects within their field of view. Several papers in the literature have focused on methods for thermal stereo calibration and rectification, ranging from patterns of heated resistors on a plate [6] to using patterns with different emissivity [7,8]. The LWIR stereo vision system here used a cold metal grid placed in front of a warm LCD monitor for initial calibration and rectification [2,3] and a heated patterned object with varying emissivity for a second camera calibration and rectification.

As with visual systems [19], radial image distortion can be the most significant distortion in each LWIR camera. Low resolution in the thermal cameras can make radial distortion the only significant distortion. Because of this, correcting distortion during the calibration process can be simplified to only account for this distortion. Figure 21 shows the removal of radial distortion

using a simplified calibration process. The images in the figure are of a cold metal grid (black) in front of a warm LCD monitor (white) with red lines overlaid to show distortion correction effects.

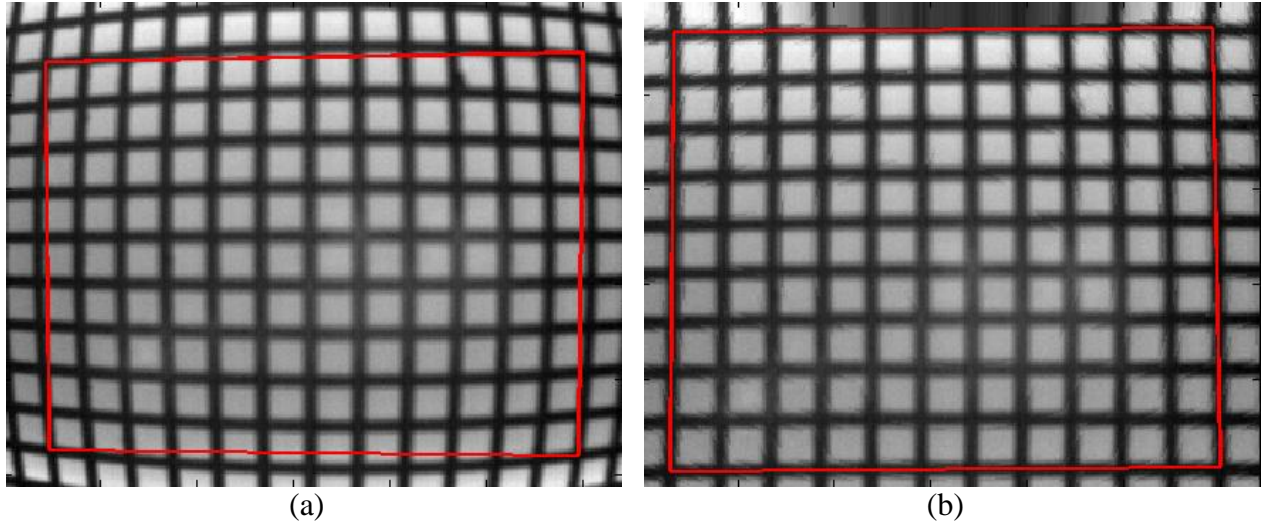


Figure 21: Image of a cold metal grid in front of a heated LCD monitor (a) before application of calibration and (b) after application of calibration.

3.2.4 Noise Handling with Matching Algorithm Selection

In addition to filtering, noise is also handled by choosing a matching (correspondence) algorithm that is robust, keeping processing time in mind. As with previous LWIR stereo vision research, a bi-directional SAD algorithm [1,2,3] has been selected for this purpose. The algorithm is based off of the SAD matching algorithm (See [16]). Local matching methods (of which SAD is a type) are known to be relatively fast for stereo matching when compared to semi-global and global methods. The selected matching algorithm here includes bi-directional matching, which makes sure left-to-right and right-to-left matches are in agreement to consider a match valid [26]. Details of the bi-directional SAD correspondence matching algorithm are provided in Appendix B. The selected disparity fill-in method discussed in the previous section further cleans up the output from stereo matching.

3.2.5 Disparity Post-Processing

Post-processing for the LWIR stereo vision system presented here includes disparity-map fill-in and conversion into distance information formats. The disparity map from the correspondence

matching step is filled-in using diamond morphology. At each selected pixel, if the most prevalent disparity in the surrounding diamond-shaped block is above a selected threshold, the diamond is filled in with that disparity value. The diamond size can be altered depending on the scene and application. The resulting disparity map is converted to a distance map and a point-cloud. This information can further be used for object locating or other tasks.

3.3 Test Scenario Description

Tests were performed to evaluate two intensity matching algorithms and sixteen image filters. These were tested with a stereo vision system consisting of two FLIR A35 uncooled microbolometers. Each FLIR A35 in this setup has a 9-mm lens and outputs 256x320 images. The raw 14-bit images were used for tests. The cameras were set to perform NUC automatically, and data was recorded in a digital format. The baseline was different for different tests.

The goal of the evaluation of intensity alignment methods was to test the methods under consideration in a scene with low intensity variation, one with high intensity variation, and one with saturated pixels. These scenes correspond to relevant firefighting scenarios. For the scene with low intensity variation, a room temperature scene was selected. For the scene with high intensity variation, a scene of a hallway with the upper portion filled with smoke was selected. A scene with a fire in view was selected to ensure proper handling of saturated pixels.

For selecting a filter, tests were performed to evaluate the effects of different filters on stereo matching. The stereo matching was evaluated for two scenarios. First, object location was evaluated on a per-object basis. Second, room boundary location was evaluated based off of ground truth for the scene for select filters. Both scenarios were evaluated in an approximately isothermal setting and with the scene being made thermally diverse (i.e. heated/cooled targets; room partially heated with smoke). The top filters from both scenarios were evaluated at their effects on feature distortion. This was evaluated by imaging a heated spherical incandescent bulb and evaluating the filtered and unfiltered cases with a circle feature detection algorithm. The details of these three evaluation methods are discussed in the section on filter evaluation.

3.4 Intensity Alignment

3.4.1 Evaluation Details

Two methods were identified as potential intensity alignment algorithms. Both methods here assume that the cameras are viewing approximately the same scene and work globally for a stereo pair. The first method is to apply a basic offset based on what each camera is viewing. This assumes that the mean intensity in each image should be equal and that the scale is invariant between two cameras. The offset is calculated and applied through Equation (4).

$$R'(u, v) = R(u, v) - \bar{R} + \bar{L}, \forall R(u, v) \in R \quad (4)$$

where R is the original right image consisting of intensity information, R' is the new right image, $R(u, v)$ is the intensity of the pixel in R located at (u, v) , and L is the left image. \bar{R} and \bar{L} are the mean of intensity values for the right and left images, respectively.

The second method applies a linear scaling and an offset based on what each camera is viewing. This method bins each image based on intensity. Next, it locates the mean intensity value for the upper half of intensities and the mean intensity value for the lower half of intensities for both left and right images. It then uses the upper-intensity and lower-intensity means to scale and offset the intensities of one image relative to the other. To apply this method, the upper and lower means are calculated:

$$\begin{aligned} L'_{upper}(u, v) &= \begin{cases} 1, & L(u, v) \geq \bar{L} \\ 0, & L(u, v) < \bar{L} \end{cases} \\ L'_{lower}(u, v) &= 1 - L'_{upper}(u, v) \\ R'_{upper}(u, v) &= \begin{cases} 1, & R(u, v) \geq \bar{R} \\ 0, & R(u, v) < \bar{R} \end{cases} \\ R'_{lower}(u, v) &= 1 - R'_{upper}(u, v) \end{aligned} \quad (5)$$

$$\begin{aligned}
L'_{mean,up} &= \frac{L'_{upper} \cdot L}{\sum L'_{upper}} \\
L'_{mean,low} &= \frac{L'_{lower} \cdot L}{\sum L'_{lower}} \\
R'_{mean,up} &= \frac{R'_{upper} \cdot R}{\sum R'_{upper}} \\
R'_{mean,low} &= \frac{R'_{lower} \cdot R}{\sum R'_{lower}}
\end{aligned} \tag{6}$$

where the multiplication in the numerators is the dot product and L, R, u , and v indicate the left and right original images and image coordinates as before. Assuming a linear relationship between the new right image R' based on the left image parameters and the old right image R yields

$$\frac{R' - L'_{mean,low}}{R - R'_{mean,low}} = \frac{L'_{mean,up} - L'_{mean,low}}{R'_{mean,up} - R'_{mean,low}} \tag{7}$$

which leads to the equation for the new right image

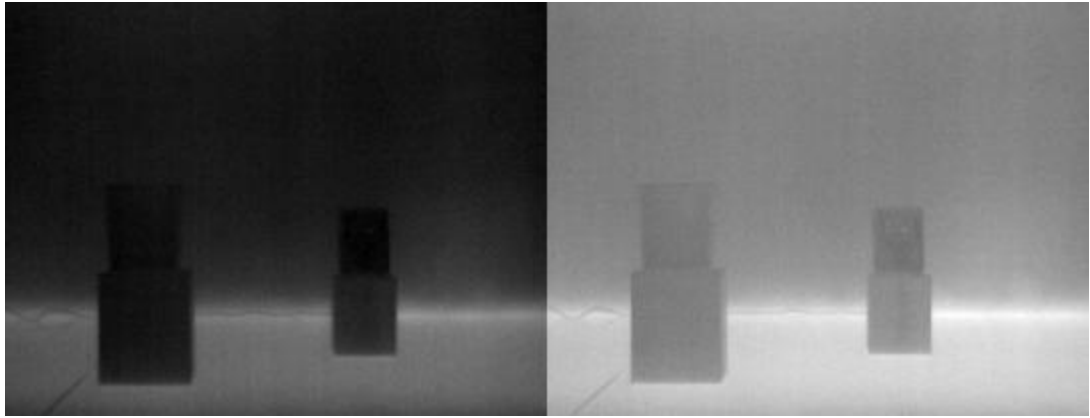
$$R' = (R - R'_{mean,low}) * \left(\frac{L'_{mean,up} - L'_{mean,low}}{R'_{mean,up} - R'_{mean,low}} \right) + L'_{mean,low} \tag{8}$$

The offset method and linear fitting method were both tested with an approximately isothermal scene and with a scene that was largely thermally diverse. Pixels within 6% of intensity saturation were ignored in calculations to avoid saturated pixels in both images skewing intensity alignment correction. The methods were also tested with a scene with fires present to ensure proper handling of saturated pixels.

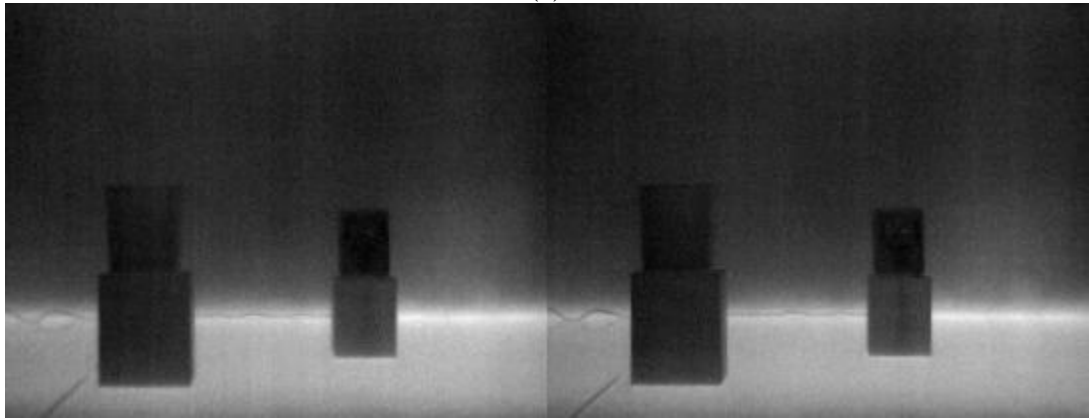
3.4.2 Results and Discussion

Images from the approximately isothermal scene for the intensity alignment test are shown in Figure 22. The first image pair is the original images before any intensity alignment has been applied. The second image pair is after the offset method has been applied. The third image pair

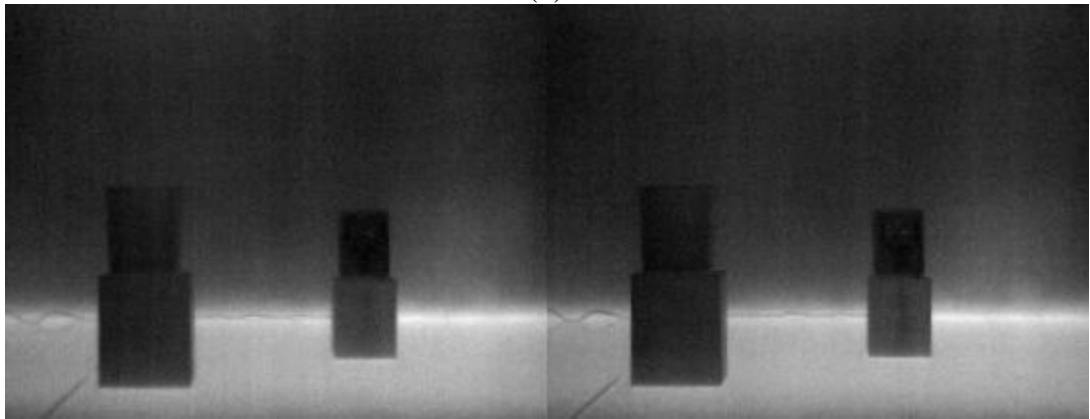
is after application of the linear scaling method. Likewise, the thermally diverse scene where smoke has heated the upper portion of a hallway while the lower portion remains at room temperature is shown in Figure 23. The images of the scene with fire present are shown in Figure 24. For display of these image sets, the intensities are linearly mapped from their original 14-bit images to 8-bit images using the same upper and lower values for each left and right image pair. Qualitatively, it appears that the offset method and linear scaling method both provide similar results better than the initial case.



(a)



(b)



(c)

Figure 22: Approximately isothermal scene image pairs (a) before intensity alignment, (b) after application of the offset method for intensity alignment, and (c) after application of the linear scaling method for intensity alignment.



(a)



(b)



(c)

Figure 23: Thermally diverse scene image pairs (a) before intensity alignment, (b) after application of the offset method for intensity alignment, and (c) after application of the linear scaling method for intensity alignment.



(a)



(b)

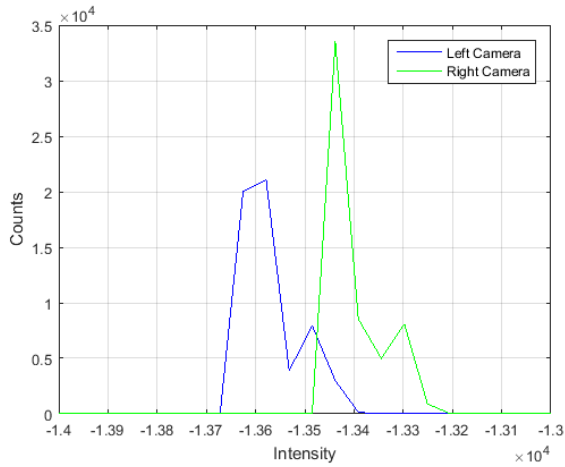


(c)

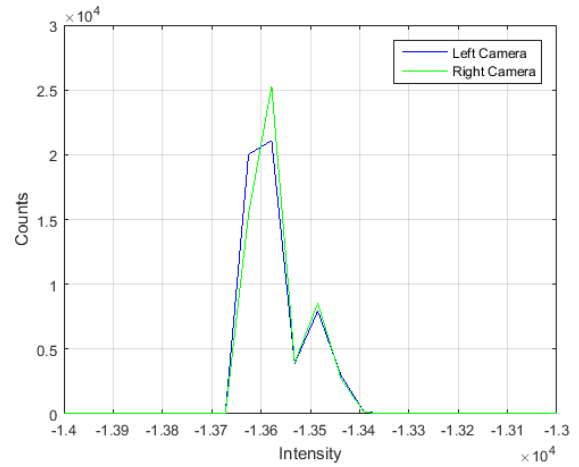
Figure 24: Pair of images for the scene with fire present (a) before intensity alignment, (b) after application of the offset method for intensity alignment, and (c) after application of the linear scaling method for intensity alignment.

Histogram were plotted to show how the intensities vary between the left and right image of each pair. The histograms for the approximately isothermal scene are shown in Figure 25 for the

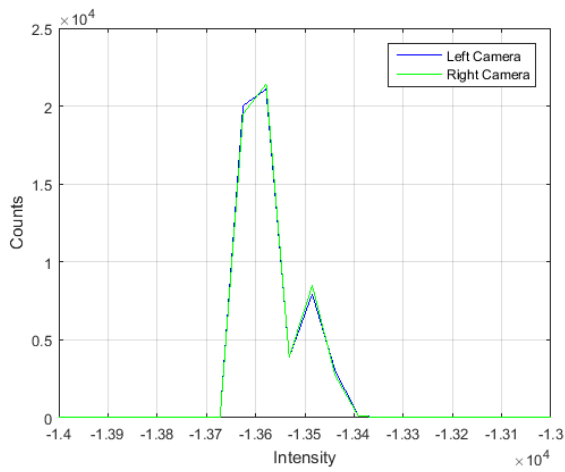
original scene and after application of each method. The histograms for the thermally diverse scene and for the scene with fire present are shown in Figures 26 and 27, respectively. The raw 14-bit camera data was read in from the cameras to range from $-16384 (-2^{14})$ to -1 . A log scale is used along the y-axis in Figure 27 to highlight the values at higher intensities. The results appear quite similar for the offset method and linear scaling method for the approximately isothermal scene and the scene with fire present. In all three cases, both methods are better than no method. However, for the thermally diverse scene, inspection of the right and left sides of the histogram data shows that the linear scaling method fits the data better than the offset method. This implies that intensities scale with scene temperature noticeably different between the left and right thermal imagers.



(a)

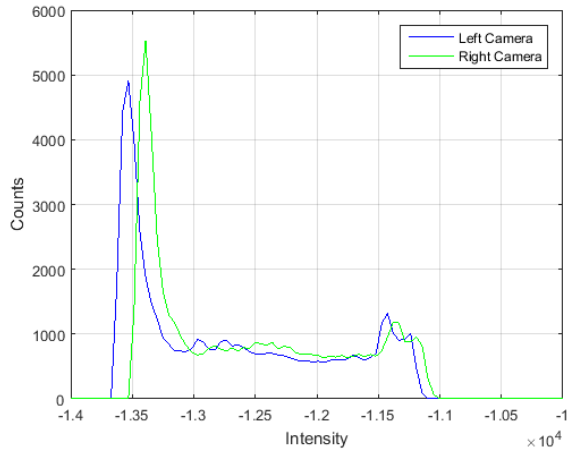


(b)

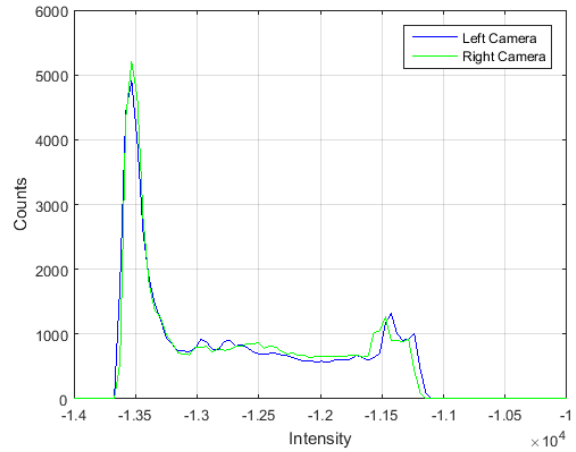


(c)

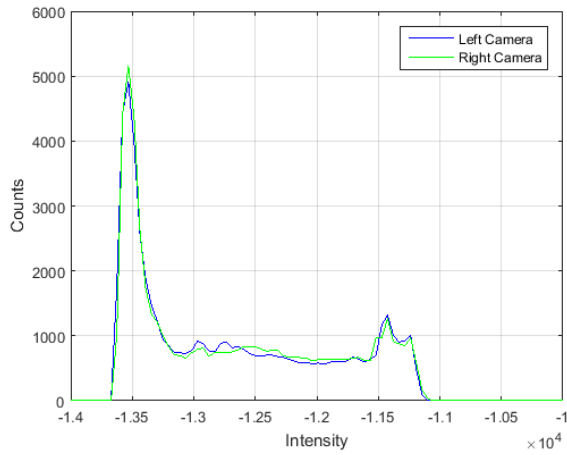
Figure 25: Histograms for the left and right images for the approximately isothermal scene for (a) the original data, (b) intensity alignment with the offset method, and (c) intensity alignment with the linear fitting method.



(a)



(b)



(c)

Figure 26: Histograms for the left and right images for the thermally diverse scene for (a) the original data, (b) intensity alignment with the offset method, and (c) intensity alignment with the linear fitting method.

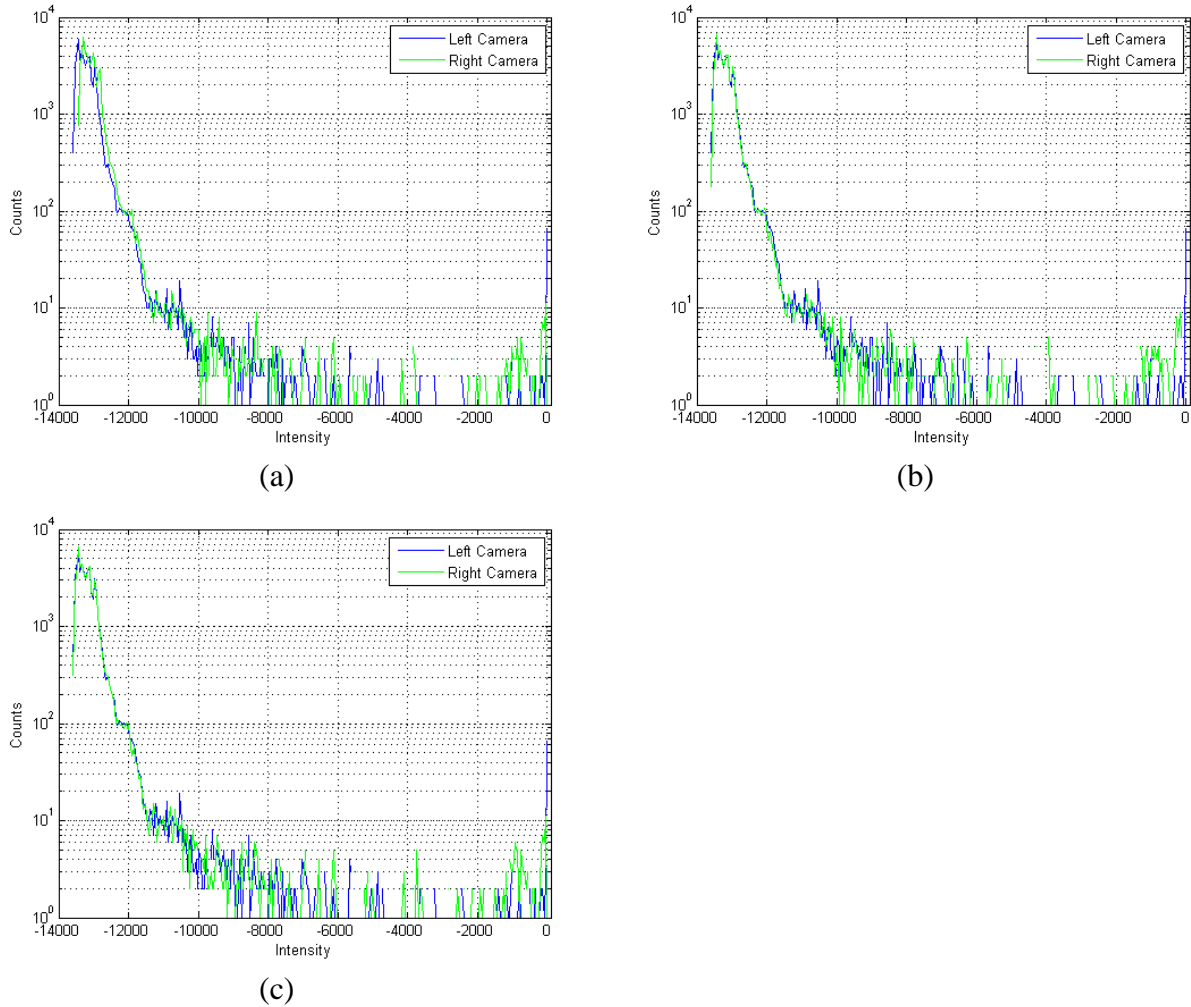


Figure 27: Histograms for the left and right images for the scene with fire present for (a) the original data, (b) intensity alignment with the offset method, and (c) intensity alignment with the linear fitting method.

Epipolar lines between the left and right camera were also plotted to show the effects of the intensity alignment methods. The 50th and 150th rows (counting from the top of the images) were plotted. The plots for the approximately isothermal scene before and after application of each method are shown in Figure 28. The plots for the thermally diverse scene and for the scene with fire present are shown in Figures 29 and 30. As with the histograms, the linear scaling method outperforms the offset method for the thermally diverse case. Both methods prove to outperform the case with no alignment in all three scenarios.

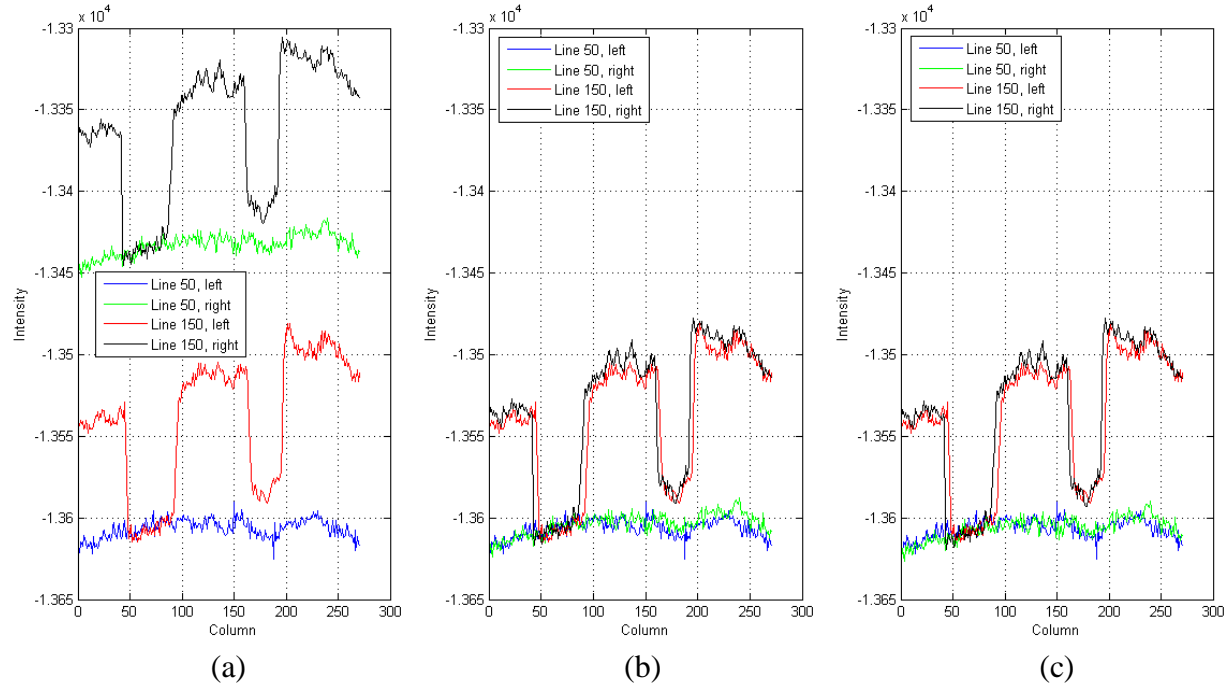


Figure 28: Epipolar line plots for the approximately isothermal scene for (a) the original data, (b) intensity alignment with the offset method, and (c) intensity alignment with the linear fitting method.

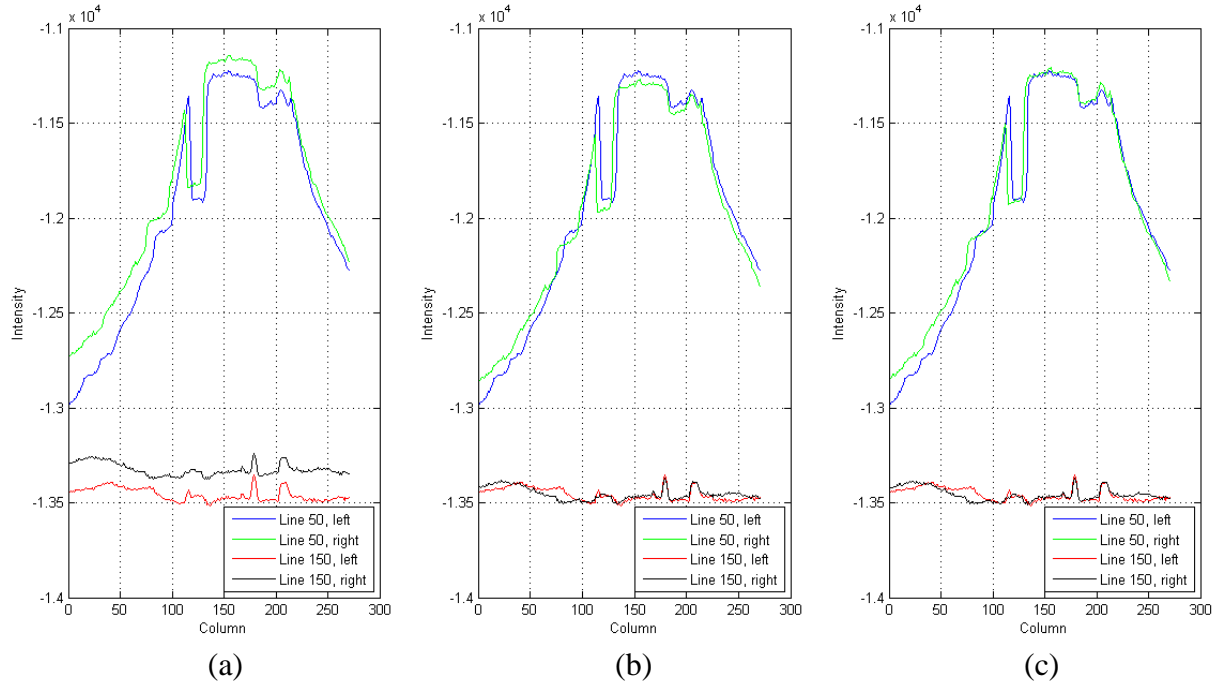


Figure 29: Epipolar line plots for the thermally diverse scene for (a) the original data, (b) intensity alignment with the offset method, and (c) intensity alignment with the linear fitting method.

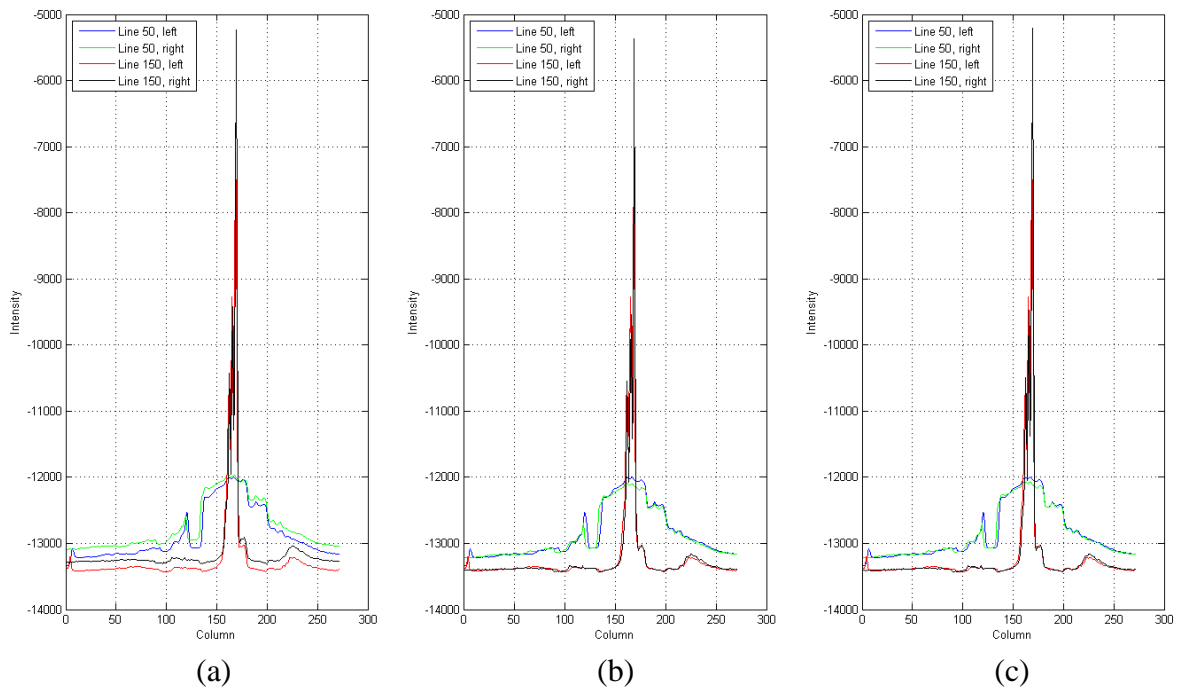


Figure 30: Epipolar line plots for the scene with fire present for (a) the original data, (b) intensity alignment with the offset method, and (c) intensity alignment with the linear fitting method.

Two features in each image pair were compared to determine the effects of intensity alignment. For the approximately isothermal scene, part of each target was selected as a feature to compare. In the thermally diverse scene, hot and cold portions of the pipe in the left side of the image were used as features. Part of the pipe and the fire were used as features for the scene with fire present. The fire feature was selected in a location of the fire that had few maxed-out intensities present. The features were located in the left and right image and quantitatively compared for the average absolute difference between the images after each method. These values are shown in Table 4.

Table 4: Change in feature intensities for both methods for the scenes.

Scene	Feature	Feature Size	Average Absolute Intensity Difference		
			Original	Offset Method	Linear Means Fitting Method
Approximately Isothermal	Left target	10x10	170.2	3.7	4.7
	Right target	10x10	175.0	5.1	4.3
Thermally Diverse	Pipe, Upper	10x10	91.5	37.5	7.6
	Pipe, Lower	10x10	139.0	10.2	6.7
Fire Present	Fire	5x5	545.0	654.0	512.5
	Pipe	10x10	111.2	14.1	12.8

Analysis of the two features selected for the approximately isothermal case in Table 4 shows that the difference between the offset method and the intensity alignment method is on the order of one. The offset method and the linear fitting method each perform better than the other method for one feature. For the thermally diverse case, the linear fitting method performs better for features at alignment for both the lower and the higher intensity features. This is due to the ability of the fitting method to scale intensities in addition to providing an offset for alignment. By scaling based on higher and lower intensity data, better alignment is achieved. For the scene with fire present, both methods fail to better align the fire feature significantly (The offset method even worsens alignment) but align the cooler feature much better than when no method is applied.

Overall, the linear fitting method provided better intensity alignment than the offset method. However, both methods proved to be better than applying no intensity alignment. The results from both methods were similar except when the scene was largely thermally diverse, so in some

cases the offset method could be chosen over the linear fitting method for simplicity or calculation time.

3.5 Noise Filtering

The effects of image filtering on stereo matching were evaluated based on stereo matching performance. Matching results for the filters were evaluated for object location in an approximately isothermal and a thermally diverse scene on a per-object basis. Matching results were evaluated for room boundary location based off of the ground truth for an approximately isothermal hallway scene and for a thermally diverse hallway scene. These two stereo matching evaluations are discussed in the next subsection. Evaluation of the filter effects on feature distortion are discussed in the subsection following that one.

3.5.1 Stereo Matching Performance

3.5.1.1 Evaluation Details

Table 5 lists several filters under consideration for improving LWIR stereo vision. The filters under consideration have been grouped into several main groups. The spatial, temporal, and spatial-temporal average filter groups contain functions that use mean, median, and mode, along with a weighted filter. These filters are applied at each pixel and evaluated using the local neighborhood for spatial filters, the previous values of the pixel for temporal filters, and a combination of the two for the spatial-temporal filters (i.e. current and previous neighborhoods at each pixel). Likewise, the spatial frequency filter is evaluated at each pixel based on its local neighborhood while the temporal frequency filter is evaluated based on the previous pixel values for each pixel. A brief description of the filters is provided here, and a more thorough description is provided in Appendix C.

Table 5: Filters under consideration for LWIR stereo vision noise removal.

Category	Filter Method	Function Name	Type (Spatial vs. Temporal)	Relevant Source	Reason
Spatial Average	Mean, mode, median	StereoAvgS	Spatial	23,24	Basic spatial averaging
	Mean shift (weighted mean)	StereoMeanShift	Spatial	23,25,26	Weighted spatial averaging
Temporal Average	Mean, mode, median	StereoAvgT	Temporal	24	Basic temporal averaging
	Weighted mean	StereoWMeanT	Temporal	24	Weighted temporal averaging
Spatial-Temporal Average	Mean, mode, median	StereoAvgST	Both		Basic spatial-temporal averaging
	Weighted mean	StereoWMeanST	Both	24	Weighted spatial-temporal averaging
Frequency	Spatial	StereoFrS	Spatial	27	Basic spatial frequency filtering
	Temporal	StereoFrT	Temporal		Basic temporal frequency filtering
Noise-Variance-Based	Local-Linear Minimum Mean-Square Error (LLMMSE)	StereoLLMMSE	Spatial	28,29	In literature for thermography applications; similar to Wiener
	Wiener	StereoWienF	Spatial	9	In literature for thermography applications; similar to LLMMSE
Wavelet (Haar)	Wiener	StereoWienFWv	Spatial	27,30, Haar: 31	Wavelet application of thermography-used filter
	Averaging	StereoAvgWv	Spatial	Haar: 31	Basic averaging in the wavelet domain
	Weighted average	StereoWMeanWv	Spatial	Haar: 31	Weighted averaging in the wavelet domain
Special	Anisotropic diffusion	StereoAniDif	Spatial	23,32	Large literature presence
	Consecutive Wiener	StereoWienFC	Spatial	9	In literature for thermography applications
	Non-Local Means (NL-Means)	StereoNLMeans	Spatial	33	Success with visual imagery

The noise-variance-based filters were selected based off of successful use in visual imagery [28,29] and in IR thermography research [9]. Both filters here are based off of the assumption that noise can be removed if its variance is known or estimated [9,28,29]. These filters have shown promising results with thermal imaging in cases where low noise in the spatial second derivative is required [9].

The wavelet-based filters selected for evaluation begin with the application of the Haar wavelet [31] at each pixel. The transformed data is then filtered using a Wiener filter, average filter, or weighted average filter. The data is then transformed out of the wavelet domain.

Several special filters have also been included for evaluation. These include the consecutive Wiener filter [9], anisotropic diffusion [23,32], and Non-Local Means (NL-means) [33]. The consecutive Wiener filter was included due to its success with thermal image filtering for thermography research [9]. Anisotropic diffusion has had good results with visual imagery [23], as had NL-means [33].

Each filter was evaluated for a variety of filter-specific parameter selections, shown in Table 6. The functions were coded into MATLAB functions and applied to two image streams (left and right from the stereo setup) at a time. The timing for processing each filter at each iteration of filter settings was stored as was the resulting image pair.

Table 6: Filter parameters.

Function Name	Parameters	Values
StereoAvgS	Method Box (kernel) size	Mean, mode, median 3,5,7,9,11
StereoMeanShift	Box size Color closeness strength Color closeness used Power of color closeness	5,9,13,17,21 2,4,8,16,32 0,1 (i.e. on/off) 1,2,3,4
StereoAvgT	Method Number of frames	Mean, mode, median 3,5,7,9,11
StereoWMeanT	Color closeness value Number of frames	2,4,8,16,32 3,5,7,9,11
StereoAvgST	Method Box size Number of frames	Mean, mode, median 3,5,7,9,11 3,5,7,9,11
StereoWMeanST	Box size Color closeness strength Spatial color closeness used Power of spatial color closeness Temporal color closeness used Power of temporal color closeness Number of frames	5,9,13,17,21 2,4,8,16,32 0,1 1,2,3,4 0,1 1,2,3,4 3,5,7,9,11
StereoFrS	Box size ("box") Cut frequency 1 ("FCut1") Cut frequency 2 (for notch/band-pass) Type	5,7,11,15,19,23,27 (0.25*(box-1)) by 1 to (0.5*(box-1)) FCut1 by 1 to (0.5*(box-1)) Low-pass, high pass, band-pass, notch
StereoFrT	Number of frames ("NFrames") Cut frequency 1 ("FCut1") Cut frequency 2 (for notch/band-pass) Type	5,7,11,15,19,23,27 (0.25*(NFrames-1)) by 1 to (0.5*(NFrames-1)) FCut1 by 1 to (0.5*(NFrames-1)) Low-pass, high pass, band-pass, notch
StereoLLMMSE	Box size Noise level	3,5,7,9,11 2,4,6,8,16,32,64,128,256
StereoWienF	Box size Noise level	3,5,7,9,11 2,4,6,8,16,32,64,128,256
StereoWienFWv	Box size (wavelet size) Wiener box size in wavelet domain Noise level*	4,8 3,5,7,9,11 5,10,50,80,100,1000,10000,20000,40000
StereoAvgWv	Box size (wavelet size) Method Averaging box size in wavelet domain	4,8 Mean, mode, median 3,5,7,9,11
StereoWMeanWv	Box size (wavelet size) Weighted averaging box size Color closeness strength Power of color closeness	4,8 5,9,13,17,21 2,4,8,16,32 1,2,3,4
StereoAniDif	Function Iterations Gamma K	Exponential, 1/k 1,10,100,200 0 by 0.01 to 0.25 1,5,10,20,50,100,200
StereoWienFC	Box size Noise level Number of consecutive applications	3,5,7,9,11 2,4,6,8,16,32,64,128,256 1,3,5,7,9
StereoNLMeans	Box size Search area box size H-parameter (color closeness strength)	3,5,7,9,11 5,10,20,40,80 1,3,5,7,9,11

*Noise level is a matrix that was varied so that the lower-frequency noise estimates were always lower or equal to the higher frequency noise estimates

In the literature, typical filter evaluation includes adding noise to an image or a set of images. Next, the images are filtered, and the results are compared to the initial images to show how well they removed the added noise [29, 30, 33]. Since the focus here is to select a filter for improved stereo matching, a different method was applied for filter selection. First, a few stereo scenes were recorded, intensity-aligned, and processed through the filters. Next, the scenes were stereo-matched and compared to a determined ground truth. Comparing the results to the ground truth provides quantitative results for the effects of each filter. This type of evaluation was performed for two types of perception goals: object detection and boundary location. Object location evaluation was based off of comparison to the ground truth of individual objects, while boundary location was evaluated based off of the entire scene. Both types of perception goals were under consideration since the effect of feature widening caused by some filters may improve object location (i.e. wider features resulting in more pixels matched at the object distance for each object) while causing boundary detection to become less accurate (i.e. matching near edges losing accuracy as features widen). In addition, the filters were also evaluated for their effects on feature distortion as discussed in a subsequent subsection.

3.5.1.1.1 Object Location

One object layout with two thermal options was selected for filter comparison for the object detection scenario. Figure 31 contains a diagram of the object detection evaluation setup. Both stereo scenes contained two targets placed at different distances from the stereo setup. One target selected was a bucket, and the other was a space heater. The setup was left at room temperature for the first scene, resulting in an approximately isothermal scene. For the second scene, the bucket was filled with ice-water and the heater turned on to result in a thermally diverse scene.

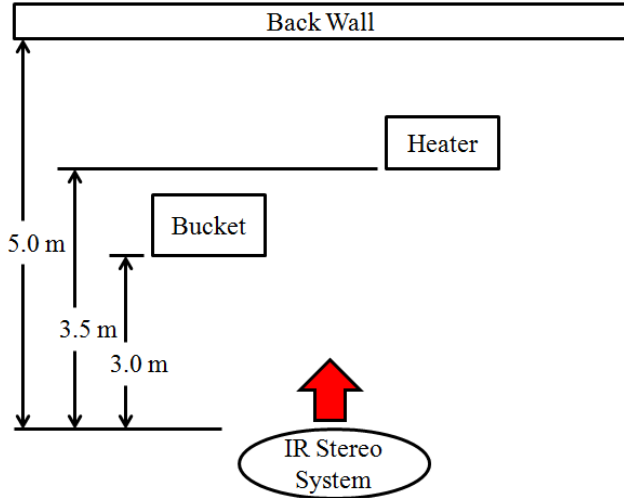


Figure 31: Top view of setup for object detection stereo matching evaluation of filters.

For both scenes, basic intensity alignment using offsets (as discussed in the previous section) was applied to the images. The resulting images were passed through the filters, and calibration and rectification were applied. Next, stereo matching was performed on edge-maps of the images pairs. The edge-maps were calculated using the horizontal and vertical Sobel operators and finding the magnitude of the resulting horizontal and vertical gradient images [23].

Stereo matching was performed in MATLAB using a bi-directional SAD (Sum of Absolute Differences) method used in previous LWIR stereo vision work [1,2,3], recording the matches and a cost-map for each image. Details of the bi-directional SAD correspondence matching algorithm are provided in Appendix B. Whole-number disparities were used (no sub-pixel calculations). For the ground truth calculation, both targets were segmented and manually aligned, as in [16,34]. Each target fell between a nominal closest disparity and a second-best nearby disparity, so evaluation of the filters included documenting the number of pixels with the nominal closest disparity value per target and the number of pixels with the second-closest disparity value per target. The closest and second-closest disparity values for each target are shown in Table 7. These values were recorded for two matching box sizes and for several stereo-matching cost-map thresholds per filter. The stereo matching settings for evaluation are shown in Table 8. The first of these parameters, “Box size”, is used to set the window size for the correspondence matching algorithm. The second parameter, “Match quality cutoff between best and second-best match”, is a threshold used to limit the disparity results to only contain top-

matching disparity values if they have a high enough cost compared to the next-best matched disparity value.

Table 7: Target closest and second-closest disparity values.

	Bucket target	Heater target
Closest disparity value to target	14	13
Second-closest disparity value to target	13	12

Table 8: Stereo matching settings: “Box size” determines the window size for the matching algorithm, and “Match quality cutoff between best and second-best match” limits the disparity map to only contain top-matching disparity values if they have a high enough cost compared to the next-best matched disparity value

Parameter	Value
Box (kernel) size (“box”)	3,5
Match quality cutoff between best and second-best match	$((\text{box}-1)/2)*[10,30,50,70,90]$

Once the stereo scenes were filtered and matched with the selected sets of parameter and stereo settings, the filters were evaluated to determine number of accurate (correct and second-best) matches, number of inaccurate matches, and number of unmatched pixels per target, based off of the calculated ground truth. The top filter settings for each filter were determined by choosing the parameter set that resulted in each filter’s highest level of accurate disparities minus inaccurate disparities averaged across the targets in the scene for each scene. Accurate disparities included best and second-best disparity value based off of the ground truth, since the ground truth resulted in a nominal and second-best disparity for each target when using whole-number disparities. The inaccurate disparities included all other matched data. Unmatched pixels were not directly used in comparison.

The top filter overall for each scene was selected from the top performing case of each filter, with processing time also considered. The top filter settings per filter for the combined data set (i.e. combining the approximately isothermal and the thermally diverse data sets) was also determined based off of the average of the accurate disparities minus inaccurate disparities per target for both targets in both scenes. Likewise, the top filter overall was determined by analyzing the matching and timing results of the top performing case of each filter.

3.5.1.1.2 Boundary Location

After evaluation of filters for object detection, several filters were removed from further evaluation based on a long processing time for the filter. These removed filters are StereoNLMeans, StereoAvgWv, and StereoWMeanWv. The remaining filters were evaluated for boundary detection in a hallway environment for the approximately isothermal (room temperature) case and for a thermally diverse case heated by fire smoke. Figure 32 contains a diagram of the hallway setup. As with the object detection filter evaluation, the images were aligned using the offset method before applying the filters. After filtering, calibration and rectification were applied to the stereo pair. The resulting images were stereo matched and evaluated using the same method and parameters as with the object detection case, with whole-number disparities in the resulting disparity maps as before.

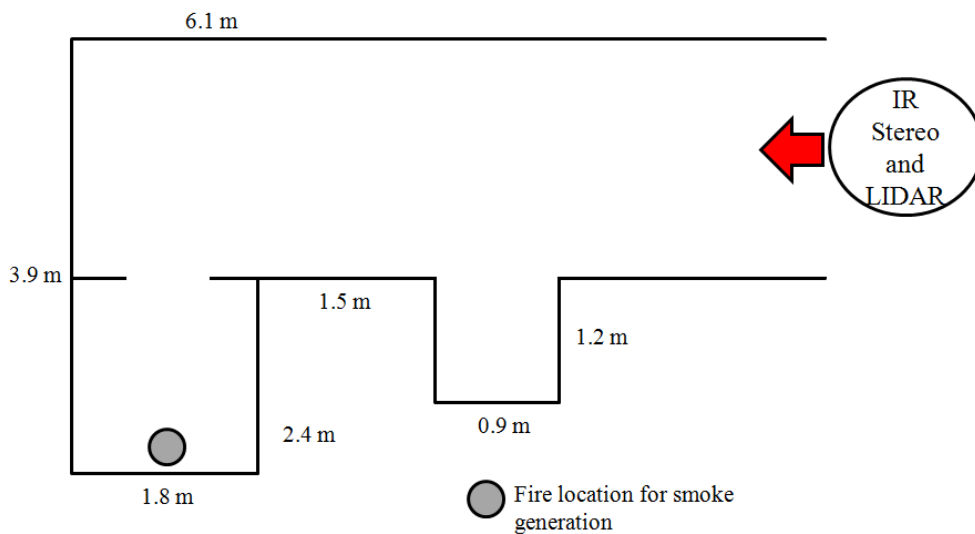


Figure 32: Top view of hallway setup for boundary location evaluation of filters.

The resulting disparity maps were compared to a ground truth 3D point cloud. The ground truth point cloud was produced using a spinning Hokuyo UTM-30LX-EW LIDAR located below the LWIR stereo vision system. For evaluation, this point cloud was aligned with the LWIR stereo vision system as discussed in Appendix D and was converted to an expected disparity map based on the stereo system properties. Holes present in the ground truth disparity map were not filled in so that all filters would only be compared to measured ground truth. The accuracy of the LIDAR was converted to a neighborhood and disparity range for each pixel in the ground truth

disparity map. During comparison, evaluated disparity levels were considered accurate if they were in this range, plus or minus a disparity level since whole-number disparities were used for the stereo system calculations. Disparity levels outside this range were considered inaccurate pixels. The top set of parameters for each filter was determined by selecting the parameter set with the highest level of accurate disparities minus inaccurate disparities. The top case for each filter was compared to determine which of the selected filters provide the best results for boundary location in these two selected scenes. This process was also performed for the combined data set of both scenes, averaging accurate and inaccurate matches together.

3.5.1.2 Results and Discussion

3.5.1.2.1 Object Location

The approximately isothermal and thermally diverse scenes used for the object detection tests are shown in Figure 33. The data in Figure 34 shows the matching results for the approximately isothermal scene for the top filter parameter and stereo parameter set of each filter. The top filter and stereo settings for each filter was determined to be the settings that resulted in the highest percentage of accurate matches minus inaccurate matches averaged between the two objects in the scene. The data labeled accurate includes disparity values that are either at the ideal whole-number disparity or the second-best whole-number disparity compared to the ground truth. The data labeled inaccurate includes all other matches. The data is listed as average percentage per target. Unmatched data is not shown and fills the remaining percentages. The data in Figure 35 shows the same thing for the thermally diverse scene. The data in Figure 36 shows the top matching result for each filter based on both objects in both scenes. Appendix E contains tabulated results of the top filter settings and stereo settings for each filter from these tests.

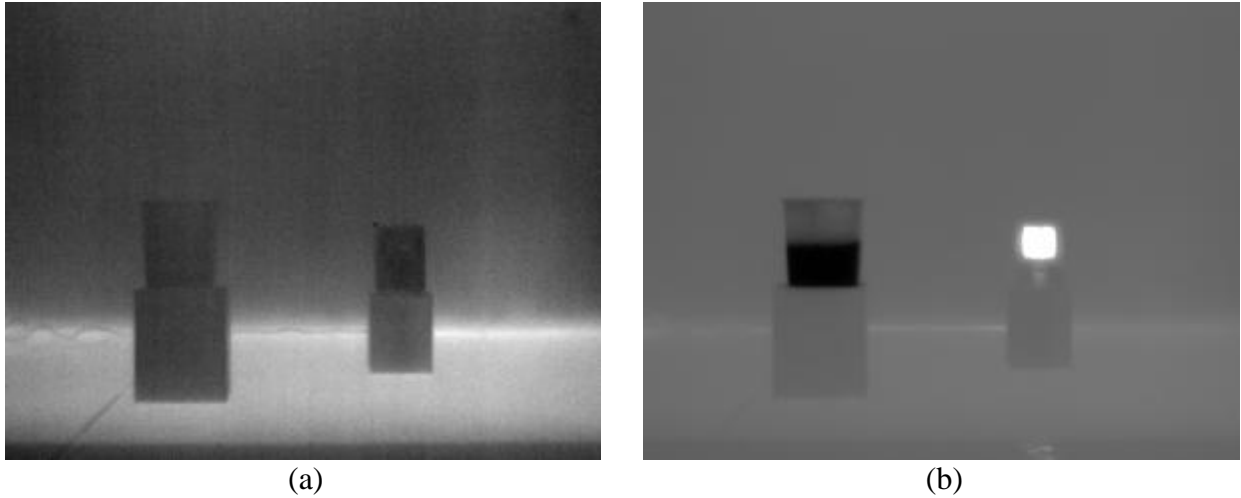


Figure 33: Unfiltered LWIR view of the object detection scene for (a) the approximately isothermal case and (b) the thermally diverse case.

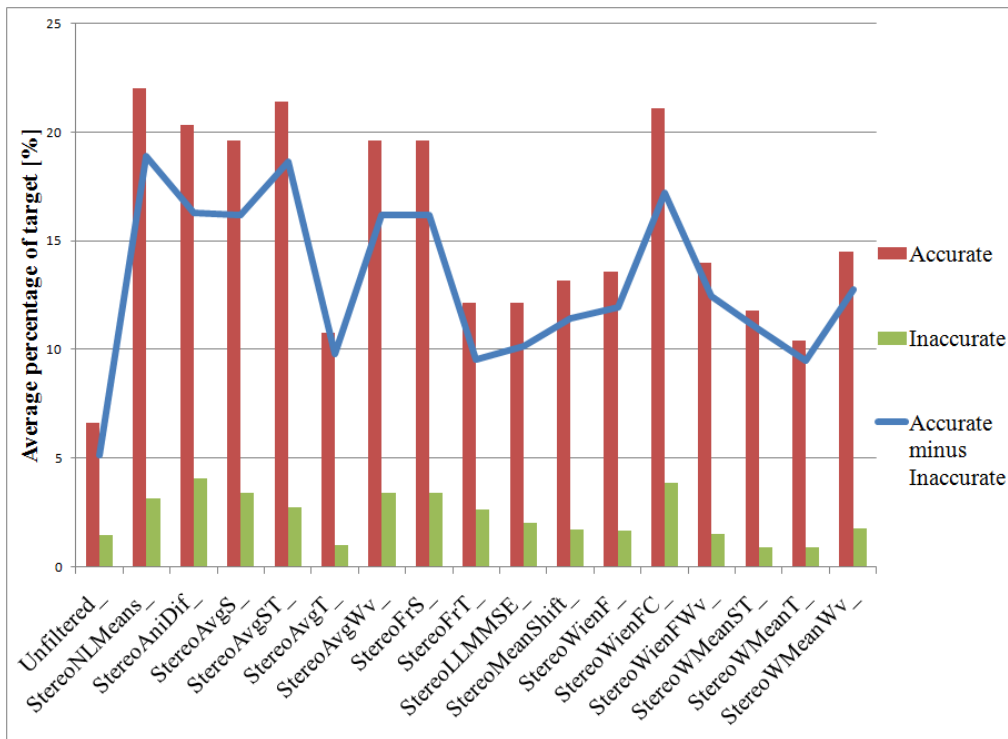


Figure 34: Accurate, inaccurate, and accurate minus inaccurate matches for the top filter parameter and stereo parameter settings for each filter for the approximately isothermal scene.

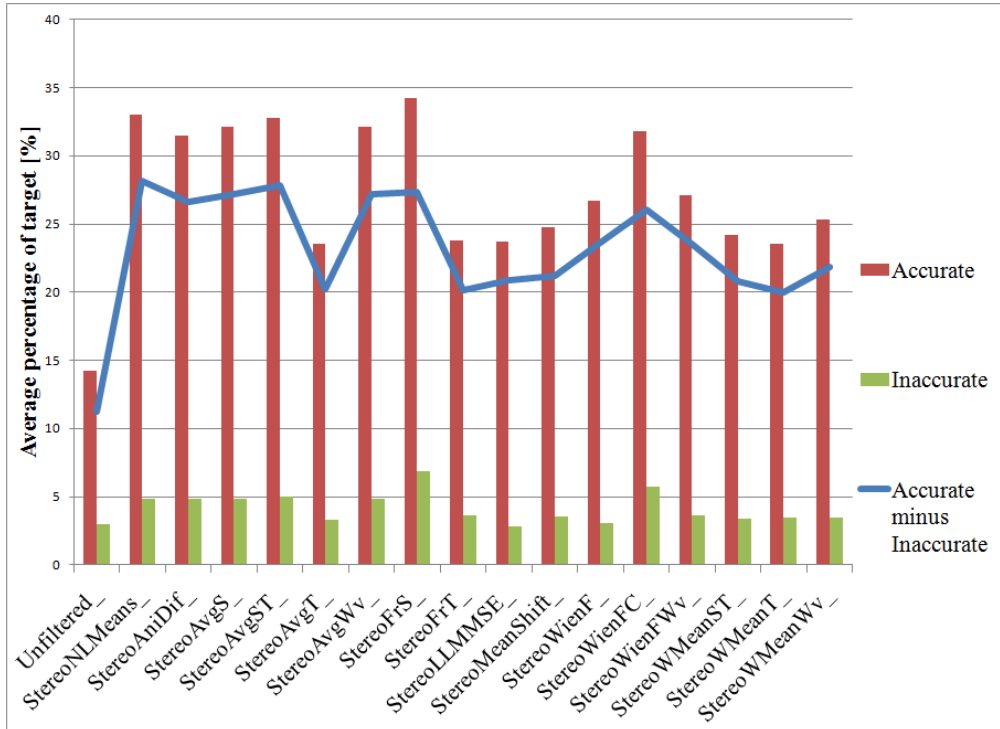


Figure 35: Accurate, inaccurate, and accurate minus inaccurate matches for the top filter parameter and stereo parameter settings for each filter for the thermally diverse scene.

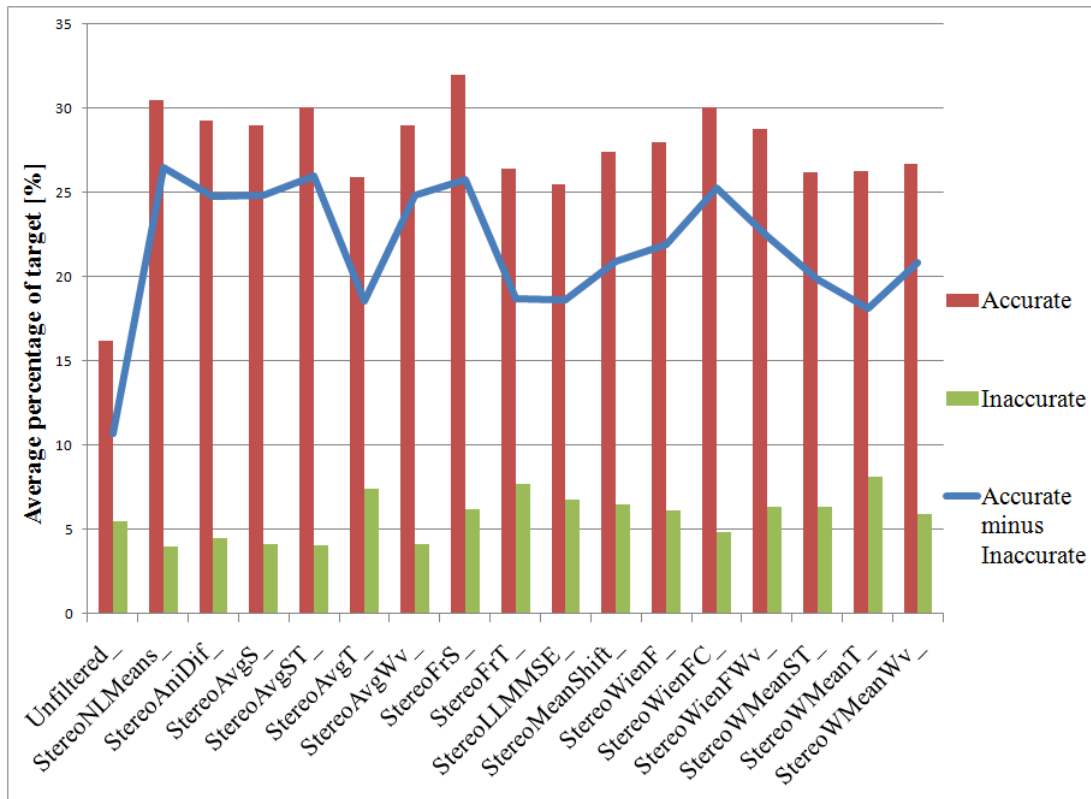


Figure 36: Accurate, inaccurate, and accurate minus inaccurate matches for the top filter parameter and stereo parameter settings for each filter for the combined scenes.

The data in Figure 34 shows that the filters giving the highest percentage of accurate matches minus inaccurate matches for object detection for the approximately isothermal scene are StereoNLMeans, StereoAvgST, and StereoWienFC. Comparing the processing times shows that the StereoNLMeans filter requires significantly more time to process stereo data than these other two filters. The results indicate that StereoAvgST can perform well for stationary (or perhaps slow-moving scenes) since it requires multiple frames. The StereoWienFC filter performs well when one image-pair is used and has a relatively low processing time, so it is considered the top filter for an approximately isothermal scene since it can handle motion (works on an individual frame pair).

The data in Figure 35 shows that several filters give a high percentage of accurate matches minus inaccurate matches for object detection for the thermally diverse scene. The StereoNLMeans, previously noted for its relatively high processing time, is again the top filter, with StereoAvgST

in the second-top position, but several other filters perform almost as well with much less processing time. The StereoWienFC, which performed well for the approximately isothermal scene, is also a top filter here, with more than 90% of the number of accurate minus inaccurate disparities that the top filter StereoNLMeans provides. For a single stereo pair, the StereoAvgS filter provided higher quality results (tied for 3rd top filter spot by quality) at a cost in processing time. If timing is more important, the StereoWienFC filter is considered a top choice here since it has low processing time and high quality, working on a pair of images from one time step.

The data in Figure 36 shows that the filters giving the highest percentage of accurate matches minus inaccurate matches for object detection for the combined scenes data set are StereoNLMeans, StereoAvgST, StereoFrS, and StereoWienFC. Once again, the relative processing time of the StereoNLMeans filter is significantly more compared to the other top filters. The StereoAvgST filter requires multiple frames, so it may be used in stationary (or perhaps slow-moving scenes). The StereoFrS and StereoWienFC filters both perform well with one-pair scenes, making them better candidates for scenes with motion. The StereoWienFC outperforms the StereoFrS at processing time with little loss in quality, so it is once again considered the top filter.

Due to high processing time, StereoNLMeans, StereoAvgWv, and StereoWMeanWv were removed from the set of filters being considered in further tests for boundary location. These filters all took more than 50 seconds as coded to filter a left and right image stream for their top filter case overall. The StereoWienFC filter took a maximum of 0.09 seconds to process a pair of images for its top filter settings in each scenario. The high quality results of the consecutive Wiener filter (StereoWienFC) are perhaps due to the way it models image noise for removal.

3.5.1.2.2 Boundary Location

The ground truth for the boundary location tests was the same for the approximately isothermal scene and the thermally diverse scene. The left raw IR images of the room temperature and thermally diverse scenes are shown in Figure 37, along with the ground truth disparity map produced from the spinning LIDAR. The ground truth is shown here with lighter grayscale values for higher disparity values (i.e. closer distances) and has black where there is no disparity

value present from the LIDAR. The images of the room temperature and thermally diverse scenes are after calibration and rectification have been applied.

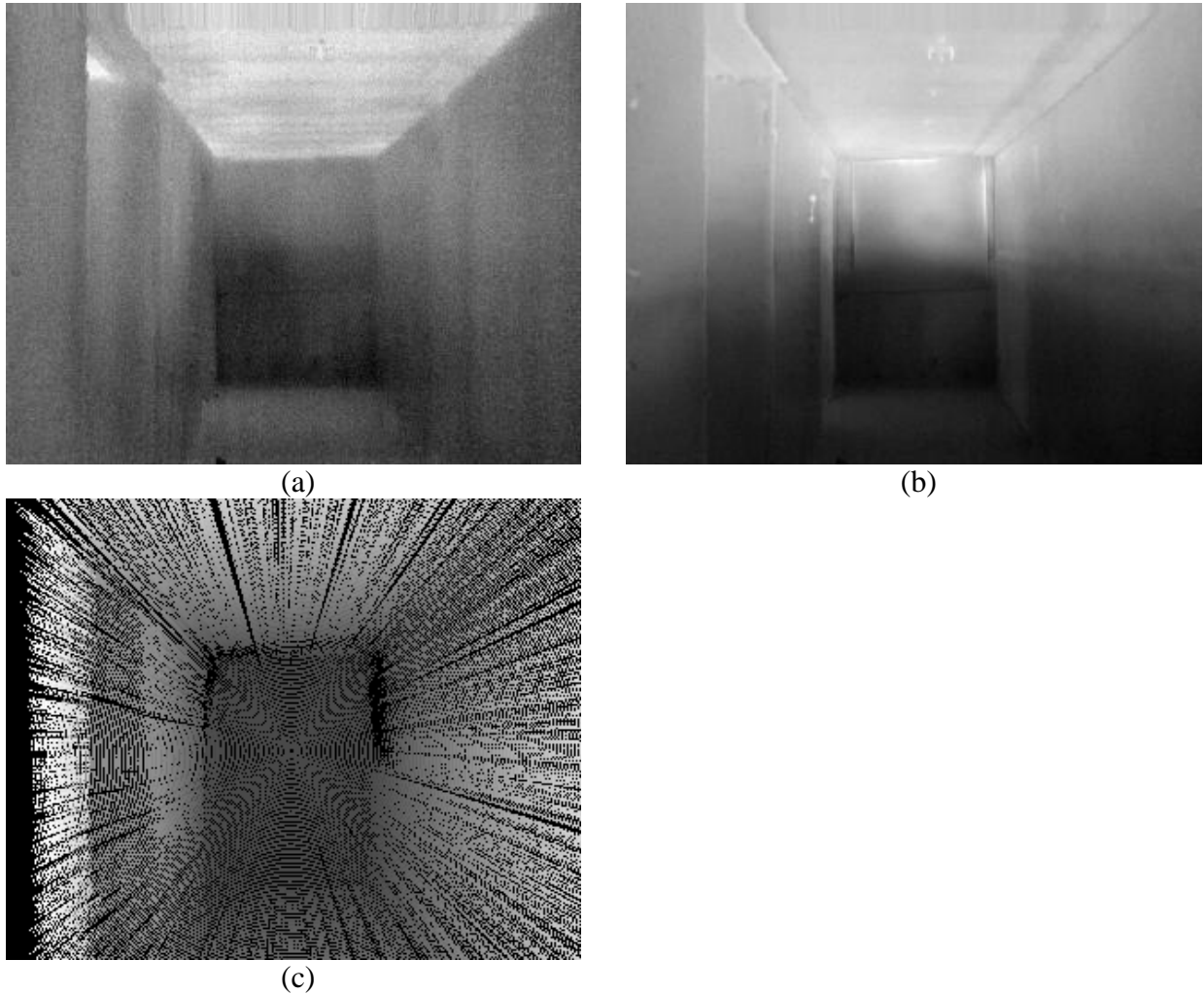


Figure 37: Left image for boundary location for (a) the approximately isothermal scene, (b) the thermally diverse scene; (c) ground truth from the LIDAR.

The data in Figure 38 shows the matching results for the room temperature scene for the top filter parameter and stereo parameter set of each filter. The top filter and stereo settings for each filter was determined to be the settings that resulted in the highest percentage of accurate matches minus inaccurate matches for the entire scene. Accurate matches include those at the ground truth disparity value and those within a disparity range and disparity map neighborhood in the ground truth determined at each point by the accuracy of the LIDAR (30 mm from LIDAR

[37]). Disparity values within one of the nominal disparity were included since the stereo system was kept to whole number disparities and rounding may be involved. Unmatched pixels fill up the remaining percentage not shown in the figure. The data in Figure 39 shows the same thing for the thermally diverse scene. The data in Figure 40 shows the top matching result for each filter based both objects in both scenes. Appendix E contains tabulated results on the top filter settings and stereo settings for each filter for all three data sets.

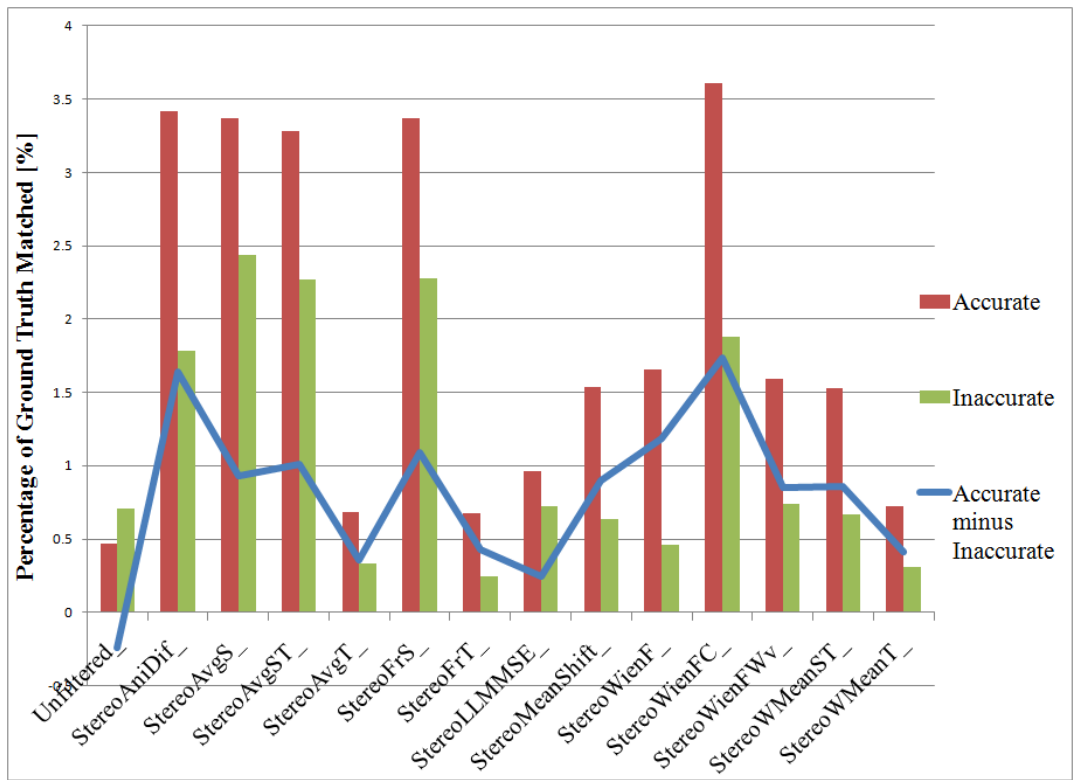


Figure 38: Accurate, inaccurate, and accurate minus inaccurate matches for the top filter parameter and stereo parameter settings for each filter for the approximately isothermal scene.

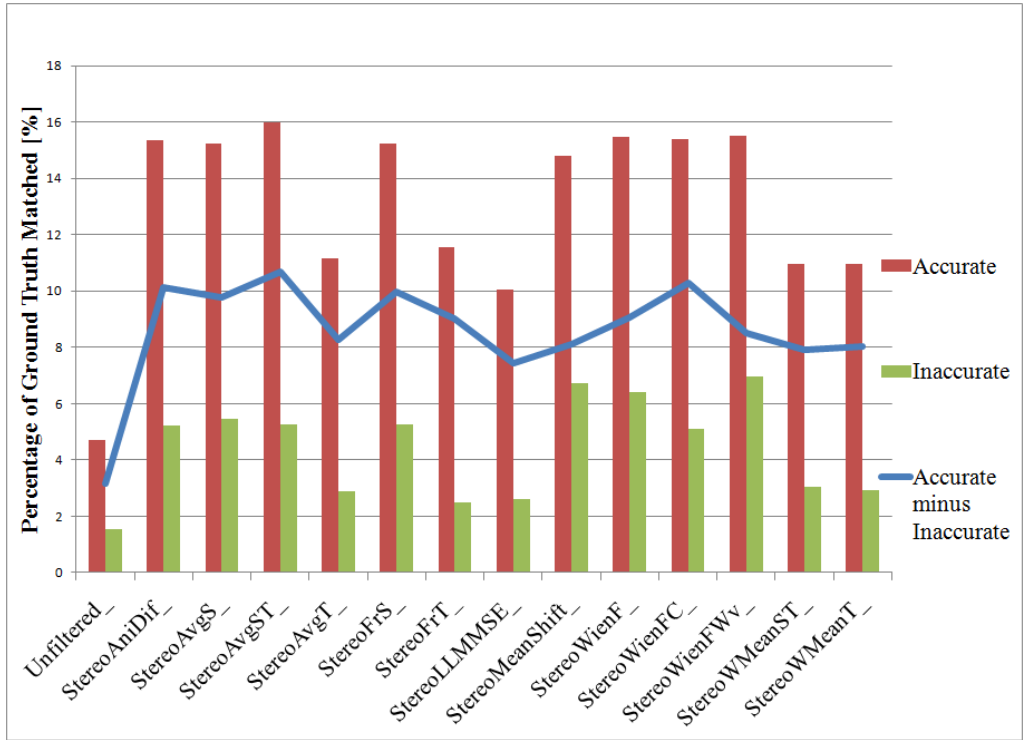


Figure 39: Accurate, inaccurate, and accurate minus inaccurate matches for the top filter parameter and stereo parameter settings for each filter for the thermally diverse scene.

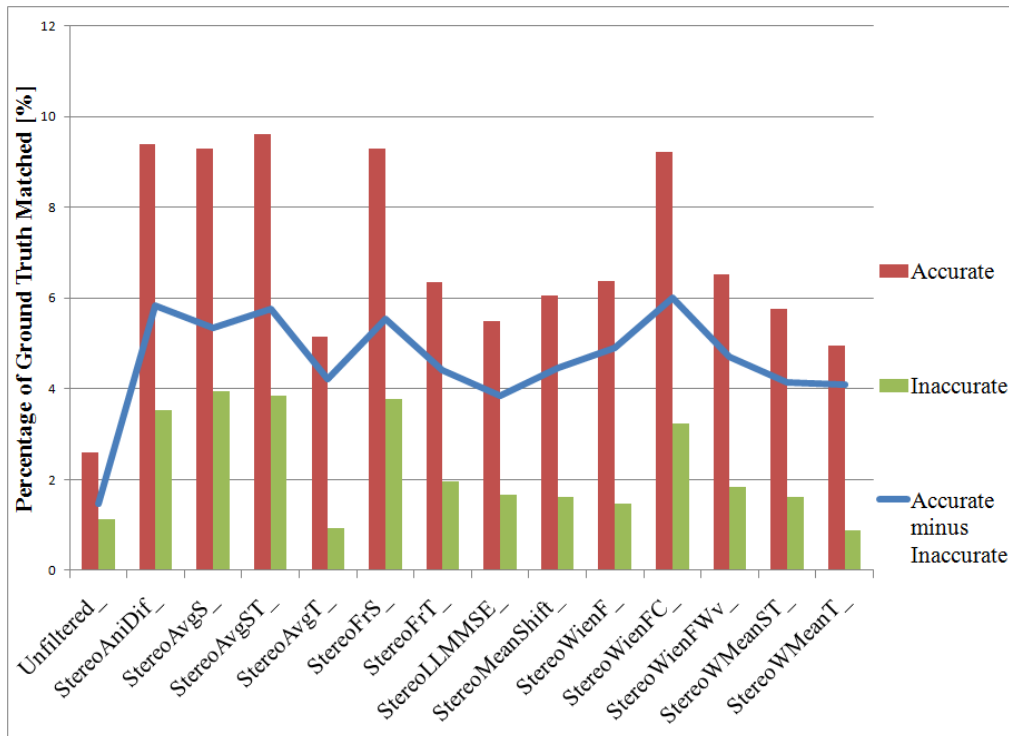


Figure 40: Accurate, inaccurate, and accurate minus inaccurate matches for the top filter parameter and stereo parameter settings for each filter for the combined scenes.

The data in Figure 38 indicates that the top filters for the approximately isothermal hallway boundary location scene are StereoWienFC and StereoAniDif. The third top filter, StereoWienF, provides less than 70% of the number of accurate minus inaccurate disparities that the top filter, StereoWienFC, provides. The StereoWienFC filter also has a fast matching time compared to top contenders and is considered the top filter here.

The data in Figure 39 indicates that the top filters for the thermally diverse hallway boundary location scene are StereoAvgST, StereoWienFC, and StereoAniDif. The top filter, StereoAvgST, requires multiple frames, so it should be used in stationary or slow-moving scenes. The StereoWienFC filter, which is faster than the other top filters, is considered the top filter here.

The data in Figure 40 indicates that the top filters for the combined hallway data sets (approximately isothermal and thermally diverse) are the StereoWienFC, StereoAniDif, and StereoAvgST filters. As mentioned for the thermally diverse hallway scene, the StereoAvgST

requires multiple frames and should only be used with stationary or slow-moving scenes. The top filter here is considered to be the StereoWienFC filter. While the percentage of accurate pixels minus inaccurate pixels is still a low value (6%), it is more than triple the percentage for the unfiltered case (< 2%).

3.5.1.2.3 Overall

The StereoWienFC filter was the top filter overall when considering quality and processing time. It provided top or near-top performance quantitatively for approximately isothermal and thermally diverse object detection and boundary location. This is perhaps due to the way the Wiener filter models noise in an image, being more efficient at removing noise than other algorithms. Relative to the other filters, it had near lowest processing time. A further discussion on the StereoWienFC filter and other top filters is provided in Appendix F.

3.5.2 Effects on Feature Distortion

3.5.2.1 Evaluation Details

The top filters from the object detection and boundary location evaluations were analyzed for their effects on features. The feature selected was a spherical light bulb which would appear circular to both cameras in the LWIR stereo vision system. The diagram in Figure 41 shows the feature detection process. First, the image is converted to an image of the gradient magnitude at each pixel using the Sobel horizontal and vertical operators. Next, the Hough Transform for circles [35] is combined with this gradient information to produce a weighted intensity map for each evaluated radius. A higher gradient level in the gradient domain produces higher intensities in the transformed domain at possible circle center locations during the conversion. In this domain, a higher intensity indicates a higher likelihood of a circle of the current radius being present. As a result, if the circle feature is close to ideal, a plot of maximum intensity versus radii size will show a peak at one radius with sharp cutoffs larger and smaller than that radius. If a circle feature is smoothed by a filter, it will show a more rounded peak in the plot of maximum intensity versus radii size.

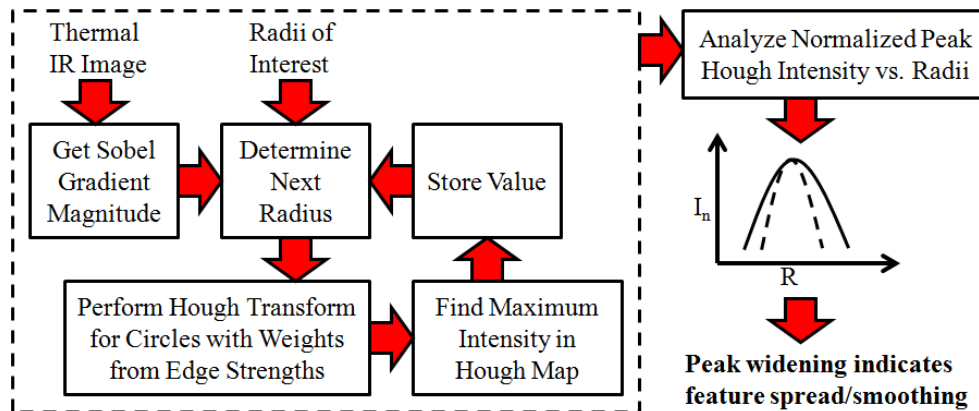


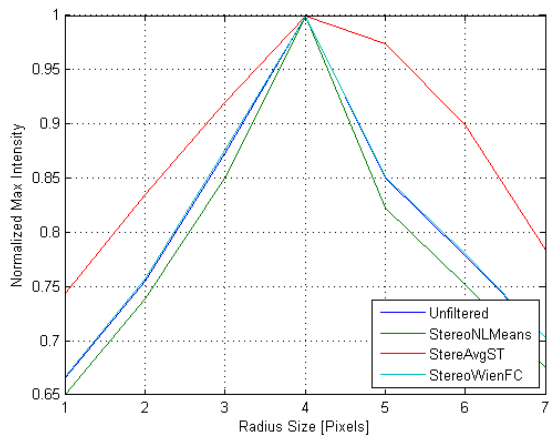
Figure 41: Process for evaluation of filter effects on feature detection using the Hough Transform for circles.

3.5.2.2 Results and Discussion

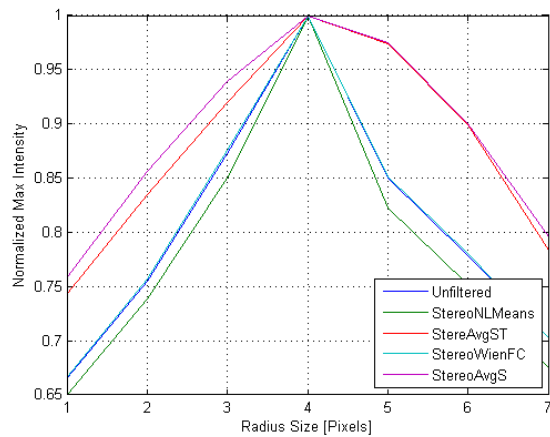
For the feature distortion tests, Table 9 lists the filters and filter settings tested. The data in Figure 42 shows the feature detection results for the top filters for the object detection scenes. In the plot, the intensity represents the likelihood that a circle of that diameter is present in the scene. Thus, a rounded peak indicates the presence of feature spread. Data is normalized per filter for the plots. The data in Figure 43 shows the feature detection results for the top filters for the boundary location scenes.

Table 9: Parameters used for filters for feature detection tests. The parameters are in the same order as the previous tables.

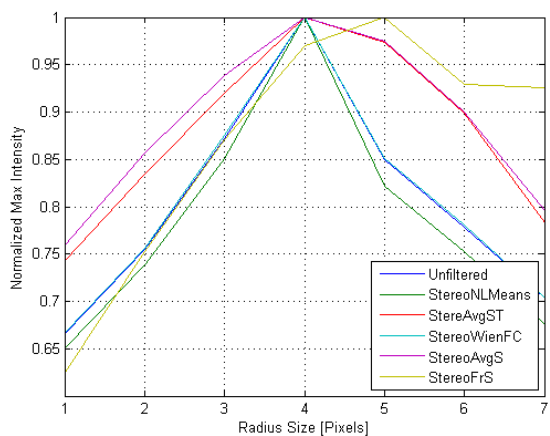
Filter	Parameters	Object Detection			Boundary Location		
		Approximately Isothermal	Thermally Diverse	Total	Approximately Isothermal	Thermally Diverse	Total
StereoNLMeans	Box size Search box size H-parameter	3 5 11	3 5 11	3 5 11			
StereoAvgST	Method Box size Num. of frames	Mean 5 7	Mean 5 11	Mean 5 9		Mean 5 3	Mean 5 7
StereoWienFC	Box size Noise level Num. of times	3 256 9	3 256 9	3 256 9	3 32 5	3 64 3	3 32 5
StereoAvgS	Method Box size		Mean 5	Mean 5			
StereoFrS	Box size Cut freq. 1 Cut freq. 2 Type			15 4 <n/a> Low-pass			
StereoAniDif	Function Iterations Gamma K				Exp 10 0.15 20	Exp 10 0.1 200	Exp 10 0.1 200
StereoWienF	Box size Noise level				3 128		3 256



(a)



(b)



(c)

Figure 42: Feature detection results for top filters from the object detection tests for (a) the approximately isothermal scene, (b) the thermally diverse scene, and (c) the combined scenes.

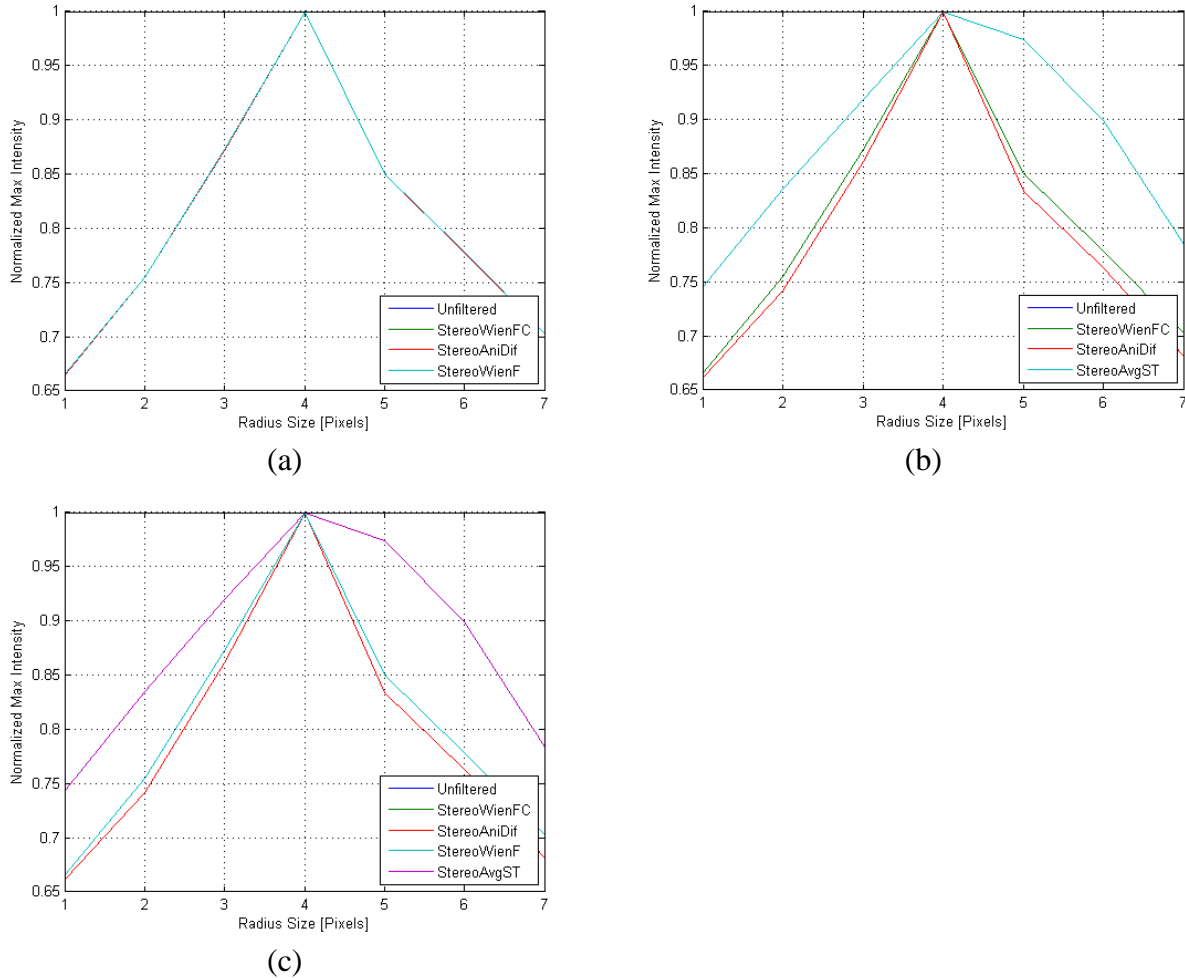


Figure 43: Feature detection results for top filters from the boundary location tests for (a) the approximately isothermal scene, (b) the thermally diverse scene, and (c) the combined scenes.

The data in Figure 42 shows that for the top filter settings for the approximately isothermal object location scene, the StereoNLMeans and StereoWienFC filters tend to preserve the circle feature found in the unfiltered image, while the StereoAvgST filter tends to smooth out the feature, widening it. The StereoWienFC filter provides a sharper peak than the unfiltered case, indicating that the circle found in the unfiltered data stands out more after this filter is applied. This is perhaps due to the way the Wiener filter models noise, making it more efficient at removing noise than some of the other filters. These results are similar for the thermally diverse object location scene. Here, the StereoAvgS filter was also plotted for its results at improving the matching results. The StereoAvgS filter with these settings smooths the feature. For the combined (i.e. approximately isothermal and thermally diverse) object location scene, the

StereoFrS was also plotted. The feature detection shows that this filter also smoothes the feature for the data set tested, causing feature widening.

The data in Figure 43 shows that for the top filter settings for the approximately isothermal boundary location scene, all three of the top filters (StereoWienFC, StereoAniDif, and StereoWienF) tend to preserve the original circular feature in the unfiltered data. For the top filter settings for the thermally diverse boundary location scene, the StereoWienFC and StereoAniDif filters tend to preserve the original circular feature, while the StereoAvgST tends to smooth it. The StereoWienFC filter overlaps the unfiltered feature detection data, while the StereoAniDif filter provides a sharper peak than the unfiltered case, indicating that the filtering causes the circular feature to stand out more than in the unfiltered case. The combined (i.e. approximately isothermal and thermally diverse) boundary location results are similar to the results for the thermally diverse scene, with the addition of the StereoWienF filter. The StereoWienF filter provided similar results to the StereoWienFC filter and the unfiltered case.

For feature detection overall, the StereoNLMeans, StereoAniDif, StereoWienF, and StereoWienFC filters tended to preserve features, with StereoAniDif and StereoWienFC each having a case of making the feature stand out more than in the original unfiltered case. The StereoAvgST, StereoAvgS, and StereoFrS all tended to smooth out the feature, widening the range of high-scoring radii for the feature. The StereoWienFC filter that performed well in the object detection and boundary location tests is recommended here considering its ability to preserve features with fast processing time.

3.6 Conclusions and Proposed Approach

Two intensity alignment algorithms and sixteen filters were quantitatively tested to determine the top methods of improving LWIR stereo vision matching. The tests on the intensity alignment algorithms showed that for the non-radiometric thermal cameras tested, a basic offset method based can be used to correct whole-image differences between the left and right images in scenes that are not largely thermally diverse. For scenes that are approximately isothermal or that have large thermal diversity, a linear fitting intensity alignment method was shown to be a better choice.

Filter tests indicated that the consecutive Wiener filter (StereoWienFC) is a top filter choice for approximately isothermal or thermally diverse scenes when performing object location or boundary location. This filter also preserved the circular feature during the filter feature tests and had one of the lowest processing times. Some other filter provided higher quality matching results at the expense of processing time. The recommended LWIR stereo vision system architecture is shown in Figure 44 for cases in which the scene is approximately isothermal or thermally diverse.

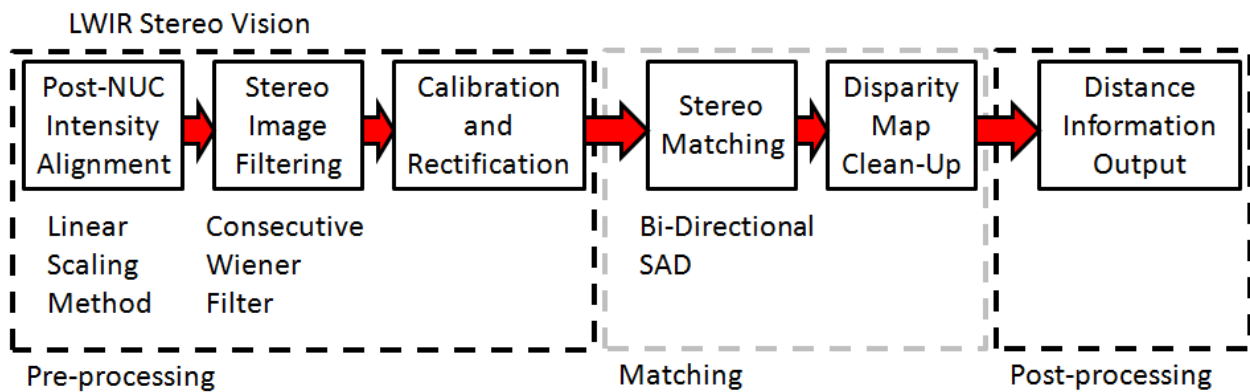


Figure 44: Recommended LWIR Stereo Vision System Architecture.

3.7 References

- [1] Starr, J. W., & Lattimer, B. Y. (2014). Evaluation of navigation sensors in fire smoke environments. *Fire Technology*, 50(6), 1459-1481.
- [2] Starr, J. W., & Lattimer, B. Y. (2012, October). A comparison of IR stereo vision and LIDAR for use in fire environments. In *Sensors, 2012 IEEE* (pp. 1-4). IEEE.
- [3] Starr, J. W., & Lattimer, B. Y. (2013, July). Application of thermal infrared stereo vision in fire environments. In *Advanced Intelligent Mechatronics (AIM), 2013 IEEE/ASME International Conference on* (pp. 1675-1680). IEEE.
- [4] McNeil, J. G., Starr, J., & Lattimer, B. Y. (2013, July). Autonomous fire suppression using multispectral sensors. In *Advanced Intelligent Mechatronics (AIM), 2013 IEEE/ASME International Conference on* (pp. 1504-1509). IEEE.
- [5] Kim, J. H., Starr, J. W., & Lattimer, B. Y. (2014). Firefighting Robot Stereo Infrared Vision and Radar Sensor Fusion for Imaging through Smoke. *Fire Technology*, 1-23.
- [6] Gschwandtner, M., Kwitt, R., Uhl, A., & Pree, W. (2011, June). Infrared camera calibration for dense depth map construction. In *Intelligent Vehicles Symposium (IV), 2011 IEEE* (pp. 857-862). IEEE.
- [7] Benezeth, Y., Jodoin, P. M., Emile, B., Laurent, H., & Rosenberger, C. (2010). Human detection with a multi-sensors stereovision system. In *Image and Signal Processing* (pp. 228-235). Springer Berlin Heidelberg.
- [8] Harguess, J., & Strangeb, S. (2014, May). Infrared Stereo Calibration for Unmanned Ground Vehicle Navigation. In *Proc. of SPIE* (Vol. 9084, pp. 90840S-1).
- [9] Rainieri, S., & Pagliarini, G. (2002). Data filtering applied to infrared thermographic measurements intended for the estimation of local heat transfer coefficient. *Experimental thermal and fluid science*, 26(2), 109-114.
- [10] Bertozzi, M., Broggi, A., Caraffi, C., Del Rose, M., Felisa, M., & Vezioni, G. (2007). Pedestrian detection by means of far-infrared stereo vision. *Computer vision and image understanding*, 106(2), 194-204.
- [11] Cheng, V. S., Zhang, S., Chen, Y., & Hao, L. (2005). A Stereo Thermographic System for Intra-operative Surgery. In *Engineering in Medicine and Biology Society, 2005. IEEE-EMBS 2005. 27th Annual International Conference of the* (pp. 1984-1987). IEEE.

- [12] Rankin, A., Huertas, A., Matthies, L., Bajracharya, M., Assad, C., Brennan, S., ... & Sherwin, G. W. (2011, May). Unmanned ground vehicle perception using thermal infrared cameras. In *SPIE Defense, Security, and Sensing* (pp. 804503-804503). International Society for Optics and Photonics.
- [13] Mouats, T., Aouf, N., Chermak, L., & Richardson, M. (2015). Thermal Stereo Odometry for UAVs.
- [14] Hajebi, K., & Zelek, J. S. (2006, June). Sparse disparity map from uncalibrated infrared stereo images. In *Computer and Robot Vision, 2006. The 3rd Canadian Conference on* (pp. 17-17). IEEE.
- [15] Hajebi, K., & Zelek, J. S. (2007, February). Dense surface from infrared stereo. In *Applications of Computer Vision, 2007. WACV'07. IEEE Workshop on* (pp. 21-21). IEEE.
- [16] Scharstein, D., & Szeliski, R. (2002). A taxonomy and evaluation of dense two-frame stereo correspondence algorithms. *International journal of computer vision*, 47(1-3), 7-42.
- [17] Shuchun, Y., Xiaoyang, Y., Lijuan, H., & Jue, W. (2011, August). Preprocessing for stereo vision based on LOG filter. In *Strategic Technology (IFOST), 2011 6th International Forum on* (Vol. 2, pp. 1074-1077). IEEE.
- [18] Hirschmüller, H., & Scharstein, D. (2009). Evaluation of stereo matching costs on images with radiometric differences. *Pattern Analysis and Machine Intelligence, IEEE Transactions on*, 31(9), 1582-1599.
- [19] Zhang, Z. (2000). A flexible new technique for camera calibration. *Pattern Analysis and Machine Intelligence, IEEE Transactions on*, 22(11), 1330-1334.
- [20] Han, Y., Xuan, G., Li, C., Li, D., & Han, H. (2012, July). Removing illumination from image pair for stereo matching. In *Audio, Language and Image Processing (ICALIP), 2012 International Conference on* (pp. 508-512). IEEE.
- [21] Wang, Z. (2010). A robust algorithm for color correction between two stereo images. In *Computer Vision—ACCV 2009* (pp. 405-416). Springer
- [22] Olbrycht, R., Wi'cek, B., & De Mey, G. (2011, September). New approach to thermal drift and gain non-uniformity correction in microbolometer detectors. In *Thermal Investigations of ICs and Systems (THERMINIC), 2011 17th International Workshop on* (pp. 1-4). IEEE.
- [23] Nixon, M. S., & Aguado, A. S. (2012). *Feature extraction & image processing for computer vision*. Academic Press.

- [24] Brailean, J. C., Kleihorst, R. P., Efstratiadis, S., Katsaggelos, A. K., & Lagendijk, R. L. (1995). Noise reduction filters for dynamic image sequences: A review. *Proceedings of the IEEE*, 83(9), 1272-1292.
- [25] Comaniciu, D., & Meer, P. (2002). Mean shift: A robust approach toward feature space analysis. *Pattern Analysis and Machine Intelligence, IEEE Transactions on*, 24(5), 603-619.
- [26] Tseng, Y. C., & Chang, T. S. (2011, July). Fast algorithm for local stereo matching in disparity estimation. In *Digital Signal Processing (DSP), 2011 17th International Conference on* (pp. 1-6). IEEE.
- [27] Motwani, M. C., Gadiya, M. C., Motwani, R. C., & Harris, F. C. (2004, September). Survey of image denoising techniques. In *Proceedings of GSPX* (pp. 27-30).
- [28] Kuan, D. T., Sawchuk, A., Strand, T. C., & Chavel, P. (1985). Adaptive noise smoothing filter for images with signal-dependent noise. *Pattern Analysis and Machine Intelligence, IEEE Transactions on*, (2), 165-177.
- [29] Wang, L., Leedham, G., & Cho, S. Y. (2007, November). Deriving filter parameters using dual-images for image de-noising. In *Intelligent Signal Processing and Communication Systems, 2007. ISPACS 2007. International Symposium on* (pp. 212-215). IEEE.
- [30] Jacob, N., & Martin, A. (2004). Image denoising in the wavelet domain using wiener filtering. *Unpublished course project, University of Wisconsin, Madison, Wisconsin, USA*.
- [31] Strang, G. (1989). Wavelets and dilation equations: A brief introduction. *SIAM review*, 31(4), 614-627.
- [32] Perona, P., & Malik, J. (1990). Scale-space and edge detection using anisotropic diffusion. *Pattern Analysis and Machine Intelligence, IEEE Transactions on*, 12(7), 629-639.
- [33] Buades, A., Coll, B., & Morel, J. M. (2005). A review of image denoising algorithms, with a new one. *Multiscale Modeling & Simulation*, 4(2), 490-530.
- [34] Baker, S., Szeliski, R., & Anandan, P. (1998, June). A layered approach to stereo reconstruction. In *Computer Vision and Pattern Recognition, 1998. Proceedings. 1998 IEEE Computer Society Conference on* (pp. 434-441). IEEE.
- [35] Yuen, H. K., Princen, J., Illingworth, J., & Kittler, J. (1990). Comparative study of Hough transform methods for circle finding. *Image and vision computing*, 8(1), 71-77.

- [36] Di Stefano, L., Marchionni, M., & Mattoccia, S. (2004). A fast area-based stereo matching algorithm. *Image and vision computing*, 22(12), 983-1005.
- [37] Hokuyo UTM 30-LX-EW, data sheet. http://www.hokuyo-aut.jp/02sensor/07scanner/download/pdf/UTM-30LX-EW_spec_en.pdf. Accessed June 2015.

4 Evidential Sensor Fusion of LWIR Stereo Vision and 3D-LIDAR for Rangefinding in Fire Environments

4.1 Introduction to Fusion System

4.1.1 Challenges with Rangefinding in Fire Environments

Previous work has shown the ability of Long-Wave IR (LWIR) stereo vision to provide useful boundary location information in fire smoke environments [1, 2, 3]. The sensing technology was shown to be useful when other systems such as LIDAR [1, 2] or visual stereo vision [1, 3] fail due to the presence of dense smoke. The same tests confirmed that in clear environments, the other sensing modalities provided better results. While being able to range-find in these two extremes (clear and smoke) is desirable, real fire environments will likely contain some scenes in-between the two extremes. For instance, as in Figure 45, a scene may have some smoke in the distance only partially blocking a LIDAR system. In this case, fusion of LWIR stereo vision with the LIDAR may provide better results than either sensor modality on its own. It is the goal of this chapter to present a sensor fusion method combining a thermal IR stereo vision system and a spinning LIDAR system for use in a range of conditions varying from clear to filled with dense smoke.

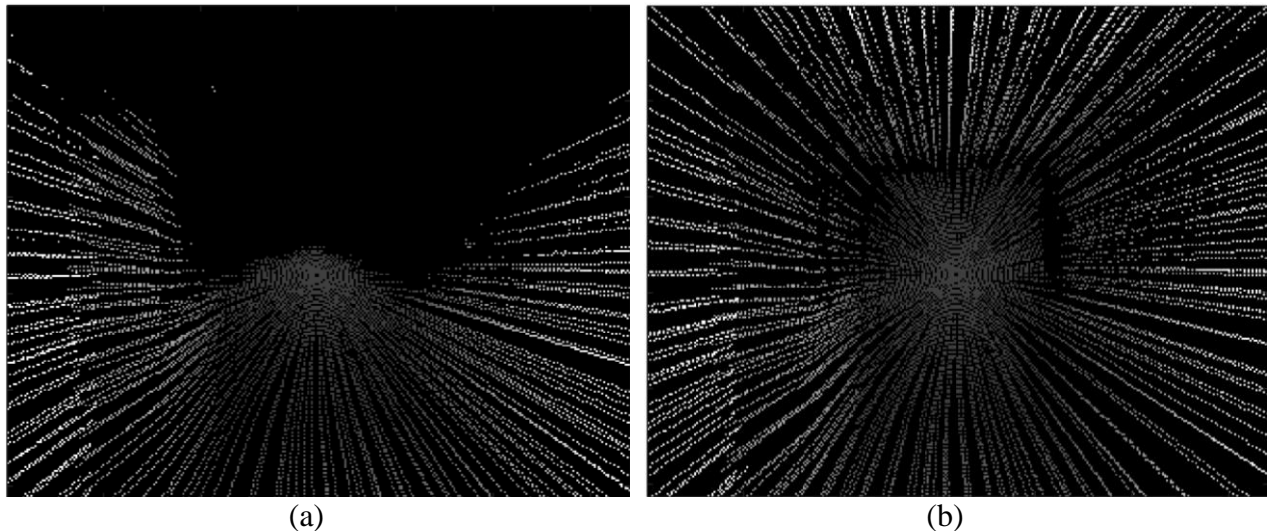


Figure 45: Hallway scene (a) with partially blocked LIDAR system due to smoke compared to (b) scene before smoke presence. Lighter values indicate closer distance out from the sensor.

4.1.2 Background of Relevant Research

Harsh environment (i.e. smoke, fog, precipitation, dust) perception has been a focus in the literature. Single-rangefinder-modality sensor setups tested include LIDAR systems [1, 2, 4], radar [1, 5, 6], and sonar [1, 7]. Some research in the literature has focused on sensor fusion for improved perception in obscured environments. One of these systems presented is a system designed to utilize LIDAR and sonar depending on the measured presence of smoke [8]. This paper presented a heuristic sensor fusion algorithm and also a fuzzy logic sensor fusion algorithm for fusion in 2-dimensional space [8]. Another system fused radar and thermal IR stereo vision to provide improved object location in dense smoke, using 1D radar range information to update less precise 2D thermal IR stereo vision object distances [9]. Another system was devised to fuse LIDAR, visual stereo vision, and radar into an occupancy grid for a mobile robot in harsh environments such as those with fog [10]. This paper presented fusion in 2-dimensional space for navigation [10].

In general, many types of fusion algorithms may be applied to a multi-sensor system. Several popular multi-sensor fusion algorithms include probabilistic (Bayesian) fusion, evidential (Dempster-Shafer) fusion, fuzzy logic, rough sets, and hybrids of these methods [11]. Neural networks [12], decision trees [13], and heuristic methods [8] have also been used. Several of these sensor fusion methods have been applied to fusing a range-finding sensor with occupancy grid maps in 2-dimensional [8, 10, 14] and 3-dimensional [15] space. One relevant system influencing the methods selected in this text includes a system focusing on fusing sonar range-data to a 2-dimensional occupancy grid [14]. This paper compared Bayesian fusion and evidential fusion for fusing the sensor and map for an updated map [14]. Another relevant system fused several images together into range data for a 3-dimensional voxel-layout of occupied and free locations using different camera views from a camera moving forward [15].

4.1.3 Chapter Focus

The focus of this chapter is on the development of an evidential (Dempster-Shafer) [11, 14, 15, 16] sensor fusion model designed to fuse LWIR stereo vision and 3D LIDAR point clouds in the voxel domain for use in fire environments. Inputs to the system are a 3D LIDAR point cloud

from a spinning planar LIDAR and a pair of images from a LWIR stereo setup. The LIDAR point cloud is separated into two point clouds based on return distance and intensity. Returns with relatively high intensity for their distance are likely to solid boundaries. Returns with relatively low intensity for their distance likely range to smoke or to solid boundaries. These returns are considered significantly attenuated and are separated to be handled differently. The low-attenuation and high-attenuation returns are stored in separate point clouds. The LWIR stereo vision images are processed to obtain a point cloud for fusion.

The spatial domain for sensor fusion was selected to be a multi-resolution set of voxel arrays due to the inherent decreasing in precision with distance from the sensor for stereo vision systems. Three levels are used from a high resolution close-range map to a lower resolution larger map. This 3D framework is similar to the 2D set of maps presented in [17].

Once the LIDAR low-attenuation and high-attenuation point clouds and the LWIR point cloud are obtained, the three point clouds need to be converted to the multi-resolution voxel domain representation prior to fusion. This voxel domain representation requires arrays of occupied space evidence and of free space evidence for the evidential fusion. Sensor models are presented for converting the LIDAR point clouds and the LWIR stereo vision point cloud to this domain. Special care is taken in the development of the sensor models for proper handling of the high-attenuation point cloud data. Once in the voxel domain, LIDAR occupied and free voxel arrays can be fused with LWIR stereo vision occupied and free voxel arrays to obtain fused occupied and free voxel arrays.

First, the fusion method details and application process are described. Next, an experimental method is presented for a test of the fusion system in actual fire smoke conditions. Two experiments were performed. One experiment tested the system a hallway fire smoke environment designed to evaluate the system in a range of conditions from a clear scene to scenes partially filled with smoke and scenes fully filled with smoke. The second is from data collected during the November 2014 demonstration of the SAFFiR project, where a humanoid robot was used to fight a fire aboard the Ex-USS Shadwell. The results of these experiments are presented and discussed.

4.2 Fusion Process

4.2.1 Fusion Space

A 3D voxel space was selected for fusion of the LWIR stereo vision and LIDAR point clouds. Due to precision inherently decreasing with distance out from the sensor for the stereo vision system, a multi-resolution set of voxel arrays was selected where higher resolution maps would be produced for close range points and lower resolution maps produced for further range points, similar to 2D grid space application in the literature [17]. The diagram in Figure 46 shows a 2D slice of the 3D multi-resolution space for the occupied voxel array and the free space voxel array for a view of a hallway with a closet and room on the left side. For the system here, three voxel resolutions were used. The highest resolution map is a voxel array with 0.1 m x 0.1 m x 0.1 m voxels extending to a 2 meter square. The second highest resolution voxel array contains 0.2 m x 0.2 m x 0.2 m voxels extending to 4 m, and the final voxel array contains 0.4 m x 0.4 m x 0.4 m voxels extending to the edge of the space considered (within 8 m). In application, the lower resolution maps cover space included in higher resolution areas, but only the highest resolution information is shown in each area for display in this work. The lower resolution data is not used in assessment of the fusion algorithm in overlapping regions where higher resolution data exists.

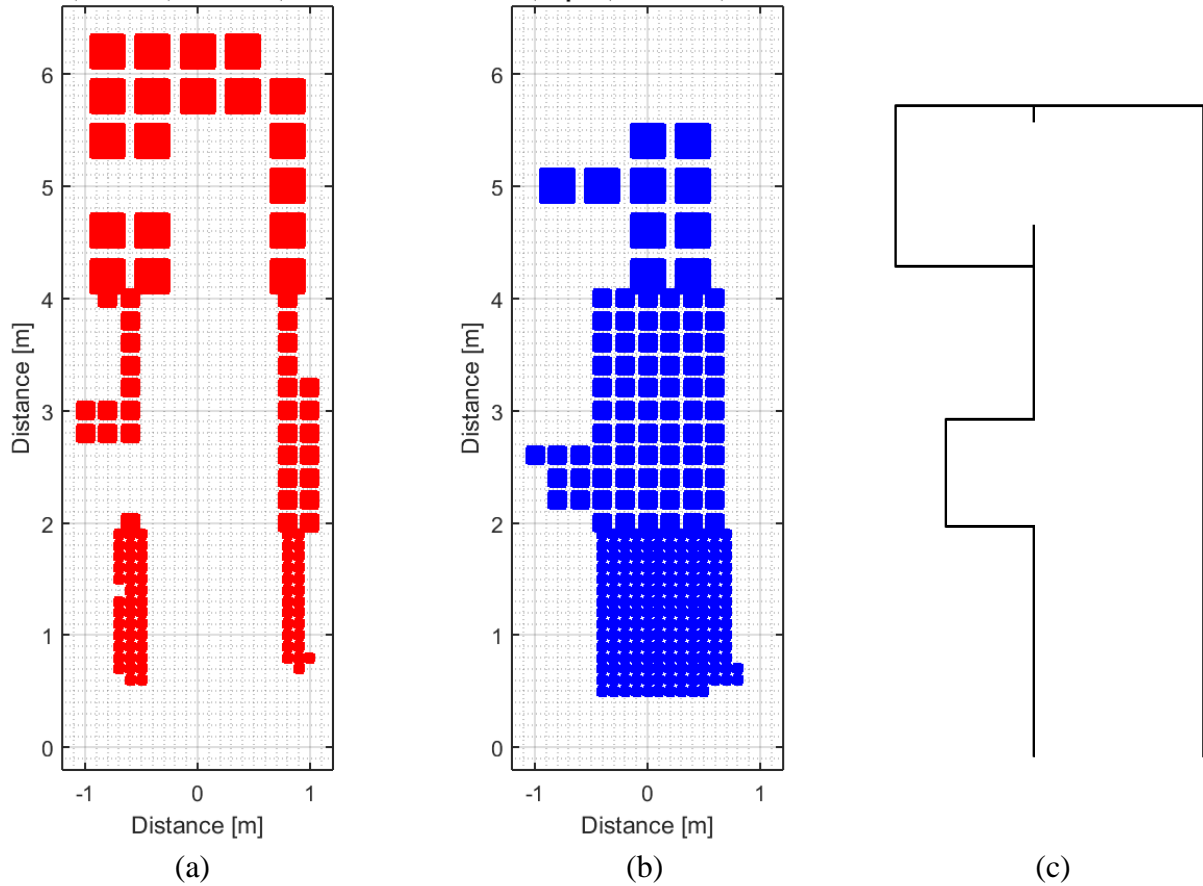


Figure 46: Horizontal 2D slice multi-resolution view of a hallway scene for (a) the occupied voxel array and (b) the free space voxel array, along with (c) the layout of the boundaries of the hallway.

4.2.2 Evidential Fusion Method

An evidential fusion method was selected based on its ability to account for ignorance [16], modeling occupied and free space separately [14]. This general evidential fusion method was chosen over a Bayesian fusion method, a special case subset of evidential fusion [16], since in the Bayesian framework a probability for a statement (e.g. probability a voxel is occupied) automatically assumes a probability to the negation of the statement (e.g. probability a voxel is empty) [16]. The evidential framework allows for separate sensor models for occupied and free space [14]. Separately handling sensor models for occupied and free space lends itself well to developing sensor models tailored to handle low-attenuation LIDAR returns that include occupied and free space information and high-attenuation LIDAR returns that contain free space information but lack evidence for occupied space at the return.

As with application of evidential fusion to sonar in [14], the framework for the state of each voxel is similar to Shafer's Ming Vase example [16]. Two mutually exclusive states are assumed for the set of possibilities, occupied (Occ) and free space (F),

$$\Theta = \{Occ, F\} \quad (9)$$

As with [14], including all subsets gives

$$A = \{\emptyset, Occ, F, \{Occ, F\}\} \quad (10)$$

where the null case is \emptyset and ignorance is accounted for in the last term, $\{Occ, F\}$. Thus, the state of each voxel at each point in time is represented by four values known as basic probability assignments, one value for each of these subsets of A . The following subsections discuss how these basic probability assignments are determined from sensor models and then how the values are fused at each voxel.

4.2.2.1 Basic Probability Assignments from Sensor models

For each voxel, a basic probability assignment is set for all four subsets of A for each sensor. It is assumed that the basic probability assignment of the null case is always 0 since each voxel is either occupied or free. For all voxels for each sensor, this results in

$$m_{i,j,k}(Case) = \left\{ \begin{array}{ll} 0, & Case = \emptyset \\ S_{Occ}, & Case = Occ \\ S_F, & Case = F \\ S_{\{Occ,F\}}, & Case = \{Occ, F\} \end{array} \right\} \forall voxels_{i,j,k} \quad (11)$$

where i, j, k is the voxel location by index. S_{Occ} and S_F are the basic probability assignments for occupied and free space states. $S_{\{Occ,F\}}$ is a measure of the ignorance of evidence for free or occupied state. Basic probability assignment are assumed to add to 1 [14], so that for all cases

$$S_{\{Occ,F\}} = 1 - (S_{Occ} + S_F) \quad (12)$$

Initially all voxels are given full evidence for ignorance ($S_{\{Occ,F\}} = 1$) and no evidence for the occupied and free space states. The occupied state and free space state basic probability assignments, S_{Occ} and S_F , are then updated based on sensor range information using a sensor

model, which in turn is used to update the ignorance value $S_{\{Occ,F\}}$. Only voxels along rays from the sensor to the points in the point cloud are updated by the sensor model.

Sensor models are used to determine information about free and occupied space along a 1-dimensional ray from the sensor to each sensor return, as shown conceptually for one return in the plot in Figure 47. For application, information from the sensor model for each return is used to produce evidence for occupied and free space in 2D or 3D occupancy grids, following a ray from the sensor to each return, as shown in Figure 48(a) for the 2D case. For the work here, this corresponds to a 3D multi-resolution voxel domain representation of the environment with a set of occupied and free space voxel arrays for each resolution. The data ranges from 0 to 1 for each voxel for both states, corresponding to a range from complete ignorance to full certainty of occupied or free voxel state. The resulting arrays can then be thresholded to set the state as in the 2D example in Figure 48(b).

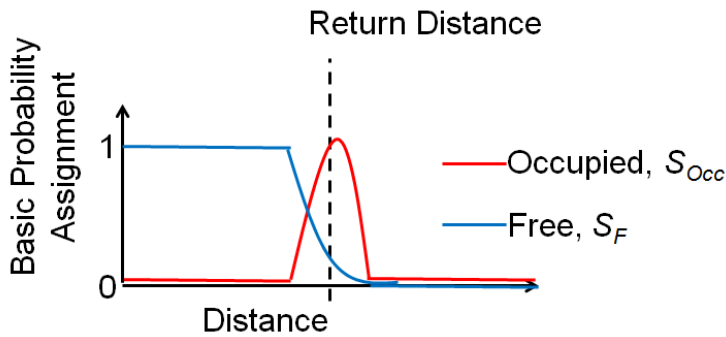


Figure 47: Sample sensor model giving basic probability assignment (evidence) versus distance to and beyond the nominal return distance.

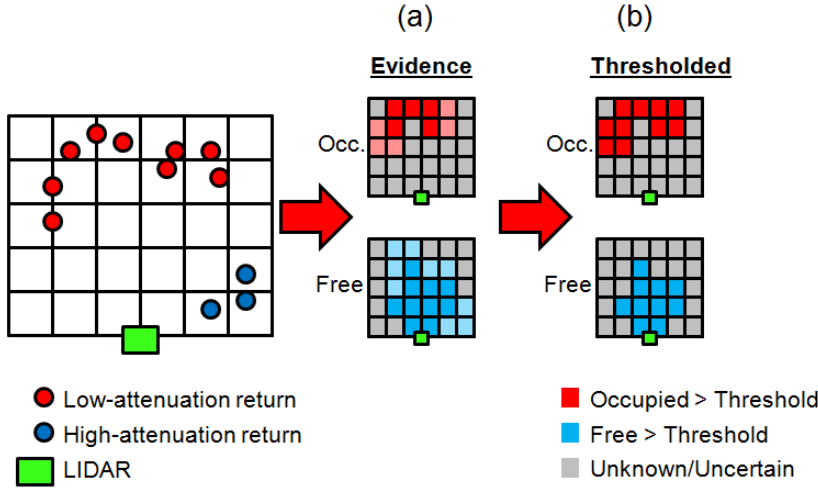


Figure 48: (a) Application of the sensor model in Figure 47 to produce 2D maps of occupied and free space evidence and (b) thresholded evidence data for indication of free and occupied space.

In application to the LIDAR, an entire set of low-attenuation and high-attenuation point clouds is used to update all voxels before fusion. Low-attenuation and high-attenuation points are handled differently. For LWIR stereo vision, one entire point cloud is used to update all voxels before fusion.

4.2.2.1.1 LIDAR Basic Probability Assignments

The basic probability assignment for the LIDAR returns is

$$m_{i,j,k,L}(Case) = \left\{ \begin{array}{ll} 0, & Case = \emptyset \\ S_{Occ,L}, & Case = Occ \\ S_{F,L}, & Case = F \\ S_{\{Occ,F\},L}, & Case = \{Occ,F\} \end{array} \right\} \forall voxels_{i,j,k} \quad (13)$$

where i, j, k is the voxel location by index. It follows that $S_{Occ,L}$ and $S_{F,L}$ are the basic probability assignments from the sensor models for the LIDAR returns, and $S_{\{Occ,F\},L}$ is a measure of the ignorance of evidence for free or occupied state. It also follows that basic probability assignment are assumed to add to 1 [14], so that for all cases

$$S_{\{Occ,F\},L} = 1 - (S_{Occ,L} + S_{F,L}) \quad (14)$$

Since the high-attenuation LIDAR returns range to smoke or to solid objects, for the high-attenuation LIDAR returns only free-space information is provided, resulting in

$$S_{Occ,L} = 0 \forall voxels_{i,j,k} | High-attenuation \quad (15)$$

For one set of LIDAR low-attenuation and high-attenuation point clouds, the LIDAR sensor models are used to produce one array of basic probability assignments for all voxels prior to fusion. The development and application of the LIDAR sensor model for both returns is presented in a following subsection.

4.2.2.1.2 LWIR Basic Probability Assignments

For the LWIR stereo vision system,

$$m_{i,j,k,IR}(Case) = \left\{ \begin{array}{ll} 0, & Case = \emptyset \\ S_{Occ,IR}, & Case = Occ \\ S_{F,IR}, & Case = F \\ S_{\{Occ,F\},IR}, & Case = \{Occ,F\} \end{array} \right\} \forall voxels_{i,j,k} \quad (16)$$

$S_{Occ,IR}$ and $S_{F,IR}$ are the basic probability assignment from the sensor models for the LWIR stereo vision returns. It again follows that

$$S_{\{Occ,F\},IR} = 1 - (S_{Occ,IR} + S_{F,IR}) \quad (17)$$

Similar to the LIDAR, the LWIR stereo vision sensor model outputs one array of basic probability assignments for all voxels for the each entire LWIR stereo vision point cloud prior to fusion. The development and application of the sensor model for the LWIR stereo vision system is presented in a subsequent section.

4.2.2.2 Evidential Fusion of Basic Probability Assignments

Similar to the map updating in [14], the LIDAR and LWIR stereo vision data is fused together using Dempster's rule of combination. This is performed at each resolution. For improved readability, the notation for the basic probability assignments is shortened

$$m_L(Case) = m_{i,j,k,L}(Case) \quad (18)$$

$$m_{IR}(Case) = m_{i,j,k,IR}(Case) \quad (19)$$

The occupied and free space voxel basic probability assignments from the fusion process at each voxel are

$$m_{Fused}(Occ) = \frac{m_L(Occ) * m_{IR}(Occ) + m_L(Occ) * m_{IR}(\{Occ, F\}) + m_L(\{Occ, F\}) * m_{IR}(Occ)}{1 - m_L(Occ) * m_{IR}(F) - m_L(F) * m_{IR}(Occ)} \quad (20)$$

and

$$m_{Fused}(F) = \frac{m_L(F) * m_{IR}(F) + m_L(F) * m_{IR}(\{Occ, F\}) + m_L(\{Occ, F\}) * m_{IR}(F)}{1 - m_L(F) * m_{IR}(Occ) - m_L(Occ) * m_{IR}(F)} \quad (21)$$

The remaining two basic probability assignments follow

$$m_{Fused}(\emptyset) = 0 \quad (22)$$

$$m_{Fused}(\{Occ, F\}) = 1 - m_{Fused}(Occ) - m_{Fused}(F) \quad (23)$$

The basic probability assignments $m_{Fused}(Case)$ represent the fused LIDAR and LWIR stereo vision environment representation for one time step for every voxel in the multi-resolution set of voxel arrays. These basic probability assignments could further be fused into an ongoing environment map being built up through time using a similar set of equations to these, similar to the work in [14]. The focus of this work is on the sensor fusion aspect prior to fusion to an environment map. The sensor models and other steps necessary for implementation are presented in subsequent sections.

4.2.3 Application of Fusion Method

The sensor fusion process specific to the LWIR stereo vision system and spinning LIDAR is shown in Figure 49. The full system architecture begins with raw LIDAR and LWIR stereo vision data and results in evidentially fused voxel arrays corresponding to a local occupied map and a local free-space map for that time step. LIDAR data is first separated into two point clouds, one for low-attenuation returns and one for high-attenuation returns based on each return intensity and distance. A sensor model is applied based on both point clouds to produce a voxel

array of evidence for occupied space and a voxel array of evidence for free space. The LWIR stereo vision images are processed and stereo-matched, with the calculated disparity map subsequently converted into a point cloud. This point cloud is then converted into occupied and free space voxel arrays for fusion. Lastly, the occupied and free space voxel arrays from the LIDAR and LWIR stereo vision system are fused using evidence-based fusion. These steps are discussed in detail in the following subsections.

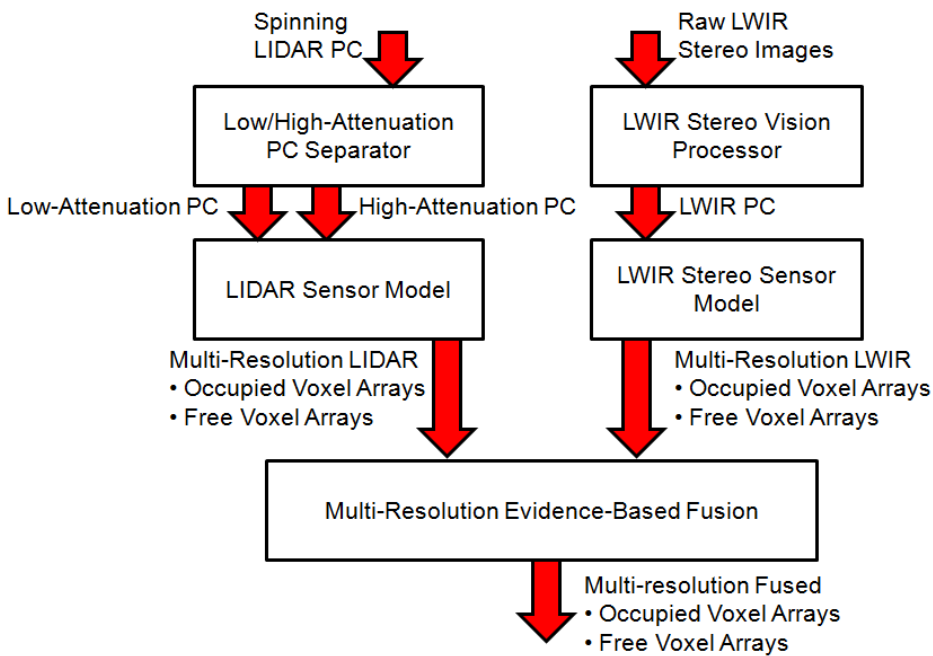


Figure 49: Sensor fusion application.

4.2.4 Fusion Process Components

4.2.4.1 LIDAR Pre-Processing

A heuristic method of separating the LIDAR low-attenuation and high-attenuation returns was produced based on the return intensity and distance information of a hallway environment in clear conditions compared to the same environment in smoke conditions. The data in Figure 50 shows plots of return intensity versus distance for both types of environments. Smoke points are plotted in black, determined to be smoke based on comparing the point cloud to baseline boundary information. Boundary points are plotted in red, also based on comparing the point cloud to baseline boundary information. A discussion on the variation in intensity from the

LIDAR for boundary returns is provided in Appendix G. A curve was fit to lower left-side of the data shown in the plot for the clear environment to be used as a threshold for separating low-attenuation and high-attenuation returns. Spatial filtering prior to thresholding is used to further improve the quality of the low-attenuation returns point cloud, as shown in the plot in Figure 50(c). The high-attenuation returns contain a mixture of points that are solid boundary returns and points that are smoke returns (i.e. free space, not occupied).

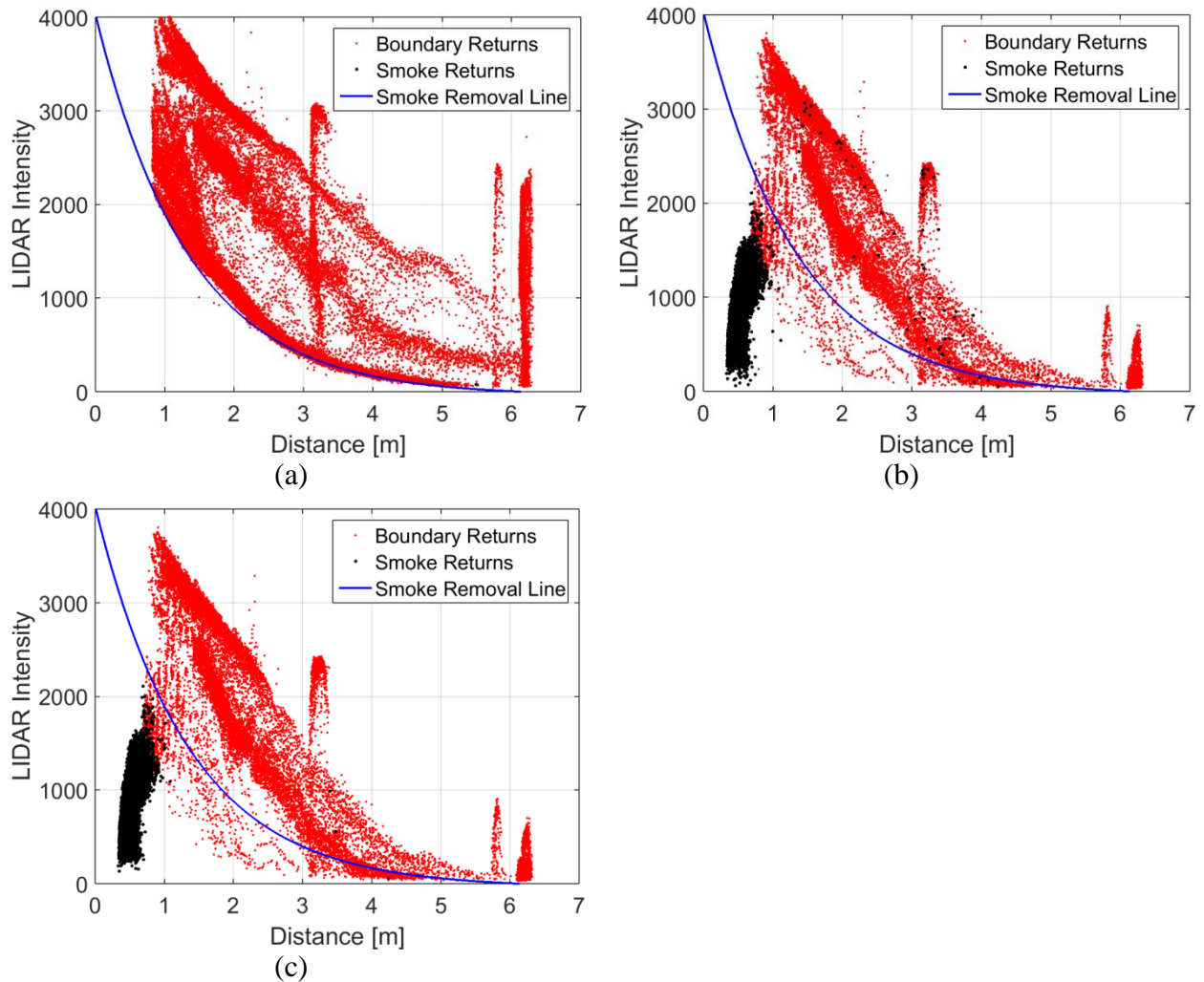


Figure 50: Intensity-distance plots for a hallway environment (a) for clear conditions, (b) in smoke conditions, and (c) in smoke conditions with outliers removed.

Figure 51 shows the process for separating the low-attenuation and high attenuation points. The point cloud is spatially filtered to remove outliers. Next, points are compared to the intensity-

distance threshold curve. Points below the curve are considered to be significantly attenuated points. After the separation processing, the resulting low-attenuation and high-attenuation point clouds are aligned to a global origin for application of the LIDAR sensor models. A discussion on the alignment of the LIDAR data and the LWIR stereo vision data to a common frame is provided in Appendix D. The effectiveness of this separation method for the experiments here is evaluated in a subsequent section.

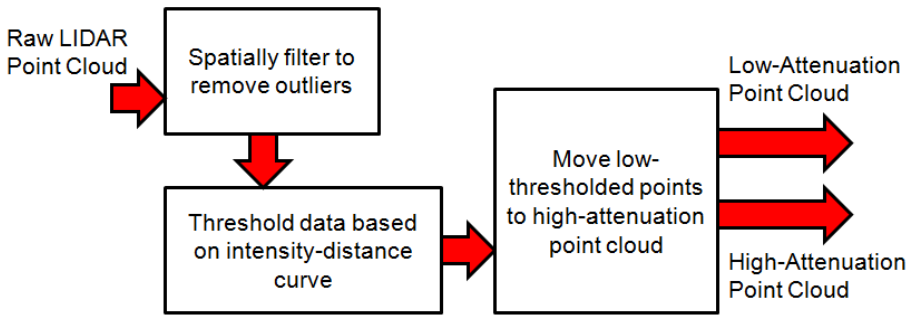


Figure 51: Low-attenuation and high-attenuation point cloud separator.

4.2.4.2 LWIR Stereo Vision Pre-Processing

The LWIR stereo vision pre-processing method is shown in Figure 52. First, the left and right 14-bit images are intensity aligned so that features in one image will have approximately the same intensity in the other image for improved stereo-matching. Next, the camera calibration and rectification are applied to the images. Consecutive Wiener filtering is used to remove noise [18], and then a bidirectional SAD correspondence matching algorithm [1, 3] is applied to the Sobel gradient magnitude matrix [19] of each image. Details of the bi-directional SAD correspondence matching algorithm are provided in Appendix B. Disparities are calculated to the nearest whole number. The resulting disparity map is converted to a point cloud that contains disparity information and matching cost information. This point cloud is aligned spatially to the global origin.

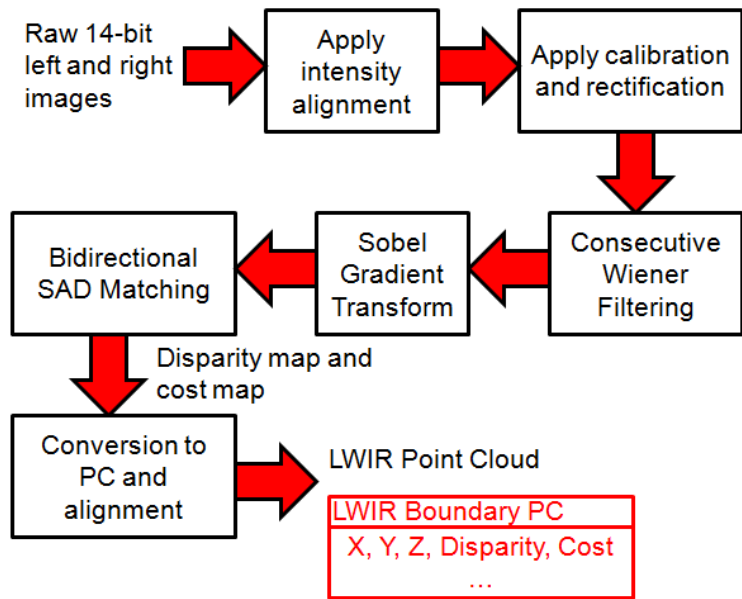


Figure 52: LWIR stereo vision pre-processing method.

4.2.4.3 Sensor Models

4.2.4.3.1 3D LIDAR (Low-Attenuation and High-Attenuation)

The sensor model for the LIDAR returns was selected to be different for low-attenuation and high-attenuation returns. Low-attenuation returns are assumed to locate a solid object, thus requiring a sensor model that provides information for the occupied voxel space and the free voxel space. High-attenuation returns are assumed to provide distance to either solid objects or smoke without the ability to distinguish. As a result, the sensor model for high-attenuation returns was selected to only provide information for the free voxel space. The plots in Figure 53 show a sample return for both types of sensor models. In the plots, the normalized return distribution and a discretized 1D grid view of evidence are shown for a return at 2.002 m with the sensor located at 0 m. Figure 53(a) shows application of the occupied evidence sensor model for a low-attenuation return, and Figure 53(b) shows application of the free space evidence sensor model for both low-attenuation and high-attenuation returns.

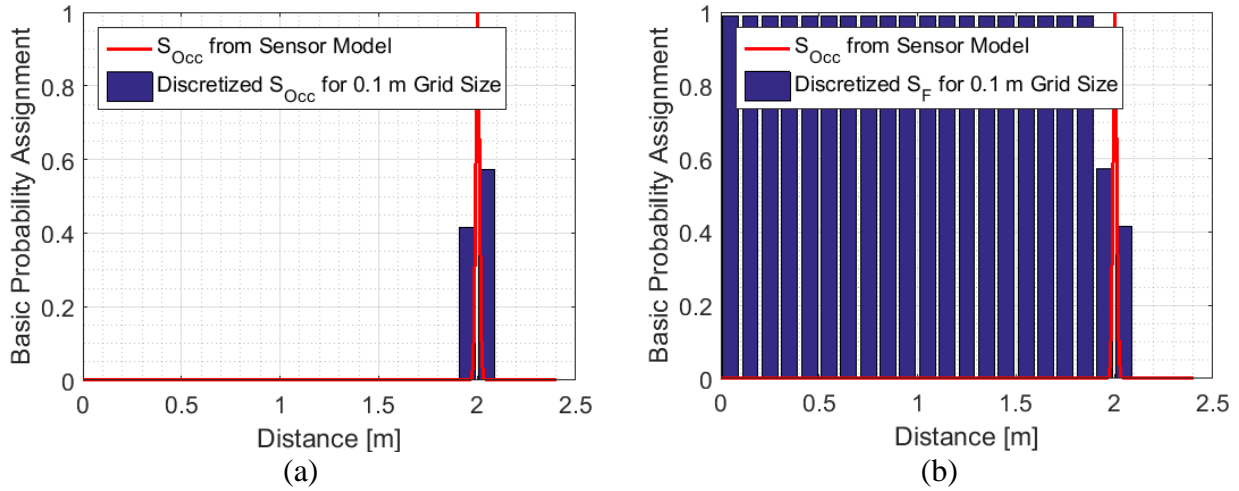


Figure 53: Sensor model for a return at 2.002 m showing (a) occupied evidence for low-attenuation returns and (b) free space evidence for low-attenuation and high attenuation returns.

The sensor model for each low-attenuation LIDAR return for the occupied voxel space is based off of a normal distribution of occupied information near the return, similar to probabilistic sensor models in the literature [20, 21]. The return standard deviation was determined to be 8.8 mm by collecting range-data from the LIDAR over time for several 50 mm x 50 mm areas on a planar surface approximately perpendicular to the sensor several meters away from the sensor. The sensor model was limited to provide an evidence value of no more than 0.99 for application. Along the ray before and after the bulk of the distribution has a value of 0 since there is no significant evidence along these parts of the ray for occupied state. This sensor model is mapped to the occupied voxel array for each point in the point cloud to produce one occupied voxel array for each LIDAR point cloud.

The sensor model for each low-attenuation LIDAR return for the free space voxel space is modeled to have high evidence of empty space in voxels up to the return and ignorance of free space (0) in voxels with the return and beyond. As with the occupied space sensor model, the upper limit of the free space evidence for the returns was set to be 0.99. The sensor model for each high-attenuation LIDAR return for the free space voxel space is the same as for the free space model for the low-attenuation LIDAR return case. The high-attenuation returns were not used to provide any occupied state evidence since each return may be to smoke instead of a solid

boundary. Each pair of low-attenuation and high-attenuation point clouds was used to produce one set of LIDAR occupied and free space voxels.

Algorithm 1 in Appendix H shows the application of the sensor model for one pair of low-attenuation and high attenuation point clouds. During application, the free-space voxel array was set to a value of 0 where the occupied voxel array had returns to improve location of planar surfaces far from perpendicular to the sensors. The occupied and free-space voxel arrays were reduced in half prior to fusion to ensure that the addition of evidences for occupied and free space would not sum to more than 1 during fusion.

4.2.4.3.2 LWIR Stereo Vision

The sensor model for the LWIR stereo vision system was designed to place evidence based on the stereo matching cost of each point, the disparity level of each point, and the number of returns affecting each voxel for the entire LWIR stereo vision point cloud. The stereo matching cost is a measure of how well the top correspondence matching disparity stands out from other possible disparity values and is a value directly output from the SAD matching algorithm. The plots in Figure 54 show applications of the occupied state sensor model for sample points in a 1D 0.1-m discretized path demonstrating effects of these parameters. Since whole-number disparities are used in calculations, the precision on each stereo match is half a disparity. Thus, the model here assumes each return provides evidence of an object within a distance range corresponding to the matched disparity plus or minus half a disparity, similar to the probabilistic sensor model in [22]. Different than in that work, the model selected here distributes the evidence over the number of affected grid spaces. At further distances, a measured disparity level will have less precision than at closer distances, so the evidence for the point is distributed over more distance (i.e. more voxels). Likewise, with better stereo matching cost and with more points affecting a given voxel, the strength of evidence is higher than for voxels with worse stereo matching cost or with few points affecting each voxel. The occupied space evidence was limited to 0.99.

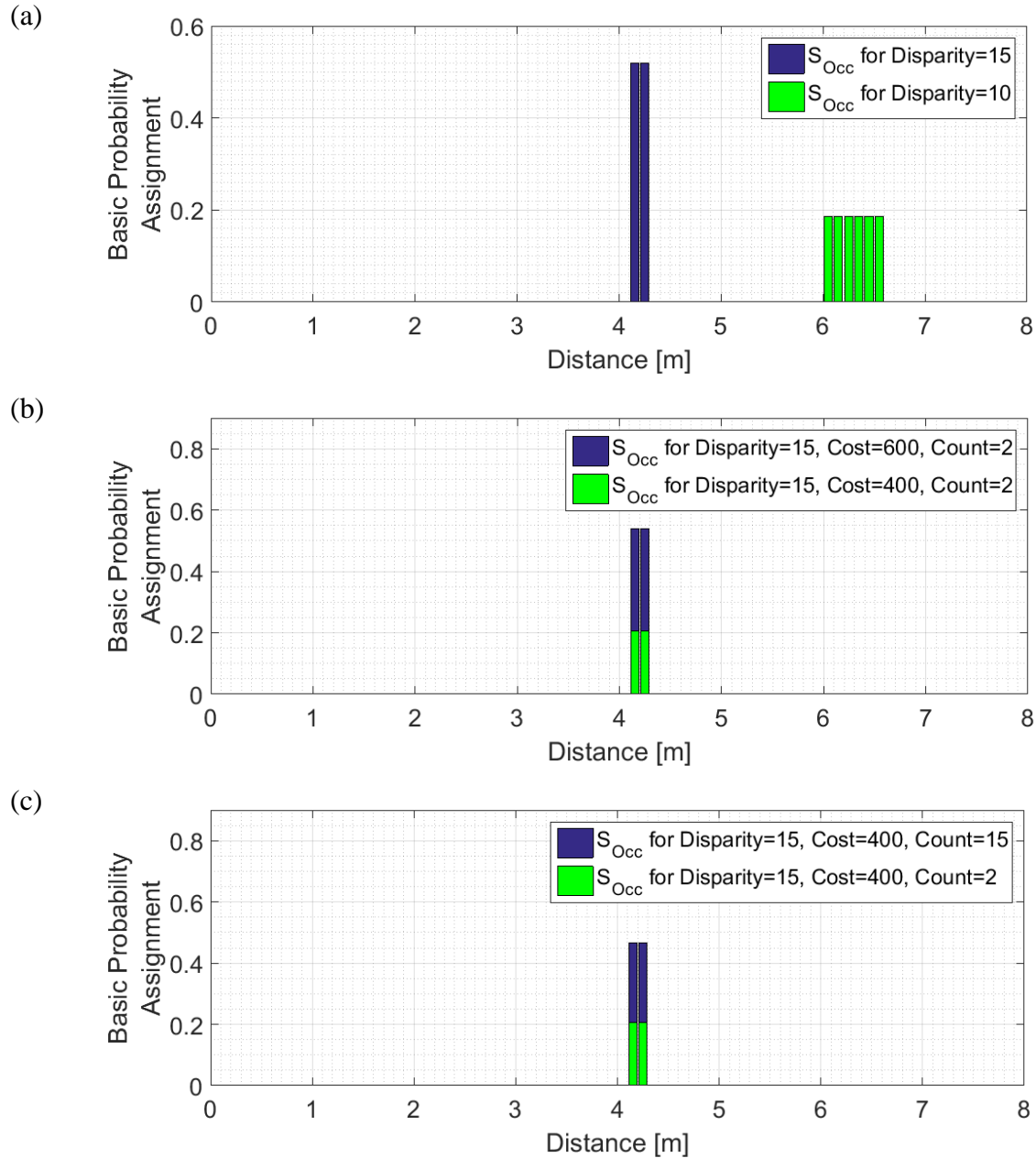


Figure 54: Plots of sample points for the LWIR stereo vision occupied state sensor model: (a) evidence distributed over more grid spaces at further distances, (b) evidence higher for higher costs, and (c) evidence higher for more points affecting the location.

The free space state sensor model provides evidence for free space up to the beginning of the occupancy grid spaces affected by the points in the occupied state sensor model. Grid spaces containing evidence of occupancy and beyond are set to 0 to indicate ignorance of information

on free space. Figure 55 shows an example application of this model in a 1D discretized space. The grid spacing is 0.1 meters. As with the occupied space, the free space evidence was limited to 0.99.

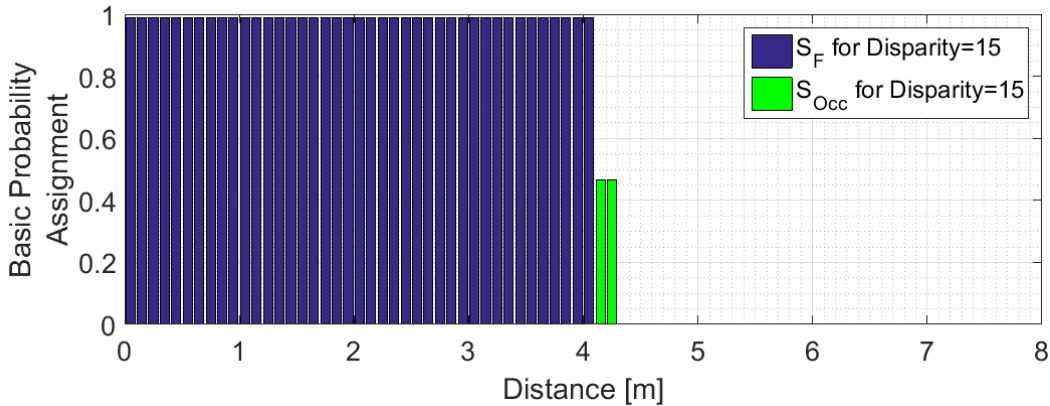


Figure 55: Example application of the free space sensor model for the LWIR stereo vision system.

The LWIR stereo vision system sensor model is applied in steps, as shown in Algorithm 2 in Appendix H. First, a ray trace to each point is used to update arrays containing information about the evidence for occupied and free space state of each voxel. During the ray trace, the highest disparity, best cost, and total number of points affecting the occupied state of the voxel domain are stored. This ray trace is also used to store the total number of points affecting the free space state of the voxel domain. Once the last point in the current point cloud is processed, the entire set of voxel arrays for cost, disparity, and number of points affecting each state of the voxel is used to produce the final occupied and free space voxel arrays, following Algorithm 3 in Appendix H. As with the LIDAR sensor model, the free space voxel array is set to 0 where the occupied space voxel array has non-zero values. Also as with the LIDAR system, the voxel array values are halved before fusion with the LIDAR results to ensure the summation of the occupied and free values would not exceed 1.

4.3 Experimental Method for Fusion Evaluation

4.3.1 Sensors

Evaluation of the fusion method was performed using a 3D spinning LIDAR and a LWIR stereo vision system mounted in a robot head. This sensor setup was mounted atop a wheeled robot platform stationary at the exit of a hallway test facility for the first experiment. The same layout of sensors was mounted atop a humanoid robot platform for the second experiment. Figure 56 shows the LIDAR and thermal IR cameras on the robot head. The LIDAR was located 0.48 m off of the ground for testing. The LWIR cameras are centered 0.09 m above the center of the LIDAR emitter with a baseline of 0.168 m.



Figure 56: Robot head setup of LIDAR and LWIR cameras.

4.3.1.1 Spinning LIDAR

The LIDAR sensor used for these tests was a Hokuyo UTM-30LX-EW, a multi-echo LIDAR. The LIDAR was mounted on a motor and rotated at a rate of 0.5 revolutions per second. ROS (Robot Operating System [23]) was used to record data from the LIDAR and motor. The furthest distance return was used when multiple returns were present. As the LIDAR rotated, individual scans were recorded for post-processing.

After gathering data, individual point clouds were constructed based on every 5 seconds-worth of data for fusion processing. The LIDAR return intensity for each point in each point cloud was also stored and later used for separation of each point cloud into a low-attenuation returns point

cloud and a high-attenuation returns point cloud. The LIDAR point clouds were saved to a series of files for post-processing.

4.3.1.2 LWIR Stereo Vision System

The LWIR stereo vision system consisted of two FLIR A35 thermal imagers. These sensors are uncooled microbolometer devices with 256x320 pixels. Each camera has a 9-mm lens. The stereo system has a baseline of 168 mm. 14-bit thermal images were recorded in ROS at a rate of 10 Hz for post-processing.

4.3.2 Hallway Fire Environment Test Setup

The sensors for the hallway experiment were aimed down the hallway shown in the diagram in Figure 57. A blockage was placed at the top of the hall exit to ensure a thick upper smoke layer. The sensors were set to log data prior to fire testing to obtain baseline information of the scene. After more than 30 seconds of logging data in the clear environment, an approximately 200 mm x 200 mm x 150 mm latex foam block was lit in the room adjacent to the hallway. Data logging from the sensors was stopped after the fire burned out and the smoke began to clear.

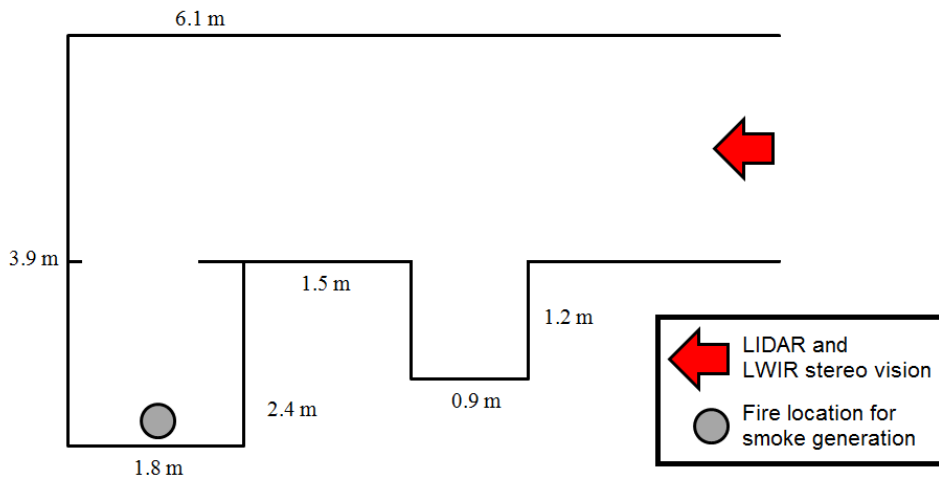


Figure 57: Hallway setup for the latex foam fire smoke test.

4.3.3 SAFFiR Demonstration Test Setup

Figure 58 contains a diagram of the scene assessed from the SAFFiR demonstration data. The scene evaluated here was with the humanoid robot standing at the entrance of a ship room containing a wood fire. The fire was approximately 0.51 m x 0.51 m x 0.38 m, made up of wood boards with a square 51 mm x 51 mm cross-section. The fire was lit with a heptane pool prior to the robot approaching the room containing the fire. A single LIDAR point cloud based on 5 seconds of data collecting and a single stereo pair of LWIR images was used for assessment of the fusion system in the conditions present during the SAFFiR demo.

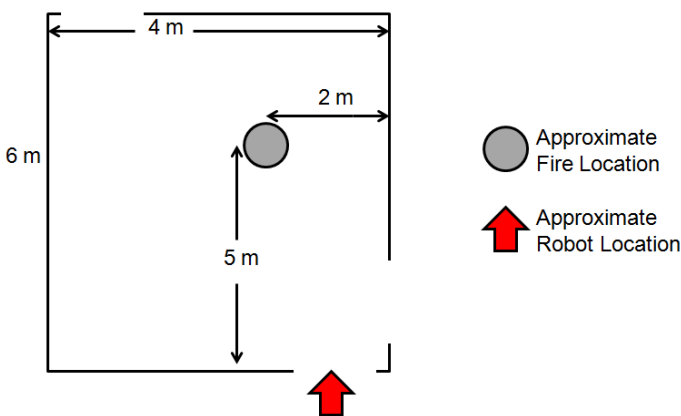


Figure 58: SAFFiR test scenario.

4.4 Results and Discussion

4.4.1 Hallway Fire Environment

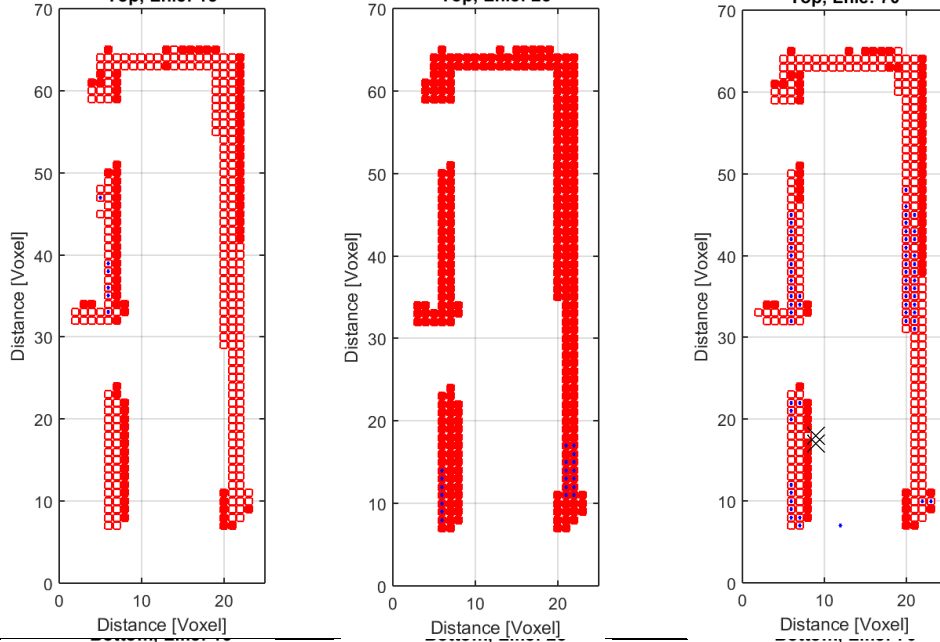
The latex foam fire test results were logged in time by a frame number tracking the number of recorded LIDAR point clouds. A total of 121 frames were recorded, and fusion was performed on every 5 frames. During the test, frames 5 and 10 were of the hallway environment before the smoke was in view. In frames 15 through 30, the smoke entered and reached its peak thickness. After this point, the smoke began to thin.

4.4.1.1 Smoke Separation

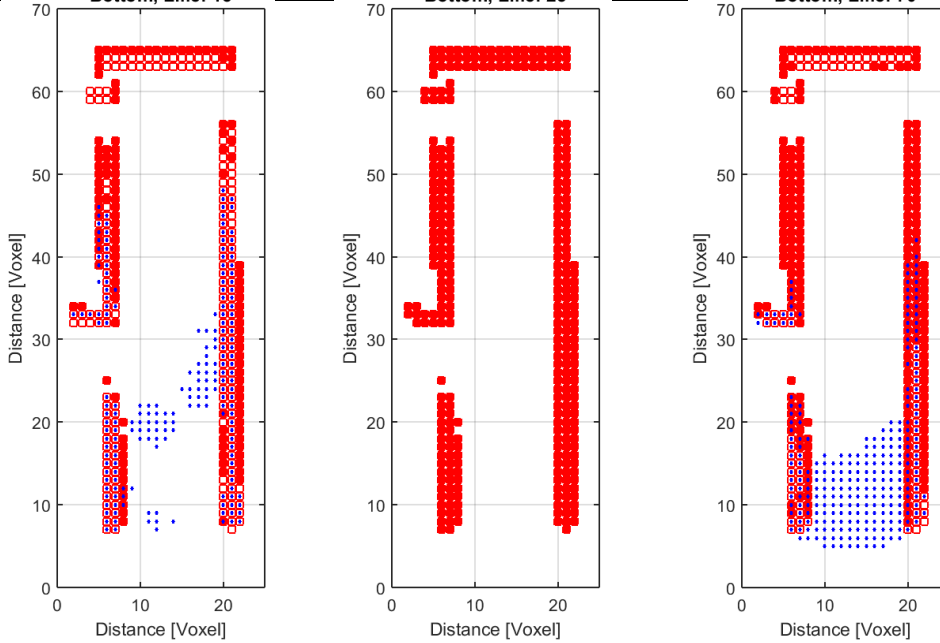
Figure 59 contains 2D horizontal slice views at two elevations in the hallway, one in the upper portion of the hallway and one in the lower portion. Filled red boxes indicate boundary returns from baseline data of the hallway environment, using a voxel representation with 0.1-m cubes for

the entire scene. Open red boxes indicate correct boundary returns from the LIDAR when comparing the data to the baseline data of the hallway boundaries. Blue dots denote returns removed due to the smoke separation algorithm. Black “x” marks are used to indicate smoke returns that were not removed from the low-attenuation LIDAR point cloud. While the smoke separation algorithm largely reduced the number of smoke returns present in the low-attenuation LIDAR point cloud, some points still made it through the algorithm. The plot in Figure 60 shows the number of smoke pixels not removed from the low-attenuation LIDAR point cloud as a percentage of entire point cloud size for the length of the test. Overall, less than 0.4% of returns in the low-attenuation point cloud were smoke points.

Top



Bottom



(a) Frame 15

(b) Frame 25

(c) Frame 70

Figure 59: Smoke removal at several frames for a horizontal slice along the top and bottom of the hallway (a) as smoke is entering, (b) once smoke is dense, and (c) as smoke is thinning.

Open red boxes indicate correct boundary returns from the LIDAR when comparing the data to the baseline data of the hallway boundaries. Blue dots denote returns removed due to the smoke separation algorithm. Black “x” marks are used to indicate smoke returns that were not removed from the low-attenuation LIDAR point cloud.

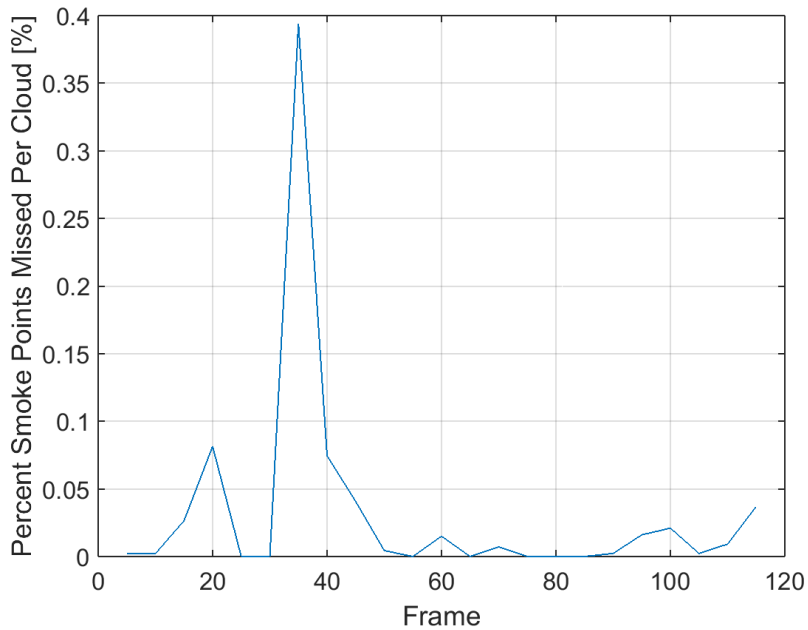


Figure 60: Percentage of smoke points not removed from low-attenuation point cloud by the smoke separation algorithm.

4.4.1.2 Evidential Fusion during Latex Foam Test

4.4.1.2.1 Visual and LWIR Imagery

Visual images at several points in time during the latex foam fire test are shown in Figure 61.

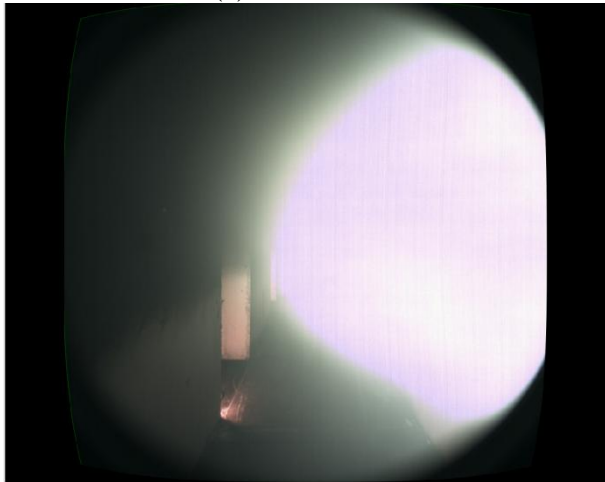
LWIR images at several points in time are shown in Figure 62. The conditions during the latex foam test ranged from clear to dense smoke and included many frames between the two extremes.



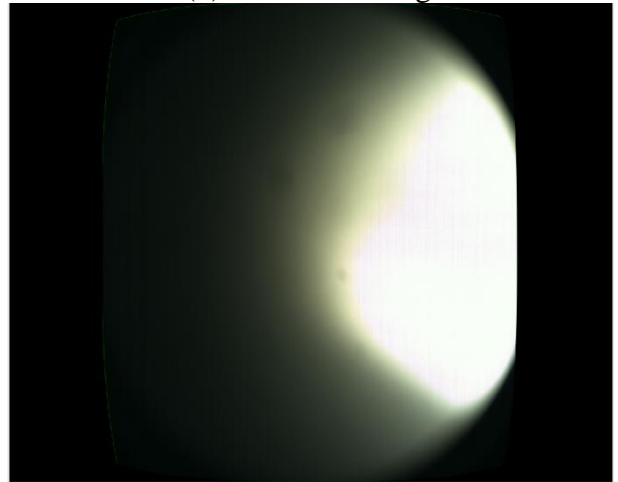
(a) Before fire



(b) Smoke entering



(c) Smoke becoming dense



(d) Smoke dense

Figure 61: Visual images during the latex foam test (a) before the fire, (b) as smoke is entering, (c) as the smoke is becoming dense, and (d) once the smoke is dense.

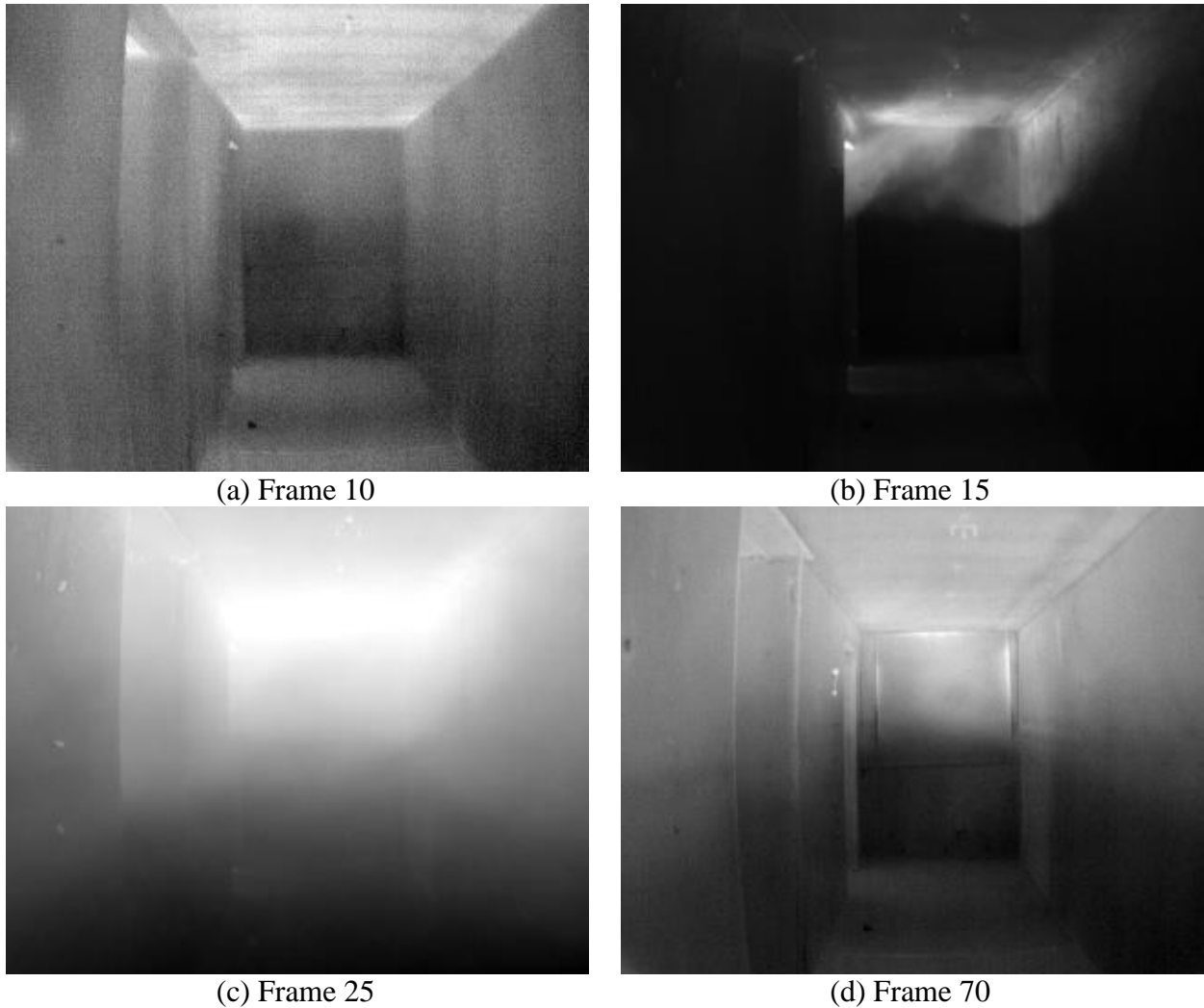


Figure 62: Raw LWIR images before processing and with linear scaling to 8-bit data type for viewing during the latex foam test (a) before the fire, (b) as smoke is entering, (c) when smoke is dense, and (d) as smoke is thinning.

4.4.1.2.2 Evidential Fusion Results

Figure 63 contains a 3D view of the baseline data of the hallway environment for the multi-resolution voxel domain for the thresholded occupied state. In the Figure, closer distances are lighter with black as a background to the data. Figures 64 and 65 contain multi-resolution 3D views of the hallway during the latex foam fire test as shown by thresholded occupied state voxels. These Figures contain the LIDAR view, the LWIR stereo vision sensor view, and the evidential sensor fusion results view. The LIDAR alone failed to provide useful information once the smoke became dense. Once the smoke began to thin, the LIDAR regained the ability to

range to part of the environment, specifically the lower portion of the hallway. The LWIR stereo vision system provided information throughout the test, mostly along the back wall and along the ceiling edges at the top of the side walls far from the sensor. The LWIR system results were sparser before the smoke entered the hallway due to the stereo matching of the scene producing higher quality results once the scene became more thermally diverse. The multi-resolution 3D views of the fusion results in these figures show that fusing the LIDAR and LWIR stereo vision system produced better results than either system alone for the occupied state for some conditions and when considering the entire range of smoke conditions together.



Figure 63: 3D view of baseline occupied state data in multi-resolution voxel domain.

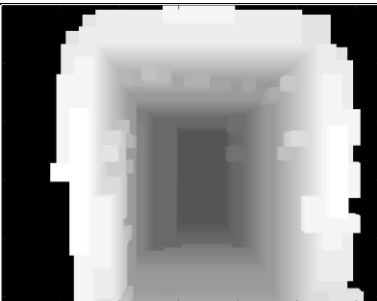
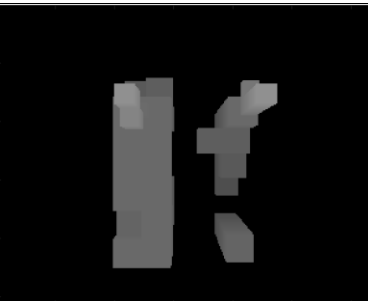
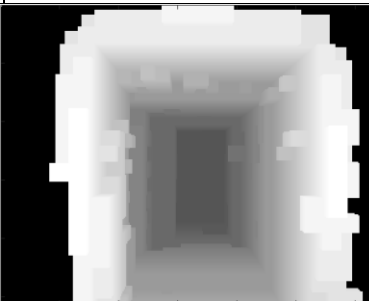
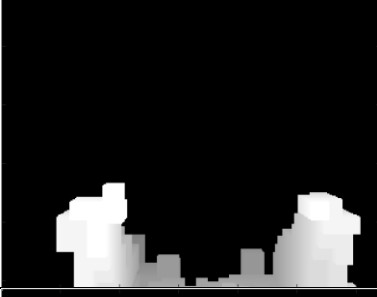
Frame	LIDAR	LWIR Stereo Vision	Fused
(a) 10			
(b) 15			
(c) 20			
(d) 25			

Figure 64: Occupied state results for the LIDAR, LWIR stereo vision system, and evidential fusion for several frames at the beginning of testing.

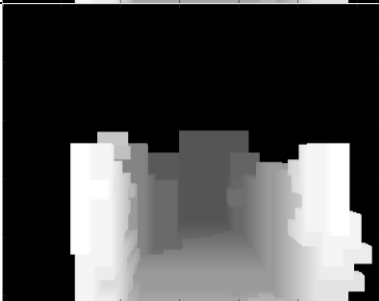
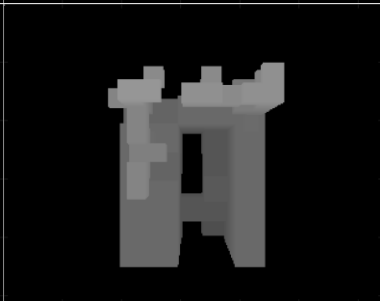
Frame	LIDAR	LWIR Stereo Vision	Fused
(a) 50			
(b) 65			
(c) 75			
(d) 105			

Figure 65: Occupied state results for the LIDAR, LWIR stereo vision system, and evidential fusion for several frames at the beginning of testing.

For further analysis, 2D horizontal slice views of the range-data for an upper and lower portion of the hallway are shown in Figures 66 through 70 for the sensors and fusion for the occupied and free space states. In the occupied state plots, red solid boxes indicate baseline information of the thresholded occupied state of the environment, and black empty boxes indicate thresholded occupied state information from the individual sensors and fusion. In the free space state blocks,

green solid boxes indicate thresholded baseline free space information, and black empty boxes indicate thresholded free space state information from the sensors and fusion. From the plots, it can be seen that as the smoke thickened, the LIDAR became worse at providing occupied space information at both elevations. However, due to the sensor model for high-attenuation returns, the space directly in front of the LIDAR in the lower slice view still showed up as empty space for the LIDAR results. Once the smoke began to thin, the LIDAR began to provide better results for the lower portion of the hallway for both occupied and free space information. As the environment heated up, the LWIR stereo vision system began to provide more occupied accurate and inaccurate points with little change in free space indication at either height in the hallway. The evidential fusion results show improvement over either sensor individually for some smoke conditions for the occupied state and for the free space state voxels.

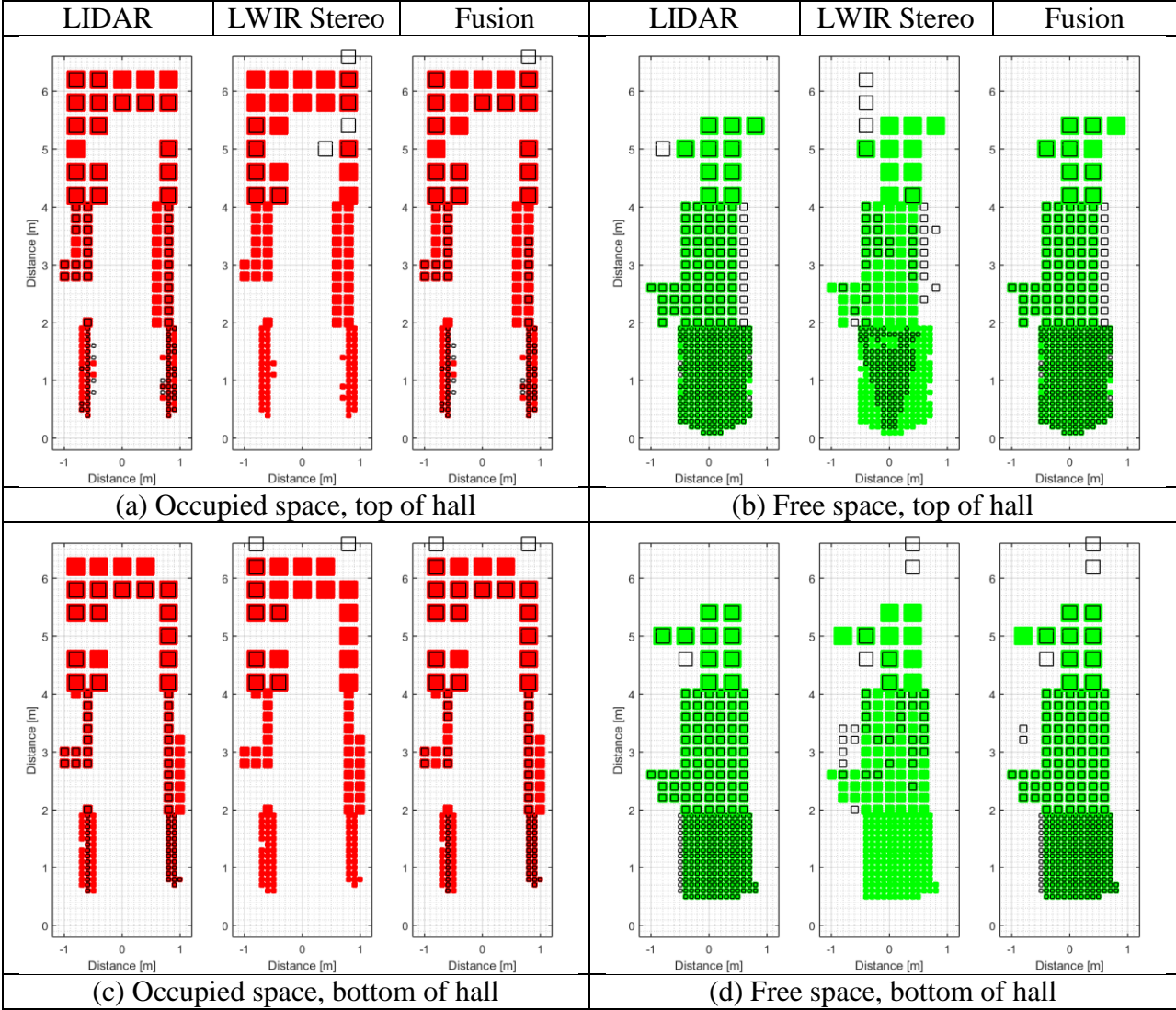


Figure 66: 2D horizontal slice views of upper and lower elevations for frame 10, before the smoke is in view.

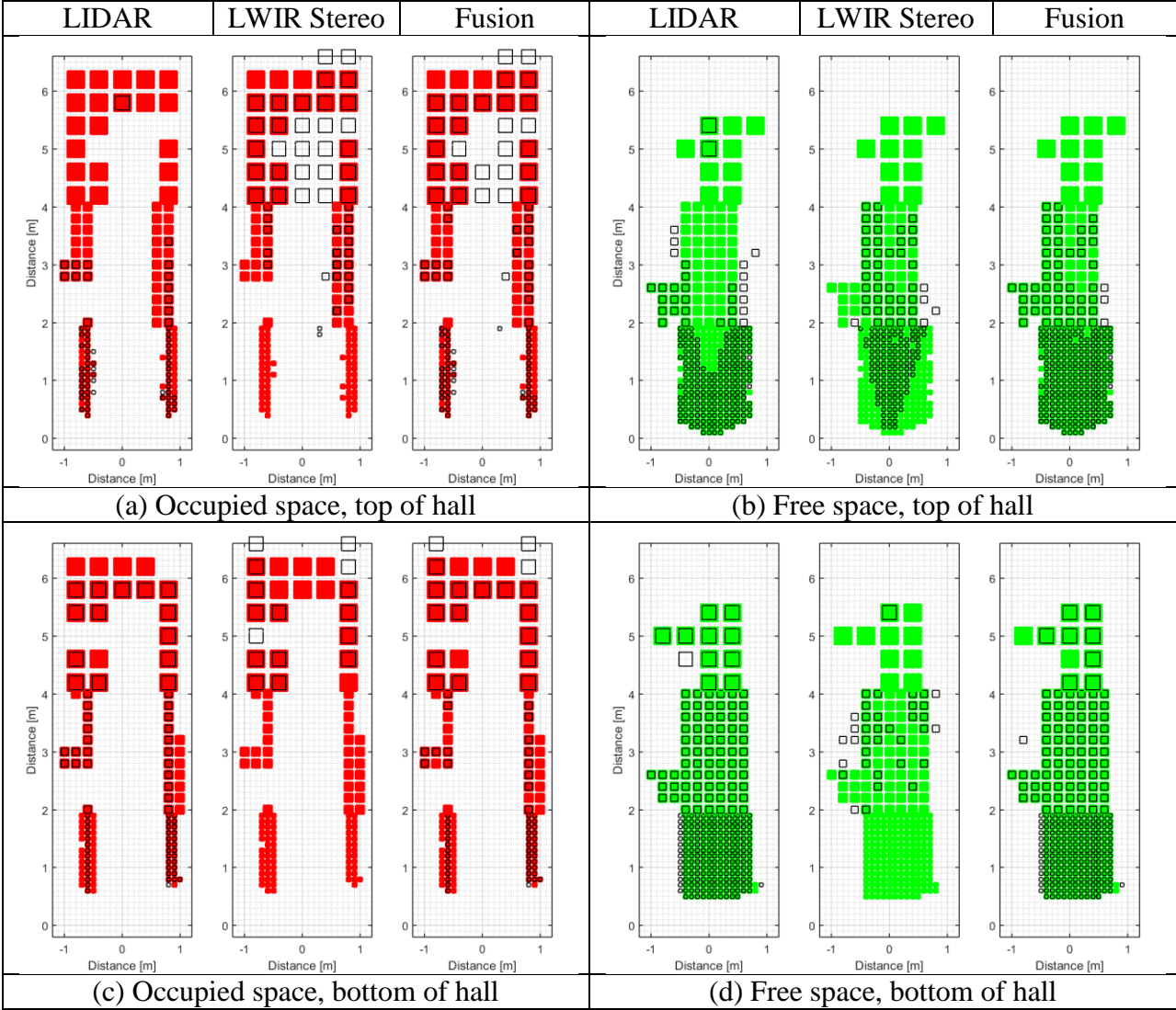


Figure 67: 2D horizontal slice views of upper and lower elevations for frame 15, as the smoke enters the scene.

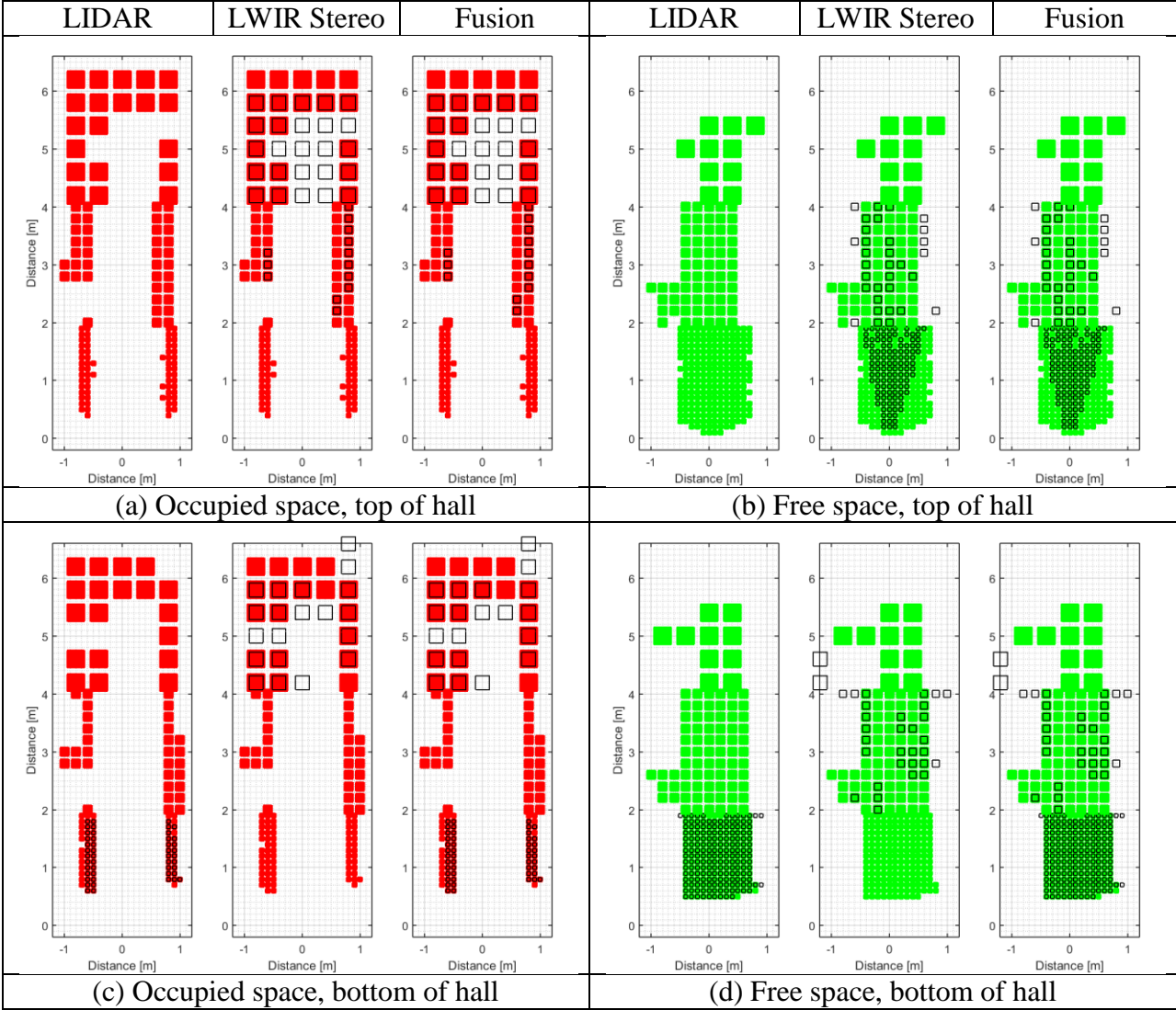


Figure 68: 2D horizontal slice views of upper and lower elevations for frame 20, when the smoke is almost at its maximum thickness.

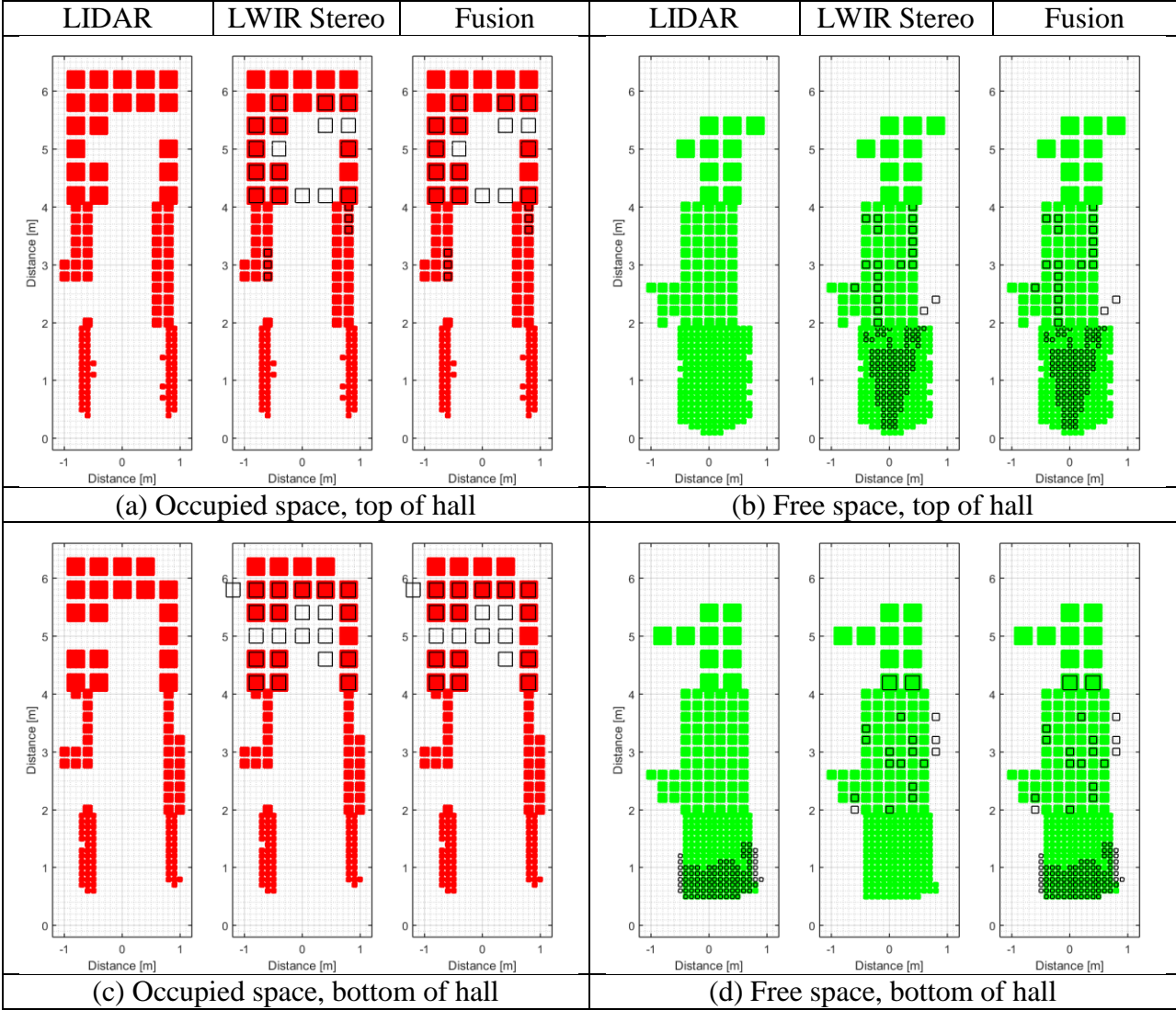


Figure 69: 2D horizontal slice views of upper and lower elevations for frame 25, when the smoke is thickest.

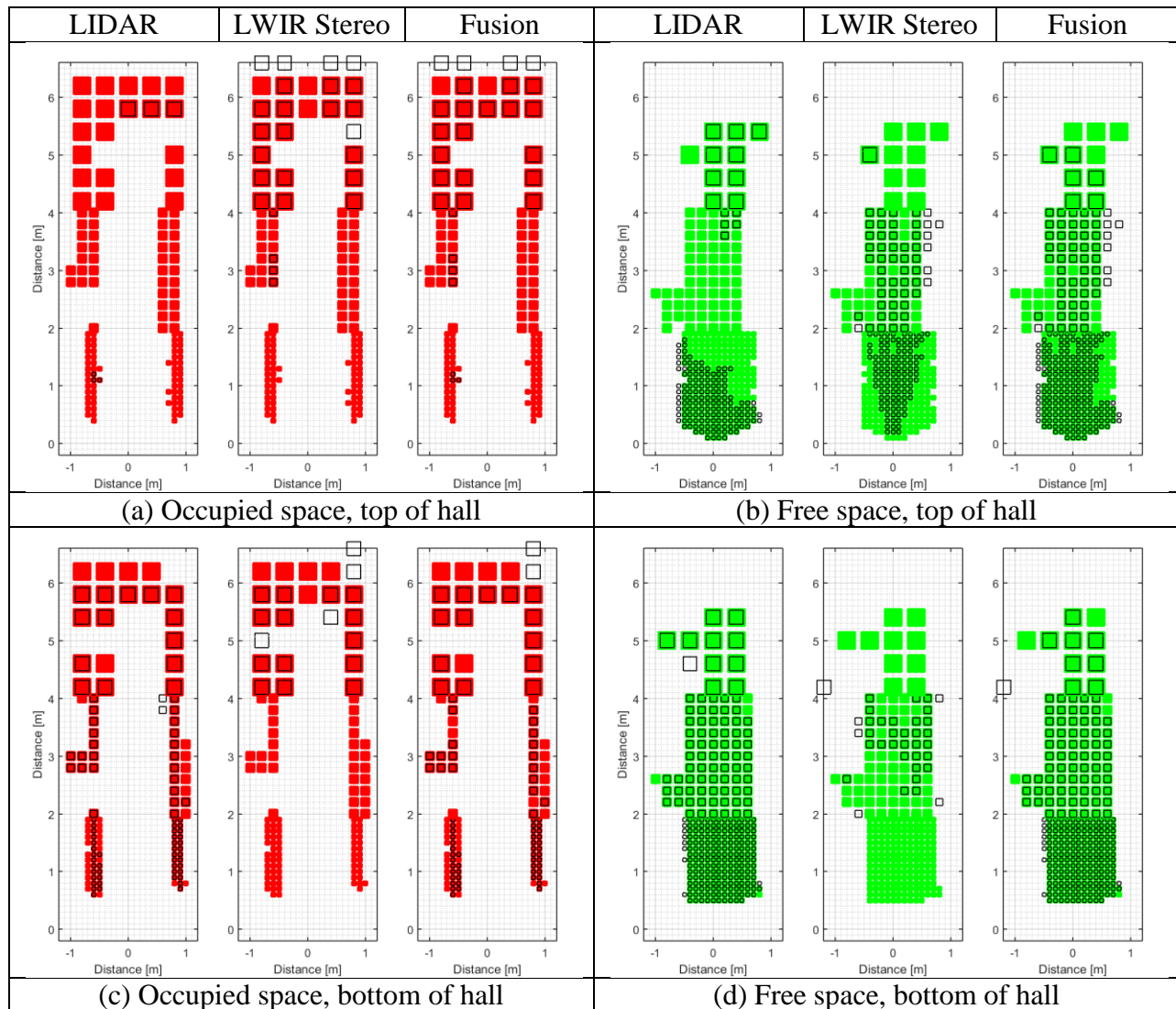


Figure 70: 2D horizontal slice views of upper and lower elevations for frame 75, as the smoke is thinning.

The overall accuracy for each sensor and for the fusion method is shown in Figure 71 for the thresholded occupied and free space voxel arrays. These plots show accuracy as a ratio of the number of voxels at each frame that have the indicated state that matches baseline state information to the total number of baseline voxels for that state. Each voxel is counted the same, regardless of voxel size/resolution. The plots in Figure 72 show the corresponding inaccuracy, the ratio of the number of voxels indicated as the state that do not match the baseline state information to the total number of baseline voxels for that state. Initially, the fusion method produced results for the occupied state that were worse than the LIDAR system by less than 5%

accuracy compared to the baseline but better than the LWIR stereo vision system by more than 60% accuracy compared to the baseline. Once the smoke came into view and the LIDAR was blocked, the fusion method provided the stereo IR results for the occupied state. As the smoke began to thin, the fusion method outperformed each individual sensor at locating the occupied voxels, with less than 5% accuracy improvement over the LIDAR. For the free space accuracy, the fusion system initially provided similar results to the LIDAR system. Once the smoke was in view, the fusion method outperformed either sensor by around 10% accuracy or more compared to the baseline, including when the LIDAR returned only high-attenuation data points. The fusion method provided similar but higher inaccuracy results compared to the individual sensors.

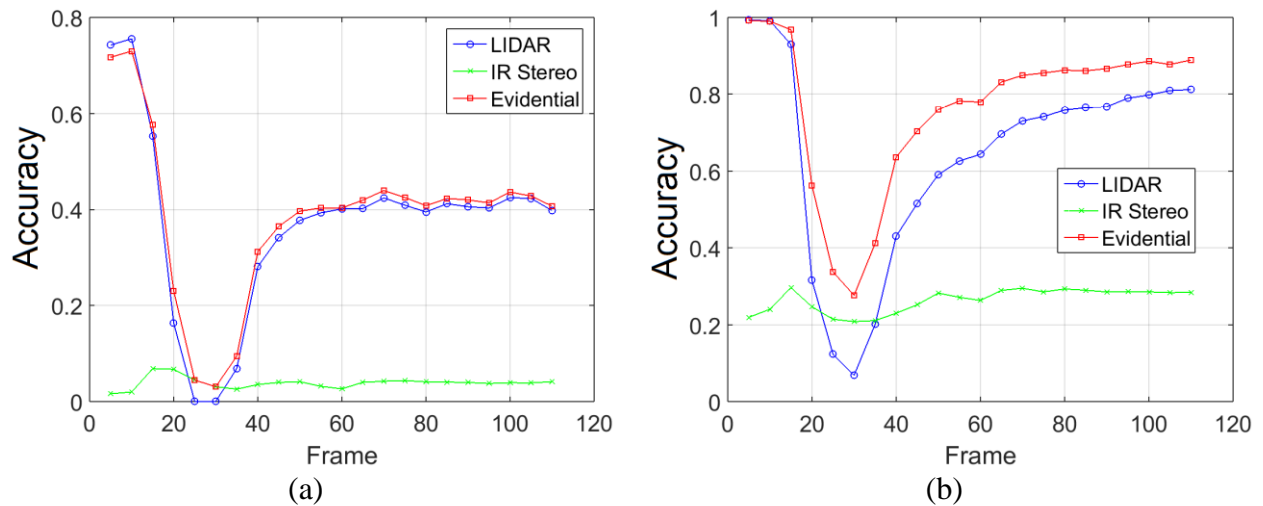


Figure 71: Accuracy for (a) occupied and (b) free space voxel data, overall.

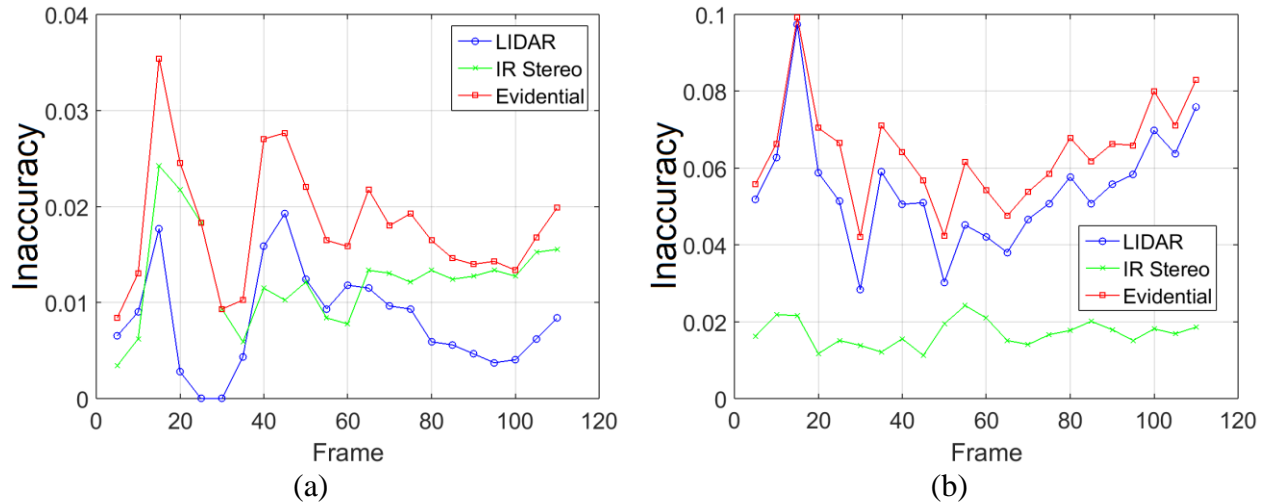


Figure 72: Inaccuracy for (a) occupied and (b) free space voxel data, overall.

The accuracy and inaccuracy plots for the upper and lower 2D horizontal slices are shown in Figures 73 through 76. For the upper slice, the fusion method provided similar but worse occupied state results than the LIDAR before the smoke entered the view. After the smoke arrived, the LIDAR sensor data dropped off for the occupied state, with the fusion system returning only the LWIR stereo vision results until the thinning of the smoke layer allowed the LIDAR to provide useful results again. The fusion method occupied state results were on the order of 10% higher accuracy compared to the baseline than the LIDAR from the point in the test when the smoke arrived and throughout the remainder of the test. Once the smoke began to thin, the fusion method combined the data to provide better results than either sensor alone for all but one processed frame. The fusion method provided a similar trend for the free space state results except that initially the fusion method provided approximately the same results as the LIDAR. The inaccuracy of the fusion method was similar to the inaccuracy of the individual sensors for both the occupied and free space states.

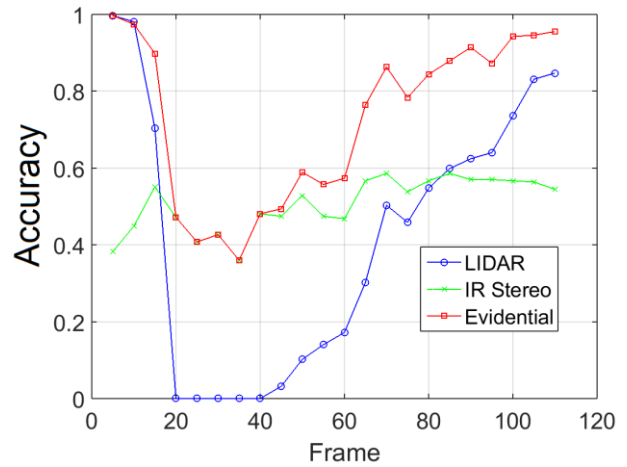
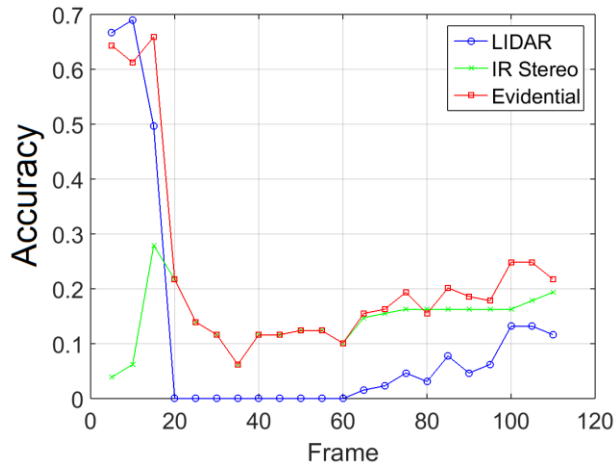


Figure 73: Accuracy for (a) occupied and (b) free space voxel data, upper 2D slice.

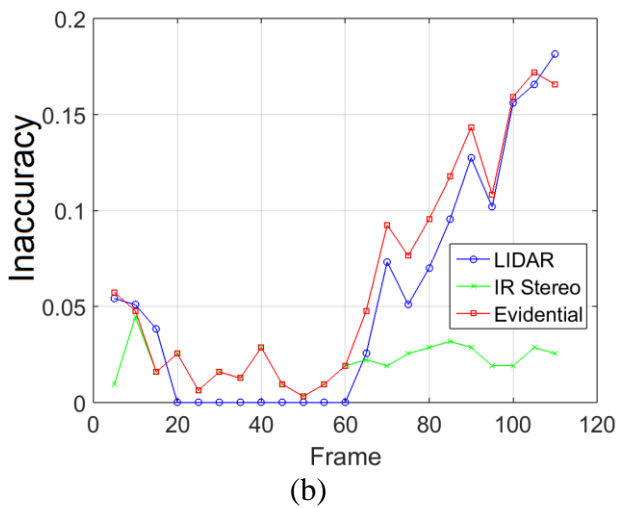
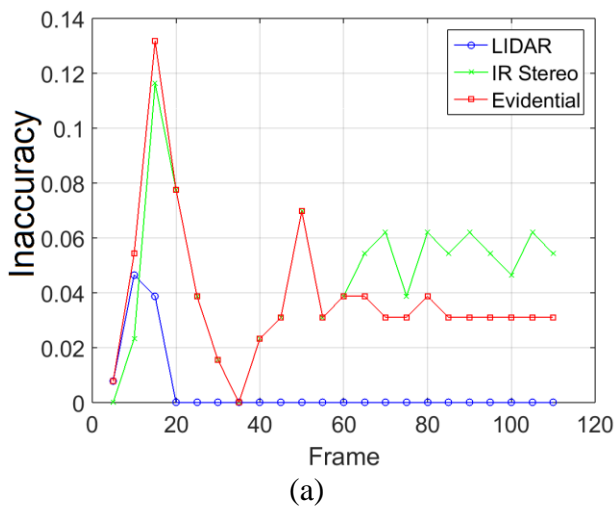


Figure 74: Inaccuracy for (a) occupied and (b) free space voxel data, upper 2D slice.

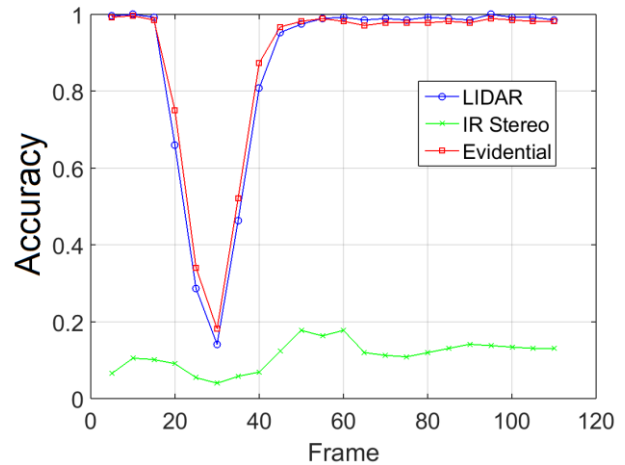
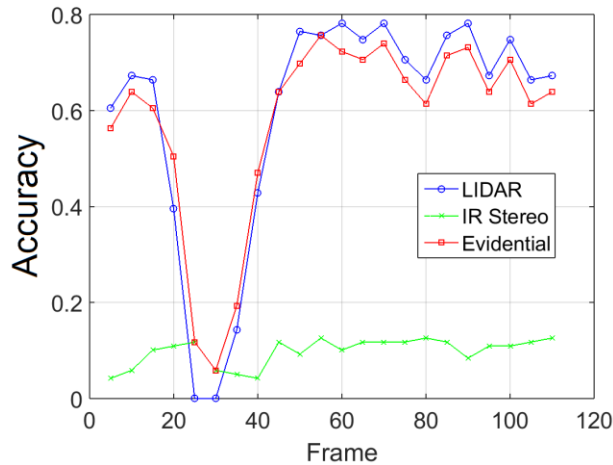


Figure 75: Accuracy for (a) occupied and (b) free space voxel data, lower 2D slice.

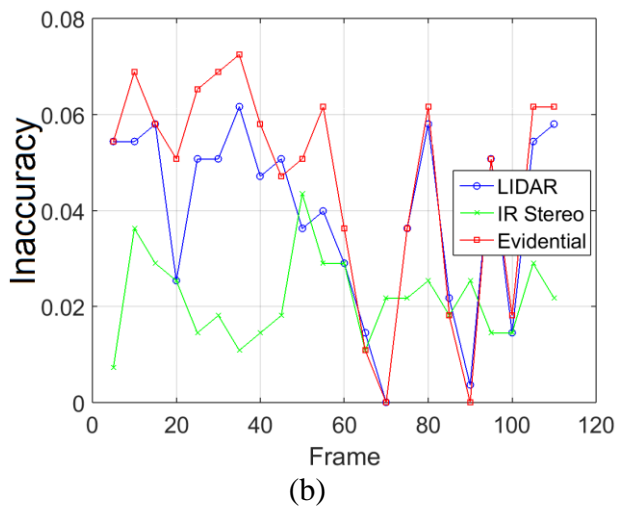
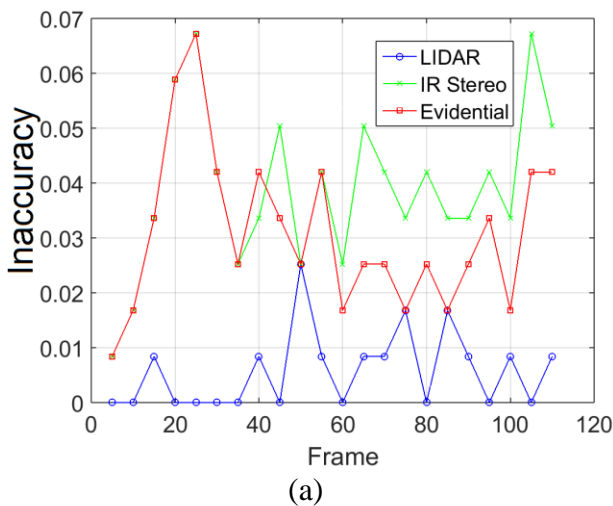


Figure 76: Inaccuracy for (a) occupied and (b) free space voxel data, lower 2D slice.

For the lower slice, the fusion method provided similar but worse results than the LIDAR for the occupied state for most of the test. However, when the smoke was thickest, the LIDAR occupied state results dropped off entirely, and the fusion method returned the LWIR stereo vision results. Just before and just after this portion of the test, the fusion method provided better results by about 5% accuracy or more compared to the baseline than either sensor alone for the occupied state. For the free space state, the fusion results were similar to the LIDAR throughout the test with highest improved results when the smoke was thickest, on the order of 10% higher accuracy

compared to baseline. The inaccuracy of the fusion method was similar to the inaccuracy of the individual sensors.

Comparing the upper and lower slice results in Figures 73 through 76 shows how the fusion method ranged in scenes in which the LIDAR was partially blocked by smoke. In these figures, the LIDAR regained visibility for providing occupied state information in the lower slice much sooner than for the upper slice due to the presence of the smoke in the upper portion of the hallway. During these frames, the LIDAR provided results similar to clear conditions for the lower slice and little or no results for the upper slice where the smoke was present. The fusion method had lower accuracy compared to the baseline for the occupied state than the LIDAR by about 5% for the lower slice but provided on the order of 10% higher accuracy compared to the baseline in the upper slice, providing data when the LIDAR provided little or no occupied state information. Comparing free space evidence at both layers shows that the LIDAR and sensor fusion provided similar results in the lower slice. However, the sensor fusion provided more than 40% free space state accuracy in the upper slice in dense smoke when the LIDAR accuracy was 0%.

Overall, the fusion method outperformed either individual sensor when considering some smoke conditions and when considering the entire test at both elevations and for the entire map for both the occupied and free space states. Before the smoke entered the scene, the LIDAR provided better information about the occupied state than the fusion method, but with thick smoke the LIDAR provided no useful occupied state information. The fusion method outperformed the LIDAR in thinning smoke at the upper elevation and provided similar but worse results to the LIDAR at the lower elevation. The fusion method free space results were similar or better to the LIDAR for the free space state for the duration of the test at both elevations and for the entire scene. The inaccuracies overall were similar for both sensors and the fusion method.

4.4.2 SAFFiR Demonstration

Figure 77 contains the filtered left LWIR image from the SAFFiR demonstration scene and a zoomed-in view of the image for comparison with point cloud data. Figure 78 contains 3D views of the SAFFiR demonstration scene for the multi-resolution voxel domain for the

thresholded occupied state. These views were rendered from a viewpoint moved forward from the robot to avoid having the outline of the doorway block view of boundaries inside the room. This figure shows the LIDAR results with high-attenuation point cloud separation, the LIDAR results if no separation is used, the LWIR stereo vision results, and the sensor fusion results. The LWIR stereo vision results were produced using a higher threshold in the SAD algorithm than used with the hallway scene for improved results. Comparing the 3D view of the LIDAR with and without separation of high-attenuation points indicates that significant errors will be present if the high-attenuation points are allowed to provide occupied state information instead of only being allowed to provide free space state information. The data in the figure shows that the LIDAR with high-attenuation returns separation is unable to range to occupied boundaries in the upper portion of the room, due to the presence of smoke. The LWIR is able to range through the smoke, and the fusion system is able to combine both sensors.

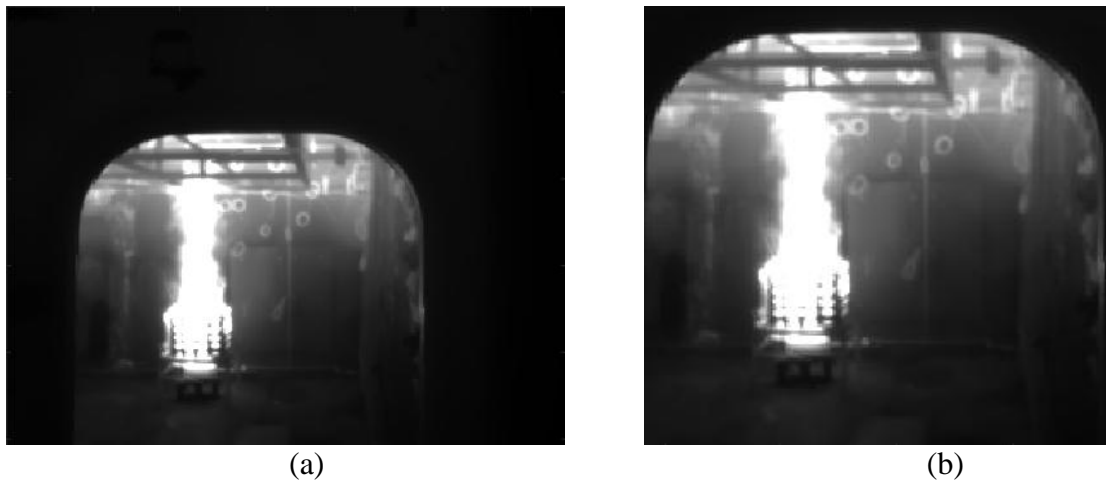


Figure 77: LWIR image from the SAFFiR demonstration, (a) filtered, and (b) filtered and zoomed-in for comparison to point cloud data.

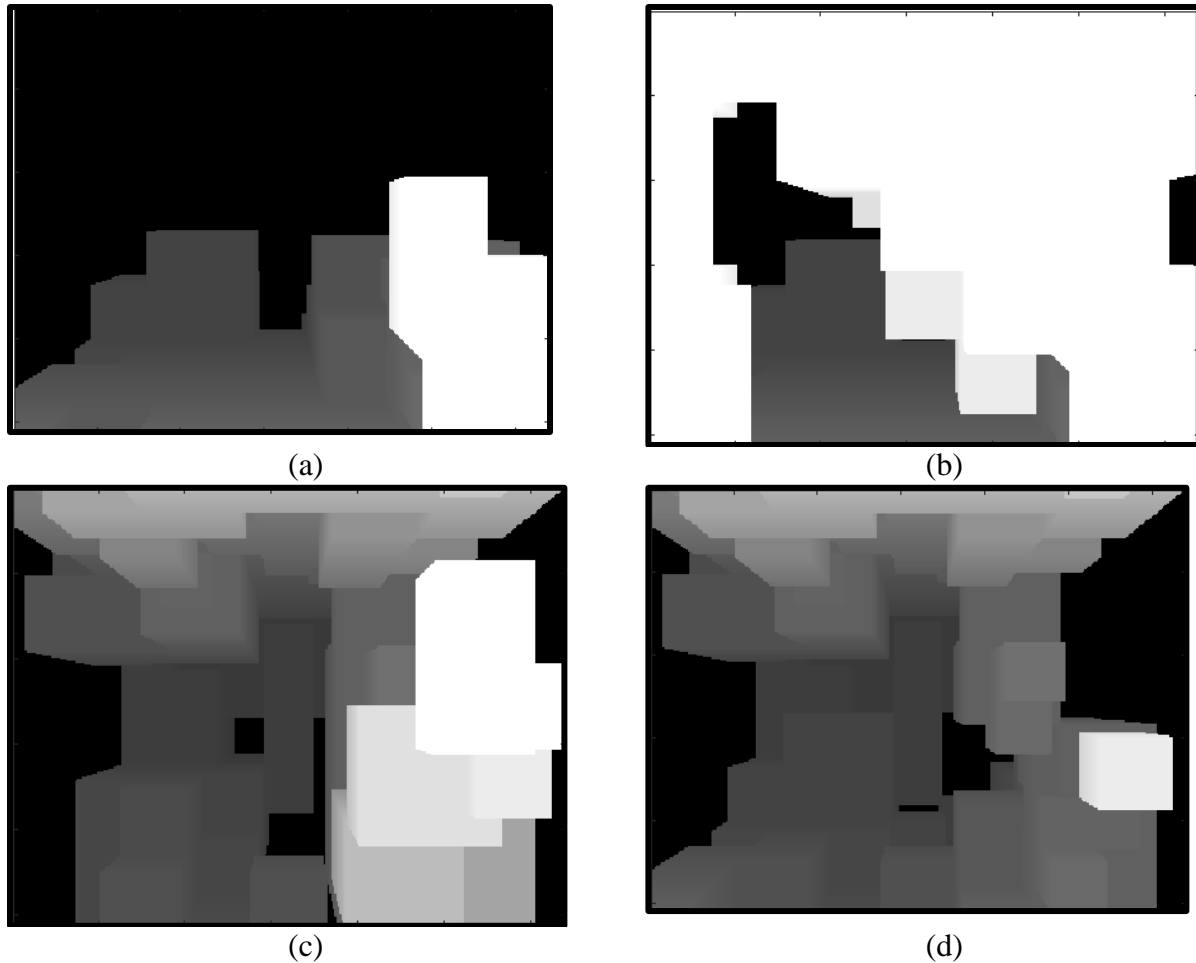


Figure 78: Occupied state results for the SAFFiR demonstration for (a) LIDAR with high-attenuation returns separation, (b) LIDAR without high-attenuation returns separation, (c) LWIR stereo vision, and (d) evidential sensor fusion.

Figure 79 contains 2D slice views of the range data for upper and lower portions of the scene for individual sensors and using the full sensor fusion method with separated use of low-attenuation and high-attenuation LIDAR returns. As with the hallway environment, the occupied state sensor fusion results show improvement over individual sensor use for the occupied state in the upper layer. In the upper layer, the occupied results at the doorway from the LIDAR and the LWIR stereo vision results further into the room both are present in the sensor fusion results. The upper layer free space state sensor fusion results similarly contain free space information from LIDAR range data to the doorway and LIDAR range data to the smoke along with LWIR free space data extending further into the room. For the lower layer, the occupied and free space state sensor fusion results appear similar to the LIDAR results.

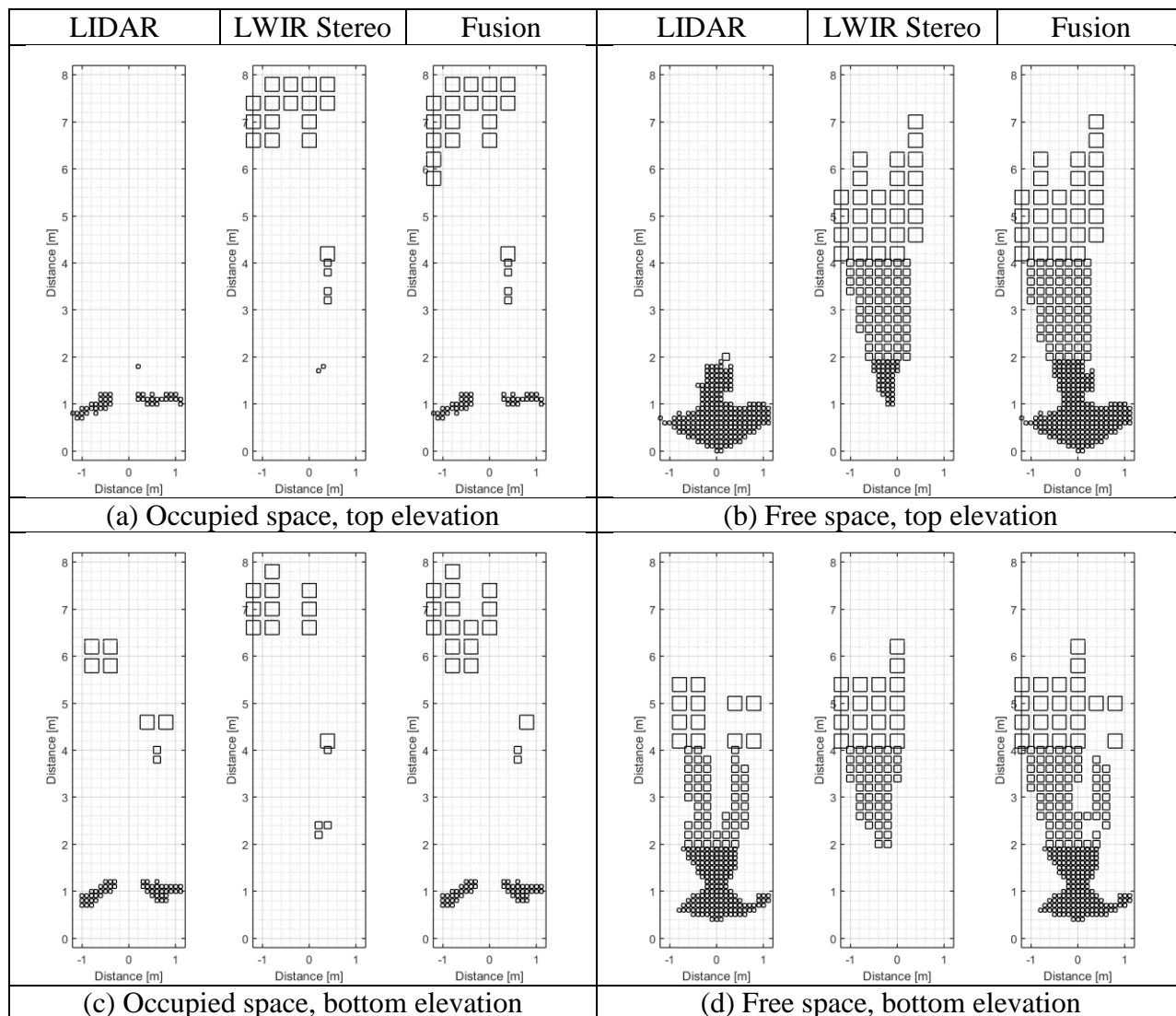


Figure 79: 2D horizontal slice views of upper and lower elevations for the SAFFiR demonstration data.

4.5 Conclusion

A framework was presented for using evidential theory to fuse 3D range information from a LWIR stereo vision system and a spinning LIDAR in a fire smoke environment with varying levels of smoke. Pre-processing steps for the LIDAR and LWIR stereo vision system were presented. A heuristic method was developed to use distance and return intensity information from the LIDAR data to separate significantly attenuated LIDAR returns from the low-attenuation returns. A sensor model for the low-attenuation LIDAR returns was used to provide

information on the evidence and ignorance of occupied and free space states for a multi-resolution 3D voxel space. A sensor model was also developed for the high-attenuation LIDAR returns to provide information about the free space voxel space, neglecting the occupied space state voxel space since high-attenuation returns may locate smoke instead of solid boundaries. The LWIR stereo vision sensor pre-processing was presented. A LWIR stereo vision sensor model was developed based on disparity level, stereo correspondence matching cost, and number of returns affecting a voxel for occupied and free space state.

Results from experiments with a hallway fire environment indicated that the LIDAR separation between low-attenuation and high-attenuation points resulted in less than 0.4% of the low-attenuation point cloud returns being smoke returns. Fusion results in the hallway environment showed that in some individual smoke scenes and over the combined full range of conditions from clear to thick smoke, the evidential fusion method provided better occupied state and free space state results than either sensor alone. For the hallway fire environment test, the scene was analyzed overall and for an upper 2D slice and lower 2D slice. For the occupied state for clear conditions, LIDAR was more accurate compared to the baseline than the sensor fusion. However, for the occupied state in dense smoke, sensor fusion provided higher accuracies compared to baseline than the LIDAR, with the LIDAR failing to provide any occupied state information for some scenes. For the occupied state as the smoke was thinning, the sensor fusion provided higher accuracies than the LIDAR overall and in the upper slicer, but the LIDAR provided higher accuracies for the lower slice, below the smoke layer. For cases where the LIDAR outperformed the sensor fusion at occupied state accuracy, the sensor fusion was typically within 5% or 10% of the LIDAR.

For the free space state, sensor fusion provided similar accuracies to LIDAR for clear conditions but had higher free space state accuracies compared to the baseline in dense and thinning smoke. Sensor fusion had the largest accuracy improvement over LIDAR when the smoke was the densest and in the upper slice. The sensor fusion provided more than 40% free space state accuracy in the upper slice in dense smoke when the LIDAR accuracy was 0%.

Data processed from the SAFFiR demonstration highlighted the need to handle significantly attenuated LIDAR returns separately than low-attenuation returns by a comparison of results with and without special treatment of the high-attenuation returns. The individual sensor results were similar to the hallway test results with the lower portion of the LIDAR data of the scene containing more occupied state information than the upper portion, due to the presence of smoke in the upper portion of the scene. The fusion system showed improved ranging results over the LIDAR in the upper slice and similar results to the LIDAR in the lower slice for both occupied and free space states. The hallway fire environment and SAFFiR shipboard environment tests collectively indicate the feasibility of applying the sensor fusion method in other fire scenarios.

4.6 References

- [1] Starr, J. W., & Lattimer, B. Y. (2014). Evaluation of navigation sensors in fire smoke environments. *Fire Technology*, 50(6), 1459-1481.
- [2] Starr, J. W., & Lattimer, B. Y. (2012, October). A comparison of IR stereo vision and LIDAR for use in fire environments. In *Sensors, 2012 IEEE* (pp. 1-4). IEEE.
- [3] Starr, J. W., & Lattimer, B. Y. (2013, July). Application of thermal infrared stereo vision in fire environments. In *Advanced Intelligent Mechatronics (AIM), 2013 IEEE/ASME International Conference on* (pp. 1675-1680). IEEE.
- [4] Randhawa, J. S., & Van der Laan, J. E. (1980). Lidar observations during dusty infrared Test-1. *Applied optics*, 19(14), 2291-2297.
- [5] Yamauchi, B. (2010, May). All-weather perception for man-portable robots using ultra-wideband radar. In *Robotics and Automation (ICRA), 2010 IEEE International Conference on* (pp. 3610-3615). IEEE.
- [6] Yamauchi, B. (2008, April). All-weather perception for small autonomous UGVs. In *SPIE Defense and Security Symposium* (pp. 696203-696203). International Society for Optics and Photonics.
- [7] Sales, J., Marín, R., Cervera, E., Rodríguez, S., & Pérez, J. (2010). Multi-sensor person following in low-visibility scenarios. *Sensors*, 10(12), 10953-10966.
- [8] Santos, J. M., Couceiro, M. S., Portugal, D., & Rocha, R. P. (2015). A sensor fusion layer to cope with reduced visibility in SLAM. *Journal of Intelligent & Robotic Systems*, 1-22.
- [9] Kim, J. H., Starr, J. W., & Lattimer, B. Y. (2014). Firefighting Robot Stereo Infrared Vision and Radar Sensor Fusion for Imaging through Smoke. *Fire Technology*, 1-23.
- [10] Yamauchi, B. (2010, April). Fusing ultra-wideband radar and lidar for small UGV navigation in all-weather conditions. In *SPIE Defense, Security, and Sensing* (pp. 769200-769200). International Society for Optics and Photonics.
- [11] Khaleghi, B., Khamis, A., Karray, F. O., & Razavi, S. N. (2013). Multisensor data fusion: A review of the state-of-the-art. *Information Fusion*, 14(1), 28-44.
- [12] Dornfeld, D. A., & DeVries, M. F. (1990). Neural network sensor fusion for tool condition monitoring. *CIRP Annals-Manufacturing Technology*, 39(1), 101-105.
- [13] Ross, A., & Jain, A. (2003). Information fusion in biometrics. *Pattern recognition letters*, 24(13), 2115-2125.

- [14] Pagac, D., Nebot, E. M., & Durrant-Whyte, H. (1998). An evidential approach to map-building for autonomous vehicles. *Robotics and Automation, IEEE Transactions on*, 14(4), 623-629.
- [15] Tirumalai, A. P., Schunck, B. G., & Jain, R. C. (1995). Evidential reasoning for building environment maps. *Systems, Man and Cybernetics, IEEE Transactions on*, 25(1), 10-20.
- [16] Shafer, G. (1976). *A mathematical theory of evidence* (Vol. 1). Princeton: Princeton university press.
- [17] Moravec, H. P. (1988). Sensor fusion in certainty grids for mobile robots. *AI magazine*, 9(2), 61.
- [18] Rainieri, S., & Pagliarini, G. (2002). Data filtering applied to infrared thermographic measurements intended for the estimation of local heat transfer coefficient. *Experimental thermal and fluid science*, 26(2), 109-114.
- [19] Nixon, M. S., & Aguado, A. S. (2012). *Feature extraction & image processing for computer vision*. Academic Press.
- [20] Adarve, J. D., Perrollaz, M., Makris, A., & Laugier, C. (2012, May). Computing occupancy grids from multiple sensors using linear opinion pools. In *Robotics and Automation (ICRA), 2012 IEEE International Conference on* (pp. 4074-4079). IEEE.
- [21] Homm, F., Kaempchen, N., Ota, J., & Burschka, D. (2010, June). Efficient occupancy grid computation on the GPU with lidar and radar for road boundary detection. In *Intelligent Vehicles Symposium (IV), 2010 IEEE* (pp. 1006-1013). IEEE.
- [22] Murray, D., & Little, J. J. (2000). Using real-time stereo vision for mobile robot navigation. *Autonomous Robots*, 8(2), 161-171.
- [23] Robot Operating System documentation page. <http://wiki.ros.org/>. Accessed September 2015.

5 Conclusion and Recommendations

5.1 Conclusion

The research presented in this document addressed the problem of rangefinding in fire smoke environments. The case for using LWIR stereo vision to address this problem was made through an analysis of the literature and through small-scale sensor perception tests. An initial LWIR stereo vision system was built and tested in a large-scale test environment for comparison against radar, LIDAR, and visual stereo vision. The results showed that LWIR stereo vision can rangefind through low visibility smoke. LWIR stereo vision was further developed for rangefinding in fire environments with quantitative selection of intensity alignment and stereo image filtering subsystems. The resulting system was combined with a spinning LIDAR using evidential fusion in a 3D multi-resolution voxel space for improved perception in varying conditions from clear scenes filled with dense smoke. The final sensor fusion system was tested in a hallway fire environment and with sensor data from a shipboard fire environment from the November 2014 SAFFiR demonstration aboard the Ex-USS Shadwell.

Chapter 2 presented initial small-scale smoke perception tests on eleven different sensors and large-scale smoke perception tests on select rangefinding sensors, including LWIR stereo vision. The results from the small-scale sensor visibility tests indicated that LWIR cameras and radar had little attenuation due to dense, low temperature smoke even when the visibility at 632.8 nm dropped below 1 m. LIDAR, visual cameras, the KinectTM depth sensor, and night vision were shown to have significant attenuation and fail at or before reaching 1 m visibility. For light, high temperature smoke, the KinectTM depth sensor and the night vision sensor were flooded with radiation from the fire, making both sensors unusable. The other electromagnetic sensors had no significant attenuation in the light, high temperature smoke. Sonar had attenuation in both cases due in large part to the smoke temperature. The large-scale tests showed that radar and LWIR stereo vision outperformed LIDAR and visual stereo vision in dense, low temperature tests in a hallway setup where the visibility was reduced to below 1 m.

Chapter 3 detailed the development and selection of the system architecture for LWIR stereo vision for rangefinding in fire environments. The development focused on rangefinding in both approximately isothermal scenes and thermally diverse scenes. Tests data showed the need for

an intensity alignment step for the LWIR cameras used in the setup. It was shown that an offset method based on the mean intensity of each image could be used if the scene at hand was approximately isothermal but that a linear fitting intensity alignment method worked better if the scene was thermally diverse. Stereo matching tests indicated that the consecutive Wiener filter was a top filter choice for approximately isothermal and thermally diverse scenes when performing object location or boundary location. This filter was shown to have little feature distortion, as measured by a test using a Hough transform for circles algorithm to assess feature distortion.

In Chapter 4, a sensor fusion method was developed to combine range data from LWIR stereo vision and a spinning LIDAR for improved perception in varying levels of conditions from clear to scenes partially or fully filled with dense smoke. This fusion was performed in a 3D multi-resolution voxel space, using evidential theory to model occupied and free space states. Prior to sensor fusion, LIDAR low-attenuation and high-attenuation returns were separated based off of return distance and intensity information to be handled separately. Sensor models were developed for both types of LIDAR returns, using the low-attenuation returns to provide occupied and free space state information and the high-attenuation returns to only provide free space state information since high-attenuation returns may range to smoke or to solid boundaries. A sensor model was also developed for LWIR stereo vision, providing evidence information based off of the disparity value, the stereo correspondence matching cost, and the number of points affecting each voxel.

The evidential sensor fusion system was evaluated against baseline data for a range of clear to smoke-filled conditions in a hallway environment. The system was also assessed in a shipboard fire scenario from data taken during the SAFFiR November 2014 demonstration. Results from experiments with a hallway fire environment indicated that the LIDAR separation between low-attenuation and high-attenuation points resulted in less than 0.4% of the low-attenuation point cloud returns being smoke returns. Fusion results in the hallway environment showed that in some individual smoke scenes and over the combined full range of conditions from clear to thick smoke, the evidential fusion method provided better occupied and free space state results than either sensor alone. For the occupied state for clear conditions, LIDAR was more accurate

compared to the baseline than the sensor fusion. However, for the occupied state in dense smoke, sensor fusion provided higher accuracies compared to baseline than the LIDAR, with the LIDAR failing to provide any occupied state information for some scenes. For the occupied state as the smoke was thinning, the sensor fusion provided higher accuracies than the LIDAR overall and in the upper slice, but the LIDAR provided higher accuracies for the lower slice, below the smoke layer. For cases where the LIDAR outperformed the sensor fusion at occupied state accuracy, the sensor fusion was typically within 5% or 10% of the LIDAR.

For the free space state, sensor fusion provided similar accuracies to LIDAR for clear conditions but had higher free space state accuracies compared to the baseline in dense and thinning smoke. Sensor fusion had the largest accuracy improvement over LIDAR when the smoke was the densest and in the upper slice. The sensor fusion provided more than 40% free space state accuracy in the upper slice in dense smoke when the LIDAR accuracy was 0%.

Data processed from the SAFFiR demonstration highlighted the need to handle significantly attenuated LIDAR returns separately than low-attenuation returns by a comparison of results with and without special treatment of the high-attenuation returns. The individual sensor results were similar to the hallway test results with the lower portion of the LIDAR data of the scene containing more occupied state information than the upper portion, due to the presence of smoke in the upper portion of the scene. The fusion system showed improved ranging results over the LIDAR in the upper slice and similar results to the LIDAR in the lower slice for both occupied and free space states. The hallway fire environment and SAFFiR shipboard environment tests collectively indicate the feasibility of applying the sensor fusion method in other fire scenarios.

5.2 Recommendations

The recommendations for future work include further improving the LWIR stereo vision system architecture. The system architecture itself should be updated to detect if a scene being viewed is approximately isothermal or thermally diverse to switch filter settings on the consecutive Wiener filter automatically when the scene changes instead of using one group of settings for all scenes. In addition, the LWIR stereo vision rangefinding may be improved by running a series

of experiments to quantitatively select a matching algorithm based on both matching quality compared to ground truth data and processing time.

The sensor fusion method should be upgraded to run in real-time. Future work should be performed to extend the sensor fusion from running on individual stationary scenes to running throughout time with robot motion, properly handling motion effects on the sensors and using the fused information to build up maps as the robot moves. Another recommendation for future work includes extending the current sensor fusion method to be able to handle other rangefinders, perhaps with the development of sensor models for visual stereo vision, sonar or radar. As with the spinning LIDAR implementation presented in this document, these sensor models should properly handle range data in both clear and smoke conditions.

Appendix A: Smoke Characterization

A.1 Introduction

The majority of sensors used on robotic platforms operate using electromagnetic waves. As a result, it is important to understand the effects fire smoke has on electromagnetic waves at a wide range of wavelengths for determining sensor performance. To identify the key characteristics of smoke that affect electromagnetic waves, the equations governing the effects of obscurants on electromagnetic waves were studied with specific focus on smoke. An experimental approach was developed to quantify the properties of a smoke from different types of fires used in evaluation of sensors in this research. In these experiments, measurements were made to quantify smoke particulate temperatures, extinction effects, concentration levels, particulate composition, agglomerated shapes, and particulate sizes. With this detailed characterization, the laser extinction data and concentration data were verified for consistency using mass specific extinction coefficient values from the literature. The expected effects of the smoke from different fires on performance of sensors operating at different wavelengths were investigated.

A.2 Optical Properties of Smoke

A.2.1 General Energy Transfer through a Volume

This section outlines the equations governing the effects of obscurants on electromagnetic waves with a specific focus on smoke. While the details of the effects are outlined in this section, the largest concern overall is on the extinction of the electromagnetic waves by the smoke particulate (more than effects from in-scattering and from the emission from the smoke). In general, these issues arise when the particulate is at high concentrations and when the particle diameter is around the same length or longer than the wavelength of interest (see extinction efficiency plots for spherical particles in [1]). With smoke particulate generally in agglomerates ranging in size of tens of nanometers to more than a micron in size [3, 6], this means that visible wavelengths (~0.4 to 0.7 microns) and near infrared wavelengths (~0.7 to 0.9 microns) will not penetrate through the obscurant as well as long wavelengths. These effects and other obscurant effects on electromagnetic waves are discussed in more detail in the following subsections.

A.2.2 General Energy Transfer through a Volume

The diagram in Figure 80 shows a control volume with energy transfer through it. The volume can consist of combinations of solids, liquid aerosols, and gases, referred to collectively as the medium. The amount of energy traveling along a path passing through the control volume is reduced due to absorption and out-scattering and increased due to emission and in-scattering [1]. The emission, scattering, and absorption depend on wavelength [1], so different wavelength radiation will respond differently for the same volume. An overview on the emission, absorption, and scattering effects on the energy entering and leaving the medium is given below.

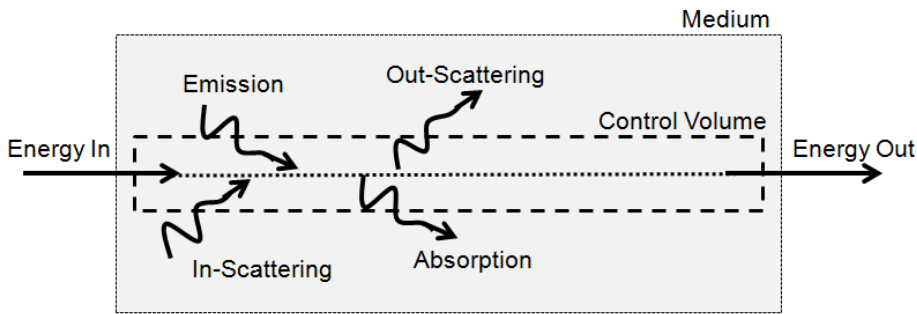


Figure 80: Radiation through a control volume around a medium.

The emission of the medium is proportional to blackbody radiation for its temperature [1] shown in the plot in Figure 81 for a blackbody emitting in air at different temperatures, assuming the control volume in Figure 80 is at equilibrium and with uniform properties (temperature, pressure, concentration levels). The emission is proportional to the upper limit of blackbody radiation via the emission coefficient of the emitting medium which varies with wavelength. This emission coefficient and the absorption coefficient of the medium are assumed equal [1]. The relationship between emission, temperature, and the absorption coefficient are shown in Equation (24) [1].

$$E = \kappa_{\lambda} * I_{\lambda,b} = \kappa_{\lambda} * \frac{2C_1}{n^2 \lambda^5 \left(\exp\left(\frac{C_2}{n\lambda T}\right) - 1 \right)} \quad (24)$$

In the equation, the blackbody radiation is $I_{\lambda,b}$ and the absorption coefficient is κ_{λ} . C_1 and C_2 are constants. The index of refraction, wavelength, and temperature are n , λ , and T , respectively. While the amount of energy emitted from the medium depends on the properties of the medium, the amount of energy absorbed by the medium depends on the energy entering into the medium,

absorbing more energy with more energy input [1]. This emission term and the absorption term can vary smoothly with wavelength for particulate matter such as soot [2] but also results in spectral lines and bands important in determining gas radiation emission and absorption at various wavelengths [1, 2].

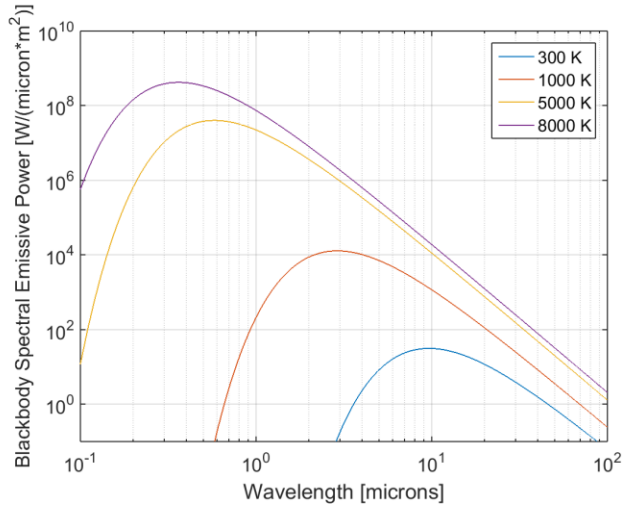


Figure 81: Blackbody spectral emissive power from Planck’s Law for a blackbody emitting in air for four temperatures.

For particles, the out-scattering and absorption follow the Lambert-Bouguer Law shown in Equation (25), simplified for a uniform medium [1].

$$I_{\lambda} = I = I_0 * \exp(-\beta * L_p) \quad (25)$$

The path length through the medium is L_p . The intensity entering and exiting the medium along the path are I_0 and I , respectively, at the wavelength of interest λ . The extinction coefficient β contains the absorption and scattering coefficients, κ_{λ} and σ_{λ} , as in Equation (26) [1].

$$\beta = \kappa_{\lambda} + \sigma_{\lambda} \quad (26)$$

Applying the emission, absorption, and scattering effects specifically to smoke is discussed in the next section.

A.2.3 Energy Transfer through Smoke

Smoke consists of varying levels of solids, liquids, and gases [3-6] at a variety of conditions. Gases typically include water vapor and carbon dioxide, in addition to other gases depending on

combustion conditions and fuel source [5]. Solids and liquids depend on combustion conditions and can include droplets and soot [4]. Flaming combustion typically results in a high level of soot, while smoldering combustion results in more liquid aerosol production [4]. The effects of these smoke components are discussed in this section, noting important trends relating smoke properties to radiation effects.

A.2.3.1 Gases

Water vapor and carbon dioxide are common gas products of combustion [5]. Other gases that are typical products of combustion, such as carbon monoxide, sulfur oxides, and nitrous oxides may also be present [5]. For these and other gases present during combustion, the spectral emission and absorption is typically modeled using spectral bands and lines, which indicate wavelength locations where absorption and emission are significant [1]. For example, water has bands of various width and shape located around 1.38, 1.87, 2.7, and 6.3 microns [1], and carbon dioxide has bands at 2.0, 2.7, 4.3, 9.4, 10.4, and 15 microns [1].

The emission increases with increasing temperature based off of Planck's Distribution and gas emissivity [1]. The strength of the absorption and emission in these bands increases with increasing concentration [1]. In addition to these magnitude changes, the shape of these spectral bands varies with pressure and temperature [1]. At high temperatures, an increase in temperature widens the bands due to Doppler line broadening [1]. Thus, the effects of gases on radiation transfer are more significant for fires resulting in more smoke gas production or in hotter smoke production than otherwise. In addition, the radiation emission effects of gases in smoke will have less effect further from the fire where the smoke temperatures are lower and where the concentration may also be lower.

A.2.3.2 Liquids and Solids

Amounts of liquids and solids in smoke vary significantly [4]. Flaming combustion typically results in a high level of soot, while smoldering combustion results in liquid aerosol production [4]. While the aerosol droplets can be spherical in shape, the soot particles typically consist of small hydrocarbon spherical particles on the order 10-100 nm which collect into agglomerates as

the particles move away from the smoke source [3, 7]. These agglomerates can grow in excess of 1 micron [3, 6].

Emission for smoke aerosols follows the blackbody radiation curve (Planck's Distribution), reduced by emissivity [1]. For soot, this emissivity has been shown to decrease with increasing wavelength and with decreasing concentration [2]. For emission effects, concentration and temperature are significant; an increase in either temperature or concentration causes an increase in emission [1, 8].

The Maxwell Equations can be used to model the particle extinction effects on radiation, but these are typically difficult to solve without making some significant assumptions [1]. Simplifying information about the particles has resulted in several methods of determining particle effects on scattering [1], some of which are shown in the Venn diagram in Figure 82. These methods include both analytical and numerical solutions [1].

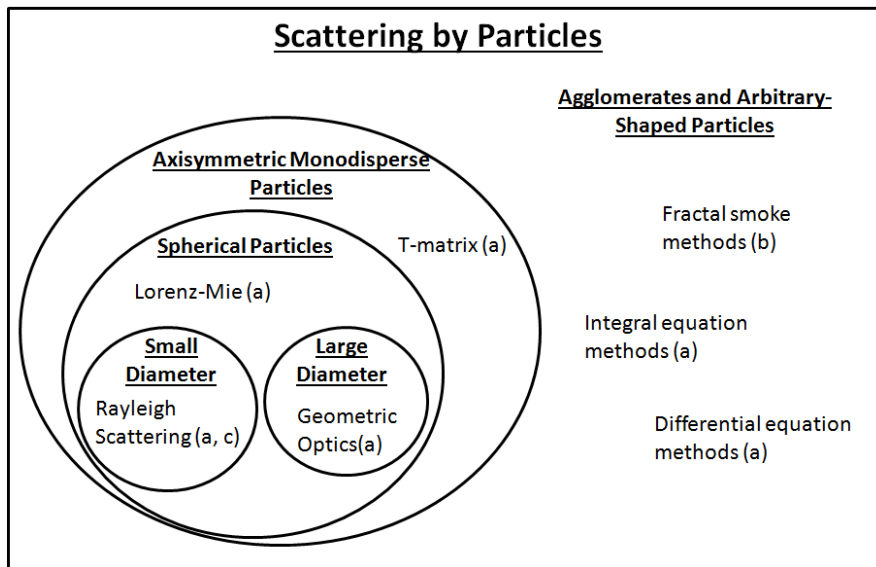


Figure 82: Venn diagram showing some methods of determining scattering effects of particles on radiation. Sources in the diagram are (a) [1], (b) [9, 10], and (c) [11].

Assuming independent and inelastic scattering and that the particles are axisymmetric and of one shape and size allows for solutions with a T-matrix approach [1]. Making a further assumption

that the particles are spheres in shape and of one size (monodisperse) allows for the extinction coefficient shown in Equation (25) to be further broken down as in Equation (27) [1].

$$I_{\lambda} = I_0 * \exp\left(\left(Q_{\lambda,a} + Q_{\lambda,s}\right) * \left(\frac{\pi D_p^2}{4}\right) * N * L_p\right) \quad (27)$$

The extinction effects depend on the absorption and scattering efficiency factors, $Q_{\lambda,a}$ and $Q_{\lambda,s}$, on the particle diameter D_p , on the path length through the medium L_p , and on the number concentration (particles per volume) N . Determining the extinction efficiency factors can be complex but can be done with Lorenz-Mie Theory [1]. In some cases, geometric optics or Rayleigh scattering approximations can be used to reduce computational load, for particle diameters that are large or small compared to wavelength, respectively [1]. Rayleigh scattering has been cited to show the ability of mm-wave radar to perceive through smoke [11]. These simplified scattering models may work well for agglomerates significantly smaller than the wavelength of interest as in [11] or for scattering predictions of smoke droplets that are approximately spherical in shape. However, the case has been made that more complex methods such as one using fractal models is necessary for more accurate results for smoke agglomerates [9, 10].

Alternatively, measuring the extinction coefficient directly at different wavelengths is another way to find the combined effects of absorption and scattering for a smoke scenario. Equation (25) is sometimes reformulated in terms of the mass specific extinction coefficient, σ_s , as in Equation (28) for smoke [12].

$$I_{\lambda} = I_0 * \exp(-\sigma_s * M_s * L_p) \quad (28)$$

The mass specific extinction coefficient relates to the extinction coefficient by

$$\sigma_s = \frac{\beta}{M_s} \quad (29)$$

In this form, the output intensity at a wavelength is related to the mass concentration M_s , the path length through the smoke L_p , and a constant value for the mass specific extinction coefficient for the smoke. This form of the equation is used for determining the mass concentration based on the intensity loss of a laser system and assumes that the smoke is made up of carbon agglomerates with small primary particles compared to the light wavelength and that the agglomerates have a low fractal dimension [12]. Typical values for the mass specific extinction

coefficient for a laser system at 632.8 nm range from about 7.8 to 10.2 m²/g in the literature, with some values lower [12, 13, 14].

The extinction measurements in the literature at different wavelengths show different extinction coefficients for different smoke scenarios [12, 15] but similar trends are present with wavelength. For the visible through thermal infrared range, increasing the wavelength has been shown to result in less extinction effects [10, 13, 15]. In effect, increasing wavelength increases visibility.

A.2.3.3 Summary of Important Smoke Quantities

Overall, absorption and emission effects of gases are most prominent at high temperatures and high concentrations. Emission effects of particulates are also most prominent at high temperatures and high concentrations. Smoke particulate radiation effects are difficult to model, but for a given smoke scenario, extinction effects are strongest at lower wavelengths and at higher concentrations.

A smoke scenario with a relatively high level of gas products can be significantly different than a smoke scenario with relatively a high level of soot products. Emission and absorption effects from the gases will diminish as the gases cool. Extinction effects from particulate can still be strong even at cooler temperatures. Based on this, lower-wavelength sensors are expected to perform worse than higher-wavelength sensors at perception through dense high-soot smoke, even with the smoke at low temperature. For soot particulate, emission effects from the particulate on sensors are expected to be worse for lower-wavelength sensors, with the strongest emission effects closer to the fire. Sensors operating at gas band wavelengths will perform worse when the affecting smoke gases are at highest concentrations and highest temperatures due to absorption and emission effects being strongest under these conditions.

A.3 Experimental Approach

The background on smoke properties highlighted the significant effects of smoke temperature and composition on sensor performance. To further analyze smoke, tests were performed to quantify characteristics for a range of smoke that is expected to evaluate sensor performance.

Latex foam, propane, and wood fires were used to generate smoke with varying levels of particulate concentration and gas temperature. Laser extinction, temperature, concentration, particle size, particle composition, and particle shape were analyzed for smoke produced by the three different fires. Each type of fire was run multiple times for data collection.

A.3.1 Test Setup

Figure 83 contains a diagram of the large-scale hallway setup used for smoke characterization tests. The hallway contained a closet half way down the hallway and a room at the end. Fires were located at the end of the hallway or in the room, and smoke travels out the open end of the hallway beneath an exhaust system. The entrance of the hallway contains a blockage 0.7 m down from the ceiling to produce a smoke layer in the hallway. The hallway was instrumented with a laser extinction system and eight thermocouples as discussed in a subsequent subsection.

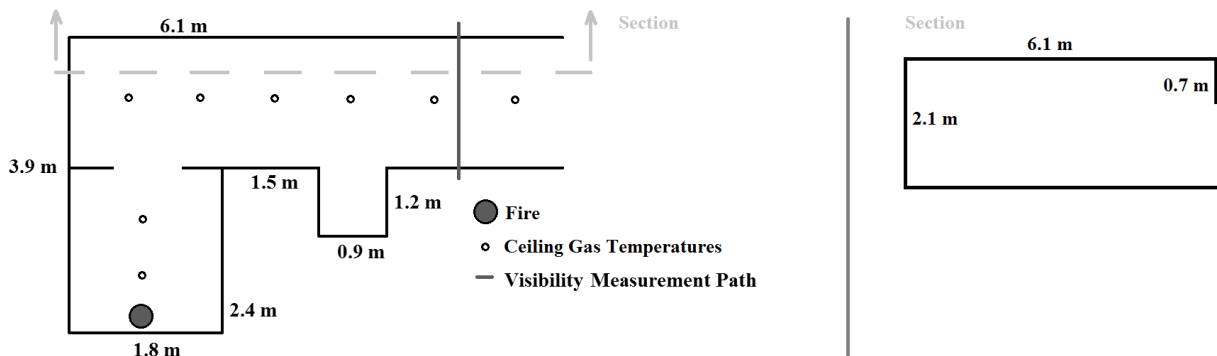


Figure 83: Hallway setup for smoke characterization tests.

A.3.2 Fuel Types

Latex foam, propane, and wood fires were used to generate smoke with varying levels of soot particulate concentration and gas temperature. Latex foam was selected due to it producing a relatively high level of soot. For the testing, a block of approximately 200 mm x 200 mm x 150 mm was used. Propane fuel was used to produce smoke with a relatively low level of soot but higher gas temperatures. The propane fire was controlled at 35 kW to an accuracy of +/-1 SLPM using an Alicat mass flow controller, MRC-250SLPM. Wood smoke was chosen as a fuel that would have a soot production between the latex foam and propane. Wood crib fires were formed using 25 mm x 25 mm x 305 mm sticks stacked six layers high with each layer having four

sticks. The wood cribs were lit using a pool of acetone approximately 0.15 L in volume. The fires were run multiple times for the measurement of smoke properties.

A.3.3 Instrumentation

The hallway setup was instrumented with eight Type K thermocouples located at 0.9 m intervals along the ceiling, approximately 12 mm below the ceiling to measure smoke temperatures along the ceiling as shown in Figure 83. The hallway was also instrumented with a horizontal laser extinction system, shown in Figure 83, 1.1 m in from the hallway entrance, 1.5 m off the ground, for light extinction measurements. Particle analyzers were placed in the hallway near the entrance for determining aerosol and soot particle size and concentration information. Gravimetric sampling was performed to obtain aerosol and soot concentration information. Particulate gathered from the gravimetric setup and from static locations in the hallway were analyzed using electron microscopy for obtaining information about particulate make-up and shape.

A.3.3.1 Laser Extinction System

The extinction coefficient and visibility at both locations were measured using a red HeNe (wavelength of 632.8 nm) laser aimed at a silicon photodiode. This system is similar to ones presented in standards for fire testing [16]. Assuming no in-scattering and no emission along the path, the average extinction coefficient for the path at 632.8 nm is calculated using Equation (30) [17], which is a different form of Equation (25).

$$\beta = -\frac{1}{L_p} \ln \frac{I}{I_0} \quad (30)$$

Optical thickness τ_λ can be evaluated using Equation (31), where the medium is optically thin if the value is significantly less than 1 or optically thick if the value is significantly greater than 1 [1].

$$\tau_\lambda = \beta * L_p \quad (31)$$

The extinction coefficient can further be converted to a visibility measurement using Equation (32), which is Jin's equation relating the extinction coefficient of an obscurant to the furthest distance a human can read a place-card sign in the obscurant [4].

$$V = \frac{C}{\beta} \quad (32)$$

Visibility depends on the empirical constant C that is between 2 and 4 [4], evaluated here at 3. For the tests here, optical thickness and visibility are evaluated. Also, the ratio of the laser intensity to the baseline intensity I/I_0 is evaluated to compare with expected intensity ratio values for recorded mass concentrations and an assumed smoke mass specific extinction coefficient.

A.3.3.2 Gravimetric Filtering

Smoke was sampled using a gravimetric filter-based system shown in Figure 6 in order to measure smoke concentration, particulate composition, particulate shape, and particulate size. The smoke was sampled 1.2 m inside the hallway and 1.6 m from the ground, at least 0.1 m above the smoke layer bottom.

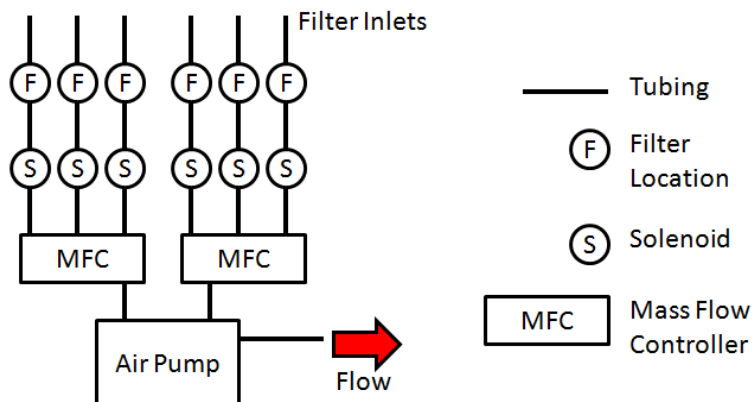


Figure 84: Filter-based system for obtaining smoke particulate concentration, particulate composition, particulate shape, and particulate size.

The sampling system contained three filters for each of the two sampling locations. Filters were 47 mm in diameter and filtering of 1 micron. To draw gas samples through the filters, a solenoid valve was activated for a certain period of time. Each filter in a pair is run through an Alicat mass flow controller (MFC), which controls and measures the flow through the filter. The filters captured both soot particulate as well as liquid aerosols.

For the filter sampling, unused 1-micron filters were dried and weighed. Next, the filters were installed, and smoke was drawn through the filters at a target flow rate of 1.0 lpm per filter for a measured amount of time per filter pair. The target flow times are shown in Table 10. The actual flow rates and times were measured. After being removed, the filters were weighed on a scale and stored in a container with Drierite desiccant to keep the samples from absorbing moisture. Two tests were performed for each fuel type, with one filter pair used per test. All filters were removed for each fuel type after both tests were completed for that fuel type. Once all the tests were completed, the samples were dried and reweighed. Filter drying causes liquid aerosols on the filters to evaporate, leaving only solids on the filters. This was accomplished by heating the filters to above 100°C for an hour. The change in weight of filters from drying after testing provides information about the amount of liquid aerosol the filters collected during tested. The measured flow rates, flow times, and filter weights were used to compute smoke concentrations. These concentration measurements include overall smoke concentrations, which include solid and liquid aerosols, and smoke particulate concentrations, which only include solids. In addition to determining concentration information, after drying, the samples were analyzed using electron microscopy as discussed later.

Table 10: Flow times for gravimetric sampling.

Fuel	Run Time, Filter Pair 1 [min]	Run Time, Filter Pair 2 [min]
Latex Foam	5	5
Propane	20	20
Wood	10	10

A.3.3.3 Electron Microscopy

Particulate samples were analyzed using Scanning Electron Microscopy (SEM) for determining particulate size and shape from imagery and for determining particulate composition. These samples were gathered using two methods. Some particulate samples were collected from the filters used in the gravimetric filtering process. Smoke particulate was also collected directly on metal sample-holders and on double-sided tape on metal sample holders designed for SEM instruments. This second method of particulate collection was done in order to capture individual agglomerates of the smoke since these agglomerates become combined when they are filtered out of the smoke using the gravimetric filtering system. These samples were put into the smoke layer for different amounts of time ranging from 1 second to 11 minutes.

SEM images were taken using an Environmental Scanning Electron Microscope (ESEM), the FEI Quanta 600 FEG. Images were also taken on a Field Emission Scanning Electron Microscope (FESEM), the LEO (Zeiss) 1550, to provide higher resolution images of the particulate. In addition to imaging the particulate, Energy Dispersive X-ray Spectroscopy (EDS) was used to check the composition of the particulate collected. This was done on the FEI Quanta 600 FEG. SEM imaging and EDS have been performed with smoke particulate in previous work in the literature for analysis on particulate make-up, shape, and size [3, 4, 10, 18].

A.3.3.4 Particle Analyzers (DRX, OPS)

Two particle analyzers were setup to determine particle size distribution and concentration for the smoke particulate. The particle analyzers used were a TSI DustTrak DRX and a TSI Model 3330 Optical Particle Sizer (OPS). These were located 1.2 m inside the hallway and 1.6 m from the ground, at least 0.1 m above the smoke layer bottom. Since particle shapes are not expected to be spherical due to agglomeration, the particle analyzer data output based on particle diameter will not correspond directly to the physical particle size of the soot particulate.

The TSI DustTrak DRX provides concentration information [mg/m^3] for particles up to 1 micron, 2.5 microns, 4 microns, 10 microns, and to the instrument maximum (15 microns), with all bins starting at the instrument minimum (0.1 microns). For this test, the instrument was set to record on one-second increments starting approximately 30 seconds before each fire was lit. The information from the beginning of the test provides baseline information about the particle distribution in the lab before a test begins.

The TSI Model 3330 Optical Particle Sizer (OPS) counts particles to provide binned concentration information [$(\# \text{ of particles})/\text{m}^3$] for 17 bins ranging, which range from starting at 0.3 microns to starting at 10 microns (the last bin ending at the instrument maximum). For this test, the instrument was set to record data every 10 seconds starting approximately 30 seconds before each fire was lit. As with the DustTrak DRX, the information from the beginning of the test provides baseline information about the particle distribution in the lab before a test begins.

A.4 Results

A.4.1 Temperature

The results from the gas temperature measurements near the ceiling are shown in Figures 85 - 87 . For the latex foam test, the peak temperature was approximately 107°C in the room with the fire. The propane test resulted in a peak temperature of 117°C, while the wood fire peaked at 254°C. The maximum gas temperature at the hallway entrance in the test using a wood crib was about 20°C higher than that measured for latex foam and propane.

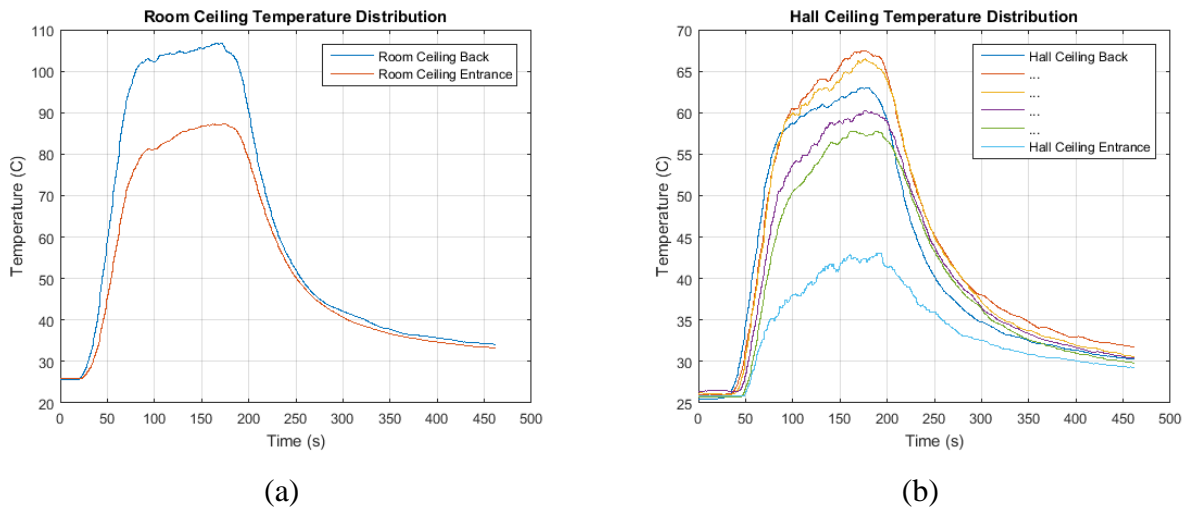


Figure 85: Latex fire smoke temperature measurements along the ceiling for (a) the room and (b) the hallway.

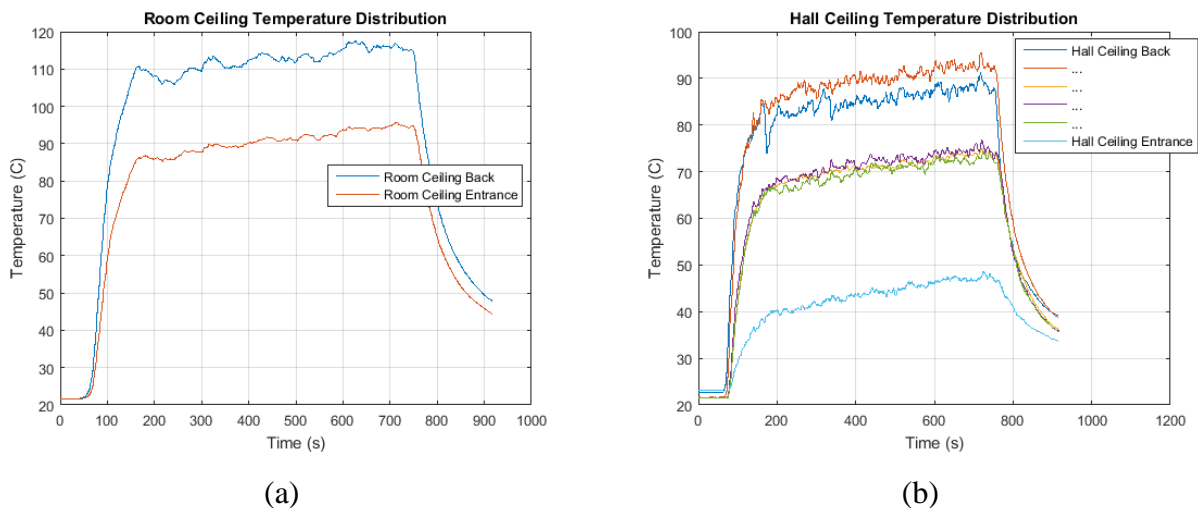


Figure 86: Propane fire smoke temperature measurements along the ceiling for (a) the room and (b) the hallway.

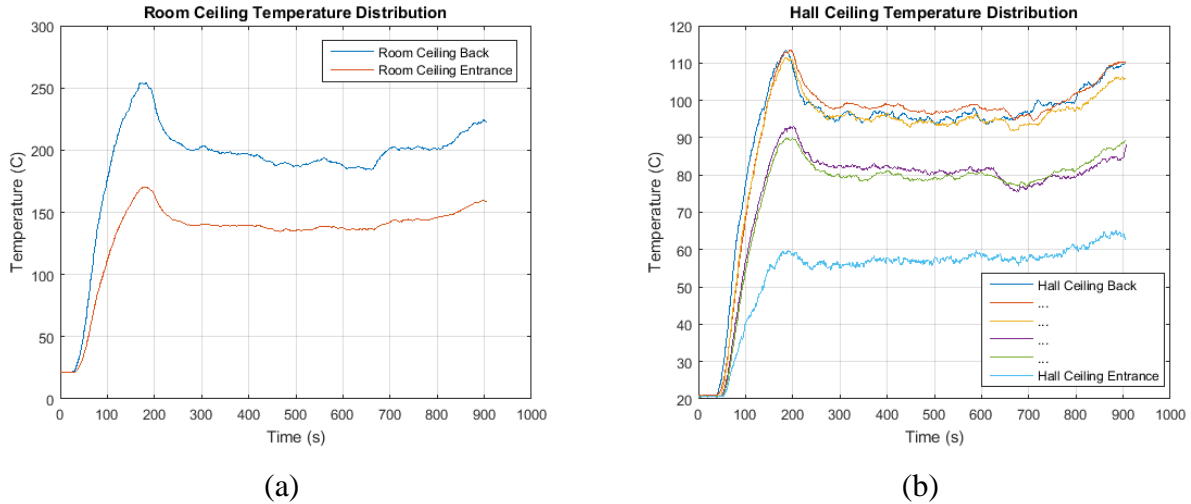


Figure 87: Wood fire smoke temperature measurements along the ceiling for (a) the room and (b) the hallway.

A.4.2 Laser Extinction Measurements

The data recorded from the laser system contains a high level of noise for all tests. The intensity ratio I/I_0 standard deviations were 0.0041, 0.0014, and 0.0020 for the latex foam, propane, and wood smoke tests' baselines, respectively. The plots in Figure 88 show filtered intensity ratio results for all three smoke types. For the latex foam smoke, as the smoke reaches the sensor, the laser quickly becomes blocked to the extent that the visibility falls below 1 m with the intensity ratio reaching approximately 0. At this point, the photodiode is effectively blocked and measurements are in the noise floor. During the testing, the optical thickness, defined in Equation (31), reaches well over a value of 1, indicating that the latex foam smoke is optically thick [1].

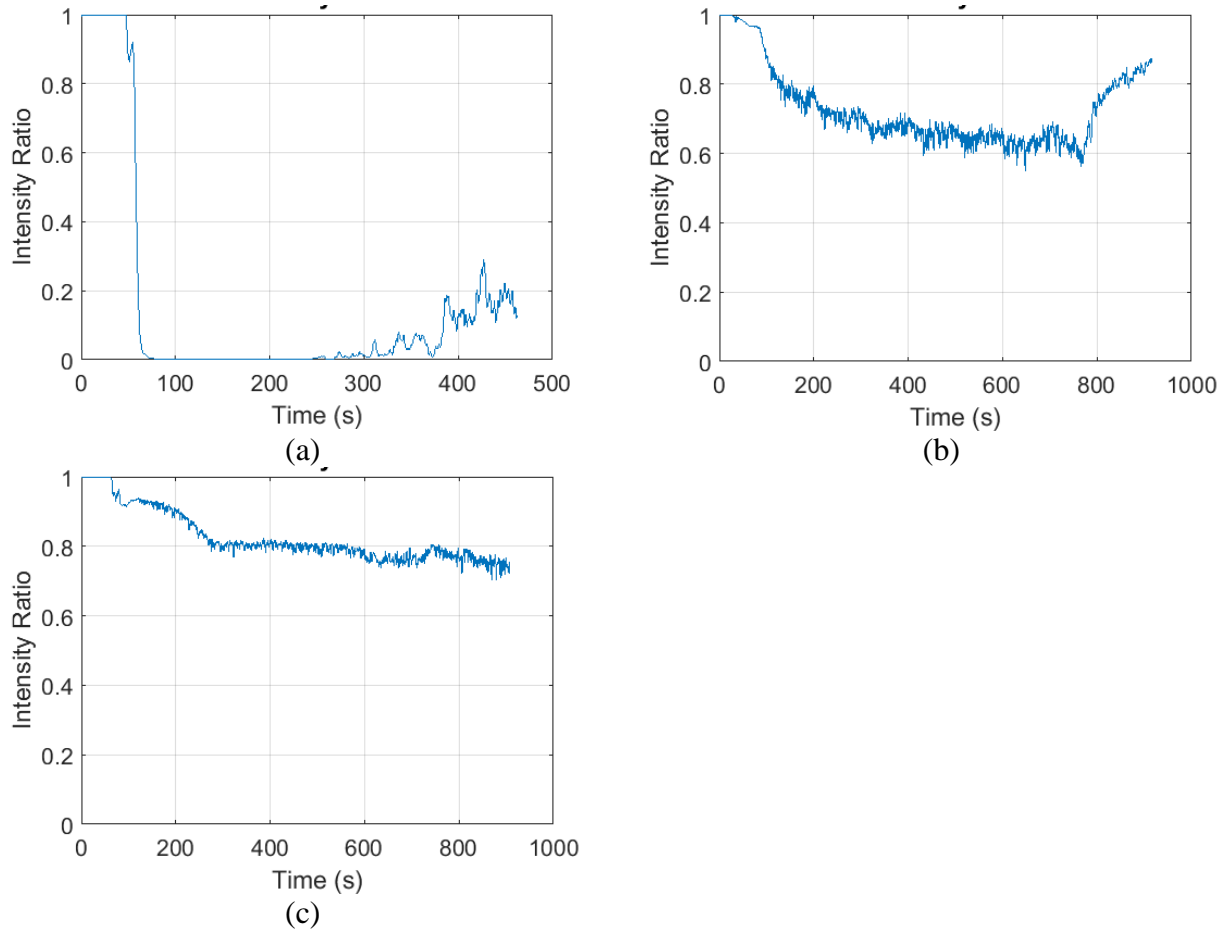


Figure 88: Intensity ratio data for (a) latex foam smoke, (b) propane smoke, and (c) wood smoke.

The propane and wood smoke measurements indicate that the visibility remained above 10 m for both smoke types, with two momentary decreases for the propane smoke. Both smokes have an optical thickness significantly less than 1, indicating that both smokes are optically thin [1]. The intensity ratio I/I_0 is shown in Table 11 for several points in time during testing for performing calculations with the recorded concentration data. The time in the table is from when the smoke first reaches the laser system.

Table 11: Propane and wood intensity ratios for different times during the tests.

Time after smoke arrival [s]	Propane	Wood
150	0.74	0.90
300	0.69	0.80
450	0.64	0.79
600	0.66	0.76
750	0.81	0.78

A.4.3 Gravimetric Filtering

A.4.3.1 Latex Foam Smoke

The mass and concentration measurements are shown in Table 12 for the latex foam tests. In the table, the smoke (combined soot and liquid aerosol) concentration is determined from the filter weight after testing and before drying. The soot concentration is determined from the filter weight after drying, and the liquid aerosol concentration is determined from the weight change of the filter from drying. The pairs of measurements are closer in value during the second test than the first test. The data shows that the average measured particulate concentration was $470 \text{ mg/m}^3 \pm 74 \text{ mg/m}^3$ (one standard deviation). The measurements are highly sensitive to the measured weight changes, which are on the order of 2 mg, so some noise in the data may be present due to weighing inaccuracy or filter damage during removal from the filter casing. The liquid removed from the filters showed a liquid concentration of about 10.6% the size of the solid concentration on average.

Table 12: Concentration measurement data from the gravimetric sampling for latex foam.

Filter Pair	Filter	Smoke Concentration [mg/m ³]	Soot Concentration [mg/m ³]	Liquid Aerosol Concentration [mg/m ³]
1	A1	640	560	80
1	B1	460	460	0
2	A2	480	380	100
2	B2	500	480	20

A.4.3.2 Propane Smoke

The mass and concentration measurements are shown in Table 13 for the propane tests. In the table, the smoke concentration is determined from the filter weight after testing and before drying. The soot concentration is determined from the filter weight after drying, and the liquid aerosol concentration is determined from the weight change of the filter from drying. The data shows that the average measured particulate concentration was $24 \text{ mg/m}^3 \pm 4.8 \text{ mg/m}^3$ (one standard deviation). The mass changes were on the order of 0.5 mg. These low mass changes for high flows indicate low concentrations. Gravimetric sampling is less accurate at measuring concentrations with low concentrations than with high concentrations due to the sensitivity of the method to mass change. Even though it is less accurate, it still provides useful information on

the order of magnitude of the concentrations. The mass removed from the filters by drying is small compared to the mass remaining on the filters after drying, indicating a larger concentration of solids than liquids collected from the smoke by the filtering process. The liquid removed from the filters showed a liquid concentration of about 15.8% the size of the solid concentration on average.

Table 13: Concentration measurement data from the gravimetric sampling for propane.

Filter Pair	Filter	Soot and Liquid Aerosol Concentration [mg/m ³]	Soot Concentration [mg/m ³]	Liquid Aerosol Concentration [mg/m ³]
1	A1	30	25	5
1	B1	25	20	5
2	A2	25	20	5
2	B2	30	30	0

A.4.3.3 Wood Smoke

The mass and concentration measurements are shown in Table 14 for the wood tests. In the table, the smoke concentration is determined from the filter weight after testing and before drying. The soot concentration is determined from the filter weight after drying, and the liquid aerosol concentration is determined from the weight change of the filter from drying. The data shows that the average measured particulate concentration was 15 mg/m³ with a standard deviation of about 21 mg/m³. One of the filters in the second test has a measured loss of mass instead of gain of mass, indicating an error in mass measurement or damage to the filter (A concentration cannot drop below 0 mg/m³). Even with double the target flow time of the latex foam test, the mass changes were on the order of 0.2 mg, about 10 times smaller than for the latex foam test. As with the propane data, these low mass changes for high flows indicate low concentrations. The mass removed from the filters by drying is on the order of the mass remaining on the filters after drying, indicating similar concentrations of liquids and solids collected from the smoke. The liquid removed from the filters showed a liquid concentration of about 117% the size of the solid concentration on average.

Table 14: Concentration measurement data from the gravimetric sampling for wood.

Filter Pair	Filter	Soot and Liquid Aerosol Concentration [mg/m ³]	Soot Concentration [mg/m ³]	Liquid Aerosol Concentration [mg/m ³]
1	A1	50	40	10
1	B1	40	20	20
2	A2	30	10	20
2	B2	10	0	20

A.4.4 Particulate Physical Characteristics

A.4.4.1 Particulate Composition

An example image output from the EDS analysis is shown in Figure 89 for a sample containing soot collected on a filter from the propane smoke. In the image in the figure, carbon from the smoke is shown in red and silicon from the filter in green. The spectrum output with carbon and silicon labeled is also shown. The EDS results confirmed that the soot from the latex foam, propane, and wood was mostly carbon-based. This indicates that there was little presence of dust collected using the gravimetric filtering system.

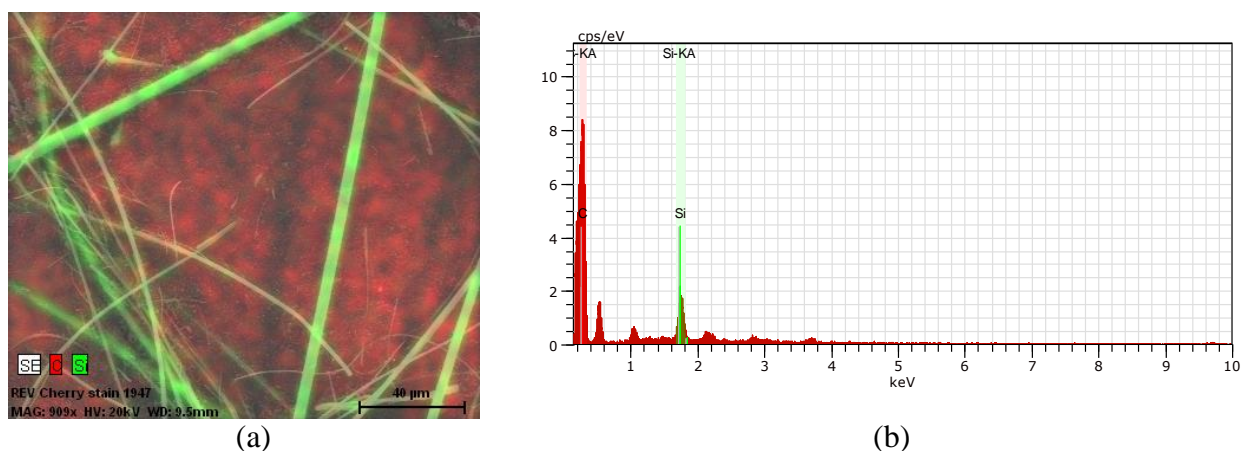


Figure 89: EDS analysis results: (a) image showing carbon from smoke (red) and silicon from filter strands (green) and (b) corresponding spectrum output plot for the image with carbon and silicon labeled.

A.4.4.2 Particulate Size and Shape

Figure 90 shows images of the smoke particulate collected on the filters from the FESEM for all three smoke types at two magnification levels. The particulate consists of many small spherical particles on the order of 10-50nm agglomerated together, with the propane soot particles noticeably smaller than the latex foam and wood smoke particles. This range of diameters for the small particles making up the agglomerates is similar to results found in the literature analyzing soot particulate from various fuel sources [3]. However, the individual agglomerates are not distinguishable in the images here since the filter collection method pulls agglomerates together. The agglomerates are better seen from the SEM images of the soot samples collected on the SEM sample holders.

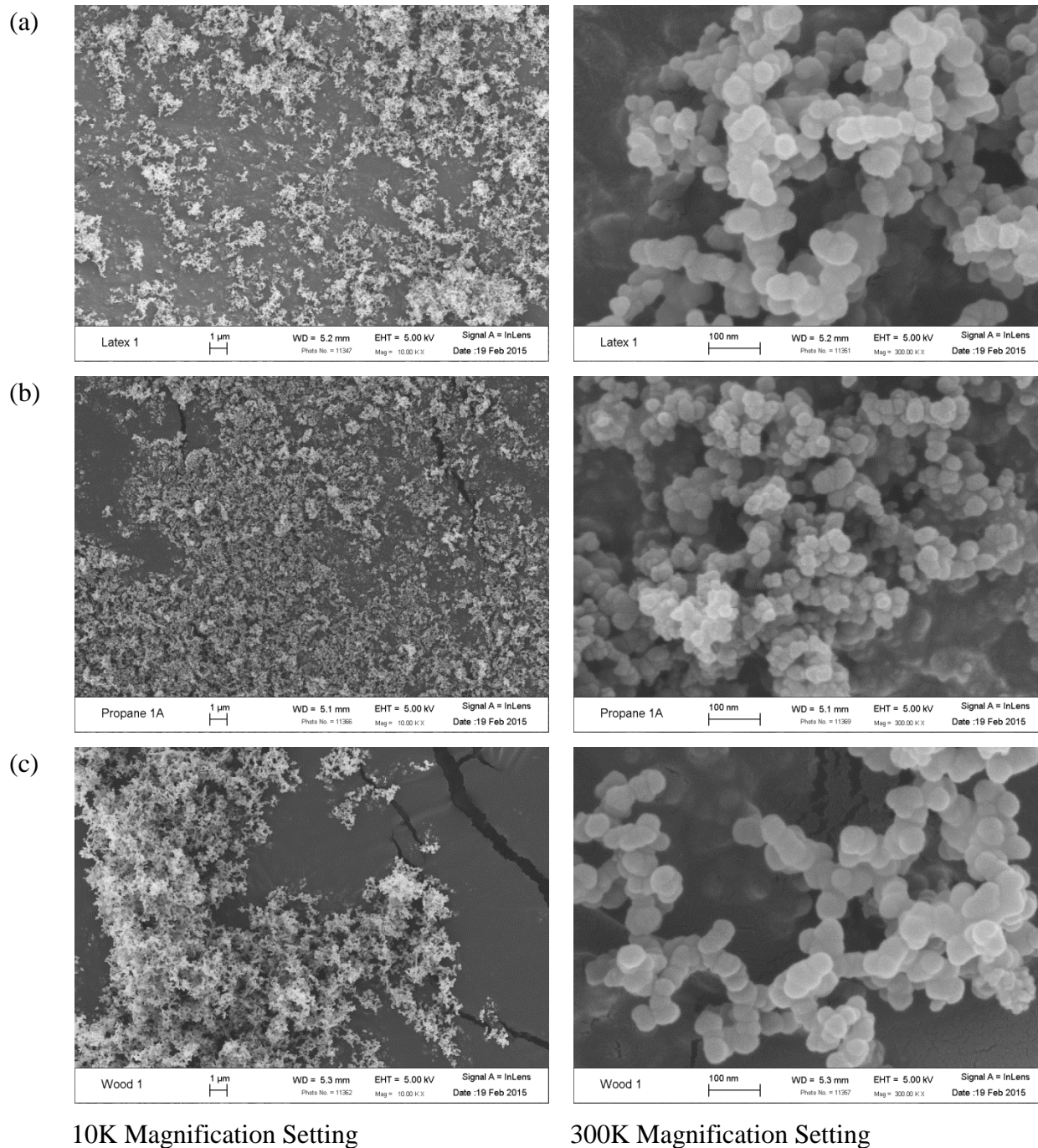
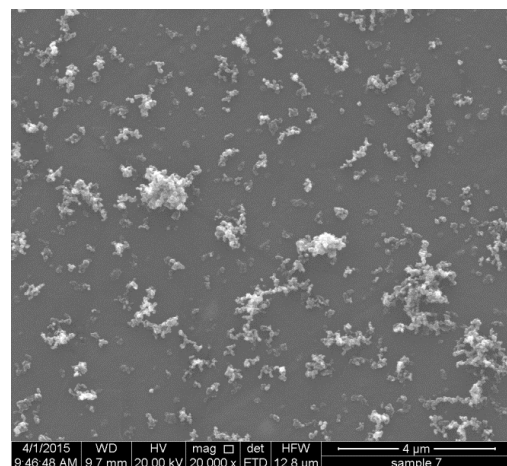
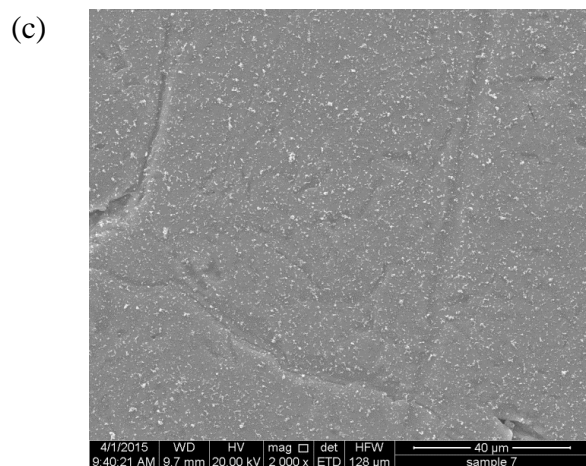
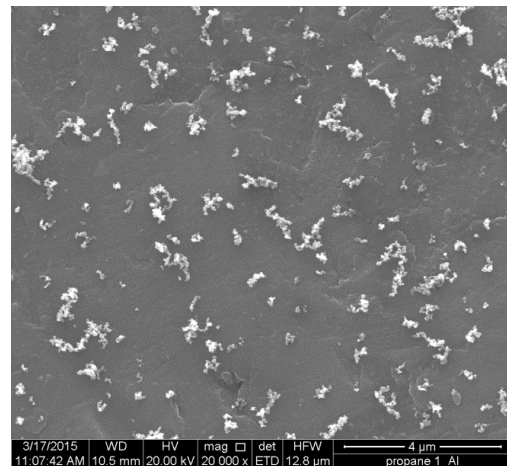
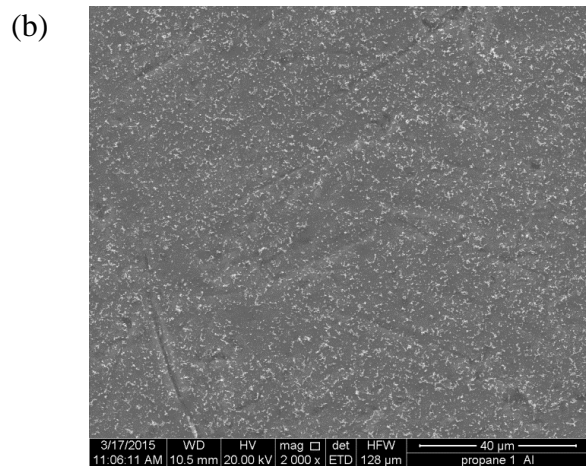
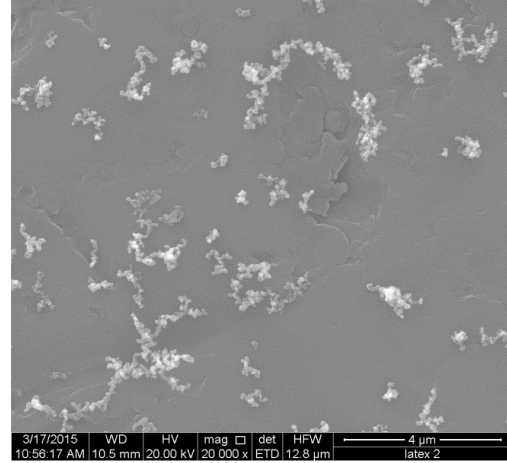
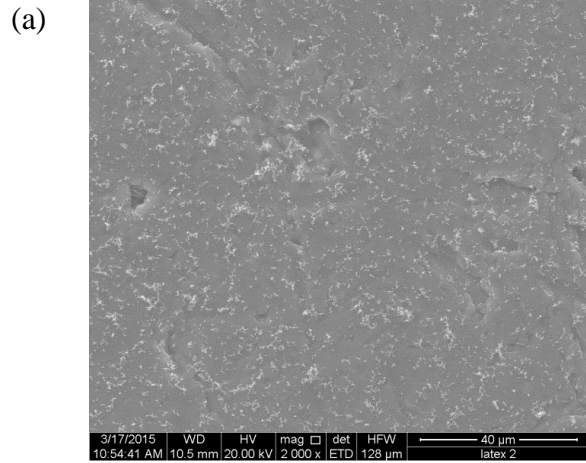


Figure 90: FESEM imaging results of filter for (a) latex foam smoke, (b) propane smoke, and (c) wood smoke at two magnification settings.

Figure 91 shows images from the ESEM of smoke particulate agglomerates collected on double-sided tape or metal of the ESEM sample-holders for all three smoke tests at two magnification levels. These smoke particulate agglomerates are on the order of 0.5-100+ microns and vary in

shape. For the samples imaged, the latex foam produced the largest agglomerates overall. For all smoke types, there are more of the smaller agglomerates than the larger ones. The size range of the agglomerates here is consistent with results found in the literature indicating many of these agglomerates grow to 1 micron and larger [3, 6]. The agglomerates are similar in appearance to electron microscopy images of soot agglomerates in the literature [3, 4, 10, 18].



2k Magnification Setting

20k Magnification Setting

Figure 91: ESEM imaging results for agglomerate collection for (a) latex foam smoke, (b) propane smoke, and (c) wood smoke at a two magnification settings.

A.4.5 Particle Size Distribution

A.4.5.1 Latex Foam Smoke

The plots in Figures 92 and 93 show the results for the latex foam test for the DustTrak DRX. The plot in Figure 92 shows the results for all bins (all starting at the instrument minimum), and the plot in Figure 93 shows the first bin and concentrations between bins. Each number following “PM” indicates a particle size in microns. In the plots, the smoke reaches the instrument around 55 seconds after the instrument was started. At this point, the smoke concentrations increase until the instrument maximum limit of 150 mg/m^3 is reached for all bins, one time step past what is shown in the figures. An analysis of the results before the instrument stopped providing useful information shows a large increase in all particle sizes, with the largest increase in the number of smaller particles.

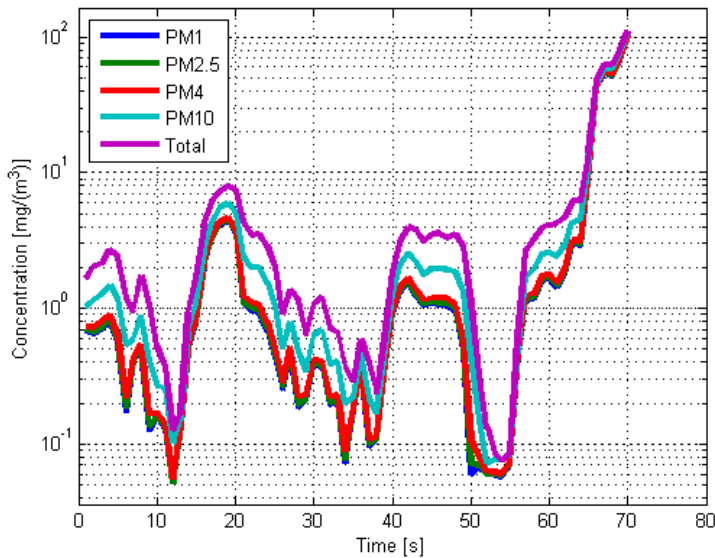


Figure 92: TSI DustTrak DRX results for the latex foam test showing concentrations for all bins.

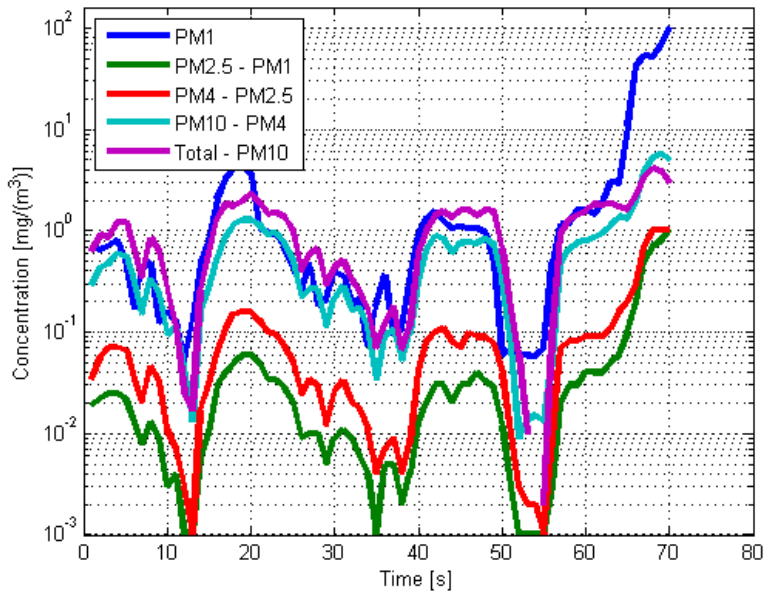


Figure 93: TSI DustTrak DRX results for the latex foam test showing the first bin and concentrations between bins.

The results from the OPS for the latex foam smoke test are shown in Figure 94. The smoke reaches the instrument around 60 seconds after the instrument was started. At this point, the concentrations increase greatly. As with the DRX, the OPS stops providing useful information during the latex foam test due to the smoke concentration becoming too large. Up to this point, however, information collected from the sensor showed that there was an increase in all bins, with the large increase in smaller particles. This trend agrees with the DRX results as seen in Figure 93.

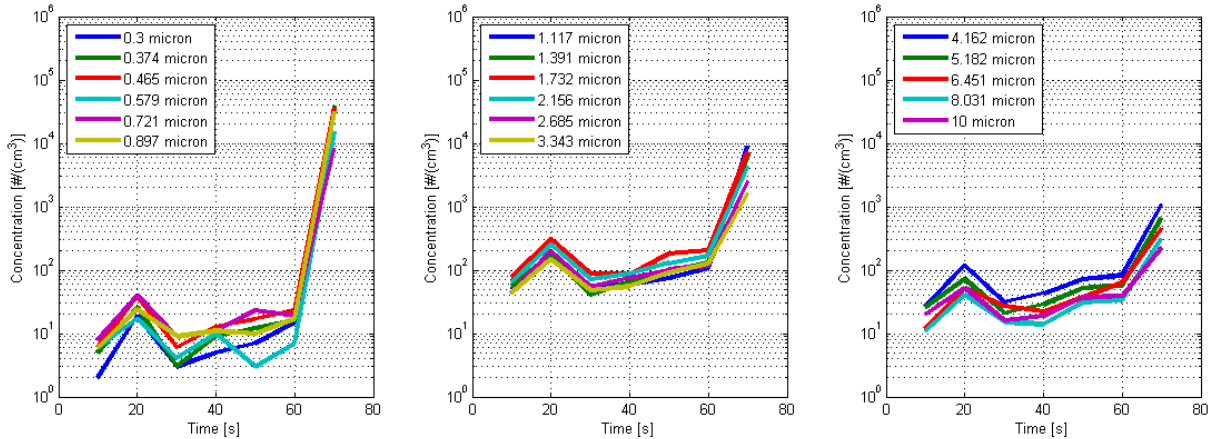


Figure 94: TSI Model 3330 OPS results for the latex foam test.

A.4.5.2 Propane Smoke

The plots in Figures 95 and 96 show the results for the propane test for the DustTrak DRX. The plot in Figure 95 shows the results for all bins (all starting at the instrument minimum), and the plot in Figure 96 shows the first bin and concentrations between bins. The DRX provides useful information for the entire propane smoke test. Aside from the beginning of the test, the data is fairly consistent throughout the test. The 1-micron bin (PM1) has a fairly constant average of 50 mg/m³ and the overall concentration is between 50 and 60 mg/m³. The highest concentration is in the smallest bin (PM1), and the second highest is in the 4 to 10 micron range about an order of magnitude less.

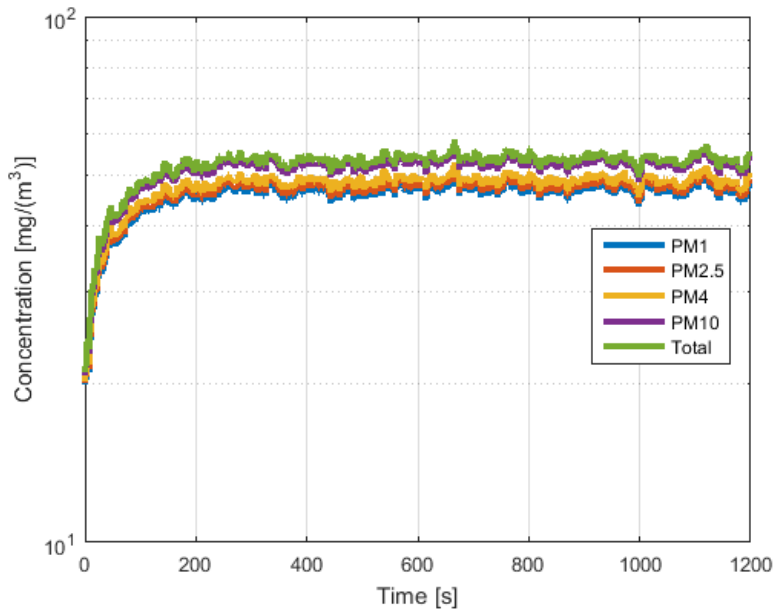


Figure 95: TSI DustTrak DRX results for the propane test showing concentrations for all bins.

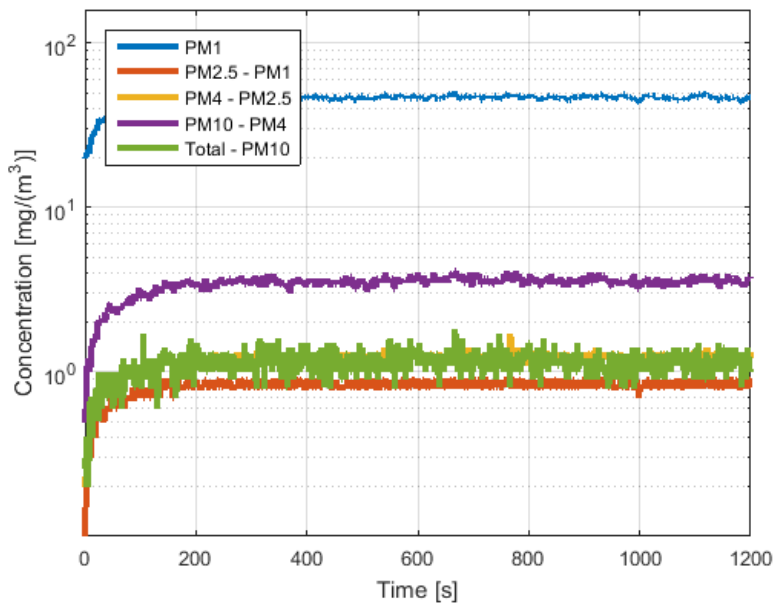


Figure 96: TSI DustTrak DRX results for the propane test showing the first bin and concentrations between bins.

The results from the OPS for the propane smoke test are shown in Figure 97. The OPS provided useful information throughout the test. The OPS indicates fairly constant concentration levels in all bins after the beginning of the test, similar to the DRX. The highest concentration occurs in the lowest bin. The next few bins result in zero values for the bulk of the test. Values in the following bins decrease with increasing bin size.

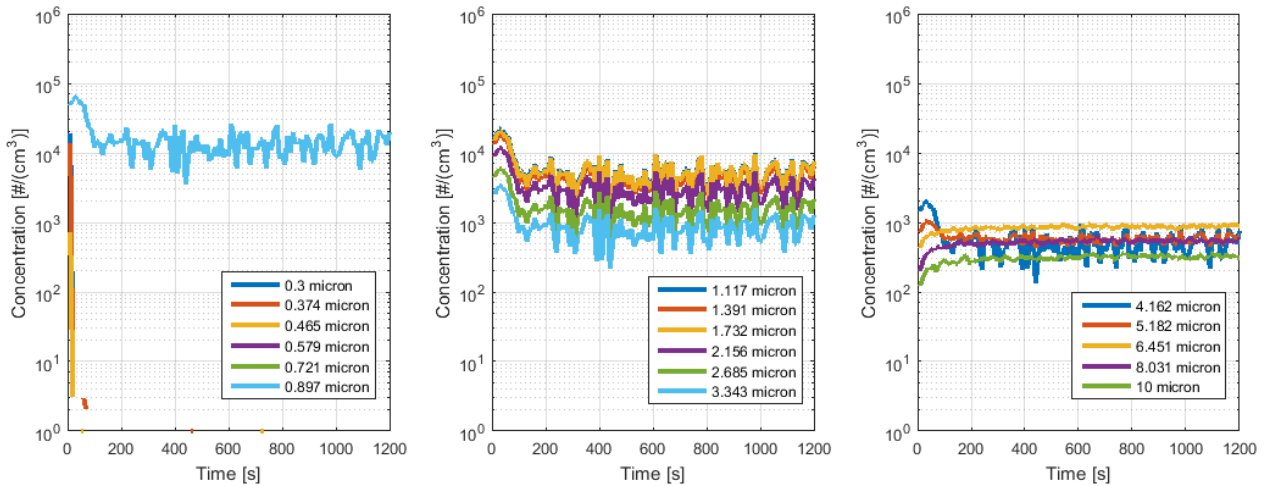


Figure 97: TSI Model 3330 OPS results for the propane test.

A.4.5.3 Wood Smoke

The plots in Figures 98 and 99 show the results for the wood test for the DustTrak DRX. The plot in Figure 98 shows the results for all bins (all starting at the instrument minimum), and the plot in Figure 99 shows the first bin and concentrations between bins. The DRX provides useful information for the entire wood smoke test. The results indicate a significant rise in the total measured concentration, due mostly to large increase in the 1-micron bin (PM1). The peak concentration for this bin is just under 50 mg/m³, while the other bins remain around the baseline values with some noise.

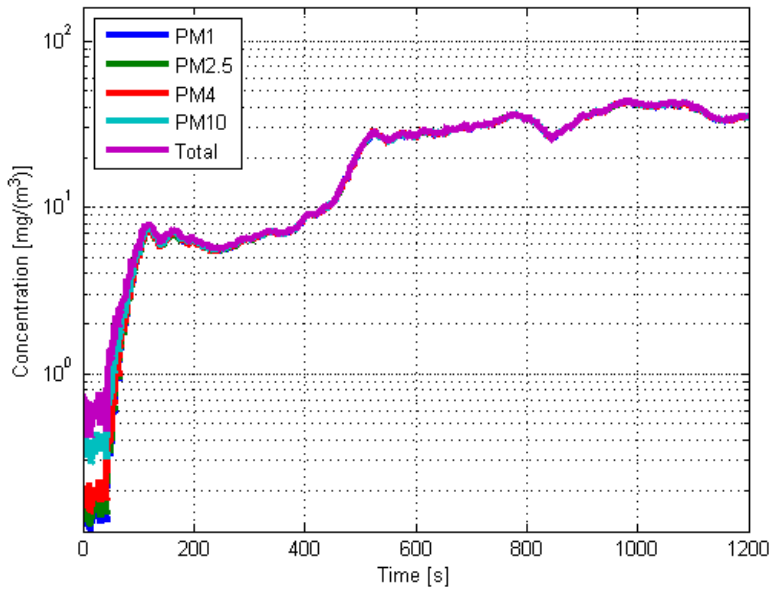


Figure 98: TSI DustTrak DRX results for the wood test showing concentrations for all bins.

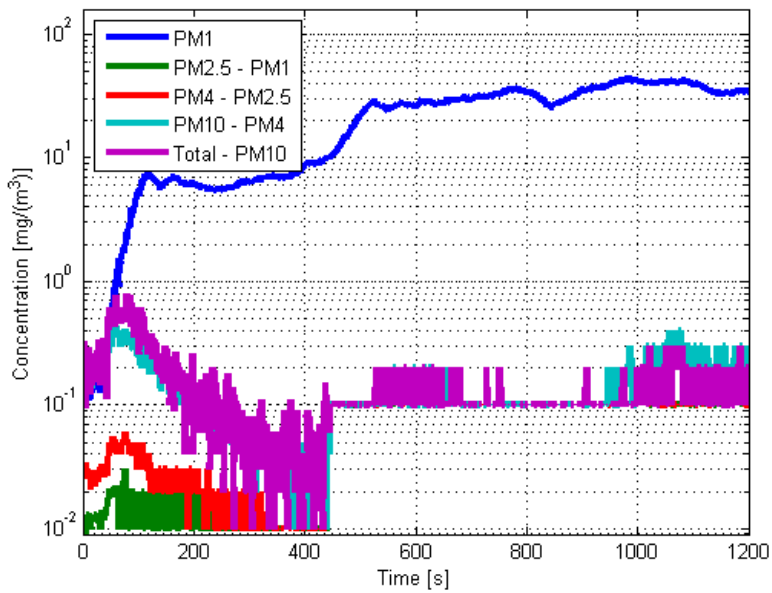


Figure 99: TSI DustTrak DRX results for the wood test showing the first bin and concentrations between bins.

The results from the OPS for the wood smoke test are shown in Figure 100. The OPS provided useful information near the beginning of the test but failed to provide useful information once the concentration became large. The OPS indicates small increases in concentration in all bins with the largest increases occurring in the lowest bins. This is consistent with the DRX results.

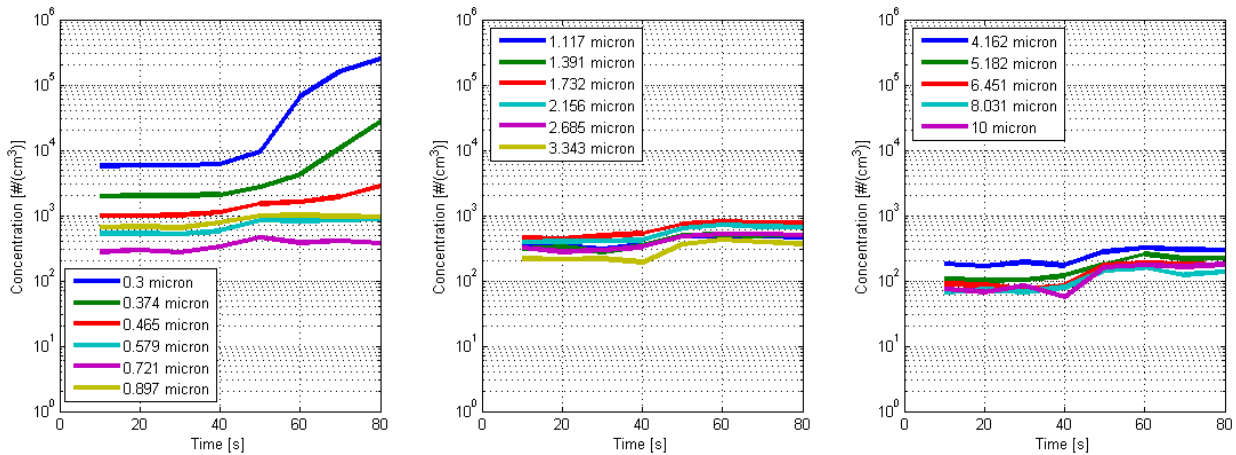


Figure 100: TSI Model 3330 OPS results for the wood test.

A.5 Discussion

First, a comparison of concentrations levels between the gravimetric filter system and the TSI DustTrak DRX is presented. Next, the laser extinction data and concentration levels are evaluated for consistency with mass specific extinction coefficient values for smoke found in the literature. Finally, the expected trends for the smoke types presented are discussed.

A.5.1 Gravimetric Filtering and Particle Analyzer Concentration Comparisons

The gravimetric filtering and DRX particle analyzer both provided concentration information. The gravimetric filtering concentration values represent average concentrations over 5 to 20 minutes depending on the test, as shown in Table 10. These concentration values are based off of measurements with 1-micron filters, which can allow a significant amount of particulate smaller than 1 micron to pass through. The DRX records data on a smaller time-scale, here set to one-second increments, and has bins starting at 0.1 microns. In spite of the differences, some comparisons can be made for the tests.

The gravimetric filtering concentration value around 470 mg/m^3 for latex foam smoke is plausible when compared to the DustTrak DRX data. The measurements of latex foam smoke with the DRX showed the smoke reaching the instrument maximum, 150 mg/m^3 , for all bins, and then failing to provide useful data. The liquid removed from the filters showed a liquid concentration of about 10.6% the size of the solid concentration on average.

Comparing the mean gravimetric filter concentration of 24 mg/m^3 for the propane smoke to the DRX value around 50 to 60 mg/m^3 shows that it is lower than expected. Since the filters used for the gravimetric system were 1-micron filters and the DRX indicated the largest concentrations in the bin spanning up to 1-micron particle size, it is likely that most of these smaller particles would have passed through the filter, with less percentage passing through at the end of the test than the beginning due to particulate build-up on the filters. This discrepancy may also in part be due to the low accuracy of the gravimetric method at low concentration levels. The liquid removed from the filters showed a liquid concentration of about 15.8% the size of the solid concentration on average.

The data shows that the average measured particulate concentration for the wood smoke was 15 mg/m^3 with a standard deviation of about 21 mg/m^3 . The DustTrak DRX data showed that most of the particles it measured were in the 0.1-1 micron bin, having a maximum concentration just below 50 mg/m^3 in that bin. Since the gravimetric value represents an average through time, a lower value for the system should be expected than this value. Also, as with the propane data, since the filters used for the gravimetric system were 1-micron filters, it is likely that most of these smaller particles would have passed through the filter, with less percentage passing through at the end of the test than the beginning due to particulate build-up on the filters. The liquid removed from the filters showed a liquid concentration of about 117% the size of the solid concentration on average.

Overall, the gravimetric filtering system and the DRX provided concentration values that are consistent. The gravimetric system provided concentration data for the latex foam when the DRX failed. The biggest discrepancy between the measured concentration levels is between the

propane gravimetric results and DRX results and is attributed to a large amount of smaller particles measured by the DRX but passing through the filters.

A.5.2 Laser Extinction and Concentration Data Consistency with Literature

The laser extinction intensity ratio I/I_0 and mass concentration M_s are related in Equation (28) by the mass specific extinction coefficient σ_s . Typical values in the literature for smoke for the mass specific extinction coefficient for a laser system at 632.8 nm range from about 7.8 to 10.2 m^2/g , with some values lower [12, 14]. Assuming a value in this range, the laser extinction and mass concentration levels can be evaluated for consistency with each other and the literature. A value of 9 m^2/g , the average of this typical range, was assumed for this analysis.

The average concentration value for the latex foam test from the gravimetric filter evaluation was around 470 mg/m^3 . Using a mass specific extinction coefficient of 9 m^2/g gives an expected intensity ratio of 0.002. The laser data intensity ratio is in a consistent range with this, giving an intensity ratio value of $0_{-0}^{+0.008}$ assuming a normal distribution with 95% confidence and truncating at 0 to prevent negative intensity values. Due to the noise in the laser data, a more precise comparison is not made. The DRX shows a concentration of about 100 mg/m^3 after about 15 seconds once the smoke arrives at the sensor for the latex foam smoke. The expected intensity ratio for this case is 0.26. The laser data is again in a consistent range with this at a value of $0.24_{-0.008}^{+0.008}$, although the precision of the laser intensity ratio in time is low, with change by one second causing a variation on the order of 0.1.

The propane and wood smokes provide data for more precise comparisons. Tables 15 and 16 show the laser intensity ratio and the expected intensity ratio based off of the gravimetric data and the DRX data. The average gravimetric filtering concentration per smoke is used for comparison at all the time steps. The average of the results for the combined set of times is also shown in the table for all three intensity ratio calculation sources. The averaged laser intensity ratio for the time steps is within 0.01 of the intensity ratio for the gravimetric results for both smoke types, well within 95% confidence (2 standard deviations) assuming a normal distribution for the laser data values, even ignoring additional uncertainty in the laser measurements and gravimetric measurements. The DRX data is close to the laser data for the wood smoke case but

is significantly lower for all times for the propane smoke case. This inconsistency may be due to choosing too large of a value for the mass specific extinction coefficient. As shown in the images in Figure 90, the propane base spherical particles are smaller than the latex foam smoke and wood smoke base particles, and a decrease in the base particle size has shown a decrease in mass specific extinction coefficient in the literature [12]. For instance, lowering the mass specific extinction coefficient to $6.5 \text{ m}^2/\text{g}$, still within the range of reported mass specific extinction coefficient values for smoke [12, 14], results in gravimetric and DRX intensity ratios of 0.79 and 0.59 respectively, both within range of the laser intensity ratio.

Table 15: Intensity ratio results for propane.

Time after smoke arrival [s]	I/I_0 , Laser	M_s [mg/m ³], Gravimetric	I/I_0 , Gravimetric	M_s [mg/m ³], DRX	I/I_0 , DRX
150	0.74	24	0.72	50	0.51
300	0.69	24	0.72	54	0.48
450	0.64	24	0.72	54	0.48
600	0.66	24	0.72	54	0.48
750	0.81	24	0.72	54	0.48
Average	0.71		0.72		0.49
± for 2 standard deviations	0.14				0.03

Table 16: Intensity ratio results for wood.

Time after smoke arrival [s]	I/I_0 , Laser	M_s [mg/m ³], Gravimetric	I/I_0 , Gravimetric	M_s [mg/m ³], DRX	I/I_0 , DRX
150	0.90	15	0.82	6	0.92
300	0.80	15	0.82	9	0.89
450	0.79	15	0.82	28	0.69
600	0.76	15	0.82	30	0.67
750	0.78	15	0.82	40	0.58
Average	0.81		0.82		0.75
± for 2 standard deviations	0.11				0.30

Overall, the laser extinction system data, the gravimetric mass concentration data, and the DRX mass concentration data are in agreement when assuming a mass specific extinction coefficient of $9 \text{ m}^2/\text{g}$ based on the typical range in the literature for latex and wood smoke and a mass specific extinction coefficient of $6.5 \text{ m}^2/\text{g}$ for the propane smoke. The need for a lower value for the propane data is likely due to the smaller base particle size for propane soot particulate when compared to latex and wood smoke particulate. The laser system has a high level of noise, so the range on these values can vary significantly. The propane and wood smoke data provided more

precise information than the latex foam smoke data for checking consistency between the measured data and the literature.

A.5.3 Expected Smoke Effects on Electromagnetic Sensors

The latex foam fire produced dense, optically thick smoke as measured by the laser system at the wavelength of 632.8 nm with a visibility dropping below 1 m. This low visibility indicates high extinction by particulate and implies poor sensor perception for sensors operating at or near this wavelength. Based on trends in the literature for smoke extinction [10, 13, 15], the extinction effects are expected to decrease with wavelength for the soot particulate, which implies better perception by higher wavelength instruments. Water vapor and carbon dioxide gas bands can also cause effects on sensors operating in the regions where these bands are and will have the strongest adverse effects on the sensors at the highest temperatures and concentrations, closest to the fire.

The wood and propane smokes tested were optically thin based on the laser measurements at the wavelength of 632.8 nm. This indicates low extinction by particulate in this region of the spectrum implying low attenuation on perception for sensors operating at or near this wavelength. The extinction should be even lower for the smoke particulate at higher wavelengths, implying even less attenuation effects on sensors operating at higher wavelengths. Effects from water vapor and carbon dioxide gas bands are the same as for the latex foam fire smoke, with affected sensors having the strongest adverse effects at the highest temperatures and concentrations, closest to the fire.

A.6 Conclusion

The equations governing smoke emission, absorption, and scattering effects have been presented, highlighting effects of temperature, concentration, and smoke make-up on electromagnetic radiation. Higher temperatures and concentration levels result in stronger effects from gas band emission and absorption. Particulate emission is also strongest at higher temperatures and concentrations. Extinction from smoke droplets and particulate depends on particle size and shape, with the general trend of less attenuation of radiation with an increase in wavelength shown in the literature for soot [10, 13, 15].

Tests were performed to quantify the characteristics of three smoke types. Latex foam, propane, and wood were selected as fuel sources with expectation of different soot concentration levels. Smoke temperature along the ceiling of the test rig, laser extinction, total concentration, and size-distributed concentration levels were measured. In addition, electron microscopy instrumentation was used to verify particulate make-up and to show particulate size and shape for the base spherical particles and for agglomerates.

The laser extinction and concentration data were compared using a mass specific extinction coefficient based on the literature. A mass specific extinction coefficient at $9 \text{ m}^2/\text{g}$ provides consistent results between the recorded laser data, recorded concentration data, and literature mass specific extinction coefficient values for the latex foam and wood smokes. The propane contains smaller base particles than the latex foam and wood smoke and has more consistent results between measurements for a value of $6.5 \text{ m}^2/\text{g}$ for the mass specific extinction coefficient. This agrees with the trend in the literature that smaller base particles results in lower mass specific extinction coefficient values [12].

The test results indicated that the latex foam smoke was optically thick at 632.8 nm, implying poor perception for sensors operating at or near this wavelength. The propane and wood smokes were optically thin at this wavelength with little attenuation expected on the perception of sensors operating at or near this wavelength. For all three smoke types, the extinction by smoke particulate is expected to decrease with increasing wavelength, implying less attenuation on the perception of higher wavelength sensors by smoke particulate. Gas band effects on sensors operating in applicable wavelength ranges are expected to be worse closer to the fire, where temperatures and concentrations of the gases are higher.

A.7 References

- [1] Howell, J. R., Siegel, R., & Menguc, M. P. (2011). *Thermal radiation heat transfer* (5th ed.). CRC press.
- [2] Docquier, N., & Candel, S. (2002). Combustion control and sensors: a review. *Progress in energy and combustion science*, 28(2), 107-150.

- [3] Drysdale, D. (2011). *An introduction to fire dynamics*. John Wiley & Sons.
- [4] DiNenno, P. J. (2008). *SFPE handbook of fire protection engineering* (4th ed.). SFPE.
- [5] Turns, S. R. (2000). *An introduction to combustion* (2nd ed.). Boston: McGraw Hill.
- [6] Butler, K. M., & Mulholland, G. W. (2004). Generation and transport of smoke components. *Fire Technology*, 40(2), 149-176.
- [7] Onischuk, A. A., Di Stasio, S., Karasev, V. V., Baklanov, A. M., Makhov, G. A., Vlasenko, A. L., ... & Panfilov, V. N. (2003). Evolution of structure and charge of soot aggregates during and after formation in a propane/air diffusion flame. *Journal of aerosol science*, 34(4), 383-403.
- [8] Dalzell, W. H., & Sarofim, A. F. (1969). Optical constants of soot and their application to heat-flux calculations. *Journal of Heat Transfer*, 91(1), 100-104.
- [9] Dobbins, R. A., Mulholland, G. W., & Bryner, N. P. (1994). Comparison of a fractal smoke optics model with light extinction measurements. *Atmospheric Environment*, 28(5), 889-897.
- [10] Roessler, D. M., & Faxvog, F. R. (1980). Optical properties of agglomerated acetylene smoke particles at 0.5145- μm and 10.6- μm wavelengths. *JOSA*, 70(2), 230-235.
- [11] Sakai, M., & Aoki, Y. (2006, August). Human and object detection in smoke-filled space using millimeter-wave radar based measurement system. In *Pattern Recognition, 2006. ICPR 2006. 18th International Conference on* (Vol. 3, pp. 750-750). IEEE.
- [12] Mulholland, G. W., & Choi, M. Y. (1998, December). Measurement of the mass specific extinction coefficient for acetylene and ethene smoke using the large agglomerate optics facility. In *Symposium (international) on combustion* (Vol. 27, No. 1, pp. 1515-1522). Elsevier.
- [13] Ouf, F., Coppalle, Alexis, Yon, Jerome, & Vendel, J. (2008). Measurement of the Mass Specific Extinction Coefficient of Acetylene, Toluene and Polymethyl Methacrylate Soot Particles in Visible and Near-Infrared Wavelengths. *Fire Safety Science*, 9, 231-240.
- [14] Mulholland, G. W., & Croarkin, C. (2000). Specific extinction coefficient of flame generated smoke. *Fire and Materials*, 24(5), 227-230.
- [15] Köylü, U. O., & Faeth, G. M. (1996). Spectral extinction coefficients of soot aggregates from turbulent diffusion flames. *Journal of Heat Transfer*, 118(2), 415-421.

- [16] Fire Research Information Services (1990), ISO 9705, International Organization for Standardization.
- [17] Ostman, B. (1992). Smoke and soot. *Heat Release in Fires*. Elsevier Science.
- [18] Fruhstorfer, P., & Niessner, R. (1994). Identification and classification of airborne soot particles using an automated SEM/EDX. *Microchimica Acta*, 113(3-6), 239-250.

Appendix B: Bi-Directional SAD Stereo Correspondence Matching

- SAD and Bi-Directional SAD Stereo Correspondence Matching

The SAD (Sum of Absolute Differences) matching algorithm is a local stereo correspondence matching algorithm [1]. The method is applied to a left and right image after functions addressing camera calibration and rectification have been applied to both images, ensuring features in one image are shifted only in one direction in the other image if visible there (epipolar constraint) [1, 2]. The goal at each pixel location of interest is to determine how much a feature appearing in one image is shifted in pixel values in the other image. This pixel shift is called a disparity value. For a horizontally mounted system rectified to an epipolar constraint, this pixel shift is in the horizontal direction, with a feature in the left image appearing further to the left in the right image, shifted only in row value. For the calibrated and rectified images, the disparity and distance are related as [2]

$$Z = \frac{Baseline * Focal}{d}$$

where Z is the distance from the cameras, $Baseline$ is the baseline distance between the cameras, $Focal$ is the focal length of the cameras, and d is the disparity value. At further distance, the disparity value is lower and the distance has a lower precision than at closer distances.

The first step in the SAD matching algorithm for one pixel of interest is to determine the difference in the intensities at and around the pixel of interest in its image to intensities in the other image at each possible disparity value allowed based on a determined range of disparity values and the precision of disparity values allowed [3]. These values are determined by summing the absolute value of the difference in pixel intensities as shown in the equation below for comparing right image intensities to a pixel of interest in the left image [3].

$$C_L(u, v, d) = \sum_{u,v \in W} abs(L(u, v) - R(u, v - d)) \quad \forall (d_{min} < d < d_{max})$$

where C_L is the resulting SAD cost value for the pixel at location u, v in the left image for a disparity d . L and R are the left and right images, respectively. W is a window centered at the pixel of interest at u, v . The absolute value function is denoted by $abs()$. The disparity d ranges from a minimum disparity d_{min} to a maximum disparity d_{max} .

The second step is to choose the disparity value that has the lowest cost for the pixel of interest, known as winner-take-all (WTA) [1]. This is shown in the equation below.

$$d_{selected,L}(u, v) = argmin(C_L(u, v, d), d) \forall (d_{min} < d < d_{max})$$

where $d_{selected,L}$ is the selected disparity level for the left image location u, v . The $argmin()$ function returns the disparity value that results in the minimum value for the cost function at the left image u, v location.

When this is performed at every pixel of interest in the baseline image, a disparity map can be constructed showing the top disparity value based on the cost. Removing disparity values that have a high value for top matching cost is sometimes performed to improve the quality of the resulting disparity map. Another method to improve the matching results is to use bi-directional matching, also called a left-right consistency check [3, 4]. For the horizontal case with the left camera as the base camera, this involves determining the disparity values for the left image and for the right image. The left image disparity is found as above, and the right image disparity is found using the equation

$$C_R(u, v, d) = \sum_{u,v \in W} abs(L(u, v + d) - R(u, v)) \forall (d_{min} < d < d_{max})$$

where C_R is the resulting left-to-right SAD cost value for the pixel at location u, v in the right image for a disparity d . The top disparity is again selected, as shown in the equation below

$$d_{selected,R}(u, v) = argmin(C_R(u, v, d), d) \forall (d_{min} < d < d_{max})$$

where $d_{selected,R}$ is the selected disparity level for the right image location u, v .

The disparity values from the right image SAD matching are translated by their disparity value back to the left camera's frame of reference, using the equation below.

$$\begin{aligned} d'_{selected,R}(u, v - d_{selected,R}(u, v)) \\ = \max(d_{selected,R}(u, v), d'_{selected,R}(u, v - d_{selected,R}(u, v))) \end{aligned}$$

where $d'_{selected,R}$ is the selected right image SAD matching value in the frame of the left image, initialized to null values to be replaced if affected by right image disparity values. This is performed for every location u, v in the right image. The $\max()$ function ensures that only the

highest disparity value affecting each location in the left frame is kept, since the conversion from the right image frame to the left image frame can result in multiple disparity values at a given left image frame location. Values between left-to-right and right-to-left matching that are similar or equal in value are kept, and other matches are discarded.

- References

- [1] Scharstein, D., & Szeliski, R. (2002). A taxonomy and evaluation of dense two-frame stereo correspondence algorithms. *International journal of computer vision*, 47(1-3), 7-42.
- [2] Chris Walker, "Stereo Vision Basics".
<http://chriswalkertechblog.blogspot.com/2014/03/stereo-vision-basics.html>. Accessed December 2015.
- [3] Unger, Christian, & Navab, Nassir. "Stereo Matching".
http://campar.in.tum.de/twiki/pub/Chair/TeachingWs09Cv2/3D_CV2_WS_2009_Stereo.pdf. Accessed December 2015.
- [4] Tseng, Y. C., & Chang, T. S. (2011, July). Fast algorithm for local stereo matching in disparity estimation. In *Digital Signal Processing (DSP), 2011 17th International Conference on* (pp. 1-6). IEEE.

Appendix C: Filter Algorithm Descriptions

The filters selected for testing for improving LWIR stereo vision matching are presented in detail here. These filters are sorted by category. References to parameter names are the same as shown in Table 6. Applicable references for the filter are included in the headings and in chapter 3 in Table 5.

- Spatial averaging
 - StereoAvgS [1, 2]

This filter operates by taking the spatial neighborhood around each pixel of interest and averaging their intensities along with the pixel of interest for a new value. The averaging is switched between mean, median, and mode via selection of the parameter “Method”. The neighborhood is varied from 3 to 11 by values of 2 to ensure symmetry and is represented by the parameter “Box (kernel) size”, represented below by N_S . An example application for this equation for one pixel in the left image L located at (u, v) is

$$L_{Out}(u, v) = \begin{cases} \text{mean}(L(u - a: u + a, v - a: v + a)), & \text{Method} = \text{mean} \\ \text{median}(L(u - a: u + a, v - a: v + a)), & \text{Method} = \text{median} \\ \text{mode}(L(u - a: u + a, v - a: v + a)), & \text{Method} = \text{mode} \end{cases}$$

where a is related to the Box size by

$$a = \frac{N_S - 1}{2}$$

- StereoMeanShift [1, 3, 4]

This filter outputs a new value for each pixel of interest based on spatial averaging with weighting, iterating to a final value using 10 passes. It is based off of the mean shift filter. The neighborhood size is represented by the parameter “Box size” and is set to 5, 9, 13, 17, or 21. A filter weight value is used to make pixels values in the neighborhood similar in value to the pixel of interest have a stronger influence in averaging than intensity values far from the value of the pixel of interest. This parameter, “Color closeness strength” is set to 2, 4, 8, 16, or 32.

Additional weighting based on closeness to the pixel of interest in the window is turned on and off using the parameter “Color closeness used”. The spatial closeness weight is also varied using a power to strengthen or lessen the application of the spatial closeness weight using the parameter “Power of color closeness” which is set to 1, 2, 3, or 4. An example application for one pixel in the left image is

$$L_{Out}(u, v, n_i) = \frac{\sum_{u_2, v_2 \in W} \left[L(u, v) * \exp \left(-0.5 * abs \left(\frac{L_{Out}(u, v, n_i - 1) - L(u_2, v_2)}{h} \right)^2 \right) * G_W(u_2, v_2, u, v)^{\frac{1}{p_S}} \right]}{\sum_{u_2, v_2 \in W} \left[\exp \left(-0.5 * abs \left(\frac{L_{Out}(u, v, n_i - 1) - L(u_2, v_2)}{h} \right)^2 \right) * G_W(u_2, v_2, u, v)^{\frac{1}{p_S}} \right]}$$

where $L_{Out}(u, v, n_i)$ is the new intensity value for the pixel location (u, v) for the current iteration n_i based on the previous iteration value and the image values at locations (u_2, v_2) encompassing the window W around the pixel of interest. For the first iteration, $L_{Out}(u, v, n_i - 1)$ is set to the image intensity at the pixel of interest. $L(u, v)$ is the image intensity value, h is the ‘‘Color closeness strength’’, and G_W is the spatial closeness weight to the power $\frac{1}{p_S}$, to account for the ‘‘Power of color closeness’’ parameter p_S . If the ‘‘Color closeness used’’ parameter is set to turn off the spatial closeness weighting, G_W becomes 1 for all values.

- Temporal Average
 - StereoAvgT [2]

This filter operates by averaging the value for each pixel for consecutive frames. The averaging is switched between mean, median, and mode via selection of the parameter ‘‘Method’’. The number of frames used in averaging is varied from 3 to 11 by values of 2 by the parameter ‘‘Number of frames’’, represented below by N_T . An example application for this equation for one pixel in the left image L located at (u, v) for frame f is

$$L_{Out}(u, v, f) = \begin{cases} mean(L(u, v, f + 1 - N_T: f)), & Method = mean \\ median(L(u, v, f + 1 - N_T: f)), & Method = median \\ mode(L(u, v, f + 1 - N_T: f)), & Method = mode \end{cases}$$

where the average is performed across N_T frames up to and including frame f for the selected method at each pixel location (u, v) .

- StereoWMeanT [2]

This filter operates similar to the function StereoMeanShift, operating on a series of values for a pixel through time (frames) instead of a spatial window around the pixel. It is not setup to iterate, unlike the StereoMeanShift filter. The parameter ‘‘Color closeness value’’ is used to weigh intensity values closer to the current pixel intensity value higher in the averaging than intensity values further from the current pixel intensity value. This parameter is set to 2, 4, 8, 16,

or 32. The number of frames used in averaging is varied from 3 to 11 by values of 2 by the parameter “Number of frames”, represented below by N_T .

$$L_{Out}(u, v, f) = \frac{\sum_{f_N=f+1-N_T:f} \left[L(u, v, f_N) * \exp \left(-0.5 * abs \left(\frac{(L(u, v, f_N) - L(u, v, f))^2}{h} \right) \right) \right]}{\sum_{f_N=f+1-N_T:f} \left[\exp \left(-0.5 * abs \left(\frac{(L(u, v, f_N) - L(u, v, f))^2}{h} \right) \right) \right]}$$

where f is the current frame, h is the “Color closeness value”, and the value f_N is used to factor in the total number of frames.

- Spatial-Temporal Average
 - StereoAvgST

This filter operates as a combination of the StereoAvgS and StereoAvgT filters, averaging over a spatial window through multiple frames (time). The averaging is switched between mean, median, and mode via selection of the parameter “Method”. The neighborhood is varied from 3 to 11 by values of 2 to ensure symmetry and is represented by the parameter “Box size”, represented below by N_S . The number of frames used in averaging is varied from 3 to 11 by values of 2 by the parameter “Number of frames”, represented below by N_T . An example application for this equation for one pixel in the left image L located at (u, v) for frame f is

$$L_{Out}(u, v, f) = \begin{cases} \text{mean}(L(u - a: u + a, v - a: v + a, f + 1 - N_T: f)), & \text{Method} = \text{mean} \\ \text{median}(L(u - a: u + a, v - a: v + a, f + 1 - N_T: f)), & \text{Method} = \text{median} \\ \text{mode}(L(u - a: u + a, v - a: v + a, f + 1 - N_T: f)), & \text{Method} = \text{mode} \end{cases}$$

where a is related to the Box size by

$$a = \frac{N_S - 1}{2}$$

- StereoWMeanST [2]

This filter operates as a combination of the StereoMeanShift function and the StereoWMeanT function. This filter outputs a new value for each pixel of interest based on spatial and temporal averaging with weighting, iterating to a final value using 10 passes. It is based off of the mean shift filter. The spatial neighborhood size is represented by the parameter “Box size” and is set to 5, 9, 13, 17, or 21. The number of frames used in averaging is varied from 3 to 11 by values of 2 by the parameter “Number of frames”. A filter weight value is used to make pixels values in the spatial-temporal neighborhood similar in value to the pixel of interest at the frame of interest

have a stronger influence in averaging than intensity values far from the value of the pixel of interest at the frame of interest. This parameter, “Color closeness strength” is set to 2, 4, 8, 16, or 32. Additional weighting based on closeness to the pixel of interest in the spatial window is turned on and off using the parameter “Spatial color closeness used”. The spatial closeness weight is also varied using a power to strengthen or lessen the application of the spatial closeness weight using the parameter “Spatial power of color closeness” which is set to 1, 2, 3, or 4. Likewise, the parameters “Temporal color closeness used” and “Temporal power of color closeness” are used to weigh heavier the pixel intensities that are closer temporally to the pixel of interest at the frame of interest. These parameter values are set the same as for the spatial equivalent parameters. An example application for one pixel in the left image is

$$Top(u, v, f, n_i)$$

$$= \sum_{f_N=f+1-N_T:f} \sum_{u_2, v_2 \in W} \left[L(u, v) \right. \\ \left. * \exp \left(-0.5 * abs \left(\frac{L_{Out}(u, v, f, n_i - 1) - L(u_2, v_2, f_N)}{h} \right)^2 \right) * G_W(u_2, v_2, u, v)^{\frac{1}{p_s}} \right. \\ \left. * G_T(f_N)^{\frac{1}{p_T}} \right]$$

$$Bottom(u, v, f, n_i)$$

$$= \sum_{f_N=f+1-N_T:f} \sum_{u_2, v_2 \in W} \left[\exp \left(-0.5 \right. \right. \\ \left. \left. * abs \left(\frac{L_{Out}(u, v, f, n_i - 1) - L(u_2, v_2, f_N)}{h} \right)^2 \right) * G_W(u_2, v_2, u, v)^{\frac{1}{p_s}} * G_T(f_N)^{\frac{1}{p_T}} \right]$$

$$L_{Out}(u, v, f, n_i) = \frac{Top}{Bottom}$$

where $L_{Out}(u, v, f, n_i)$ is the new intensity value for the pixel location (u, v) at the frame f for the current iteration n_i based on the previous iteration value and the image values at locations (u_2, v_2) encompassing the window W around the pixel of interest for the total number of frames N_T . The value f_N is used to factor in the total number of frames. For the first iteration, $L_{Out}(u, v, f, n_i - 1)$ is set to the image intensity at the pixel of interest at the frame of interest. $L(u, v, f)$ is the image intensity value at frame f , and h is the “Color closeness strength”. G_W is

the spatial closeness weight to the power $\frac{1}{p_S}$, to account for the “Spatial power of color closeness” parameter p_S . If the “Spatial color closeness used” parameter is set to turn off the spatial closeness weighting, G_w becomes 1 for all values. G_T is the temporal closeness weight to the power $\frac{1}{p_T}$, to account for the “Temporal power of color closeness” parameter p_T . If the “Temporal color closeness used” parameter is set to turn off the temporal closeness weighting, G_T becomes 1 for all values.

- Frequency
 - StereoFrS [5]

This filter operates in the spatial frequency domain. A spatial neighborhood around each pixel of interest is converted to the frequency domain using a Fast Fourier Transform (FFT). The neighborhood size is represented by the parameter “Box size” and is set to 5, 7, 11, 15, 19, 23, or 27. The frequency filter type is varied by the parameter “Type” to be low-pass, high-pass, band-pass, or notch. Cut frequencies are set with the parameters “Cut frequency 1” and “Cut frequency 2” with the second only used for band-pass and notch filters. The “Cut frequency 1” parameter is varied by 1 from

$$(0.25 * (N_S - 1)) \text{ to } (0.5 * (N_S - 1))$$

where N_S is the Box size. The “Cut frequency 2” parameter is varied by 1 from the “Cut frequency 1” value to

$$(0.5 * (N_S - 1))$$

In application, these two frequency terms are used to set values outside the desired range to 0. The data is then converted back out of the frequency domain using an Inverse Fast Fourier Transform, with the absolute value used to avoid complex numbers appearing in the final image data.

- StereoFrT

This filter operates in the temporal frequency domain. The number of frames used in the filter is set with the “Number of frames” parameter to 5, 7, 11, 15, 19, 23, or 27. For collection of values for each pixel is converted to the frequency domain using a Fast Fourier Transform. The frequency filter type is varied by the parameter “Type” to be low-pass, high-pass, band-pass, or notch. Cut frequencies are set with the parameters “Cut frequency 1” and “Cut frequency 2”

with the second only used for band-pass and notch filters. The “Cut frequency 1” parameter is varied by 1 from

$$(0.25 * (N_T - 1)) \text{ to } (0.5 * (N_T - 1))$$

where N_T is the Number of frames. The “Cut frequency 2” parameter is varied by 1 from the “Cut frequency 1” value to

$$(0.5 * (N_T - 1))$$

In application, these two frequency terms are used to set values outside the desired range to 0. The data is then converted back out of the frequency domain using an Inverse Fast Fourier Transform, with the absolute value used to avoid complex numbers appearing in the final image data.

- Noise-Variance-Based
 - StereoLLMMSE [6, 7]

This filter operates using a Local Linear Minimum Mean Square Error (LLMMSE) approach. It’s similar to the Wiener filter, making assumptions about the variance of the noise in the system. The filter operates spatially. The neighborhood size is represented by the parameter “Box size” and is varied from 3 to 11 by 2. The noise level is set by the parameter “Noise level” and is set to 2, 4, 6, 8, 16, 32, 64, 128, or 256. The new pixel value is as

$$L_{Out}(u, v) = \bar{W}(u, v) + (L(u, v) - \bar{W}(u, v)) * \frac{v_f(W(u, v))}{v_f(W(u, v)) + o_n}$$

where \bar{W} is the mean of the neighborhood window around and including the pixel of interest, $L(u, v)$ is the original image intensity at location (u, v) , v_f is the variance of the window around and including the pixel of interest, and o_n is the assumed noise variance, “Noise level”.

- StereoWienF [8]

This filter operates using the MATLAB `wiener2` function, applying a Wiener filter. The Wiener filter removes noise under the assumption that it is additive white Gaussian noise [8]. The neighborhood size is represented by the parameter “Box size” and is varied from 3 to 11 by 2. The noise level is set by the parameter “Noise level” and is set to 2, 4, 6, 8, 16, 32, 64, 128, or 256. The equation for the updated image is listed in the MATLAB image processing toolbox function. For the pixel at one location, this can be re-written as

$$L_{Out}(u, v) = \bar{W}(u, v) + (L(u, v) - \bar{W}(u, v)) * \left(\frac{\max(0, v_f(W(u, v)) - o_n)}{\max(v_f(W(u, v)), o_n)} \right)$$

where \bar{W} is the mean of the neighborhood window around and including the pixel of interest, $L(u, v)$ is the original image intensity at location (u, v) , v_f is the variance of the window around and including the pixel of interest, and σ_n is the assumed noise variance, “Noise level”. When the local variance is greater than the assumed noise variance, then the output value is influenced by the difference between the value of the pixel of interest and the mean of the local window. This results in smoothing of low-texture regions and results in preservation of high-texture regions which have a relatively high variance.

- Wavelet (Haar)
 - StereoWienFWv [5, 9, 10]

This filter operates in the Haar wavelet domain using Wiener filtering. Haar decomposition and reconstruction matrices are used to transform data to this domain. These are 4x4 or 8x8 window sizes, set with the “Box size (wavelet size)” parameter. The data from this conversion is kept for each pixel, resulting in 4x4 or 8x8 data per pixel of interest. Thus, each level of 4x4 or 8x8 data has its own data matrix for all pixels of interest. Each level in this 4x4 or 8x8 data is filtered with neighboring values corresponding to the same level in adjacent pixels using a Wiener filter. The neighborhood size used for filtering at each level for each pixel of interest is represented by the parameter “Wiener box size in wavelet domain” and is varied from 3 to 11 by 2. The noise level options at each level in the 4x4 or 8x8 data was set to 5, 10, 50, 80, 100, 1000, 10000, 20000, or 40000. These were set with the “Noise level” parameter and varied so that the lower-frequency (i.e. closer to the start of the 4x4 or 8x8 data) values were always lower or equal to the higher-frequency noise values. The MATLAB `wiener2` function was used for determining the filtered data at each level. The data is converted back to the original domain using the Haar decomposition and reconstruction matrices used initially.

- StereoAvgWv [10]

This filter operates similar to the StereoWienFWv filter, updating data in the Haar wavelet domain. Unlike the StereoWienFWv filter, this filter uses an average at each level in the transformed data rather than the Wiener filter. Haar decomposition and reconstruction matrices are used to transform data to this domain. These are 4x4 or 8x8 window sizes, set with the “Box size (wavelet size)” parameter. The data from this conversion is kept for each pixel, resulting in 4x4 or 8x8 data per pixel of interest. Thus, each level of 4x4 or 8x8 data has its own data matrix for all pixels of interest. Each level in this 4x4 or 8x8 data is filtered with neighboring values

corresponding to the same level in adjacent pixels using an average. The averaging is switched between mean, median, and mode via selection of the parameter “Method”. The neighborhood used for the averaging at each level for each pixel is varied from 3 to 11 by values of 2 to ensure symmetry and is represented by the parameter “Averaging box size in wavelet domain”. The data is converted back to the original domain using the Haar decomposition and reconstruction matrices used initially.

- StereoWMeanWv [10]

This filter operates similar to the StereoWienFWv filter, updating data in the Haar wavelet domain. Unlike the StereoWienFWv filter, this filter uses a weighted mean average at each level in the transformed data rather than the Wiener filter. Haar decomposition and reconstruction matrices are used to transform data to this domain. These are 4x4 or 8x8 window sizes, set with the “Box size (wavelet size)” parameter. The data from this conversion is kept for each pixel, resulting in 4x4 or 8x8 data per pixel of interest. Thus, each level of 4x4 or 8x8 data has its own data matrix for all pixels of interest. Each level in this 4x4 or 8x8 data is filtered with neighboring values corresponding to the same level in adjacent pixels using a weighted mean. In effect, each level of the transformed data is its own image to which the StereoWMeanST filter is applied. The neighborhood used for the averaging at each level for each pixel is set to 5, 9, 13, 17, or 21 and is represented by the parameter “Weighted averaging box size”. The “Color closeness strength” and “Power of color closeness” are the same as for the StereoWMeanST filter and were varied with the same values listed with that filter description. Once each level of the data is processed, the data is converted back to the original domain using the Haar decomposition and reconstruction matrices used initially.

- Special

- StereoAniDif [1, 11]

This filter operates in the spatial domain using one of two functions for anisotropic diffusion. During smoothing, boundaries are preserved using intensity difference information between each pixel and its neighbors [1]. The output image is determined iteratively. The “Functions” parameter is used to switch the function from “Exponential” to “1/k”. The number of iterations is set to 1, 10, 100, or 200 with the “Iterations” parameter. “Gamma” is a parameter for the functions that varies from 0 by 0.01 to 0.25. “K” is another parameter for the functions that is set to 1, 5, 10, 20, 50, 100, or 200. The output for one pixel of interest for one iteration level is

$$L_{Out}(u, v, n_i) = L_{Out}(u, v, n_i - 1) + g * (c_N * d_N + c_E * d_E + c_W * d_W + c_S * d_S)$$

where n is the iteration number, with the initial $L_{Out}(u, v, n_i - 1)$ set to the original image intensity $L(u, v)$, and g is the parameter “Gamma”. The values d_N , d_E , d_W , and d_S are measures of the difference between the previous pixel value of the pixel of interest and the previous pixel value for the pixels adjacent to the pixel of interest (i.e. “North”, “East”, “West”, and “South”):

$$d_N = L_{Out}(u - 1, v, n_i - 1) - L_{Out}(u, v, n_i - 1)$$

$$d_E = L_{Out}(u, v + 1, n_i - 1) - L_{Out}(u, v, n_i - 1)$$

$$d_W = L_{Out}(u, v - 1, n_i - 1) - L_{Out}(u, v, n_i - 1)$$

$$d_S = L_{Out}(u + 1, v, n_i - 1) - L_{Out}(u, v, n_i - 1)$$

Similarly, the values c_N , c_E , c_W , and c_S factor in the function. For the “Exponential” function,

$$c_N = \exp\left(-\left(\frac{d_N}{k}\right)^2\right)$$

$$c_E = \exp\left(-\left(\frac{d_E}{k}\right)^2\right)$$

$$c_W = \exp\left(-\left(\frac{d_W}{k}\right)^2\right)$$

$$c_S = \exp\left(-\left(\frac{d_S}{k}\right)^2\right)$$

where k is the parameter “K”. For the “1/k” function,

$$c_N = \frac{1}{1 + \left(\frac{d_N}{k}\right)^2}$$

$$c_E = \frac{1}{1 + \left(\frac{d_E}{k}\right)^2}$$

$$c_W = \frac{1}{1 + \left(\frac{d_W}{k}\right)^2}$$

$$c_S = \frac{1}{1 + \left(\frac{d_S}{k}\right)^2}$$

The values for d_N , d_E , d_W , and d_S and c_N , c_E , c_W , and c_S are updated at each iteration.

- StereoWienFC [8]

This filter operates by applying a Wiener filter to image data multiple times in a row. The Wiener filter removes noise under the assumption that it is additive white Gaussian noise [8]. The first pass of the filter removes much of the noise, with consecutive passes further smoothing the data [8]. The consecutive passes for smoothing have previously been applied to gradient information when smooth gradient information was desired for thermography purposes [8]. Here, the multiple passes are applied to the image itself for smoothing. The parameters are the same as for the filter StereoWienF previously described. The number of passes on the image data is set with the “Number of consecutive applications” parameter and is varied from 1 to 9 by 2. For each application of the Wiener filter, when the local variance is smaller than the assumed noise variance, the updated pixel value at each location of interest is just the mean of the local window.

The application of this consecutive filter depends on the local variance and assumed noise variance. When the local variance is smaller than the assumed noise variance, the updated pixel value at each location of interest is just the mean of the local window. When the local variance is greater than the assumed noise variance, then the output value is influenced by the difference between the value of the pixel of interest and the mean of the local window. This results in smoothing of low-texture regions and results in preservation of high-texture regions which have a relatively high variance. Over each consecutive application, the low-texture regions become further smoothed with the edges still preserved.

- StereoNLMeans [12]

This filter operates by comparing a window around each pixel of interest to windows around other pixels in the image. Data from this comparison is used to update the pixel of interest. If the window at another location is similar to the window around the pixel of interest, its center pixel value will weigh heavier in an average of compared window center values than locations where the window was less similar to the window around the pixel of interest. In effect, the pixel value is updated based on a weighted average of surrounding pixels, where the weighting is determined by the similarity of windows around the pixels to the window around the pixel of interest. The window size is represented by the parameter “Box size” and is varied from 3 to 11 by 2. The parameter “Search area box size” locates how many pixels before and after the pixel

of interest in rows and columns to use in comparisons and is set to 5, 10, 20, 40, or 80. If the value of this parameter results in an image location out of bounds, it is ignored. A filter weight value is used to make pixel values in the window being searched similar in value to the corresponding pixel values in the window around the pixel of interest have a stronger influence in averaging than intensity values far from the value of the corresponding pixel values in the window around the pixel of interest. This parameter, “H-parameter (color closeness strength)” is set to 1, 3, 5, 7, 9, or 11.

- References

- [1] Nixon, M. S., & Aguado, A. S. (2012). *Feature extraction & image processing for computer vision*. Academic Press.
- [2] Brailean, J. C., Kleihorst, R. P., Efstratiadis, S., Katsaggelos, A. K., & Lagendijk, R. L. (1995). Noise reduction filters for dynamic image sequences: A review. *Proceedings of the IEEE*, 83(9), 1272-1292.
- [3] Comaniciu, D., & Meer, P. (2002). Mean shift: A robust approach toward feature space analysis. *Pattern Analysis and Machine Intelligence, IEEE Transactions on*, 24(5), 603-619.
- [4] Tseng, Y. C., & Chang, T. S. (2011, July). Fast algorithm for local stereo matching in disparity estimation. In *Digital Signal Processing (DSP), 2011 17th International Conference on* (pp. 1-6). IEEE.
- [5] Motwani, M. C., Gadiya, M. C., Motwani, R. C., & Harris, F. C. (2004, September). Survey of image denoising techniques. In *Proceedings of GSPX* (pp. 27-30).
- [6] Kuan, D. T., Sawchuk, A., Strand, T. C., & Chavel, P. (1985). Adaptive noise smoothing filter for images with signal-dependent noise. *Pattern Analysis and Machine Intelligence, IEEE Transactions on*, (2), 165-177.
- [7] Wang, L., Leedham, G., & Cho, S. Y. (2007, November). Deriving filter parameters using dual-images for image de-noising. In *Intelligent Signal Processing and Communication Systems, 2007. ISPACS 2007. International Symposium on* (pp. 212-215). IEEE.
- [8] Rainieri, S., & Pagliarini, G. (2002). Data filtering applied to infrared thermographic measurements intended for the estimation of local heat transfer coefficient. *Experimental thermal and fluid science*, 26(2), 109-114.

- [9] Jacob, N., & Martin, A. (2004). Image denoising in the wavelet domain using wiener filtering. *Unpublished course project, University of Wisconsin, Madison, Wisconsin, USA.*
- [10] Strang, G. (1989). Wavelets and dilation equations: A brief introduction. *SIAM review*, 31(4), 614-627.
- [11] Perona, P., & Malik, J. (1990). Scale-space and edge detection using anisotropic diffusion. *Pattern Analysis and Machine Intelligence, IEEE Transactions on*, 12(7), 629-639.
- [12] Buades, A., Coll, B., & Morel, J. M. (2005). A review of image denoising algorithms, with a new one. *Multiscale Modeling & Simulation*, 4(2), 490-530.

Appendix D: LIDAR and LWIR Stereo Vision Alignment

In order to align 3D LIDAR and LWIR stereo vision data, the LIDAR data was first translated to the LWIR stereo vision left LWIR camera frame for a scene of interest. This translation was performed using the ideal homogeneous transform matrix connecting the LIDAR data in its frame to the left camera frame. This LIDAR data was then converted to an expected disparity map (or distance map) for the LWIR stereo vision system based on the camera baseline, focal length, and image size information. Since the translation step and conversion to expected camera output step are both based on an ideal system, further alignment was necessary. To further align the data, this LIDAR output disparity map was manually aligned with the left LWIR camera image (after calibration and rectification functions were applied to the image) for the scene of interest. This was performed for each system (the wheeled robotic platform and the humanoid robotic platform). The homogeneous transform matrix and image rotations and translations were used for alignment, taking into account the accuracy of the LIDAR. The accuracy of each disparity value in pixel location and disparity depth was recorded for each LIDAR disparity. Features in the disparity map and their corresponding features in the LWIR image were aligned. Figure 101 shows the aligned data as aligned for the hallway test scenario.

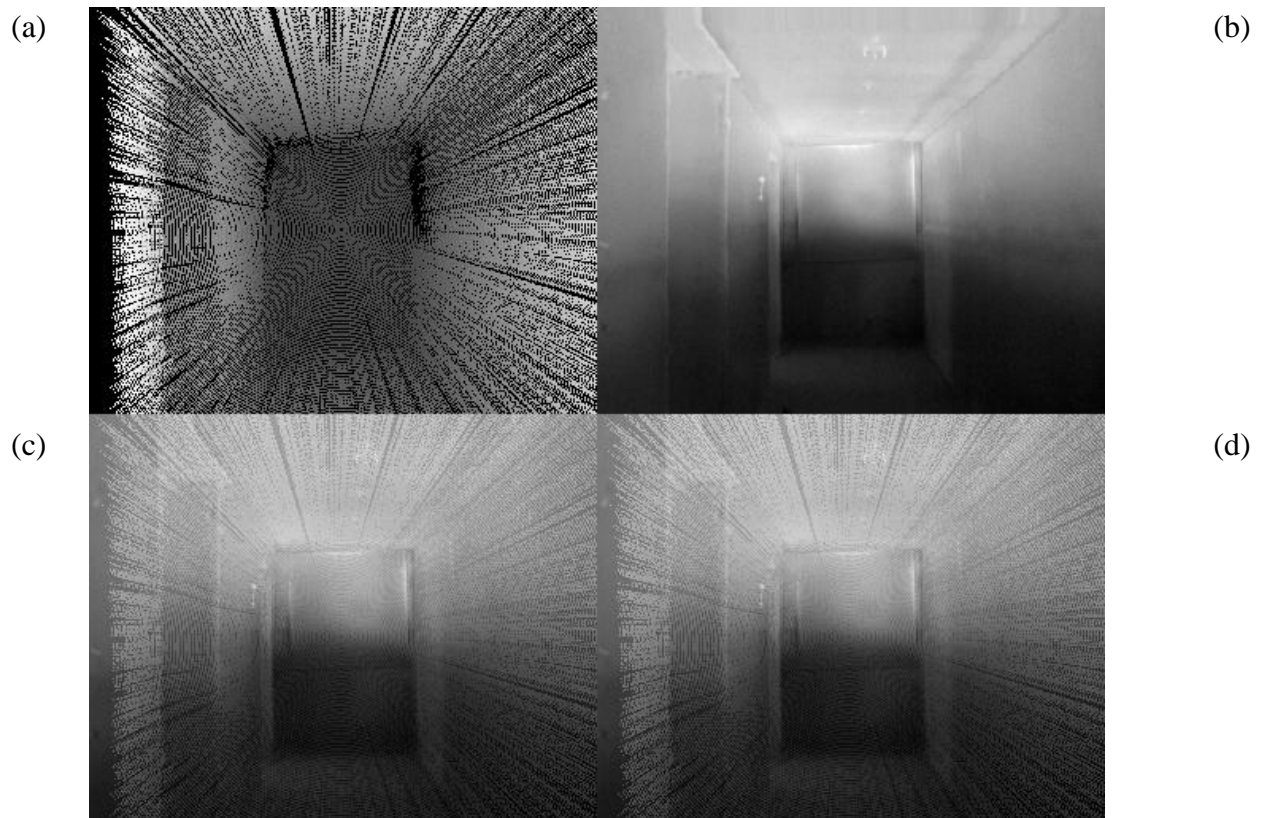


Figure 101: Images of LWIR stereo vision and LIDAR alignment for a hallway scene: (a) aligned LIDAR output of expected disparity map for the left LWIR camera frame; (b) left LWIR image of the scene after calibration and rectification processing; (c), (d) merged image of LIDAR disparity data and LWIR left image.

Appendix E: Tabulated Results for LWIR Stereo Vision System Filter Tests

- **Object Location Test Filter and Stereo Matching Settings**

Table 17 indicates the top setting for each filter for all three data sets (approximately isothermal, thermally diverse, and combined scenes) for the object location tests. Table 18 lists the stereo settings for the top filter settings for the object location tests.

Table 17: Parameter values for each filter for top performance for the object detection tests.

Function Name	Parameters	Approx. Isothermal	Thermally Diverse	Total
StereoAvgS	Method Box (kernel) size	Mean 5	Mean 5	Mean 5
StereoMeanShift	Box size Color closeness strength Color closeness used Power of color closeness	5 32 0 4	5 32 0 4	5 32 0 4
StereoAvgT	Method Number of frames	Mean 5	Mean 5	Mean 5
StereoWMeanT	Color closeness value Number of frames	2 5	2 5	2 5
StereoAvgST	Method Box size Number of frames	Mean 5 7	Mean 5 11	Mean 5 9
StereoWMeanST	Box size Color closeness strength Spatial color closeness used Power of spatial color closeness Temporal color closeness used Power of temporal color closeness Number of frames	5 2 0 4 0 4 7	5 16 0 4 1 4 11	5 16 0 4 1 4 11
StereoFrS	Box size ("box") Cut frequency 1 ("FCut1") Cut frequency 2 (for notch/band-pass) Type	5 1 <n/a> Low-pass	11 3 <n/a> Low-pass	15 4 <n/a> Low-pass
StereoFrT	Number of frames ("NFrames") Cut frequency 1 ("FCut1") Cut frequency 2 (for notch/band-pass) Type	11 3 <n/a> Low-pass	11 6 <n/a> Low-pass	11 4 <n/a> Low-pass
StereoLLMMSE	Box size Noise level	3 16	3 16	3 16
StereoWienF	Box size Noise level	3 256	3 256	3 256
StereoWienFWv	Box size (wavelet size) Wiener box size in wavelet domain Noise level	4 3 40000 (all)	4 3 10000 (all)	4 3 10000 (all)
StereoAvgWv	Box size (wavelet size) Method Averaging box size in wavelet domain	4 Mean 5	4 Mean 5	4 Mean 5
StereoWMeanWv	Box size (wavelet size) Weighted averaging box size Color closeness strength Power of color closeness	4 9 32 4	4 9 32 2	4 9 32 4
StereoAniDif	Function Iterations Gamma K	Exp 10 0.1 100	Exp 10 0.1 200	Exp 10 0.1 200
StereoWienFC	Box size Noise level Number of consecutive applications	3 256 9	3 256 9	3 256 9
StereoNLMeans	Box size Search area box size H-parameter (color closeness strength)	3 5 11	3 5 11	3 5 11

Table 18: Stereo settings for top filter settings for the object detection tests.

Function Name	Parameters	Approx. Isothermal	Thermally Diverse	Total
All filters	Box size	5	5	5
StereoAvgS	Match quality cutoff	20	20	20
StereoMeanShift	Match quality cutoff	60	20	20
StereoAvgT	Match quality cutoff	100	20	20
StereoWMeanT	Match quality cutoff	100	20	20
StereoAvgST	Match quality cutoff	20	20	20
StereoWMeanST	Match quality cutoff	100	20	20
StereoFrS	Match quality cutoff	20	20	20
StereoFrT	Match quality cutoff	60	20	20
StereoLLMMSE	Match quality cutoff	60	20	20
StereoWienF	Match quality cutoff	60	20	20
StereoWienFWv	Match quality cutoff	60	20	20
StereoAvgWv	Match quality cutoff	20	20	20
StereoWMeanWv	Match quality cutoff	60	20	20
StereoAniDif	Match quality cutoff	20	20	20
StereoWienFC	Match quality cutoff	20	20	20
StereoNLMeans	Match quality cutoff	20	20	20

- **Location of Room Boundaries Test Filter and Stereo Matching Settings**

Table 19 indicates the top filter settings for all three data sets (approximately isothermal, thermally diverse, and combined scenes) for the room boundary location tests. Table 20 lists the stereo settings for the top filter settings for the room boundary location tests.

Table 19: Parameter values for each filter for top performance for the boundary location tests.

Function Name	Parameters	Approx. Isothermal	Thermally Diverse	Total
StereoAvgS	Method Box (kernel) size	Mean 5	Mean 5	Mean 5
StereoMeanShift	Box size Color closeness strength Color closeness used Power of color closeness	5 32 0 4	5 32 0 4	5 32 0 4
StereoAvgT	Method Number of frames	Mean 5	Mean 7	Mean 7
StereoWMeanT	Color closeness value Number of frames	2 7	2 9	2 9
StereoAvgST	Method Box size Number of frames	Mean 5 11	Mean 5 3	Mean 5 7
StereoWMeanST	Box size Color closeness strength Spatial color closeness used Power of spatial color closeness Temporal color closeness used Power of temporal color closeness Number of frames	5 16 0 4 1 4 7	5 2 0 4 0 4 7	5 16 1 4 0 1 7
StereoFrS	Box size ("box") Cut frequency 1 ("FCut1") Cut frequency 2 (for notch/band-pass) Type	5 1 <n/a> Low-pass	5 1 <n/a> Low-pass	5 1 <n/a> Low-pass
StereoFrT	Number of frames ("NFrames") Cut frequency 1 ("FCut1") Cut frequency 2 (for notch/band-pass) Type	5 1 <n/a> Low-pass	15 4 <n/a> Low-pass	15 4 <n/a> Low-pass
StereoLLMMSE	Box size Noise level	3 16	3 16	3 16
StereoWienF	Box size Noise level	3 128	3 256	3 256
StereoWienFWv	Box size (wavelet size) Wiener box size in wavelet domain Noise level	4 3 40000 (all)	4 3 100 (low-freq) 40000 (high-freq)	4 3 100 (low-freq) 40000 (high-freq)
StereoAniDif	Function Iterations Gamma K	Exp 10 0.15 20	Exp 10 0.1 200	Exp 10 0.1 200
StereoWienFC	Box size Noise level Number of consecutive applications	3 32 5	3 64 3	3 32 5

Table 20: Stereo settings for top filter settings for the boundary location tests.

Function Name	Parameters	Approx. Isothermal	Thermally Diverse	Total
All filters	Box size	5	5	5
StereoAvgS	Match quality cutoff	20	20	20
StereoMeanShift	Match quality cutoff	60	20	60
StereoAvgT	Match quality cutoff	100	60	100
StereoWMeanT	Match quality cutoff	100	60	100
StereoAvgST	Match quality cutoff	20	20	20
StereoWMeanST	Match quality cutoff	60	60	60
StereoFrS	Match quality cutoff	20	20	20
StereoFrT	Match quality cutoff	100	60	60
StereoLLMMSE	Match quality cutoff	60	60	60
StereoWienF	Match quality cutoff	60	20	60
StereoWienFWv	Match quality cutoff	60	20	60
StereoAniDif	Match quality cutoff	20	20	20
StereoWienFC	Match quality cutoff	20	20	20

Appendix F: Analysis of Performance of Top LWIR Stereo Vision Image Filters

This appendix presents some of the top performing filters in the object and boundary location tests and the effects of these filters on images. The filters discussed here are StereoNLMeans, StereoAvgST, StereoWienFC, and StereoAniDif. StereoNLMeans, StereoAvgST, StereoWienFC were the top three performing filters in the approximately isothermal scene for the object location tests. These filters also performed well in the thermally diverse scene for object location. The StereoWienFC filter was also the top performing filter for the approximately isothermal scene for the boundary location tests, with StereoAniDif providing the second best results. Both filters also performed well in the thermally diverse scene for boundary location.

- StereoNLMeans [1]

This filter operates by comparing a window around each pixel of interest to windows around other pixels in the image. Data from this comparison is used to update the pixel of interest. If the window at another location is similar to the window around the pixel of interest, its center pixel value will weigh heavier in an average of compared window center values than locations where the window was less similar to the window around the pixel of interest. In effect, the pixel value is updated based on a weighted average of surrounding pixels, where the weighting is determined by the similarity of windows around the pixels to the window around the pixel of interest.

This filter was the top performing filter for the approximately isothermal scene for the object location tests. The top filter settings were to use a window size of 3 (“Box size” parameter), a search box area of 11 (5 pixels before and after the pixel of interest in rows and columns, “Search area box size” parameter = 5), and a color closeness weight of 11 for the “H-parameter (color closeness strength)” parameter.

This filter works under the assumption that each image will contain many pixels with similar values and similar windows. It operates by averaging these values based on window similarity to remove noise effects in the imagery. Unlike spatial weighted average filtering (StereoMeanShift and StereoWMeanST filter functions also tested, for example) that determines an updated value

based on individual pixel similarity, in application, this means that windows that are most similar will weigh heaviest on the output value of each pixel, which leaves dissimilar windows to weigh less. As a result, similar valued pixels that have dissimilar windows do not provide as strong influence on results as they would with spatial weighted averaging. This can be beneficial, for instance, along an edge in the scene, where similar locations along the edge will all have strong averaging effects on each other due to having similar windows while pixels away from the edge with dissimilar windows will have weak effects.

In application, increasing the search area box size provides more smoothing to the image since it causes more pixels to influence the final pixel value. This is demonstrated in the plot in Figure 102, where a line across the approximately isothermal scene for the object location tests is plotted with two search area window sizes. In the figure, the top performing setting for the object location tests is shown along with a setting with a smaller “Search area box size” parameter value.

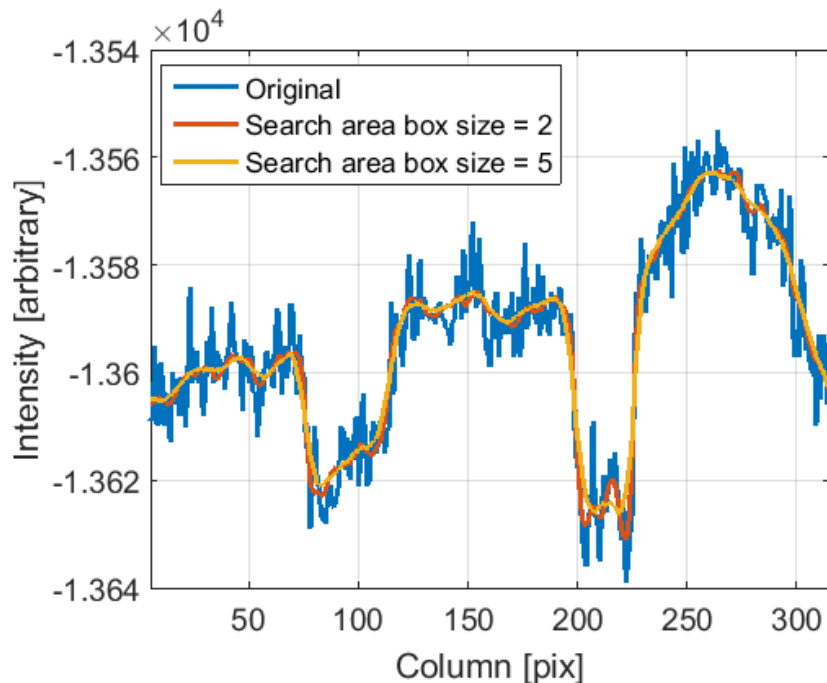


Figure 102: Effects from Non-Local Means filter on a row across both targets in the approximately isothermal scene for the object location tests. The top performing setting is shown (“Search area box size” = 5) and the results with a smaller search box is shown (“Search area box size” = 2).

- StereoAvgST

This filter operates as a combination of the StereoAvgS and StereoAvgT filters, averaging over a spatial window through multiple frames (time). This filter requires the scene to be stationary or slow-moving since multiple frames are being used in averaging, which is a drawback to using the filter. The filter works well if the spatially surrounding pixels are distributed evenly around the desired value of the pixel of interest and if the pixel of interest and its surrounding pixels vary through time evenly around the desired value of the pixel of interest. The noise removed is assumed to be distributed evenly about the desired pixel output value.

The top filter for the approximately isothermal scene, the thermally diverse scene, and the combined scene for the object location tests used the mean filter (“Method” parameter) with a neighborhood “Box size” parameter of 5. The “Number of frames” varied depending on the scene, with 7 frames resulting in top results for the approximately isothermal scene, 11 frames resulting in the top results for the thermally diverse scene, and 9 frames resulting in the top results for the combined scene. The effects of the filter on the approximately isothermal scene for the object location tests are shown for a row across both targets in the plot in Figure 103. In the plot, there is a noticeable change with the addition of the 7 frame averaging of the filter but little change between 7 and 11 frames for the approximately isothermal scene. Figure 104 contains two plots which show a row across both targets in the thermally diverse scene and a zoomed-in view at the left side of the left target. The results here also show noticeable smoothing comparing the original data to the 7 frame averaging and little change between 7 and 11 frames.

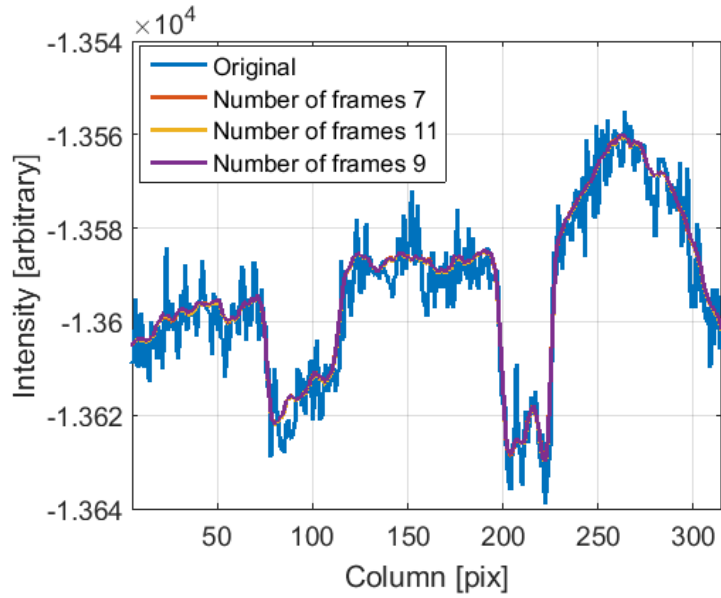


Figure 103: Effects from the StereoAvgST filter on a row across both targets in the approximately isothermal scene for the object location tests. The “Number of frames” is shown for the top case for the approximately isothermal scene (7), for the thermally diverse scene (11), and for the combined scene (9).

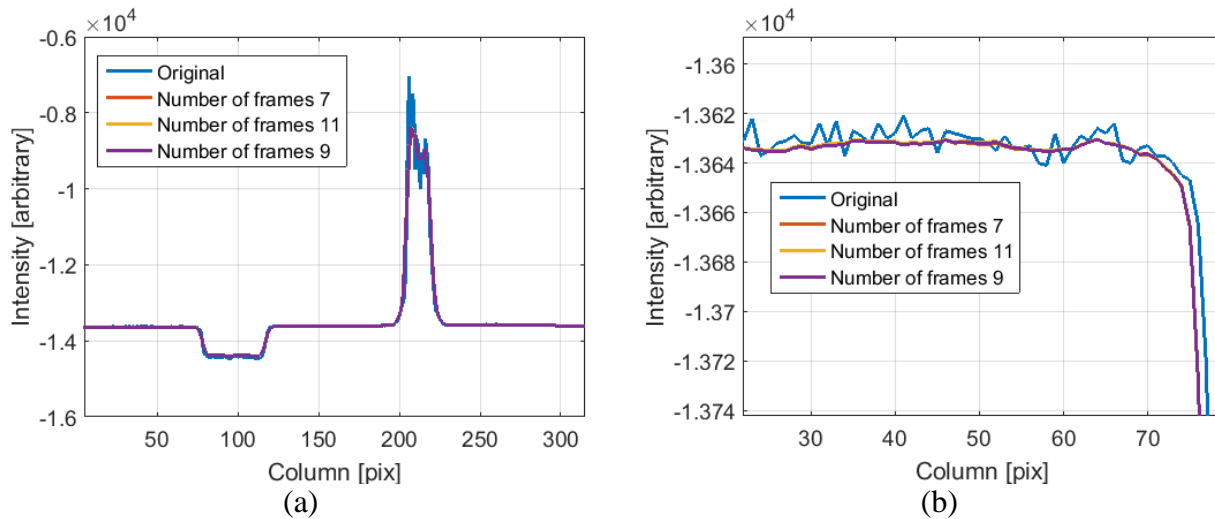


Figure 104: Effects from the StereoAvgST filter on a row across both targets in the thermally diverse scene for the object location tests. The “Number of frames” is shown for the top case for the approximately isothermal scene (7), for the thermally diverse scene (11), and for the combined scene (9): (a) view of the entire row and (b) zoomed-in view at the left side of the left target.

- StereoWienFC [2]

This filter operates by applying a Wiener filter to image data multiple times in a row. The Wiener filter removes noise under the assumption that it is additive white Gaussian noise [2]. The first pass of the filter removes much of the noise, with consecutive passes further smoothing the data [2]. The consecutive passes for smoothing have previously been applied to gradient information when smooth gradient information was desired for thermography purposes [2]. Here, the multiple passes are applied to the image itself for smoothing.

The application of this consecutive filter depends on the local variance and assumed noise variance. When the local variance is smaller than the assumed noise variance, the updated pixel value at each location of interest is just the mean of the local window. When the local variance is greater than the assumed noise variance, then the output value is influenced by the difference between the value of the pixel of interest and the mean of the local window. This results in smoothing of low-texture regions and results in preservation of high-texture regions which have a relatively high variance. Over each consecutive application, the low-texture regions become further smoothed with the edges still preserved.

The parameters for the top filter for all scenes for the object location tests used a “Box size” of 3, a “Noise level” of 256, and 9 consecutive applications of the Wiener filter (“Number of consecutive applications” parameter). The effects of the consecutive applications on the approximately isothermal scene for the object location tests are shown in the plot in Figure 105 for a row crossing both objects. The first pass removes many of the jumps in intensity with further passes smoothing the results.

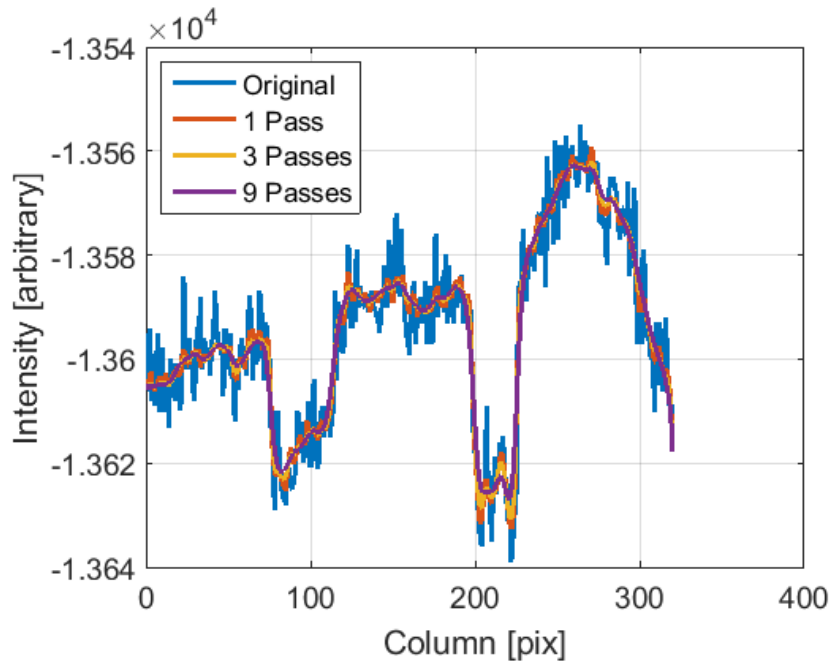


Figure 105: Effects from the StereoWienFC (consecutive Wiener) filter on a row across both targets in the approximately isothermal scene for the object location tests for the top case number of passes (9) and two other values for “Number of consecutive applications”.

The approximately isothermal scene, thermally diverse scene, and combined scene all used a “Box size” of 3, but had differing noise level values and differing number of consecutive applications for the boundary location tests. For the approximately isothermal scene and for the combined scene, the noise level for the top filter was 32 (“Noise level” parameter) with 5 consecutive applications (“Number of consecutive applications” parameter). For the thermally diverse case, the noise level for the top filter was 64 with 3 consecutive applications. A comparison of both settings on the approximately isothermal scene for the boundary location tests is shown in the plots in Figure 106 for a row across the lower portion of the hallway and a row across the upper portion of the hallway. The results for both settings appear similar here. The plots in Figure 107 show the same data for the thermally diverse scene. The similarity between the results from both filter settings is highlighted in the plot in Figure 108, which has a zoomed-in view around the peak intensity of the plot in Figure 107(b). As with the object location tests, the first pass of the filter removes much of the noise with consecutive passes further smoothing the data. This further smoothing depends on the local variance and assumed noise variance. As seen in Figure 108, the location of edges (i.e. intensity jumps) appear to be

the same location for both filters with changes most visible in the flatter (i.e. low intensity variation) part of the plot, confirming the conservation of edges and smoothing of low texture regions.

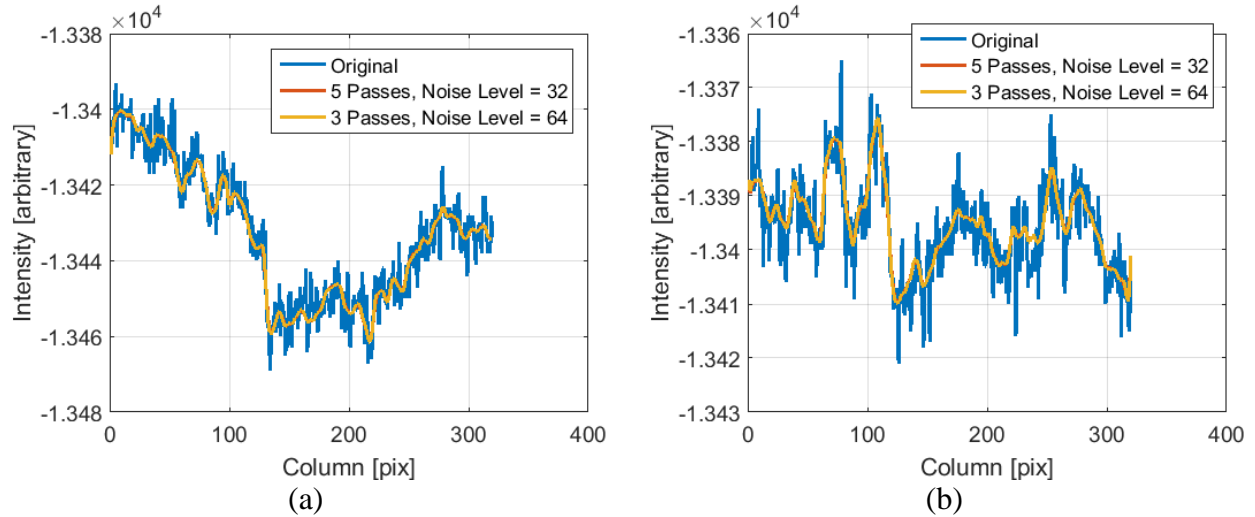


Figure 106: Effects from the StereoWienFC (consecutive Wiener) filter on a row across the hallway in the approximately isothermal scene for the boundary location tests for two settings: (a) lower portion of the hallway and (b) upper portion of the hallway.

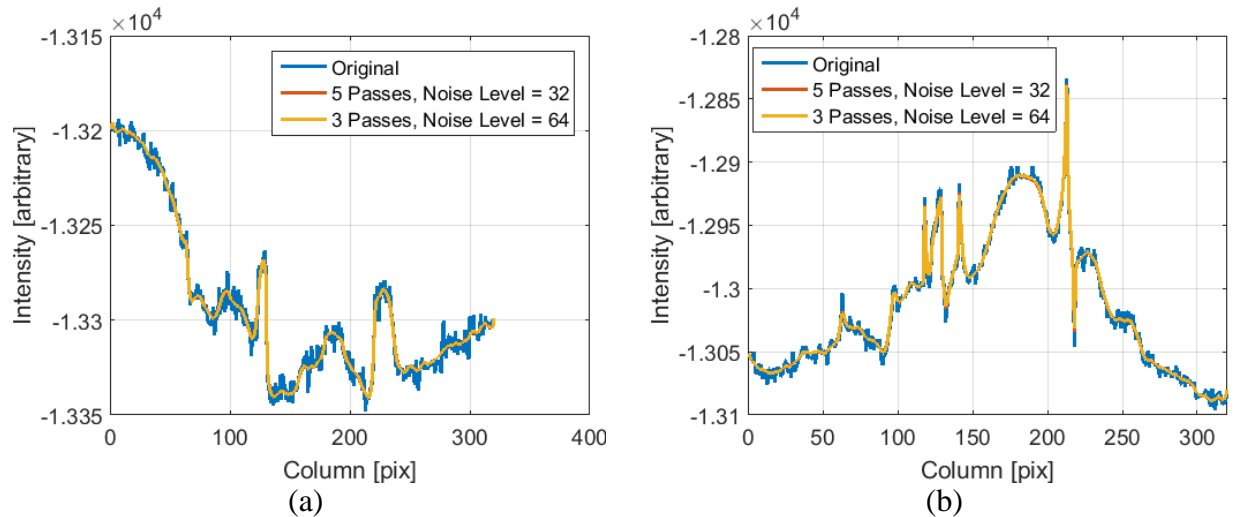


Figure 107: Effects from the StereoWienFC (consecutive Wiener) filter on a row across the hallway in the thermally diverse scene for the boundary location tests for two settings: (a) lower portion of the hallway and (b) upper portion of the hallway.

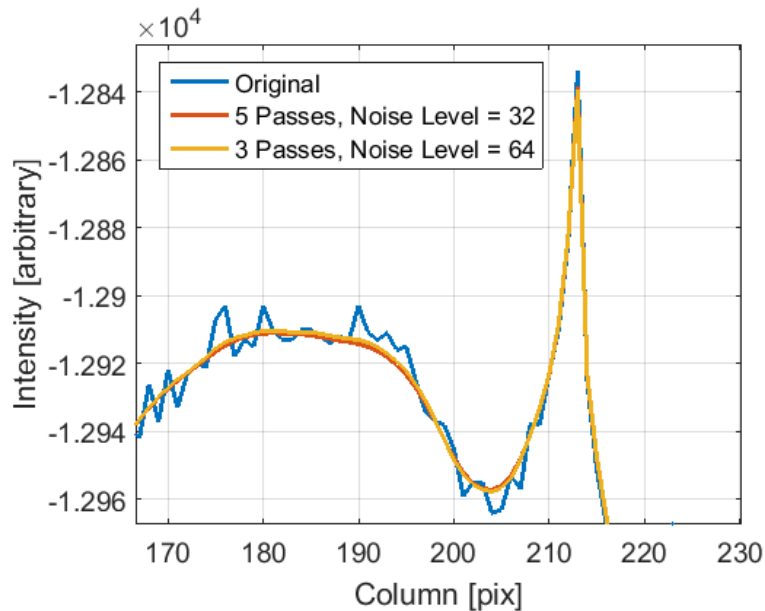


Figure 108: Zoomed-in view showing effects from the StereoWienFC (consecutive Wiener) filter on a row across the upper portion of the hallway in the thermally diverse scene for the boundary location tests for two settings.

- StereoAniDif [3, 4]

This filter operates in the spatial domain using one of two functions for anisotropic diffusion. During smoothing, boundaries are preserved using intensity difference information between each pixel and its neighbors [3]. The output image is determined iteratively.

The function type (“Function” parameter) for the top filter for the approximately isothermal scene, the thermally diverse scene, and the combined scenes for the boundary location tests was the exponential function (“Exponential”) with 10 for the “Iterations” parameter. The “Gamma” and “K” values were 0.15 and 20, respectively, for the approximately isothermal scene and 0.1 and 200 for the thermally diverse scene and combined scenes. The plot in Figure 109 shows both filter settings in a lower and an upper image row of the approximately isothermal scene for the boundary location tests. Little difference is present between both settings for the approximately isothermal scene for the boundary location tests.

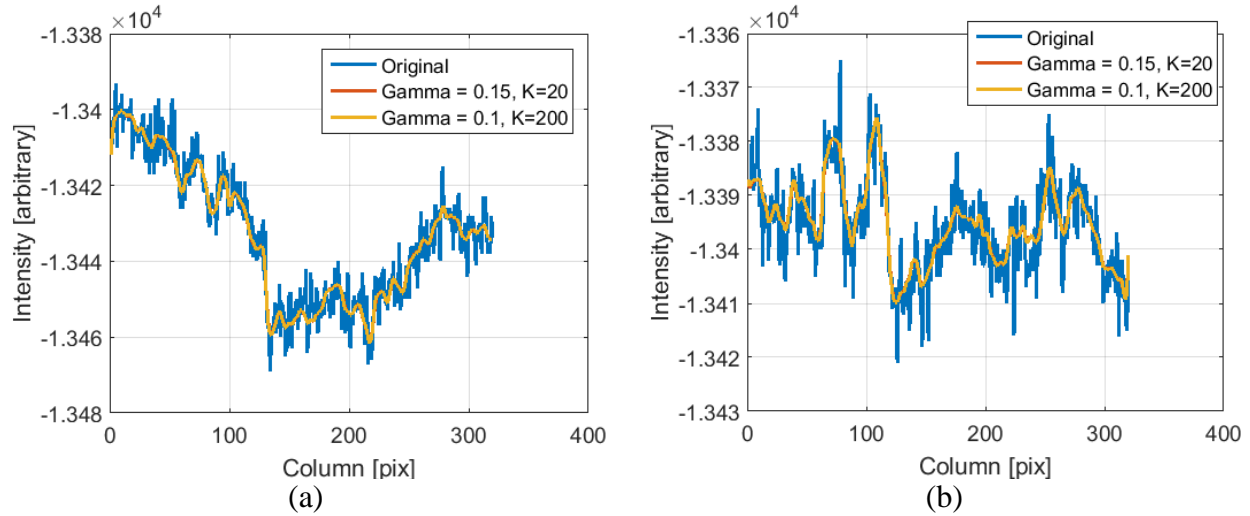


Figure 109: Effects from the StereoAniDif function on a lower and upper row across the hallway in the approximately isothermal scene for the boundary location tests: (a) lower row and (b) upper row.

Figure 110 contains plots of the thermally diverse scene for an upper and lower row for the thermally diverse scene for the boundary location tests. Due to the application of the exponential function, an increase in “K” results in an exponential increase in the effects of the intensity difference across each pixel of interest and its neighbors, while an increase in “Gamma” has a linear increase in the effects of the intensity difference. This is visible in the plot in Figure 110. Increasing the values causes more changes to happen at each iteration based on differences in image intensity. Figure 111 shows a zoomed-in view of the area around the peak intensity of the upper row shown in Figure 110. The top parameter setting values for the thermally diverse scene cause the peak to be lower than when using the top parameter setting values for the approximately isothermal scene for the boundary location tests.

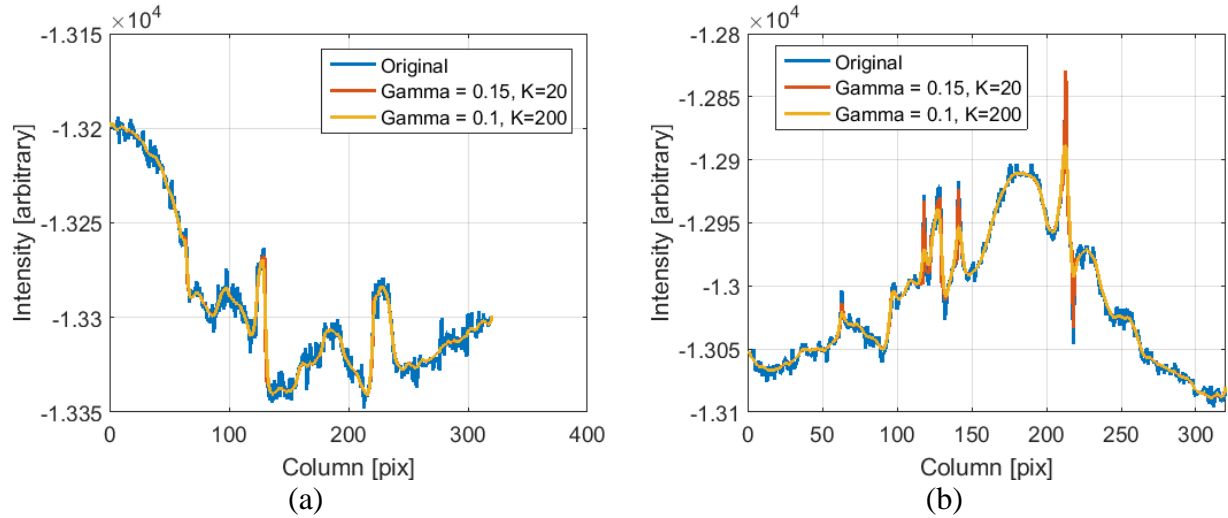


Figure 110: Effects from the StereoAniDif function on a lower and upper row across the hallway in the thermally diverse scene for the boundary location tests: (a) lower row and (b) upper row.

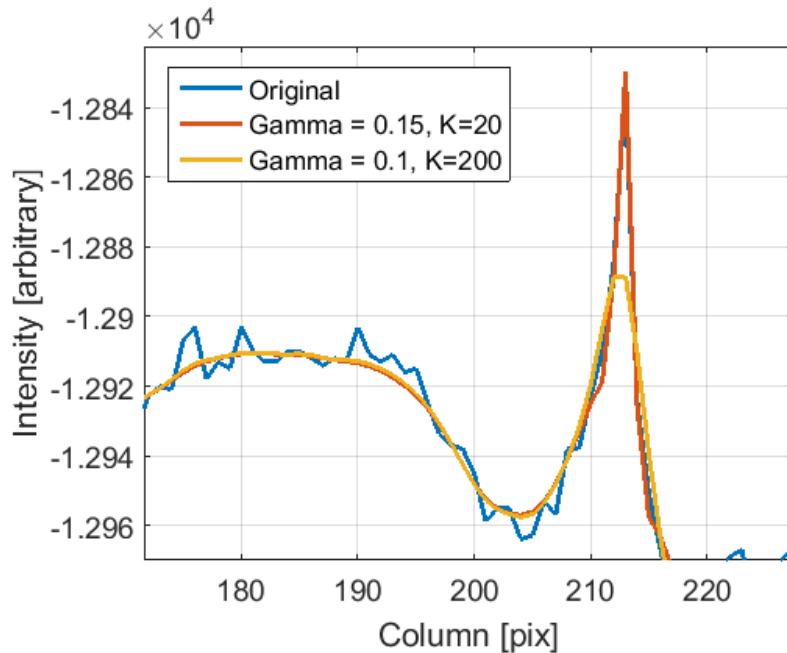


Figure 111: Zoomed-in view of the area around the peak intensity shown in the upper row plot of the last figure for the thermally diverse scene for the boundary location tests.

- Summary of top filters

The plot in Figure 112 shows the intensities along an image row of the approximately isothermal scene crossing both targets for the object location tests for the top filter settings for the three top filters for the approximately isothermal scene. The plot in Figure 113 shows the same filters

with the top settings for the thermally diverse scene, applied to the thermally diverse seen. The plots in Figure 114 show zoomed in images of the data in Figure 113 for the left and right targets, respectively. In the approximately isothermal case, all three filters visibly reduce noise with the StereoNLMeans and StereoWienFC filters producing similar results for most locations along the row, with the StereoAvgST appearing to have more variation. For the thermally diverse case, the results along the row indicate the StereoAvgST results are removed from the original data more than the StereoNLMeans and StereoWienFC results.

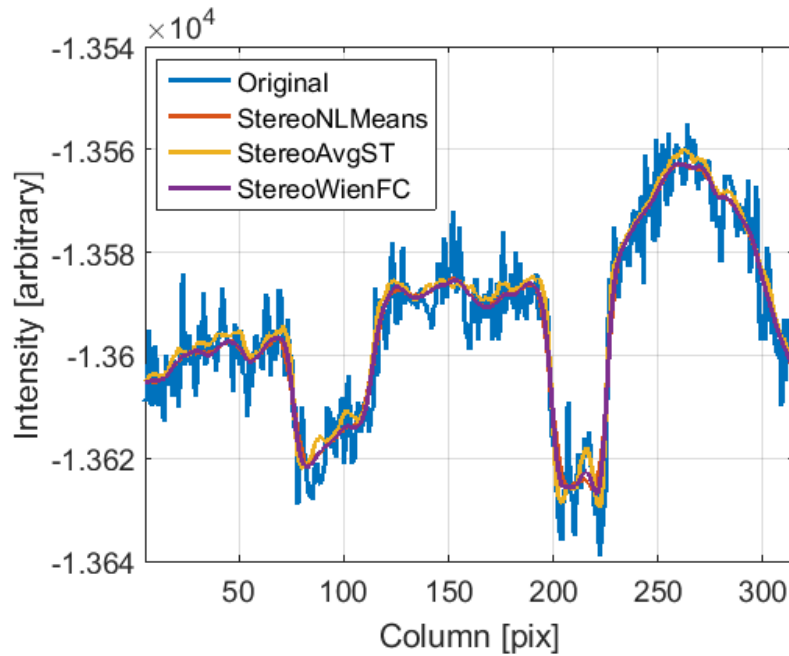


Figure 112: Filter results from top performing filters for the approximately isothermal scene for the object location tests.

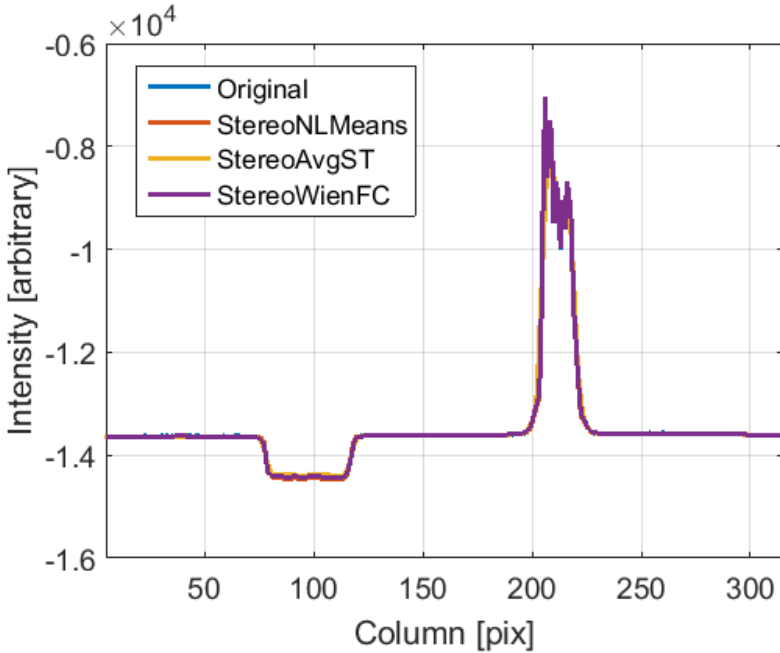


Figure 113: Filter results from top performing filters for the thermally diverse scene for the object location tests.

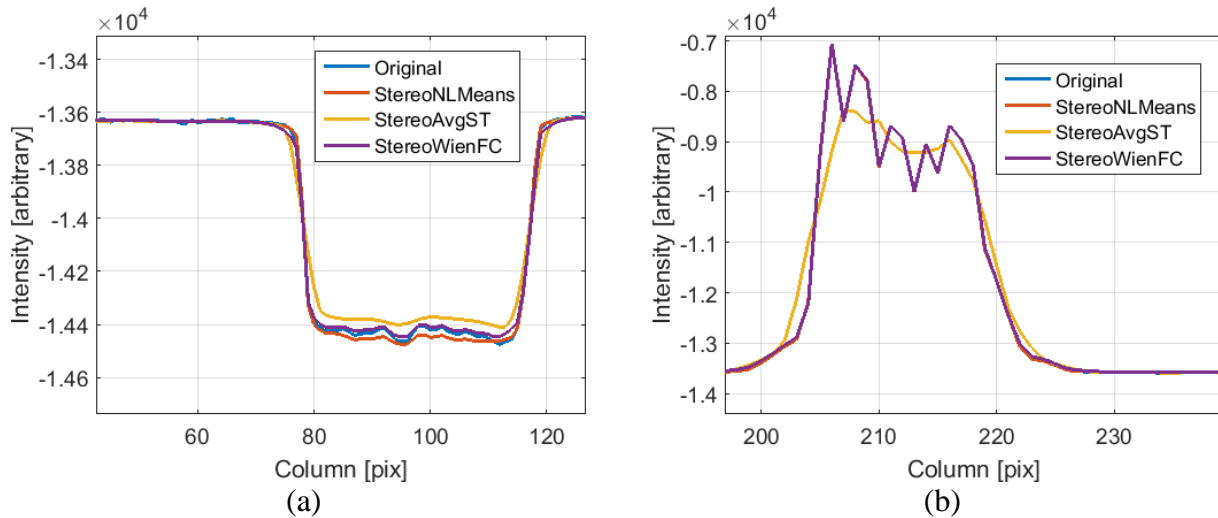


Figure 114: Zoomed-in view of (a) the left target and (b) the right target for the thermally diverse scene for the object location tests for top performing filter settings.

The plot in Figure 115 shows data along an image row for the top two filters with the top performing settings for the approximately isothermal scene for the boundary location tests. The plot in Figure 116 shows the same filters for the thermally diverse scene for the boundary

location tests for the top settings for that scene. Both filters visibly reduce noise with similar resulting curves for the rows shown. The largest discrepancy is in the upper layer for the thermally diverse case. There are sharp peaks in the data that are eroded more by the StereoAniDif filter than by the StereoWienFC. This is due to the consecutive Wiener filter more strongly preserving boundaries by its design than the anisotropic diffusion filter.

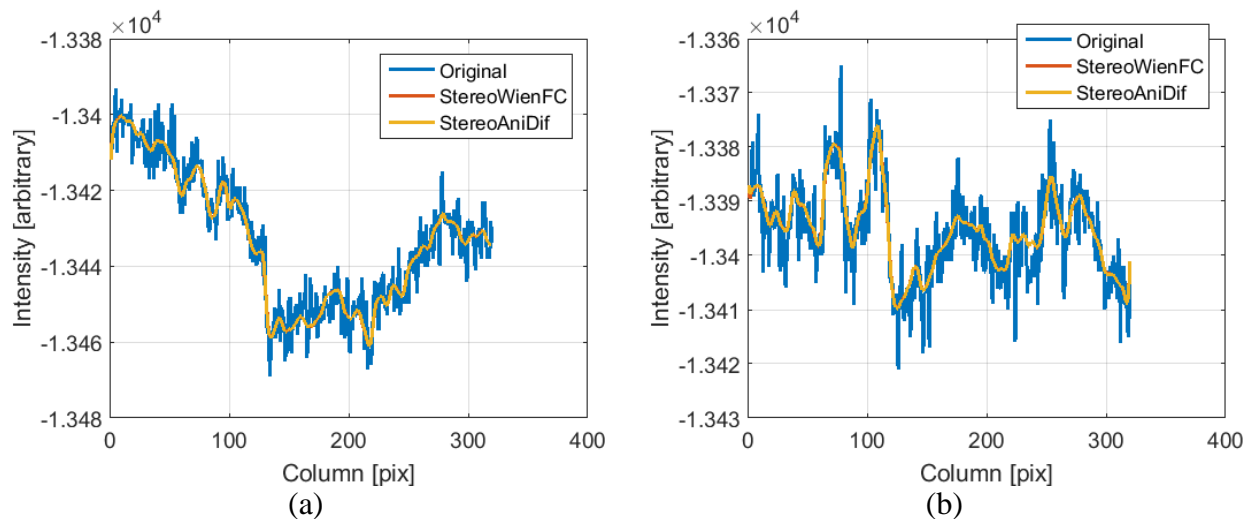


Figure 115: Effects from top performing filters for the approximately isothermal scene for the boundary location tests: (a) lower row and (b) upper row.

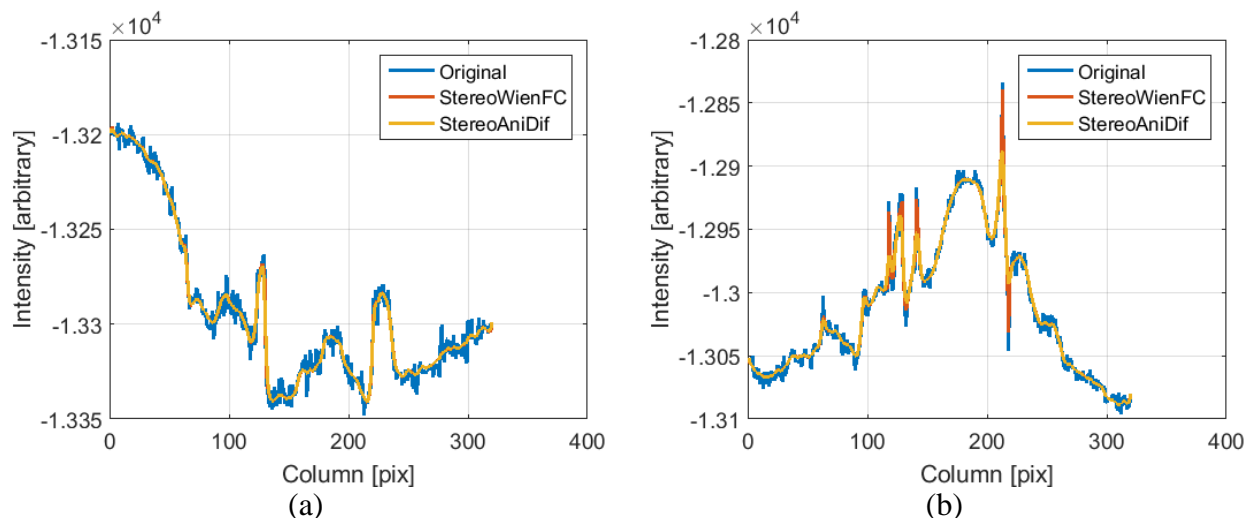


Figure 116: Effects from top performing filters for the thermally diverse scene for the boundary location tests: (a) lower row and (b) upper row.

- References

- [1] Buades, A., Coll, B., & Morel, J. M. (2005). A review of image denoising algorithms, with a new one. *Multiscale Modeling & Simulation*, 4(2), 490-530.
- [2] Rainieri, S., & Pagliarini, G. (2002). Data filtering applied to infrared thermographic measurements intended for the estimation of local heat transfer coefficient. *Experimental thermal and fluid science*, 26(2), 109-114.
- [3] Nixon, M. S., & Aguado, A. S. (2012). *Feature extraction & image processing for computer vision*. Academic Press.
- [4] Perona, P., & Malik, J. (1990). Scale-space and edge detection using anisotropic diffusion. *Pattern Analysis and Machine Intelligence, IEEE Transactions on*, 12(7), 629-639.

Appendix G: Discussion of LIDAR Intensity Variations

There is variation in the intensity of the LIDAR returns to solid boundaries. This is due to a combination of the angular dependence on the reflectivity of the surface the LIDAR beam is hitting and a general variation in the reflectivity of the surface due to surface material and soot build-up on the surfaces from previous fire tests. Surfaces with angles close to parallel to the beam have weaker (lower intensity) returns as do surfaces covered in soot. This soot-build-up is largely in the upper portion of the hallway. Figure 117 contains images to show this for a clear LIDAR frame. In the figure, the upper left and right images contain intensity information for a hallway scene as given by the LIDAR returns. These correspond to the disparity map in the lower left portion of the figure, and an IR image of the same hallway after a fire test is shown in the lower right portion of the figure. The intensity for this frame (shown in the upper two images of the figure) ranges from 47 to 4682 depending on the location of the LIDAR return. In the top left image, the intensity is shown, scaled from 0 to 4682 with 0 representing non-LIDAR return locations. In the top right image, all intensity values are increased by a constant to highlight low intensity values difficult to see in the top left image. In both intensity displays, brighter color indicates higher intensity with black indicating no LIDAR return information.

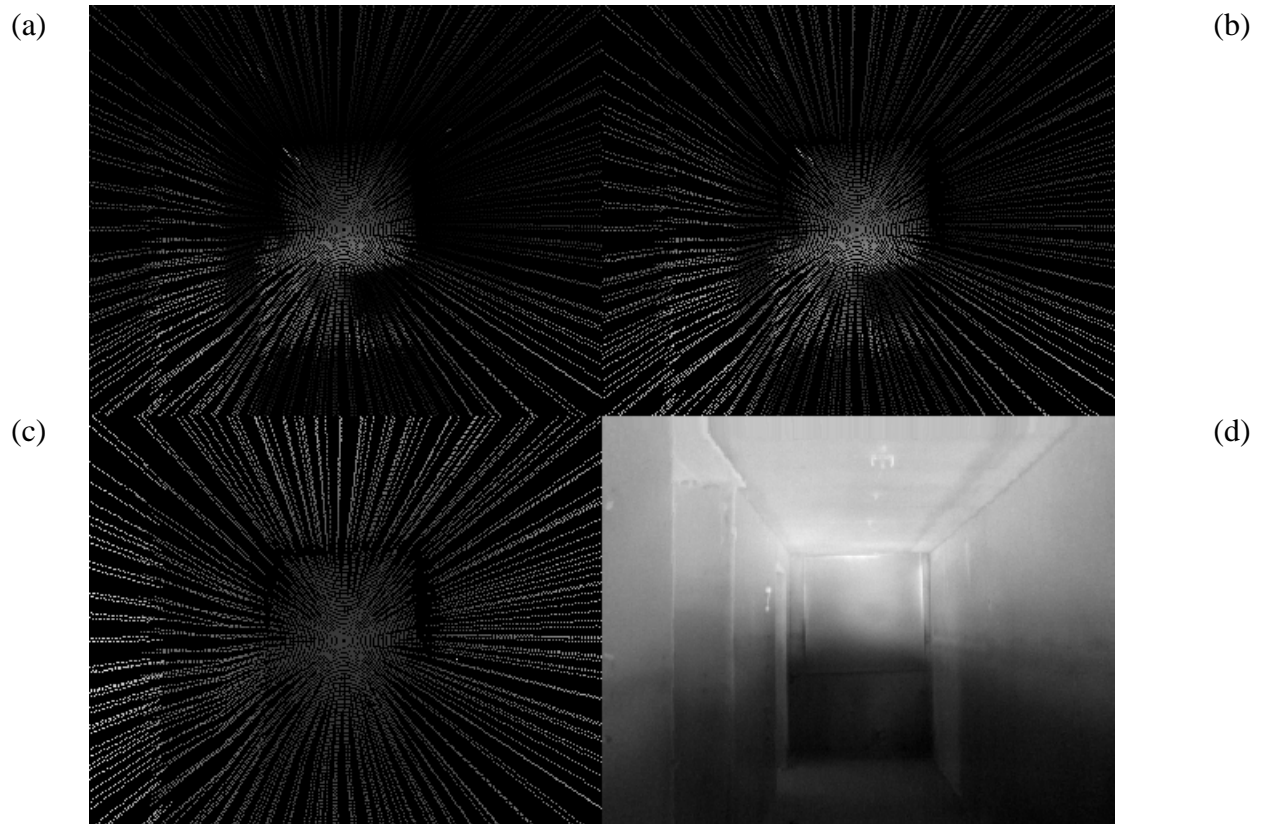


Figure 117: Intensity information for a hallway scene. (a) Intensity values scaled from 0 to max intensity with 0 indicating no return; (b) Intensity values with an added constant to differentiate low intensity values from locations with no LIDAR return information; (c) corresponding disparity information from the LIDAR; (d) IR image of the hallway after a test.

Appendix H: Algorithms for Sensor Model Application

The sensor model application for the low-attenuation and high-attenuation point clouds is shown in Algorithm 1. The sensor model application for the LWIR stereo vision point clouds is shown in Algorithms 2 and 3.

Algorithm 1: LIDAR sensor model application.

LIDAR Sensor Model Application	
1	//Initialize voxel arrays
2	$m_{i,j,k,L}(Case) = \begin{cases} 0, & Case = \emptyset \\ 0, & Case = Occ \\ 0, & Case = F \\ 0, & Case = \{Occ, F\} \end{cases} \forall voxels_{i,j,k}$
3	$S_{Occ,L} = 0 \forall voxels_{i,j,k}$ to store sensor model evidence for occupied state for all voxels
4	$Pres_O = 0 \forall voxels_{i,j,k}$ as a binary indicator of presence of evidence for occupied state for all voxels
5	$S_{F,L} = 0 \forall voxels_{i,j,k}$ to store sensor model evidence for free space state for all voxels
6	
7	//Update voxels along ray based on sensor model
8	for each point in point cloud
9	ray trace from sensor to point and past
10	if occupied state evidence for current voxel from current point, update
11	$S_{Occ,L}$, to current sensor model evidence if greater
12	$Pres_O$, to 1 to indicate presence of evidence for occupied state
13	
14	else if free state evidence for current voxel from current point, update
15	$S_{F,L}$ to current sensor model evidence if greater
16	
17	end //if
18	end //ray trace
19	end //for
20	
21	//Calculate evidences for occupied and free space voxel arrays
22	$S_{F,L} = S_{F,L} * (Pres_O == 0) \forall voxels_{i,j,k}$
23	$S_{\{Occ,F\},L} = 1 - (S_{Occ,L} + S_{F,L}) \forall voxels_{i,j,k}$
24	$m_{i,j,k,L}(Case) = \begin{cases} 0, & Case = \emptyset \\ S_{Occ,L}, & Case = Occ \\ S_{F,L}, & Case = F \\ S_{\{Occ,F\},L}, & Case = \{Occ, F\} \end{cases} \forall voxels_{i,j,k}$

Algorithm 2: LWIR stereo vision sensor model application.

LWIR Stereo Vision Sensor Model Application	
1	//Initialize voxel arrays
2	$Cost_N = 0 \forall voxels_{i,j,k}$ to store highest cost affecting each voxel for occupied state
3	$Disp_N = 0 \forall voxels_{i,j,k}$ to store highest disparity affecting each voxel for occupied state
4	$C_O = 0 \forall voxels_{i,j,k}$ to count number of points affecting each voxel for occupied state
5	$C_F = 0 \forall voxels_{i,j,k}$ to count number of points affecting each voxel for free space state
6	
7	//Update voxels along ray based on point location, disparity, and cost
8	for each point in point cloud
9	ray trace from sensor to point and past
10	if occupied state evidence for current voxel from current point, update
11	$Cost_N$ with highest cost
12	$Disp_N$ with highest disparity
13	Increment C_O
14	
15	else if free state evidence for current voxel from current point, update
16	Increment C_F
17	
18	end //if
19	end //ray trace
20	end //for
21	
22	Calculate evidences for occupied and free space voxel arrays using other algorithm

Appendix I: Permissions

- Permission for chapter 3, which is based off of the accepted form of a paper that appears as part of Starr, Joseph W. and Lattimer, B. Y. (2013) "Evaluation of Navigation Sensors in Fire Smoke Environments" in Fire Technology Journal. The final publication is available at link.springer.com. Location: <http://link.springer.com/article/10.1007/s10694-013-0356-3> and DOI: [10.1007/s10694-013-0356-3](https://doi.org/10.1007/s10694-013-0356-3)

Copyright email from publisher for accepted journal article:



Joseph Starr <jwstarr@vt.edu>

Copyright Transfer Statement (CTS) for your article in Fire Technology (356)

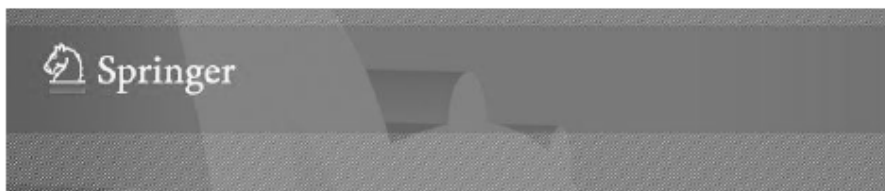
1 message

Springer <springerauthorquery@springeronline.com>

Sun, Jul 28, 2013 at 10:56 PM

Reply-To: "authorhelpdesk@springer.com" <authorhelpdesk@springer.com>

To: "jwstarr@vt.edu" <jwstarr@vt.edu>



Copyright Transfer

29.07.2013

visit us at springer.com

Confirmation of your Copyright Transfer

Dear Author,

Please note: This e-mail is a confirmation of your copyright transfer and was sent to you only for your own records.

The copyright to this article, including any graphic elements therein (e.g. illustrations, charts, moving images), is hereby assigned for good and valuable consideration to Springer Science+Business Media New York effective if and when the article is accepted for publication and to the extent assignable if assignability is restricted for by applicable law or regulations (e.g. for U.S. government or crown employees). Author warrants (i) that he/she is the sole owner or has been authorized by any additional copyright owner to assign the right, (ii) that the article does not infringe any third party rights and no license from or payments to a third party is required to publish the article and (iii) that the article has not been previously published or licensed.

The copyright assignment includes without limitation the exclusive, assignable and sublicensable right, unlimited in time and territory, to reproduce, publish, distribute, transmit, make available and store the article, including abstracts thereof, in all forms of media of expression now known or developed in the future, including pre- and reprints, translations, photographic reproductions and microform. Springer may use the article in whole or in part in electronic form, such as use in databases or data networks for display, print or download to stationary or portable devices. This includes interactive and multimedia use and the right to alter the article to the extent necessary for such use.

An author may self-archive an author-created version of his/her article on his/her own website and/or the repository of Author's department or faculty. Author may also deposit this version on his/her funder's or funder's designated repository at the funder's request or as a result of a legal obligation, provided it is not made publicly available until 12 months after official publication by

Springer. He/she may not use the publisher's PDF version, which is posted on <http://link.springer.com>, for the purpose of self-archiving or deposit. Furthermore, Author may only post his/her own version, provided acknowledgement is given to the original source of publication and a link is inserted to the published article on Springer's website. The link must be accompanied by the following text: "The final publication is available at <http://link.springer.com>".

Prior versions of the article published on non-commercial pre-print servers like arXiv.org can remain on these servers and/or can be updated with Author's accepted version. The final published version (in pdf or html/xml format) cannot be used for this purpose. Acknowledgement needs to be given to the final publication and a link must be inserted to the published article on Springer's website, accompanied by the text "The final publication is available at link.springer.com". Author retains the right to use his/her article for his/her further scientific career by including the final published journal article in other publications such as dissertations and postdoctoral qualifications provided acknowledgement is given to the original source of publication.

Author is requested to use the appropriate DOI for the article. Articles disseminated via <http://link.springer.com> are indexed, abstracted and referenced by many abstracting and information services, bibliographic networks, subscription agencies, library networks, and consortia.

After submission of the agreement signed by the corresponding author, changes of authorship or in the order of the authors listed will not be accepted by Springer.

This is an automated e-mail; please do not reply to this account. If you have any questions, please go to our help pages.

Thank you very much.

Kind regards,

Springer Author Services

Article Details

Journal title

Fire Technology

DOI

10.1007/s10694-013-0356-3

Copyright transferred to

Springer Science+Business Media New York

Article title

Evaluation of Navigation Sensors in Fire Smoke Environments

Corresponding Author

Joseph Starr

Transferred on

Mon Jul 29 04:56:34 CEST 2013

What would you like to do next?

[The New SpringerLink](#)

[Your Book Can Live Forever!](#)

Delivering results with the speed, accuracy and convenience that today's researchers need.

[FIND OUT MORE](#)

Did you publish a book before 2005? Contact us to make your book available again in print and online as part of the Springer Book Archives!

[FIND OUT MORE](#)

Visit other Springer Sites

- **SpringerLink** : Look inside our eJournals and eBooks
- **SpringerImages** : Find all graphics of our publications
- **SpringerProtocols** : Database of reproducible protocols in life & biomedical sciences
- **SpringerMaterials** : Numerical data & functional relationships in science & technology

Service Contacts

Springer Customer Service Center

Haberstr. 7
69129 Heidelberg
Germany
phone: +49 6221 345 0
fax: +49 6221 345 4229
email:
subscriptions@springer.com
Questions:
authorhelpdesk@springer.com

Springer New York, LCC

233 Spring Street
New York, NY 10013
USA
phone: +1 212 460 1500 or 800-SPRINGER
(Weekdays 8:30am - 5:30pm ET)
fax: +1 212-460-1700
email: journals-ny@springer.com
Questions:
authorhelpdesk@springer.com